Stochastic multiscale modeling of dynamic recrystallization

Thesis by
Abbas Davud Tutcuoglu

In Partial Fulfillment of the Requirements for the
Degree of
Doctor of Philosophy

CALIFORNIA INSTITUTE OF TECHNOLOGY
Pasadena, California

2019
Defended March 18, 2019

Abbas Davud Tutcuoglu
ORCID: 0000-0003-2360-706X

ACKNOWLEDGEMENTS

The first time I visited Caltech was during the summer of 2014 when I was working on my Master's thesis with Prof. Carmel Majidi at Carnegie Mellon University in Pittsburgh, PA. Almost five years later, in this thesis, I am summarizing the research I conducted both at Caltech, in the sunny state of California, and ETH Zurich, in the picturesque country of Switzerland. To get to this point, however, necessitated the continuous motivation and support from my colleagues, friends, and family.

First, I would like to thank Prof. Dennis Kochmann for the myriad opportunities he has granted me. As an advisor, he helped me to structure the way I am conducting research and provided essential feedback, guidance, and ideas. His course on continuum mechanics provided a profound basis, which assisted me throughout my studies. Finally, tasks such as the administration of the group server and the code repository allowed me to get substantial practical experience. I would also like to thank Prof. Kaushik Bhattacharya for the ideas shared with me in our meetings along with the invaluable feedback in the writing of my first contribution. Prof. Chiara Daraio's and Prof. Guruswami Ravichandran's suggestions during my candidacy in December 2017 led me to the topic of my second contribution for which I would like to express my gratitude. I thank the chair of my thesis, Prof. Michael Ortiz, for the feedback he gave Siddhant Kumar and me for our respective third contribution.

I always felt lucky to be part of a fun group of people that were continuously helpful, and that made coming to work on a Monday morning enjoyable. As pronounced proponents of a constructive feedback culture, I would like to guide particular gratitude to my former office mates and close friends, Bastian and Raphael. Research in computational solid mechanics is seldom the result of the work of one, and therefore I also thank Andrej, Greg, Siddhant, Vidyasagar and Yannick for stimulating discussions. Outside the lab, I would like to thank Jorge, Marcel, Vin, Amanda, Gautham, Magnus, Simon, Thomas, Maria and Arthur for more than three most delightful years. This collaboration was made possible through the support of the Army Research Laboratory under Cooperative Agreement Number W911NF-12-2-0022, for which I am deeply grateful.

It is of no surprise that a Ph.D. is an energy-consuming undertaking and for me to be able to cope with this challenge in my life, I am eternally grateful for the support from my new Southern Tyrolean neighbor and – last but not least – my parents.

ABSTRACT

Materials by design is a core driver in enhancing sustainability and improving efficiency in a broad spectrum of industries. To this end, thermo-mechanical processes and many of the underlying phenomena were studied extensively in the context of specific cases. The goal of this thesis is threefold: First, we aim to establish a novel numerical model on the micro- and mesoscale that captures dynamic recrystallization in a generalized framework. Based on the inheritance of the idea of state switches, we term this scheme *Field-Monte-Carlo Potts method*. We employ a finite deformation framework in conjunction with a continuum-scale crystal plasticity formulation and extend the idea of state switches to cover both grain migration and nucleation. We introduce physically-motivated state-switch rules, based on which we achieve a natural marriage between the deterministic nature of crystal plasticity and the stochastic nature of dynamic recrystallization. Using a novel approach to undertake the states-switches in a transient manner, the new scheme benefits from enhanced stability and can, therefore, handle arbitrary levels of anisotropy. We demonstrate this functionality at the example of pure Mg at room temperature, which experiences strong anisotropy through the different hardening behavior on the $\langle c + a \rangle$-pyramidal and prismatic slip systems as opposed to the basal slip systems as well as through the presence of twinning as an alternative strain accommodating mechanisms. Building on this generalized approach, we demonstrate spatial convergence of the scheme along with the ability to capture the transformation from single- to multi-peak stress-strain behavior.

Second, motivated by the lack of transparency concerning the benefits of high-fidelity approaches in the modeling of dynamic recrystallization, we present two derivative models of the Field-Monte-Carlo Potts method, both of which afford reduced computational expense. One model preserves the spatial interpretation of grains, but imposes a Taylor assumption regarding the distribution of strain; the other reduces the spatial notion of a grain to a volume fraction in the idea of a *Taylor model*. In order to concentrate on the differences in accuracy between the various approaches, we fit all three schemes to experimental data for pure copper, which allows us to employ a well-understood crystal plasticity-based constitutive model and to simultaneously provide sufficient data for the analysis of the texture, stress and grain-size evolution. Owing to the large strains attained in these simulations, using the FFT-based scheme, we achieve capturing a precursor of *continuous dynamic*

recrystallization. For low temperatures, the Taylor model fails to replicate the nucleation-dominated recrystallization process, whereas, at high temperatures, it shows compelling agreement with experiments and the two higher-fidelity models both in terms of the homogenized stress-evolution and the microstructural evolution.

Finally, we present a novel multiscale analysis of thermo-mechanical processes through coupling of the computationally efficient Taylor model for modeling dynamic recrystallization on the mesoscale to a *max-ent based meshfree approach* on the macroscale in the idea of *vertical homogenization*. We analyze the severe plastic deformation-based process of *equal channel angular extrusion*, which is intriguing from a numerical perspective due to the heavily localized zone of extensive shear deformation. By employing novel tools on the microscale regarding the stable update of internal variables as well as a careful interpretation of macroscale boundary conditions, we present the first multiscale analysis of a severe plastic deformation process informing simultaneously about the evolution of stress, texture and grain refinement. We attain convincing qualitative agreements for the evolution of the plunger force and texture. As an outlook on future investigations, we analyze multiple passes of the same billet in the form of route C with emphasis on the texture evolution after the second pass.

PUBLISHED CONTENT AND CONTRIBUTIONS

- A. Vidyasagar, A.D. Tutcuoglu, and D.M. Kochmann. Deformation patterning in finite-strain crystal plasticity by spectral homogenization with application to magnesium. *Computer Methods in Applied Mechanics and Engineering*, 335: 584 – 609, 2018. ISSN 0045-7825. doi: https://doi.org/10.1016/j.cma.2018.03.003. URL http://www.sciencedirect.com/science/article/pii/S0045782518301208.
  A. D. T. participated in the development of the numerical methods.

- A.D. Tutcuoglu, A. Vidyasagar, K. Bhattacharya, and D.M. Kochmann. Stochastic modeling of discontinuous dynamic recrystallization at finite strains in hcp metals. *Journal of the Mechanics and Physics of Solids*, 122:590 – 612, 2019. ISSN 0022-5096. doi: https://doi.org/10.1016/j.jmps.2018.09.032. URL http://www.sciencedirect.com/science/article/pii/S0022509618303569.
  A. D. T. developed the theory, performed numerical simulations and participated in the writing of the manuscript.

- A.D. Tutcuoglu, Y. Hollenweger, A. Stoy, and D.M. Kochmann. High- vs. low-fidelity models for dynamic recrystallization in copper. *Under review*, 2019.
  A. D. T. developed the theory, performed numerical simulations and participated in the writing of the manuscript.

- A.D. Tutcuoglu, S. Kumar, Y. Hollenweger, and D.M. Kochmann. A multiscale meshfree approach to modeling ECAE. *In Preparation*, 2019.
  A. D. T. participated in the development of the theory, the design and analysis of numerical simulations and the writing of the manuscript.

TABLE OF CONTENTS

Acknowledgements . . . iii
Abstract . . . iv
Published Content and Contributions . . . vi
Table of Contents . . . vii
List of Illustrations . . . ix
List of Tables . . . xviii
Chapter I: Introduction . . . 1
1.1 Motivation . . . 1
1.2 Physical classification of recrystallization . . . 2
1.3 Numerical approaches to modelling dynamic recrystallization on the mesoscale . . . 6
1.3.1 Grain-homogenized methods . . . 7
1.3.2 Phase-field method . . . 9
1.3.3 Monte-Carlo Potts . . . 13
1.3.4 Cellular automata . . . 16
1.4 Modeling of thermo-mechanical processes on the macroscale . . . 18
1.5 Outline of this thesis . . . 19
Chapter II: Stochastic modeling of discontinuous dynamic recrystallization using the Field Monte Carlo Potts Method – Application to Magnesium . 22
2.1 Introduction . . . 22
2.2 RVE-level constitutive model and discretization . . . 26
2.2.1 Finite-strain crystal plasticity continuum model . . . 26
2.2.2 Polycrystal response and FFT-based homogenization . . . 30
2.3 A stochastic model for recrystallization . . . 33
2.3.1 Monte-Carlo-Potts model: probability of state switching . . 34
2.3.2 Monte-Carlo-Potts model: state switches . . . 36
2.3.3 Monte-Carlo-Potts model: Incremental realization of a state switch . . . 38
2.3.4 Alternative definitions of state switches due to GBM . . . 41
2.4 Verification of the numerical scheme: Scaling and Convergence . . . 43
2.4.1 Scaling of the number of MCP sampling points with changing grid size for GBM . . . 43
2.4.2 Scaling of the number of MCP sampling points with changing grid size for NCL . . . 45
2.4.3 Dependence of the homogenized behavior on statistical MCP sampling . . . 46
2.5 Results: Microstructural evolution and resulting stress–strain response during ECAE . . . 47
2.6 Influence of the FMCP model parameters . . . 52

2.6.1 Numerical temperature . . . 53
2.6.2 Critical nucleation and migration thresholds . . . 53
2.6.3 Number of MCP sampling points . . . 55
2.7 Discussion . . . 57
2.8 Conclusions . . . 59
Chapter III: Validation and comparison with computationally inexpensive alternatives – Application to Copper . . . 61
3.1 Introduction . . . 61
3.2 Crystal plasticity model for single-crystalline Cu . . . 65
3.3 Taylor model for polycrystalline Cu . . . 67
3.3.1 Theory . . . 67
3.3.2 Model calibration and convergence study without recrystallization . . . 70
3.3.3 Simulated material response with recrystallization . . . 73
3.4 Field Monte-Carlo Potts Models . . . 77
3.4.1 FMCP model for DRX . . . 77
3.4.2 FMCP model under the Taylor assumption (FMCP×Taylor) . . . 79
3.4.3 FMCP under full field simulation (FMCP×FFT) . . . 83
3.5 Discussion . . . 87
3.6 Conclusions . . . 90
Chapter IV: Modeling thermo-mechanical processes involving dynamic recrystallization – Application to ECAE . . . 91
4.1 Introduction . . . 91
4.2 Max-ent and updated-Lagrangian . . . 96
4.3 Computational challenges in ECAE modeling . . . 100
4.3.1 Time integration . . . 100
4.3.2 ECAE process & boundary conditions . . . 103
4.3.3 Simulation protocol . . . 104
4.4 Results . . . 105
4.4.1 Convergence . . . 105
4.4.2 Strain homogeneity . . . 107
4.4.3 Reorientation excluding recrystallization effects . . . 109
4.4.4 Grain refinement . . . 110
4.4.5 Plunger force and homogenized energy evolution . . . 110
4.4.6 Reorientation including recrystallization . . . 113
4.4.7 Multipass . . . 114
4.5 Conclusion . . . 116
Chapter V: Conclusions & Outlook . . . 119
5.1 Summary . . . 119
5.2 Future directions . . . 120
5.2.1 Retrieving parameters from the lower scale . . . 121
5.2.2 Coupling the Field Monte Carlo Potts scheme to a vertex method . . . 122
5.2.3 Improved Taylor model . . . 123
Bibliography . . . 125

LIST OF ILLUSTRATIONS

Number *Page*

1.1 Categorization of recrystallization mechanisms. (i) Based on the processing conditions, recrystallization can be categorized into static (temperature-driven) and dynamic (simultaneous to loading) recrystallization. (ii) Furthermore, depending predominantly on material parameters such as the stacking fault energy (SFE), these two categories can be sub-categorized into continuous (referring to the continuous transformation of low-angle subgrain subgrain boundaries into high-angle grain boundaries), discontinuous (sudden nucleation of a grain endowed with a high-angle grain boundary), geometric (referring to the emergence of high-angle boundaries after the initial grains' smallest dimension reaches around two to three subgrain sizes) and post-dynamic (posterior to loading) recrystallization. . . . 3

1.2 Illustration of discontinuous and continuous dynamic recrystallization. Initially, the deformation drives the generation and motion of dislocations. (a) During discontinuous dynamic recrystallization, this eventually causes local instabilities that allow for the emergence of pristine nuclei. Further deformation leads to the growth of these nuclei based on the favorable difference in stored energy compared to the surrounding plastically distorted grains. Simultaneously, new grains nucleate along the boundary of the initial grain and around the newly nucleated grains to form the necklace structure characteristic for discontinuous dynamic recrystallization. (b) In the case of continuous dynamic recrystallization, strain heterogeneity within the grains causes the evolution of subgrain structures equipped with low-angle grain boundaries. Continuous application of deformation ultimately allows these low-angle grain boundaries to transform into high-angle grain boundaries. 6

1.3 Illustration of a set of generalized interpretations concerning grain boundary migration and grain nucleation in the framework of grain-homogenized methods such as the one presented in Wenk and Tomé [183]. 8

1.4 Illustration of the phase-field method, including a depiction of the diffuse interface between grains as well as grain boundary migration and nucleation. 11
1.5 Illustration of the implementation of a Monte-Carlo Potts model in a finite deformations framework, including the interpretation of both grain boundary migration and nucleation through state-switches. . . . 15
2.1 Schematic overview of the presented model, which uses an extended crystal plasticity formulation whose FFT-based discrete solution allows for the coupling to a Monte-Carlo-Potts description of recrystallization. 25
2.2 Schematic view of the state switch procedure: $n_{\mathrm{MC,GBM}}$ MCP sampling points are chosen from only those grid points adjacent to GBs, and $n_{\mathrm{MC,NCL}}$ sampling points from all n grid points. For each chosen grid point, possible options for state switches include the nucleation of a new grain (shown in yellow) or the adaption of the grain orientation of one of the neighboring points across a GB. In the latter case, the current energy $\mathcal{I}$ of each chosen sampling point is compared to its energy $\tilde{\mathcal{I}}$ after a possible state switch, by adopting the orientation of a neighboring grid point lying within an adjacent grain; the probability of switching depends on the energy difference $E = \tilde{\mathcal{I}} - \mathcal{I}$. Shown is also the definition of volume element ΔV and surface element ΔS. . . 34
2.3 Acceptance threshold w as a function of the (normalized) energy difference for various values of T_S and ΔE_{cr} (normalized by some reference temperature T_s^r). 36
2.4 Visualization of the update process for NCL (**a**-**c**) and GBM (**d**-**f**): (**a,d**) selection of a sampling point k (*marked in red*) and – in the case of GBM – its neighboring reference point j (*marked in black*) at time t_α, (**b,e**) instantaneous update of the inelastic variables at time t_α, and (**c,f**) gradual update of $\boldsymbol{F}_k^{\mathrm{r}}$ over time $[t_\alpha, t_{\alpha+n^*}]$ along with mechanical equilibration at each time step, resulting in the matching of $\boldsymbol{F}_k^{\mathrm{e}}$ of the chosen sampling point k with identity in the case of NCL and that of the neighboring grid point j in the adjacent grain at the end of the process in the case of GBM. Imposed changes are *red*, while changes resulting from mechanical equilibration appear in *blue*. 38

2.5 Schematic illustration of the time stepping scheme: at each time step the RVE is equilibrated, internal variables are updated, and n_{MC} sampling points are checked for grain nucleation or migration. If either is initiated (step b from Figure 2.4), then the scheme of Figure 2.4 starts, including a gradual adjustment of $\boldsymbol{F}^{\mathrm{e}}$ through adjusting $\boldsymbol{F}^{\mathrm{r}}$ over n^{*} time steps. 39

2.6 Comparison of GBM for a newly nucleated grain (shown in *blue*) embedded within a bicrystal (only one of the two original crystals is shown in *red*) for $n = 32^3$ (*top*), $n = 48^3$ (*center*) and $n = 64^3$ (*bottom*), when using the scaling relations introduced in Section 2.3.1. The five snapshots capture different average strain levels, using the aforementioned simple shear setup. 44

2.7 Quantitative comparison of the volume and surface area of the newly nucleated grain in Figure 2.6, demonstrating grid size-independent GBM kinetics across three different RVE discretizations with $n = 32^3, 48^3, 64^3$. 45

2.8 Comparison of the average shear stress $P^{*}_{13} = \langle P_{13} \rangle$ vs. average shear strain F^{*}_{13} for $n = 32^3, 48^3, 64^3$, using the scaling of the number of MCP sampling points with n as introduced in Section 2.3.1. 47

2.9 Evolution of the grain size distribution shown as histograms of RVE volume fractions of the grain volumes, thresholded by 0.10%, 0.25%, 0.50%, 1.0%, and 2.0% for average shear strain levels of 1.80% (*red*), 2.35% (*yellow*), 3.25% (*green*) and 3.90% (*purple*) as compared to the initial distribution (*blue*, on the top) for $n = 32^3$ (*left*), $n = 48^3$ (*center*) and $n = 64^3$ (*right*). 48

2.10 Illustration of the (negligible) influence of the random seed used for MCP sampling point selection under otherwise identical conditions including the same initial microstructure comprising 128 grains with two misorientation ranges of the c-axis with respect to the [101]-pole, viz. $\pi/16$ (*top*) and $\pi/8$ (*bottom*). Each set of four curves corresponds to four repeated runs (we have computed relative errors with respect to a fifth run whose homogenized stress levels are referred to as $\langle P^{\dagger}_{13} \rangle$). 49

2.11 Evolution of the $P^{*}_{13} = \langle P_{13} \rangle$ shear stress vs. the applied shear strain F^{*}_{13}. Markers denote the strains corresponding to the grain, shear stress and inelastic strain energy density distributions across the RVE appear in Figs. 2.13, 2.12 and 2.14, respectively. 50

2.12 Evolution of the P_{13} shear stress distribution at the ten strain levels marked in Figure 2.11. The initiation and completion of each recrystallization wave agrees well with the, respectively, highest and lowest stresses found across the RVE. 51
2.13 Evolution of the grain distribution, shown at the strain levels marked by points A through J in Figure 2.11: the color code emphasizes the microstructural evolution from the initial grain structure (*gray*) through a first recrystallization wave (new grains shown in *red*) and a second recrystallization wave (new grains in *blue*). The observed recrystallization waves correlate well with the stress–strain behavior of Figure 2.11. 52
2.14 Evolution of the inelastic strain energy density $W^{\mathrm{sl}} + W^{\mathrm{tw}}$ at the ten strain levels marked in Figure 2.11. Each recrystallization wave relates to a decrease in the accumulated stored energy density through the nucleation and growth of grains. 53
2.15 Evolution of volume fraction of recrystallized material as obtained from the simulations in Section 2.5, shown both on a linear (*left*) as well as on a double-logarithmic scale (*right*) with three representative slopes p computed at $t - t_{\mathrm{RX}} = 100\mathrm{s}, 300\mathrm{s}, 750\mathrm{s}$. 54
2.16 Influence of variations in the simulation temperature T_S on the multi-peak stress–strain behavior. 55
2.17 Effects of variations in $\Delta E_{\mathrm{cr,NCL}}$ and $\Delta E_{\mathrm{cr,GBM}}$ on the homogenized stress–strain behavior (all energy densities given in units of GPa). Unless otherwise indicated, we used the critical energy thresholds listed in Table 2.2. 56
2.18 Effects of variations in $n_{\mathrm{MC,NCL}}$ and $n_{\mathrm{MC,GBM}}$ on the homogenized stress–strain behavior for *high* critical energy thresholds $\Delta E_{\mathrm{cr,NCL}} = -10^{-3}\ \mathrm{Jm}^{-3}$ and $\Delta E_{\mathrm{cr,GBM}} = -6 \cdot 10^{-4}\ \mathrm{Jm}^{-3}$, and in like manner *low* critical energy thresholds $\Delta E_{\mathrm{cr,NCL}} = -5 \cdot 10^{-4}\ \mathrm{Jm}^{-3}$ and $\Delta E_{\mathrm{cr,GBM}} = -10^{-4}\ \mathrm{Jm}^{-3}$. 57
2.19 Evolution of the temperature-dependent single-to-multi-peak transition for Mg alloy AZ61 (Mg-6.1Al-1.1Zn-0.18Mn (wt%)) subjected to hot isothermal compression tests at a constant strain rate of $0.1\ \mathrm{s}^{-1}$ performed by a thermal simulation machine posterior to annealing conducted at 400°C for 60 min; data taken from Liao et al. [101]. . . 58

3.1 Illustration of the optimized fitting process for informing high-fidelity models through computationally inexpensive models. 64
3.2 Homogenized stress-strain behavior for a uniaxial compression test up to 100% true compressive strain in 100,000 load steps for grain counts of 10 (*blue*), 50 (*orange*), 100 (*yellow*), 200 (*red*), and 1000 (*green*) and temperatures of 725 K (*left*), 775 K (*right*), and 875 K (*bottom*). Each data point is based on 100 repetitions with each run characterized by a different random initial texture. The one-sigma stress band correspond to the interval around the mean (*emphasized using solid lines*) with a total width of two standard deviations. Results are compared to experimental data (*dashed*) from Blaz et al. [18]. (We note that results are plotted up to slightly different maximum strain levels for better differentiability.) 71
3.3 One-sigma band of the true compressive stress vs. true compressive strain as obtained from our Taylor model with DRX (averaged over 200 random initial textures), compared to experimental data from Blaz et al. [18] (*dashed*) and numerical results from Mellbin et al. [110] (*dash-dotted*) for $T \in \{725, 775, 875\}$ K. 73
3.4 Evolution of the non-recrystallized volume fraction for all initial grains (*solid line*) and for all grains nucleated within the outlined ranges of strains (*dashed lines*) for temperatures of 725, 775 and 875 K. The initial average grain diameter is at 78 μm in the experiments. The experimental and numerical final average diameter at 875 K lie at 34 μm and 30 μm, respectively. Blue crosses for 775 K denote the experimentally estimated fraction of material that has not yet undergone recrystallization. 74
3.5 Pole figures of the [111]-pole for $T \in \{725, 775, 875\}$ K with point sizes scaled by the respective grain volume fractions at five different true compressive strain levels $\varepsilon_{\text{true}}$. Colors indicate initial grains (red) and grains nucleated up to a true compressive strain of 25% (bright-blue), 50% (purple), 75% (dark-blue), and 100% (bright-green). . . . 76
3.6 Stress evolution captured by the FMCP×Taylor model including (*solid*) and excluding (*dotted*) surface contributions within the energetic grain nucleation criterion. We compare the results to experimental data from Blaz et al. [18] (*dashed*) and numerical results from Mellbin et al. [110] (*dash-dotted*). 80

3.7 Volume fraction evolution of recrystallization waves defined in 20 % true strain intervals for $T \in \{725\,\mathrm{K}, 775\,\mathrm{K}\}$ including and excluding surface contributions to the energetic nucleation criterion in the FMCP×Taylor model. Crosses correspond to the estimated data from the experimental microstructure evolution at 775 K reported by Blaz et al. [18]. Also reported in the diagrams are predicted average grain diameters based on average grain volume fractions and the total volume V_0 we have introduced before. 81

3.8 Illustration of the difference in migration behavior due to necklace formation as obtained from the FMCP models and the Taylor model. Once a nucleated grain (green) is surrounded by newly nucleated grains (red), that grain experiences an impediment to GB migration despite a possibly lower energy state compared to the original grains (white). On the contrary, in the Taylor model (*c.f.* Section 3.2) a nucleated grain will grow as long as its energy density is lower than the unweighted average energy density (see (3.15)) without any constraint from neighboring grains. 82

3.9 Evolution of the σ_{33} distribution over the deformed RVE across five true strain levels for a) 10 grains, b) 200 grains as well as c) 200 grains including recrystallization. We amplifiy local deviations from the affine deformation by a factor of 100 for visualization purposes. . 84

3.10 Mean stress evolution from 20 RVE realizations of the FMCP×FFT model (*solid*) compared to experimental data from Blaz et al. [18] (*dashed*). Conducted with the original values for Q and G_0 from Table 3.1 both without DRX at a) 725 K and b) 775 K (in order to stress the over-approximation of stresses when using the Taylor assumption) and c) with DRX (to elucidate the differences to the results obtained in Figure 3.6). 85

3.11 Pole figure of the ⟨111⟩-pole family for 725 K (*top*) and 775 K (*bottom*), illustrated using a *de la Vallée Poussin* orientation distribution function). We display the pole data from FMCP×FFT simulations at five different levels of true compressive strain, viz. $\varepsilon_{\text{true}} \in \{-0.2, -0.4, -0.6, -0.8, -1.0\}$, and complement them by the corresponding pole data for the Taylor model at $\epsilon_{\text{true}} = -1.0$ for comparison. The shown intensities (with blue and yellow values corresponding, respectively, to the minimum and maximum intensities) were obtained by weighting the orientation associated with (i) each grid point by $1/n$ in the FMCP model and (ii) each grain by its volume fraction in the Taylor model. 86

3.12 Tracking the misorientation of the [111] poles with the compression axis within a large grain inside the RVE (shown as two bodies due to the periodic boundary conditions) reveals the formation of two subgrains within the grain. The colors of the transparent grains do not refer to the misorientation – they solely represent different grains. 87

4.1 Illustration of the vertical homogenization framework coupling maxent at the macroscale with the Taylor model at the mesoscale and a crystal plasticity model on the subgranular microscale. 95

4.2 Illustration of the influence of $\boldsymbol{\beta}$ on the support of the shape functions. We randomly generated 7000 nodes in a two-dimensional space and endowed each one with a shape function N^a as per (4.6). The column at each node corresponds to the value of the associated shape function at $\boldsymbol{x} = (0,0)^T$. The different choices in $\boldsymbol{\beta}$ reflect growing levels of anisotropy starting from an isotropic approximation in (b) to a severely anisotropic representation in (c). 98

4.3 Illustration of the differences between the total- and the updated-Lagrangian formulation using the example of ECAE. Nodes and material points are visualized by black and red points, respectively. In the total-Lagrangian setting (*dashed*), the total deformation gradient $\boldsymbol{F}_{n+1}$ is a mapping from the initial configuration to the deformed configuration, while the updated-Lagrangian setting interprets $\boldsymbol{F}_{n+1}$ a mapping from the previous configuration (at time t^n) to the current configuration. 99

4.4 Illustration of the time-integration on the macro-, meso- and microscale. We note, that subscripts denoting the association of a grain with a macroscale point were omitted everywhere but in the description of the first step in favor of improved readability. 102
4.5 Schematic depiction of the initial configuration of the billet along with boundary conditions and dimensions. We used Dirichlet boundary conditions for imposing the plunger displacement (1) and to constrain the nodes on all surfaces with normal parallel to the in-plane z-component as well as the walls above the chamfers (2). Further, we modelled the outer and inner chamfer with dimensions w_1 and w_2, respectively, using wall potentials. Wall potentials also describe the lower and upper wall past the bend (3). 105
4.6 Temporal convergence as depicted via four different timesteps dt excluding recrystallization. For comparison, we also provide the energy evolution for the case that includes both migration and nucleation capabilities. 107
4.7 Illustration of the deformation of the billet via the displacement of nodes (*red*) and material points. The coloring of material points scales with the local in-plane shear strain F_{12}. The F_{12} distribution is further illustrated using a 2D view on the xy-plane at $z = 0.5$ based on an interpolation using radial-basis function kernels (rbf) at $t_{\max}/2$ and $t_{\max}$. 108
4.8 Reorientation evolution of the $\langle 111 \rangle$ pole family illustrated via a stereographic projection onto the (001)-plane at 0, $t_{\max}/4$, $t_{\max}/2$, $3t_{\max}/4$, and $t_{\max}$. The blue and yellow labels next to each pole figure represent, respectively, the minimum and maximum intensity. The reorientation evolution in each of the three columns labelled A, B and C correspond to the associated material points marked in the leftmost column. This analysis excludes recrystallization. 111
4.9 Interpolation of the distribution of the average grain volume across the $z = 0.5$ plane using radial-basis function kernels (rbf) at $t_{\max}/2$ and $t_{\max}$. 112
4.10 Evolution of the scaled plunger force via integration of the Cauchy stress over the top surface for simulations including and excluding recrystallization. 113

4.11 Reorientation evolution of the ⟨111⟩ pole family illustrated via a stereographic projection onto the (001)-plane at $t_{max}/4$, $t_{max}/2$, $3t_{max}/4$, and t_{max} for scenarios excluding (top) and including (bottom) recrystallization effects. The blue and yellow labels next to each pole figure represent, respectively, the minimum and maximum intensity. The pole figures correspond to the current orientation of all grains at the material point marked in red. 115

4.12 Evolution of the material points during a multipass idealizing a 180° turn including the impact on the texture and of the ⟨111⟩ pole family in stereographic projection onto the (001)-plane at $t_{max}/8$, $t_{max}/4$, $3t_{max}/8$, $t_{max}/2$, $5t_{max}/8$, $3t_{max}/4$, $7t_{max}/8$, and t_{max}. The blue and yellow label next to each pole figure represent, respectively, the minimum and maximum intensity, while the red marking highlights the material point to which the pole figure corresponds. 117

LIST OF TABLES

Number *Page*

2.1 Material parameters used in the extended crystal plasticity model for Mg after Chang and Kochmann [26]. We note that parameter τ_0, the critical resolved shear stress, has been modified from the original model, since we used the formulation of Chang and Kochmann [26] in an implicit context, whereas here we use an explicit formulation that does not suffer from numerical complications by introducing a hard threshold into the rate-dependent model (c.f. Chang et al. [27]). . 31

2.2 MCP model parameters chosen for the subsequent simulations of dynamic recrystallization, unless otherwise noted. 36

3.1 Parameters defining the Cu material model introduced in Section 3.2 as well as the two recrystallization constants from Sections 3.3 and 3.4. 68

3.2 Further parameters used for the Taylor, the FMCP models (both FMCP×Taylor and FMCP×FFT). 82

3.3 Difference in computational expenses for one simulation at 725 K, using 24 physical cores and description of the flow for the reduced-order based parameter fitting. 89

4.1 Macroscale parameters defining the geometry, boundary conditions, and the meshfree solver. Variables marked with a † refer to variables normalized with respect to length. For a description of the shape function cut-off tolerance ϵ_{cut} and the initial connectivity cut-off region $\boldsymbol{M}_0^p$, we refer to Kumar et al. [91]. 106

Chapter 1

INTRODUCTION

1.1 Motivation

Among the primary factors influencing the strength of a metal or an alloy lies the average grain size and shape. The renown Hall-Petch relation shows the impact of grain refinement on strength [59, 124] by postulating an inverse relationship between the yield strength and the square root of the average grain size. Grain refinement can, however, also influence other macroscopic parameters. In general, wear, fatigue and corrosion resistance as well as ductility and hardness experience an improvement, whereas creep resistance deteriorates with grain refinement [40, 151]. Numerous forming processes can achieve this reorganization of the polycrystalline grain structure, including accumulative roll bonding [141], asymmetric rolling [24], equal channel angular extrusion [147], high-pressure torsion [21], multi-directional forging [49], and twist extrusion [17] (see, *e.g.*, Estrin and Vinogradov [40], Hallberg [60], Huang and Logé [68]). These processes belong to the class of severe plastic deformation techniques, which are characterized by the grain refinement induced through large plastic strains; Estrin and Vinogradov [40] provide an extensive review over a wide range of established and novel severe plastic deformation methods. Throughout the past decades, research on the optimization of these processes gathered extensive empirical knowledge [45, 48, 65, 88, 93, 98, 178, 199]. In view of an ever-rising number of metallic alloys and the many parameters that define each one of the above processes, the tailoring of a material's performance for a specific application calls for a computational framework capable of describing the microstructural evolution. Such numerical means of optimization are particularly valuable for metal alloys with a complex structure, including those with hexagonal closed pack crystallography, which inherently causes a severe anisotropy that is partially responsible for the challenges associated with the thermo-mechanical treatment of magnesium alloys [88, 115]. At room temperature, the low number of closed-packed slip systems yields difficult formability conditions [42, 131]. Higher temperatures, however, facilitate the activation of the non-closed-packed slip systems, which can be beneficial during forming, provided the right combination of texture and loading [5, 131]. However, changes in the microstructure, *e.g.*, in the sense of grain refinement, can alter the texture and therefore again aggravate

formability. This illustrative example demonstrates the difficulty in tailoring certain classes of metals. The example also emphasizes the need mentioned above for a numerical framework on the micro- and macro-scale to gain a better understanding of the evolution of grain size and texture, which can then be used to optimize processing routes.

1.2 Physical classification of recrystallization

For certain classes of metals – including iron, titanium, cobalt, and their respective alloys – the restructuring of the microscale is possible by inducing phase transformations through cooling [35]. This method does, however, not apply to copper, nickel, and aluminum as well as their alloy derivatives. Here, a complete change of the microstructure – in the sense of both modified average grain size and shape – is only possible after deformation through a process termed recrystallization. Doherty et al. [35] define recrystallization as "the formation and migration of high angle grain boundaries driven by the stored energy of deformation", where high angle boundaries are generally defined through a misorientation of at least 10-15° [35, 60, 68].

Recrystallization occurs in various ways. Figure 1.1 illustrates the categorization, which derives from several factors, which we briefly summarize in this section. *Static recrystallization* is a temperature-driven process that takes place under slowly-varying, creep-like loading conditions such as annealing [144, 194]. An increase in the average grain size generally accompanies static recrystallization and consequently has a negative impact on the strength properties. Alloying with rare earth metals allows mitigating this deficiency as Zhang et al. [194] reported after enriching Mg-Zn-Zr alloys with Er and subjecting them to static recrystallization at high temperatures. We can classify static recrystallization based on the dominant driving force [68]. Discontinuous static recrystallization refers to the nucleation of fine, pristine crystallites by a process termed static recovery. Driven by the reduction of stored surface and inelastic energy, the nuclei consume the surrounding strain hardened matrix resulting in the aforementioned grain-coarsening effect [166]. In contrast, the precipitation of fine particles along grain boundaries and the subsequent coarsening of the dispersoid stimulates continuous static recrystallization, which describes a change in microstructure induced through subgrain growth. As these subgrains continuously deform, their low-angle grain boundaries steadily develop into high angle grain boundaries, thus ultimately leaving the material with a new microstructure [162].

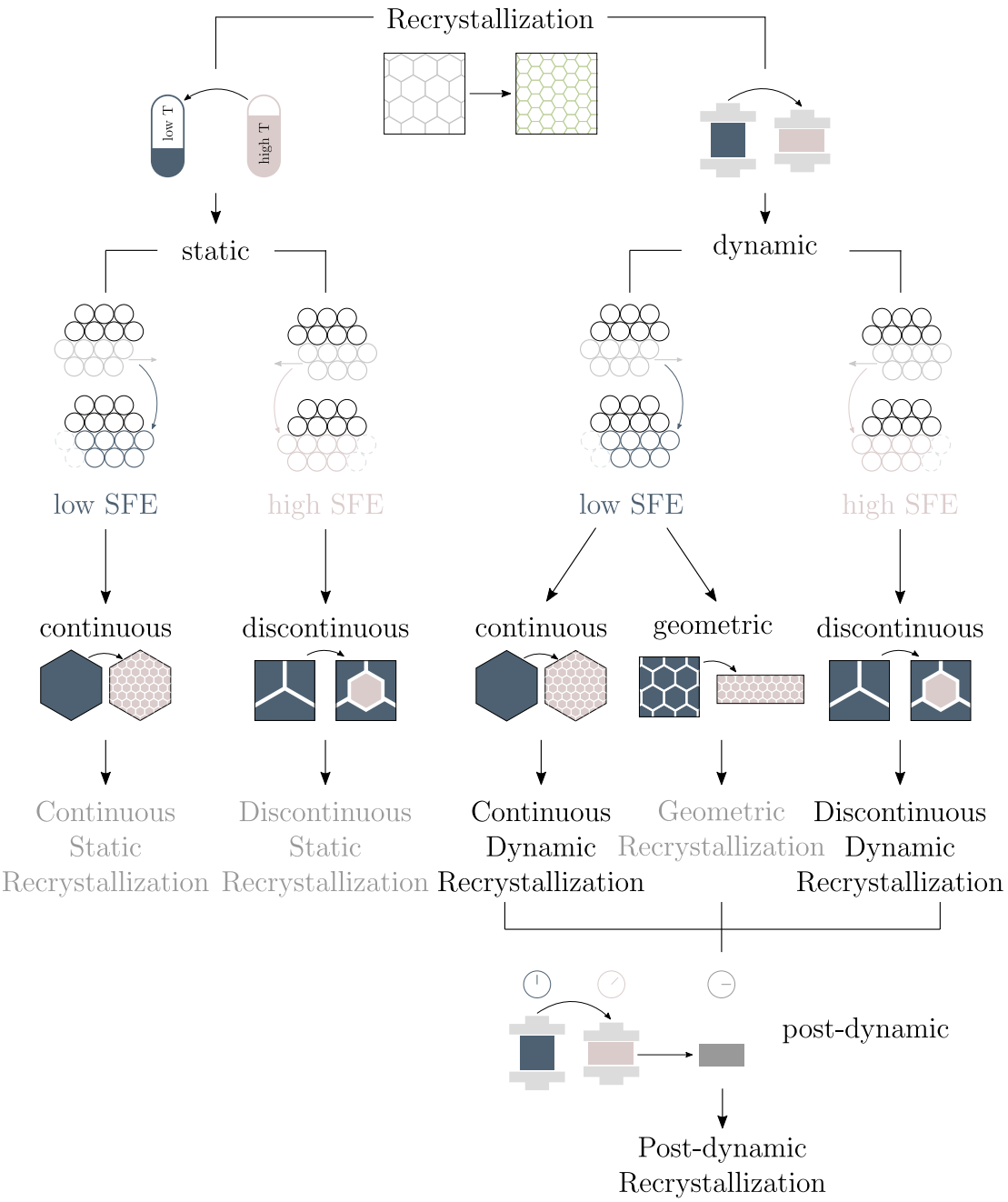

Figure 1.1: Categorization of recrystallization mechanisms. (i) Based on the processing conditions, recrystallization can be categorized into static (temperature-driven) and dynamic (simultaneous to loading) recrystallization. (ii) Furthermore, depending predominantly on material parameters such as the stacking fault energy (SFE), these two categories can be sub-categorized into continuous (referring to the continuous transformation of low-angle subgrain subgrain boundaries into high-angle grain boundaries), discontinuous (sudden nucleation of a grain endowed with a high-angle grain boundary), geometric (referring to the emergence of high-angle boundaries after the initial grains' smallest dimension reaches around two to three subgrain sizes) and post-dynamic (posterior to loading) recrystallization.

Occurring at higher loading rates, *dynamic recrystallization*[1] emerges from the competition between recrystallization and continued plastic deformation such as during equal channel angular extrusion. Similar to static recrystallization, we further categorize dynamic recrystallization based on the microstructural processes into two main subcategories. Generally present in high-stacking-fault-energy metals such as aluminum, *continuous dynamic recrystallization* describes the gradual transformation of subgrain structures formed from dislocation networks into new grains, resulting in grain refinement [14, 56, 167].

Discontinuous dynamic recrystallization describes the process of *grain nucleation* at high-energy sites and the subsequent grain growth by *grain boundary migration* [30, 42, 43], which predominantly occurs in metals with low to medium stacking fault energy such as copper [9, 18, 50] or magnesium [144]. While it is generally acknowledged that the reduction of stored elastic and plastic strain energy density [155, 169] drives nucleation, the exact criterion for the onset of nucleation remains a subject of debate: [144, 164] propose a critical dislocation density ansatz which postulates that nucleation is only possible if the local dislocation density surpasses this critical threshold. Other reports concentrate on a critical (plastic) strain [28, 30] or a critical inelastic strain energy density [110], instead. As a competing mechanism, the difference in stored strain energy between neighboring grains with differing plastic histories [60, 68] results in the migration of grain boundaries. Thus, discontinuous dynamic recrystallization involves the interplay between three phenomena – severe plastic deformation of a polycrystal, grain boundary migration, and grain nucleation. The availability of active recovery processes explains the dependence of dynamic and static recrystallization on the stacking fault energy. Atomic lattices endowed with a high stacking-fault energy generally allow recovery processes, such as dislocation climb, to act sufficiently fast and to keep the dislocation density or the inelastic strain energy density below the threshold mentioned above. In low-to-medium stacking fault metals, however, this recovery process is relatively slow compared to the accumulation and motion of dislocation, which ultimately requires the discontinuous nucleation of a pristine grain to attain a thermodynamically stable state. The general perception sees continuous and discontinuous dynamic recrystallization as the main recrystallization processes co-occurring with deformation. Figure 1.2 illustratively summarizes the underlying physics, while Doherty et al. [35], Hallberg [60], Huang and Logé [68], Sakai et al. [144] provide in-depth re-

[1]Note that *dynamic* refers to the fact that the recrystallization mechanisms occur during continued plastic deformation. It does not imply the presence of inertia or shocks.

views of the respective fields.

Owing to its relatively late discovery, *geometric recrystallization* has – to this point – experienced the least attention among the three dynamic recrystallization types, both from an experimental and a numerical point of view (see, *e.g.*, Sakai et al. [144]). Observed at high strains, it describes the grain-refinement through the formation of equiaxed grains with high-angle grain boundaries during hot deformation [68]. The origin of these new grains lies in the elongation of the original grains and the simultaneous generation of local serrations due to a pronounced subgrain structure. Despite little influence at small strains, these serrations allow for the formation of new grain boundaries endowed with high angle misorientations as high angle boundaries belonging to the original grains approach each other. This transformation into a new microstructure is observable around the time when the thickness of the elongated grains reaches around one to two times the size of a subgrain [68].

Although the above introduction to static and dynamic recrystallization processes covers an extensive depiction of the different microstructural mechanisms inherent to recrystallization, they are non-exhaustive in the sense that mixtures of the above or similar derivatives are possible. In the case of discrete dynamic recrystallization, the creation of high angle boundaries provides new surfaces along which new grains can nucleate. This behavior is frequently observed in hexagonal closed packed metals such as magnesium, where nucleation can develop along twin boundaries [126], but can also theoretically occur along high angle boundaries generated through continuous dynamic recrystallization [60]. Furthermore, although we generally associate dynamic recrystallization with the change in microstructure while deformation is active, grain nucleation and growth can still occur based on the earlier mentioned energetic principles posterior to the loading phase. We usually refer to this retarded occurrence as metadynamic recrystallization or post-dynamic recrystallization [68, 144] to distinguish it from recrystallization processes which appear simultaneously to loading. Finally, we note that grain refinement can also be achieved without any deformation, *e.g.*, by changing the composition of an alloy. For aluminum, the addition of boron and titanium to the melt of Al-7Si-0.3Mg alloy allowed for the induction of additional grain refinement [82]. In like manner, the addition of solutes such as zirconium, silicon, and calcium to pure magnesium impedes the growth process during solidification, thus achieving a decrease in the average grain size [99]. The interest in this thesis lies, however, in the grain-refinement-induced strengthening of metal alloys with a specific composition; the

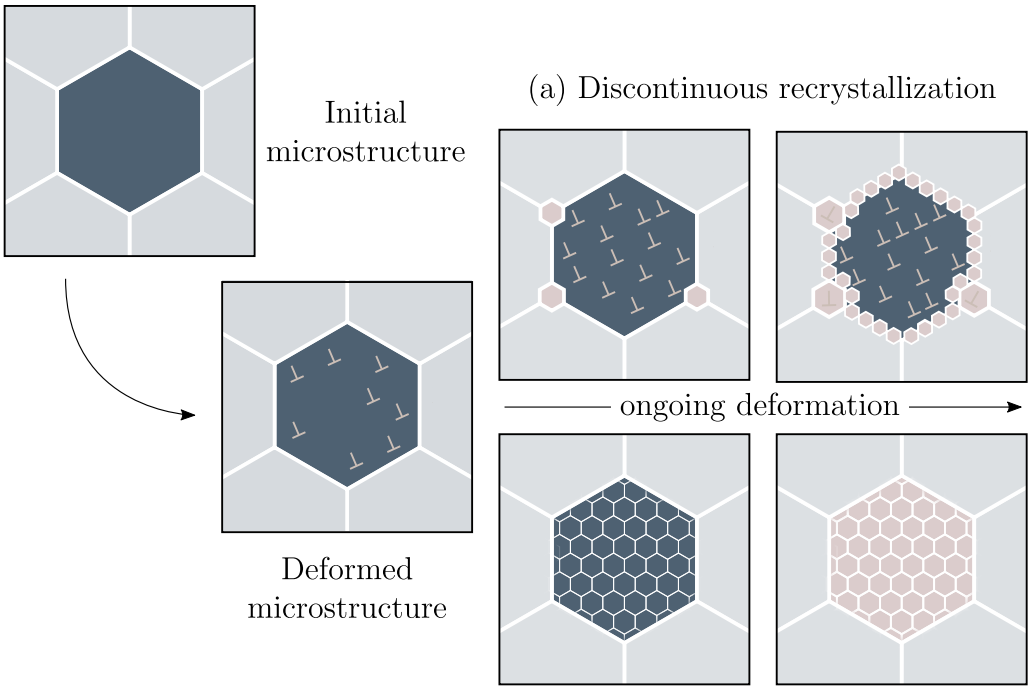

Figure 1.2: Illustration of discontinuous and continuous dynamic recrystallization. Initially, the deformation drives the generation and motion of dislocations. (a) During discontinuous dynamic recrystallization, this eventually causes local instabilities that allow for the emergence of pristine nuclei. Further deformation leads to the growth of these nuclei based on the favorable difference in stored energy compared to the surrounding plastically distorted grains. Simultaneously, new grains nucleate along the boundary of the initial grain and around the newly nucleated grains to form the necklace structure characteristic for discontinuous dynamic recrystallization. (b) In the case of continuous dynamic recrystallization, strain heterogeneity within the grains causes the evolution of subgrain structures equipped with low-angle grain boundaries. Continuous application of deformation ultimately allows these low-angle grain boundaries to transform into high-angle grain boundaries.

physics behind precipitation and solidification is therefore out of scope.

1.3 Numerical approaches to modelling dynamic recrystallization on the mesoscale

In this section, we provide brief summaries on three of the most widely used numerical methods for the modeling of discontinuous dynamic recrystallization on the (sub)granular scale. We attach particular emphasis to the realization of migration and nucleation models and do not discuss the underlying dislocation density or crystal plasticity models are not discussed in much detail at this point. Furthermore,

we note that those three methods do not exhaust available recrystallization models. We merely based our choice on their impact on the field as well as their contributions to this work. Hallberg [60] provides a general review on methods including cellular automata [11, 55, 127, 191], vertex methods [110, 152], and the level-set method [15, 37]. Sakai et al. [144] and Huang and Logé [68] further complement this contribution by a more in-depth physical analysis of recrystallization including a summary of numerical developments[2].

1.3.1 Grain-homogenized methods

Numerous methods build on the assumption that the entire entity of a grain can be deprived of the notion of space and summarized through a homogenized set of states. We refer to this set of schemes as *grain-homogenized methods*. Although the various approaches that belong to this category differ significantly from one to another, the set of states usually comprises a volume fraction $\eta_{i\in\{1,\dots,N_g\}}$, a set of internal variables $\boldsymbol{Q}_{i\in\{1,\dots,N_g\}}$ as well an orientation tensor $\boldsymbol{R}_{i\in\{1,\dots,N_g\}}$ or a related measure which allows distinguishing grains. Based on the viscoplastic self-consistent model [181, 182] – which affords a compromise between the Taylor model [168] (upper bound on stress) and the Sachs model [140] (lower bound on stress) – the scheme presented in Wenk and Tomé [183] realizes grain migration through a time-evolution law of the volume fraction. Assuming a linear dependence on the difference between the energy of a grain and the system's average energy, they postulate a the volume fraction rate through

$$\frac{\partial \eta_i}{\partial t} = -\kappa_{\mathrm{GBM}} \left(W_i - \frac{1}{N_g} \sum_{i=1}^{N_g} W_i \right) \eta_i^{2/3}, \tag{1.1}$$

with migration rate coefficient κ_{GBM} and grain-specific stored energy density W_i. The scaling of the change in volume fraction by its volume fraction raised to the power of $2/3$ hinges on the assumption of a spherical growth of the associated grain boundary area. Although this is a reasonable assumption during the growth stage of a nucleus, it is not representative of a grain's consumption by its surrounding grains, as shown in analyses of Adam et al. [1]. We note that the *ad-hoc* evolution principle from (1.1) requires normalization of all grains by the total volume. Further, every

[2]We note that the nomenclature we use in this section may differ significantly from the ones employed in some of the contributions in the respective fields as we picked the variable designations in favor of improved comparability. Lastly, we constrain our presentation to the finite deformations framework. Although the majority of contributions rely on a small strain ansatz or do not even carry the notion of a strain, we decided to pursue this approach, as the formulations of mobility and nucleation are compatible either way and all subsequent chapters build on a finite deformation framework.

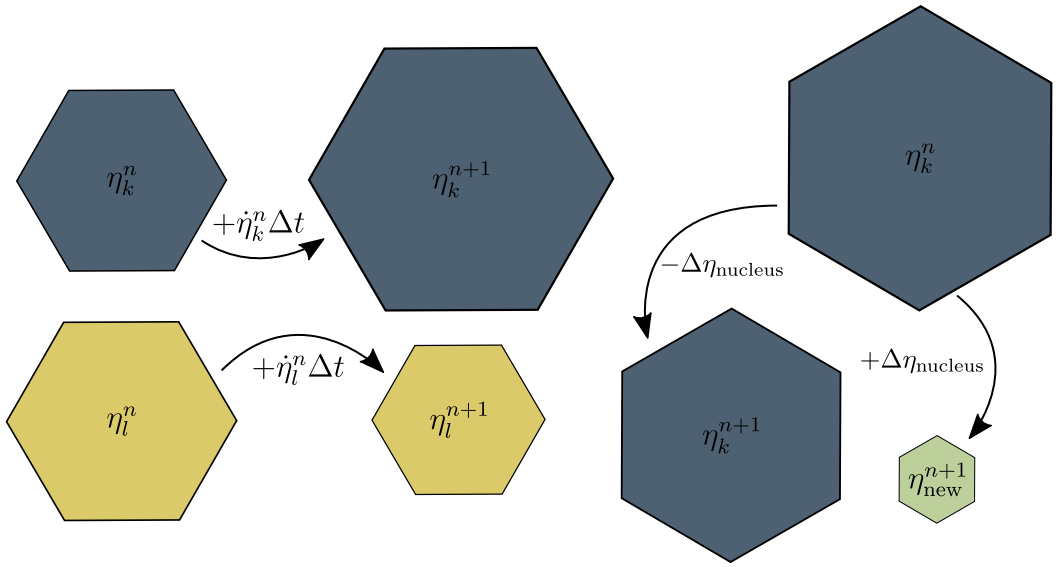

Figure 1.3: Illustration of a set of generalized interpretations concerning grain boundary migration and grain nucleation in the framework of grain-homogenized methods such as the one presented in Wenk and Tomé [183].

grain entails a parent and a recrystallized volume fraction via $\eta_i = \eta_{i,parent} + \eta_{i,nucleus}$, with $\eta_{i,nucleus}$ initially set to 0. The nucleation criterion is deterministic and occurs as soon as the equivalent strain reaches a threshold. At this point, $\eta_{i,nucleus}$ is set to the size of a nucleus at the expense of $\eta_{i,parent}$. The size of a nucleus varies linearly with the grain's size as well as the equivalent strain rate. $\eta_{i,nucleus}$ then evolves according to (1.1) with the nucleus being at zero accumulated energy since, by design, it does not harden. The orientation of the nucleus is set to the orientation of the parent grain. As $\eta_{i,nucleus}$ reaches a specific fraction of $\eta_{i,parent}$, the nucleated volume fraction is transferred into the original volume fraction of the parent grain, which updates the inelastic strain accordingly.

Figure 1.3 illustrates the main idea of migration and nucleation in the framework of a grain-homogenized method, such as the one presented in Wenk and Tomé [183]. Although this type of model allows the inclusion of both nucleation and grain growth, the lack of spatial resolution causes various challenges:

- In the absence of space, curvature-driven growth is difficult to account for in these models. Attempts to penalize the grain boundary area can be found in the growth model for subgrains by Cram et al. [30]. In their work – which reduces the notion of a grain's spatial component into a radius – they tracked subgrain

growth in a phenomenological fashion to include the additional surface area due to the subgrains in the nucleation model for discontinuous dynamic recrystallization. The growth of grains again appears in linear dependence to the change in stored energy without any information on the surface area. However, the component of the subgrain growth stemming from capillary effects is inversely proportional to the grain boundary area, thus effectively penalizing subgrains endowed with a large surface. The necklace-formation characteristic for discontinuous dynamic recrystallization (see, *e.g.*, Huang and Logé [68]) is another phenomenon that models of this class in general do not capture due to the lack of a notion of space.

- To this point, models that fall into this category tend to isolate their analysis on specific parts of dynamic recrystallization without trying to capture dynamic recrystallization as a whole. While Wenk and Tomé [183] managed to verify experimental findings from Zhang and Karato [196] concerning the qualitative influence of recrystallization onto texture evolution, the nature of their nucleation model forbade the capturing of any realistic grain refinement. Although the notion of a homogenized stress does exist in their model, they provide no information concerning its evolution, and it is likely that the *ad-hoc* structure did not permit the replication of experimental stress evolutions. The work of Cram et al. [30] – which replaced the viscoplastic self-consistent model from Wenk [181, 182] by an iso-work-increment assumption [19] – allowed recovering experimental results concerning the evolution of grain refinement and stress with a satisfactory agreement. However, lacking the explicit notion of a grain rotation, they could not track texture evolution.

1.3.2 Phase-field method

Among the methods that attracted most attention in the modeling of recrystallization stands the *phase-field method* [28, 113, 155, 197, 198]. In this approach, each one of the N_g grains is associated with a continuous order parameter $\eta_{i\in\{1,\dots,N_g\}} : [0, t_{\max}] \times \Omega \to [0, 1]$ defined throughout the time interval $[0, t_{\max}]$ and across space in the form of a *representative volume element* (RVE) Ω. The order parameter $\eta_i = \eta_i(t, \boldsymbol{X})$ describes the local volume fraction of grain i. At some point inside of grain i, we, therefore, have $\eta_i = 1$ and $\eta_j = 0$ for some other grain j. In a diffuse way, we model the grain boundary between grain i and grain j via $0 < \eta_i, \eta_j < 1$

and $\eta_{k\in\{1,\dots,N_g\}/\{i,j\}} = 0$. The phase-field method further imposes

$$\sum_{i=1}^{N_g} \eta_i(t, \boldsymbol{X}) = 1 \qquad \forall t \in [t, t_{\max}], \boldsymbol{X} \in \Omega. \tag{1.2}$$

A general form for the total energy stored in the system is provided by Hallberg [60] as

$$\mathcal{I} = \int_\Omega \left[f(\{\eta_i, \boldsymbol{F}_i, \boldsymbol{Q}_i\}_{i\in\{1,\dots,N_g\}}) + \sum_{i=1}^{N_g} \frac{\gamma}{2} (\nabla\eta_i)^2 \right] dV. \tag{1.3}$$

Here, the first term accounts for the internal energy at some point in space through an interpolation function f, which takes into account the local volume fraction of all grains, as well as their respective deformation gradient $\boldsymbol{F}$ and a set of internal variables $\boldsymbol{Q}$. In the case of phase-field methods, the notion of an internal energy entails the elastic energy, inelastic energy as well as a chemical potential. A Ginzburg-Landau term generally accounts for the chemical potential, which creates a driving force for the individual order parameters towards 0 or 1. The second term includes information on the curvature and acts as a penalization of grain boundary surface with surface penalization constant γ. Allen-Cahn kinetics of the form [6]

$$\frac{\partial\eta_i}{\partial t} = -\kappa\frac{\delta\mathcal{I}}{\delta\eta_i} = -\kappa\left(\frac{\partial\mathcal{I}}{\partial\eta_i} - \Delta\eta_i\right), \tag{1.4}$$

naturally integrate grain boundary migration into such a diffuse-interface description through. We note that in distinction to the Cahn-Hilliard equation, (1.4) does not preserve the global total volume of an order parameter, which is appropriate given the nature of grain boundary migration. Figure 1.4 illustrates a crude depiction of the above theory. While the phase field method is ideal for the modeling of microstructures via migration, its structure poses a number of challenges:

- The aforementioned interpolation between states does not derive from a physical principle, as the presence of two grains at one point in space and time already is a mere artifact of the phase-field ansatz. Among the simpler approaches stands the work of Sreekala and Haataja [155], who solely tracked two order parameters, namely recrystallized and non-recrystallized material. In their work, they weighted the elastic, inelastic and surface energy contribution by a function of the form $H(\eta) = \eta^3/3 - \eta$, where η denotes the recrystallized volume fraction. Chen et al. [28] used an interpolation function of the form $H = H(\eta_i) = -2\eta_i^3 + 3\eta_i^2$, with $i \in \{1, \dots, N_g\}$, based on

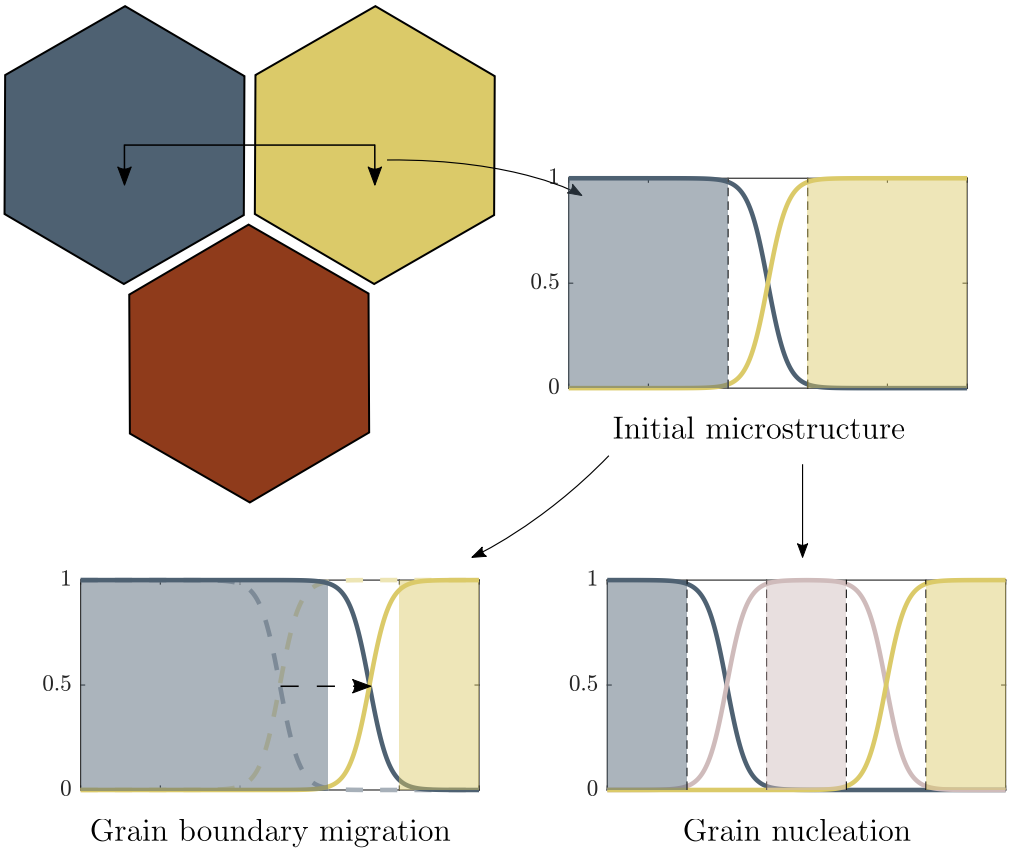

Figure 1.4: Illustration of the phase-field method, including a depiction of the diffuse interface between grains as well as grain boundary migration and nucleation.

which they interpolated individual grain parameters, which we then used in the aforementioned energetic interpolation rule f from (1.3). The exact choice of interpolation functions often owes to mathematical convenience more than physics [155].

- Phase field methods, in general, assume the tracking of one set of elastic and inelastic parameters per order parameter at every point in space (see, *e.g.*, Zhao et al. [197, 198]), which especially in light of a large number of nucleated grains can become computationally expensive. Chen et al. [28] circumvent this issue by extrapolating the average values of the inelastic strain to areas where it is not the dominant order parameter. This extrapolation rule effectively constrains the space in which the update of some grain's internal variables is necessary to the space in which this grain is dominant. Takaki et al. [164] reduced the number of elastic and inelastic variables to one per grain by imposing a Taylor assumption and thus – in general – violating linear momentum conservation. This automatically implies a homogeneous

stress distribution across grains and therefore prevents the capturing of any heterogeneities.

- The nucleation of grains requires an ad-hoc introduction of a new order parameter. To overcome the adversary effects of the surface penalizing term as well as the Ginzburg-Landau potential, Chen et al. [28] hold the newly introduced grains at a constant level for a specified period of time until their favorable energy state (they initially possess a pristine state) allows them to stabilize or to grow.

- Our general assumption is that nuclei inhibit a significantly reduced dislocation density compared to their parent grains. A high stress state surrounding the area of nucleation, however, poses a challenge to both the update of the local inelastic state as well as the elastic solver. Chen et al. [28] and Zhao et al. [197, 198] mitigate this issue by assuming that recrystallized grains do not undergo further inelastic deformation. This simplification in return prevents recrystallized grains from undergoing subsequent recrystallization, which prevents them from capturing, *e.g.*, the steady state. We note, that Chen et al. [28] considers static recrystallization, where this assumption is valid as nucleation and migration are temperature-driven, and no further deformation occurs at this point.

Phase-field models allow replicating the theoretical results from the Johnson-Mehl-Avrami-Kolmogorov (JMAK) model by Avrami [13], Johnson and Mehl [79], Kolmogorov [86] (see, *e.g.*, Takaki et al. [164]). Furthermore, the natural integration of grain boundary migration renders the phase-field method suitable for cases where multiple recrystallization waves are unlikely, such as in the analysis of static recrystallization [28]. Although highly parallelizable, the large number of inelastic and elastic states that require tracking renders the phase-field method computationally increasingly inefficient for a large number of grains. Approximative measures such as the Taylor assumption, which Takaki et al. [164] employed, allow constraining of the computational expense associated with an order parameter to its support, but the underlying assumptions reduce the model's applicability. Since a regular grid is suitable as the discretization of the RVE, we can reduce the computational expense the elastic solver carries with it by using an FFT-based solver [28, 197, 198]. We note that due to their diffuse interface, Gibbs phenomena are of little concern in the framework of phase-field methods.

1.3.3 Monte-Carlo Potts

Based on the idea of energy-dependent state switching, the Monte-Carlo Potts method affords a natural implementation of both grain boundary migration as well as of nucleation and is, therefore, one of the most widely used numerical methods for discontinuous dynamic recrystallization [1, 8, 25, 72, 135, 138, 157, 184]. Every point in the RVE Ω is uniquely associated with exactly one grain via $s : \Omega \rightarrow [1, ..., N_g]$ with N_g denoting the number of grains. Initially, every grain association is linked to exactly one orientation through the rotation tensor $\boldsymbol{R}_{i\in\{1,...,N_g\}}$. In all generality, $\boldsymbol{u} = \boldsymbol{u}(\boldsymbol{X})$ and $\boldsymbol{Q} = \boldsymbol{Q}(\boldsymbol{X})$ describe the deformation field and internal variables, respectively, across Ω[3]. The total energy for a Monte-Carlo Potts method in a finite deformations framework comprises contributions from the strain energy density $W = W(\boldsymbol{F}(\boldsymbol{X}), \boldsymbol{Q}(\boldsymbol{X}))$ as well as the surface tension via

$$\mathcal{I} = \int_\Omega W(\nabla \boldsymbol{u}(\boldsymbol{X}), \boldsymbol{Q}(\boldsymbol{X}))dV + \int_\Gamma \gamma(s(\boldsymbol{X}^-), s(\boldsymbol{X}^+))dS, \tag{1.5}$$

where Γ is the set of all grain boundaries and $\boldsymbol{X}^+$, as well as $\boldsymbol{X}^-$, are convenient ways of referring to the two orientation associations on both side of the grain. The misorientation between the two grains at the boundary, which $\boldsymbol{R}(\boldsymbol{X}^+)$ and $\boldsymbol{R}(\boldsymbol{X}^-)$ readily provide, can then influence the contribution to the surface penalization function γ. The Monte-Carlo Potts method requires a discretization Ω_Δ of Ω. Historically, this discretization adopts a regular grid with square cells in 2D and cubic cells in 3D (see, *e.g.*, Hallberg [60]), although non-regular grids are possible. Discretizing the energy formulation from (1.5) yields

$$\mathcal{I} = \sum_{\boldsymbol{X}_i\in\Omega_\Delta} W(\nabla \boldsymbol{u}(\boldsymbol{X}_i), \boldsymbol{Q}(\boldsymbol{X}_i))\Delta V + \sum_{j\in\mathcal{S}_i} \gamma(s(\boldsymbol{X}_i), s(\boldsymbol{X}_j))\Delta S, \tag{1.6}$$

with unit cell volume ΔV, unit cell surface ΔS and the set of all neighbor cells of $\boldsymbol{X}_i$, $\mathcal{S}_i$. A stochastic model, which accepts and rejects state switches based on their energetics, naturally realizes the energy-minimizing nature of grain migration. During one time step – which owing to the lack of a characteristic time-scale is also often referred to as a Monte-Carlo step [60] – n_{MC} points in Ω are randomly chosen, for each one of which a state switch is considered. A state switch at a point $\boldsymbol{X}_i$ in its most general sense describes a change of grain association, namely from $s(\boldsymbol{X}_i)$ to $s(\boldsymbol{X}_{j\in\mathcal{S}_i})$, the grain association of any of the neighbors. Studies which use this lean definition of a state switch concentrate solely on curvature-driven

[3] We note that many of the early works relied on a phenomenologically distributed internal energy, which often had no relation to the actual elastic or inelastic deformation state. To account for these cases, we attribute such a randomly distributed internal energy to the internal variables.

migration (see, *e.g.*, Anderson et al. [8], Cetinel et al. [25]). The notion of a state switch can, however, also comprise the elastic and inelastic state, in which case we would need to define both a deformation state in the form of $\nabla \boldsymbol{u}^*(\boldsymbol{X}_i)$ and a new set of internal variables $\boldsymbol{Q}^*(\boldsymbol{X}_i)$. Their respective new states can in general depend on the (in)elastic state of the neighbor with whom a state switch is considered. In favor of compatibility, the total deformation state is in general not subjected to changes, *i.e.*, $\nabla \boldsymbol{u}^*(\boldsymbol{X}_i) = \nabla \boldsymbol{u}(\boldsymbol{X}_i)$. For every one of the n_{MC} points and every potential state switch, the difference in energy $\Delta \mathcal{I}$ across the hypothetical state switch follows from the energy in the non-switched state $\mathcal{I}$ and the switched state $\tilde{\mathcal{I}}$. Using an energy-change-dependent threshold $w^{\mathrm{th}}(\Delta \mathcal{I})$ alongside a randomly generated number $w \sim \mathcal{U}([0,1])$, the formerly hypothetical state switch is accepted if $w < w^{\mathrm{th}}(\Delta \mathcal{I})$ and rejected otherwise. While the exact form of threshold functions varies greatly among contributions [132], most of them derive from the well-known Glauber dynamics [60]

$$w^{\mathrm{th}}(\mathcal{I}) = \frac{\kappa_{\mathrm{GBM}}}{2}\left[1 - \tanh\left(\frac{\Delta \mathcal{I}}{2 k_b T_s}\right)\right], \tag{1.7}$$

with migration rate coefficient κ_{GBM}, Boltzmann constant k_b and numerical temperature T_S. Atomic jump probabilities in the form of an Arrhenius law inspired the above form, which satisfies the condition of higher thresholds for more favorable energy changes (*i.e.*, more negative energy changes). We further note, that – in general – the numerical temperature does not equate to the process temperature [60]. Nucleation generally describes the choice of a number of sites per time-step at which one defines a new orientation along with a new set of inelastic variables. The nucleation condition and rates resemble their respective counterparts in many other numerical methods and we therefore discuss them no further at this introductory level.

In contrast with the phase-field method, the Monte-Carlo Potts method provides a natural implementation for both nucleation and migration and further accomplishes to incorporate the stochastic nature of recrystallization. Like for the previous two models, various challenges arise due to its inherent structure:

- Implementation requires the inclusion of linear momentum conservation (or equilibrium), since state heterogeneities are integral to the capturing of, *e.g.*, stress concentrations near the boundary. Owing to the predominantly square or cubic grid elements alongside the periodic boundary conditions that derive from vertical homogenization, an FFT-based solver (see, *e.g.*, Eisenlohr et al.

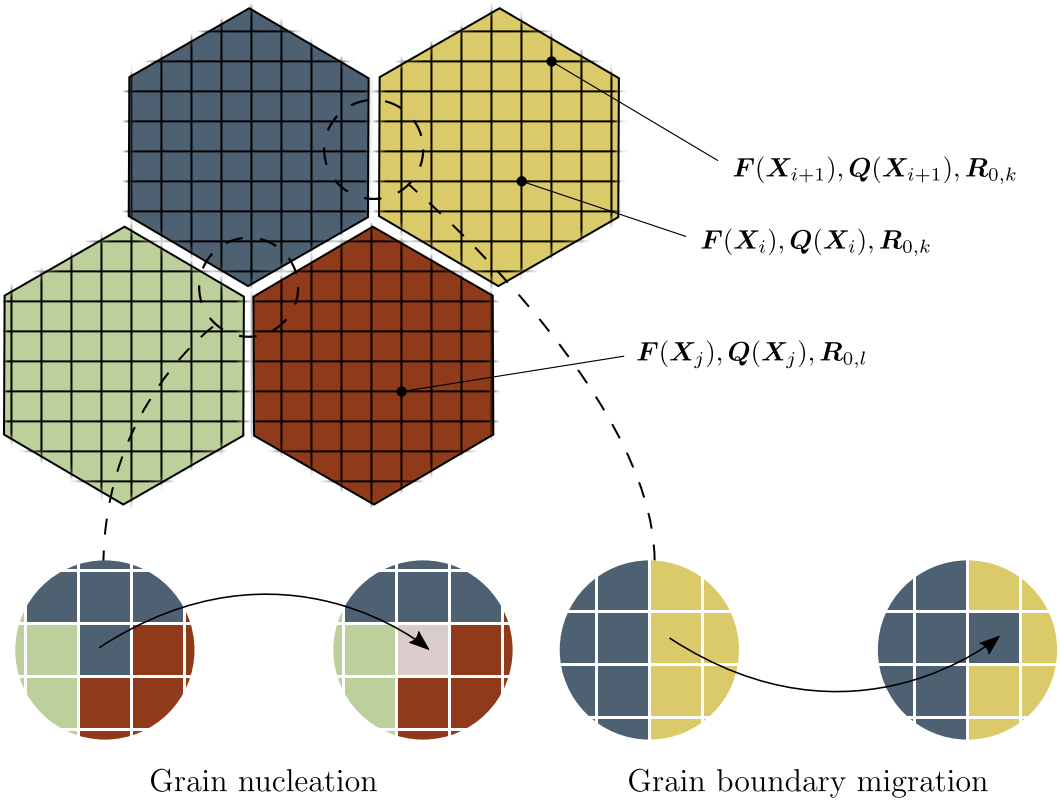

Figure 1.5: Illustration of the implementation of a Monte-Carlo Potts model in a finite deformations framework, including the interpretation of both grain boundary migration and nucleation through state-switches.

[36], Lebensohn and Needleman [95], Lebensohn et al. [96], Vidyasagar et al. [176, 177]) is a natural choice in this framework. The unique association of cells to grains, however, leads to sharp interfaces, which sine- and cosine functions cannot reconstruct, ultimately causing ringing artifacts (Gibbs phenomena). For a discussion of the application of FFT-based solvers in crystal plasticity, the associated effects of discontinuities, and possible ways of mitigating them, we refer to Eisenlohr et al. [36], Shanthraj et al. [148], Vidyasagar et al. [177].

- Again, due to the binary association of a cell to precisely one grain, the discretization geometry heavily influences the migration behavior. This is not necessarily an issue confined to cubical unit cells, as it can also occur, *e.g.*, for tetrahedral elements. Ivasishin et al. [72] proposed a modification to (1.6), in that they weighed the surface penalization term by a factor that depends on the local geometry of the boundary. Taking into account this additional shape factor helps to incorporate information corresponding more closely to

the curvature. We note that the phase-field method readily accomplishes this through the Laplacian in (1.4).

- Similar to the phase-field method, the instantaneous change of the inelastic state in an environment subjected to high stresses can be challenging. Despite the frequent employment in the modeling of recrystallization, to the author's best knowledge, the work of Adam et al. [1] is the only Monte-Carlo Potts method capable of satisfying linear momentum conservation. Recrystallized grains are, however, again not capable of undergoing further inelastic deformation. Consequently, recrystallized grains grow without undergoing further nucleation as the nucleation criterion does not account for the elastic contribution to the stored energy term. This simplifying approach circumvents the issue of the high stresses which cause difficulties for the update of the inelastic variables but do not allow for the modeling of significant grain refinement as the large equiaxed grains in their work show.

The Monte-Carlo Potts model provides a suitable environment for the modeling of dynamic recrystallization including both migration and nucleation, along with favorable conditions for the employment of an efficient FFT-based solver [1]. Rollett et al. [138] achieved qualitative replication of recrystallization behavior in terms of the strain-rate- and temperature-dependent transition from single- to multi-peak flow. Concerning static recrystallization, Monte-Carlo Potts has helped to obtain valuable insights into the different stages – from primary recrystallization up to the evolution of large equiaxed grains, including information on the grain size [1, 184] and texture evolution [1]. The inherent assumption that recrystallized grains do not undergo subsequent nucleation, however, largely prevents the extension of this model to dynamic recrystallization, despite its favorable properties.

1.3.4 Cellular automata

The Monte-Carlo method presents a numerical means of incorporating the stochastic nature of recrystallization in an energy-based fashion. Cellular automata are an alternative means of adopting a stochastic framework for the modeling of recrystallization on regular grids. Although the differences are marginal, we introduce this method as it complements the phase-field and the Monte-Carlo Potts model as one of the more popular means to simulate recrystallization.

We consider the same energetic formulation as in a Monte-Carlo Potts method (1.5), with a discretized equivalent (1.6). At every node $\boldsymbol{X}_i \in \Omega_\Delta$ in the discretized spatial

domain, we consider a state switch with a node belonging to the set of boundary nodes $\mathcal{S}(\boldsymbol{X}_i)$, for which a popular choice consists in the nearest neighbor model. Using the most favorable change in energy related to every node $\boldsymbol{X}_i \in \Omega_\Delta$, we evaluate a corresponding grain boundary speed via

$$v(\boldsymbol{X}_i) = \Delta\mathcal{I}(\boldsymbol{X}_i). \tag{1.8}$$

Since we endow each node with a discrete state, we cannot readily include the notion of a continuous velocity. To circumvent this issue, we define a maximum velocity as

$$v_{\max} = \max_{\boldsymbol{X}_i \in \Omega_\Delta} v(\boldsymbol{X}_i), \tag{1.9}$$

and use this maximum velocity along with the local velocity $v(\boldsymbol{X}_i$ to infer a threshold of the form $w^{\text{th}}(\boldsymbol{X}_i) = \kappa_{\text{GBM}} v(\boldsymbol{X}_i)/v_{\max}$. Finally, we generate a random number $w(\boldsymbol{X}_i) \sim \mathcal{U}([0,1])$, based on which we accept the formerly hypothetical state change at $\boldsymbol{X}_i$ if $w(\boldsymbol{X}_i) < w^{\text{th}}(\boldsymbol{X}_i)$ and reject otherwise.

Goetz and Seetharaman [55] were among the first to apply the concept of cellular automata to recrystallization. Using an exclusively dislocation-density based material model, they were able to qualitatively capture necklace-like dynamic recrystallization behavior. Unlike numerous studies that assume recrystallized grains to be final in the sense, that they do not undergo further recrystallization, they applied the same evolution law for the dislocation density of nuclei as for the initial grains. This approach allowed them to confirm theoretical considerations from Sakai and Jonas [143] in terms of the transition from single- to multi-peak flow curves. They did, however, neither account for stress-equilibrium nor include a notion of texture. Yazdipour et al. [191] demonstrated that dynamic recrystallization can quantitatively capture experimental data at various temperatures and strain rates. They further their approach closely to this particular loading scenario, as, *e.g.*, the evolution of the dislocation density followed a constant increment. Popova et al. [127] were the first to address the satisfaction of linear momentum conservation. In their work on hot compression of the Mg alloy AZ31, they endowed basal, prismatic and pyramidal slip systems with different hardening moduli and further captured twinning. They used a finite element approach to obtain the distribution of dislocation densities and obtained a considerable agreement with experimental results involving dynamic recrystallization up to strains of 35%. However, unlike

the two other methods we addressed, they did not allow recrystallized grains to undergo further inelastic deformation of any kind, which explains the limitation of their analysis to 35% strain.

In this short description of cellular automata, we have demonstrated the similarity to the Monte-Carlo Potts model. We note that Monte-Carlo Potts methods historically tended to use Glauber dynamics in close relation to atomic jump probabilities. Different to that, cellular automata generally build on a simple linear law regarding the dependence of migration speed and stored energy difference. Cellular automata further distinguish themselves from Monte-Carlo Potts methods through an increased computational expense as all boundary nodes at each time-step require simultaneous treatment. Given the minuscule differences and the simple translation between these two schemes, in subsequent studies, we focus on state-switch based rules according to the convention used in Monte-Carlo Potts methods without loss of generality.

1.4 Modeling of thermo-mechanical processes on the macroscale

Many of the above studies were constrained to the micro- or mesoscale, as either the focus lay in the modeling of the recrystallization mechanisms on the (sub)granular scale, or as the computational expense associated with these high-fidelity approaches made integration into a macroscale simulation unfeasible. The urge for optimizing the design of thermo-mechanical processes, however, motivated various studies dedicated fully or partially to the macroscale. We can divide these approaches into two categories: One group of investigations aims towards a mostly qualitative understanding of the influence of process and design parameters – particularly on the strain and stress distribution – without explicitly accounting for the underlying microstructural evolution. Since, however, the softening induced through slip-based deformation and recrystallization affects the macroscale stress response, phenomenological power-law constitutive relations serve as crude approximations. Applications include asymmetric rolling [77, 102], differential speed-rolling [78], equal channel angular extrusion [4, 47, 63, 103], and high-pressure torsion [44]. The results from these studies grant qualitative insights, *e.g.*, into the influence of friction [103], the strain homogeneity of the final sample [4, 77, 78] or the optimization of processes to achieve such [47], but also into more quantitative aspects including the force or torque required to perform the processing [44, 77].

The other group aims for an increasingly quantitative investigation of thermo-mechanical processing, thus alleviating the assumption that the impact of microstruc-

tural changes on the macrostructure is negligible. The reach of these works ranges from predominantly academic interest including contributions on non-uniform compression [165] or plane-strain compression [125], to applications of industrial interest, including cold rolling [61], hot rolling [110, 190], and equal channel angular extrusion [150]. While some approaches hinge on a material point analyses before and after processing [150], others rely on the notion of a grain size as a phenomenological concept without introducing grains as an individual entity with their own set of (in)elastic states [61, 63]. In the idea of vertical homogenization, Pinna et al. [125], Soho et al. [153], Yamaguchi et al. [190] coupled macro- and mesoscale to allow for an analysis of texture evolution, while Takaki et al. [165] used this approach to track the evolution of the average grain size.

The surmount part of recrystallization works draws from the well-established finite element method (see, *e.g.*, Figueiredo et al. [44], Hallberg et al. [63], Ji and Park [77]). Yet severe plastic deformation processes inherently comprise large deformations, which raises concerns regarding accuracy and stability of their respective findings. In light of those shortcomings, mesh-free methods recently gained attention in the modeling of process simulations as the absence of a mesh mitigates the need to account for, *e.g.*, rising error bounds with heavily distorted elements or negative volume. The *smooth particle hydrodynamics method* has provided insights into, *e.g.*, equal channel angular extrusion [41, 89, 104] or extrusion processes [129]. Despite its advantages, smooth particle hydrodynamic methods face other challenges such as the inclusion of boundary conditions, which – to this end – they solely achieve through restrictive, *ad-hoc* measures (see, *e.g.*, Ma and Hartmaier [104]). Alternative mesh-free methods that alleviate these shortcomings comprise *maximum information-entropy* [75] based meshfree methods presented in Arroyo and Ortiz [10], Kumar et al. [91], Sukumar [160], which yet remain to be tested in the framework of severe plastic deformation techniques.

1.5 Outline of this thesis

In Section 1.3, we addressed four of the currently most prominent numerical methods on the mesoscale. From the late 20th century until today, the contributions to this field showed tremendous advances, as initial studies – which mainly concentrated on a qualitative depiction of recrystallization – complement recent studies aimed equally at a qualitative understanding. To this end, however, these methods imposed restrictions in ways that narrow down their applicability to individual cases. In favor of a generalized depiction of dynamic recrystallization, we present

a novel method, which naturally combines the stochastic nature of recrystallization with the deterministic principles of crystal plasticity. Using this approach, which we term *Field-Monte-Carlo Potts method*, we demonstrate the ability to track dynamic recrystallization in metals with moderate anisotropy, such as copper, but also with severe anisotropic inelasticity including magnesium. We abandon the simplifying assumption of small strains, which many adopt for convenience and provide information on the evolution of flow stress, grain size, and texture. A common shortcoming in this field of research consists in the lack of transparency concerning the gain in accuracy of the ever-increasing fidelity. By providing two models that derive from the Field-Monte-Carlo Potts method without including all of its details, we attempt to enhance transparency. In order to concentrate on a comparison of recrystallization kinetics, we fit the Field-Monte-Carlo Potts model and its derivatives to experimental data for pure copper, as we have a good understanding of the purely slip-based behavior for this particular metal. We use the results from this analysis to assess in which cases computationally less expensive alternatives suffice to capture the central measures of dynamic recrystallization, namely texture evolution, grain refinement, and the homogenized stress evolution. Lastly, we benefit from the availability of this computationally inexpensive alternative and provide a novel multiscale framework for the analysis of severe plastic deformation processes. Combining the micro-, meso-, and macroscale, this new model allows gaining information on the local evolution of the three central measures we mentioned above across the processed sample. The new framework alleviates the restriction of previous works on severe plastic deformation (*c.f.* Section 1.4) and affords a framework to realize one of the major goals of *materials by design*, namely the tailoring of thermo-mechanical processes for individual applications.

The structure of the remaining parts of this thesis is as follows: In Chapter 2 we present the *Field Monte-Carlo Potts model*. We borrow the concept of state switches from Monte-Carlo Potts models and extend them via physically-motivated state switching rules for both the elastic and inelastic state variables. Using a novel transient interpretation of recrystallization, we provide tools that allow for stable handling of a broad spectrum of metals – isotropic and anisotropic – and demonstrate the idea based on a finite-deformations, slip-twin-interaction model for pure Mg. Chapter 3 validates the model from Chapter 2 using transient experimental data for copper endowed with a face-centered cubic crystallography. We further introduce a new computationally efficient Taylor model as the first grain-homogenized model capable of simultaneously tracking grain refinement as well as stress and texture

evolution. Using this, we identify the benefits and drawbacks of high-fidelity models – represented by the Field Monte-Carlo Potts model – and propose a direction for future research on the mesoscale modeling of dynamic recrystallization. In Chapter 4, we employ the Taylor model as a material model within a macroscale simulation of equal channel angular extrusion based on the meshfree maximum-entropy method by Kumar et al. [91]. We address the computational challenges arising through the shear induced at the bend and propose novel solutions that can be employed without restriction in other multiscale simulations. With respect to key performance indicators of processed billets, we use this framework to analyze grain refinement, texture evolution, and strain homogeneity. Finally, we use Chapter 5 to discuss the impact of these novel methods and the myriad insights from Chapter 2 to 4 and give a statement on past, current and future developments of the research on dynamic recrystallization from the micro- to the macroscale.

Chapter 2

STOCHASTIC MODELING OF DISCONTINUOUS DYNAMIC RECRYSTALLIZATION USING THE FIELD MONTE CARLO POTTS METHOD – APPLICATION TO MAGNESIUM

A.D. Tutcuoglu, A. Vidyasagar, K. Bhattacharya, and D.M. Kochmann. Stochastic modeling of discontinuous dynamic recrystallization at finite strains in hcp metals. *Journal of the Mechanics and Physics of Solids*, 122:590 – 612, 2019. ISSN 0022-5096. doi: https://doi.org/10.1016/j.jmps.2018.09.032. URL http://www.sciencedirect.com/science/article/pii/S0022509618303569.

Preamble

The author (A.T.) established the recrystallization model on the mesoscale and conducted simulations for different scenarios, while A. Vidyasagar (A.V.) and A.T. implemented the FFT-based solver.

2.1 Introduction

In Chapter 1, we provided a brief introduction into the currently available numerical models for the simulation of dynamic recrystallization at the mesoscale, which varied greatly in terms of their objectives and assumptions. A significant number of approaches refrained from solving for a deformation field, that satisfies linear momentum conservation [30, 110, 113, 157, 164, 183, 184]. Instead, simplifying models including the Taylor model [164], the Sachs model [105], the self-consistent viscoplastic model [183], and the iso-work-increment assumption [30] – all of which assume grainwise-constant states – govern the distribution of the deformation gradient across grains. These assumptions generally provide a reasonable approximation so long as localized effects are not dominant. In the presence of strong anisotropy, however, heterogeneities become increasingly important, especially at grain boundaries, where one grain is significantly more favorably aligned for plastic flow than the other. Alternatively – especially in early works using the Monte-Carlo Potts models – several approaches assumed a phenomenological stored energy field independent of the evolution of the deformation state. The exact distribution of these fields in general followed a probabilistic distribution [72, 121, 158] or drew experimental data from EBSD measurements [76]. Several approaches aimed to find a solution to the conservation of linear momentum via the finite element method [15, 16, 134, 135]

or FFT-based approaches [1, 28, 197, 198]. Although these works investigated both static and dynamic recrystallization, they share the assumption that recrystallized grains do not undergo inelastic deformation, which automatically impedes further nucleation. Particularly for processes involving large strains, this assumption poses a significant restriction to the modeling of dynamic recrystallization, as an entirely recrystallized material can only accommodate strain via elastic deformation. Along with several physical phenomena, which this approach cannot capture, the effective stress-strain response inhibits a much stiffer response vis a vis experimental results and multi-peak stress-strain behavior is entirely unrecoverable.

In like manner, the range of inelastic models employed in these studies covered various levels of fidelity. A number of approaches build on the Kocks-Mecking model [106] for the evolution of the dislocation density [11, 32, 62, 122, 164]. This method, however, hinders the analysis of metals that possess a strongly inhomogeneous set of slip systems. The framework of finite strain crystal plasticity affords more involved approaches [1, 28, 110, 127, 197, 198]. Models using this continuum level way of capturing slip-based deformation generally hinge on power law updates with high exponents to approximate the rate-independence inherent to slippage [69]. These power laws, in return, render the inelastic updates vulnerable to instability, as the large exponents require small timesteps to attain sufficient accuracy [85]. It is evident that the combination of a crystal plasticity model which is prone to instabilities along with recrystallization kinetics – which involve nearly instantaneous changes of the deformation state of the microstructure – poses a challenge. Consequently, many of these models impose assumptions to cope with this short-coming which generally include the perception of recrystallized grains deforming in an exclusively elastic way or the renunciation from fully-resolved methods.

Early works on the numerical modeling of recrystallization primarily aimed for a better fundamental understanding of the underlying mechanisms of grain boundary migration and nucleation. In this context, it comes as no surprise that the material models employed to capture the inelastic deformation due to slippage and other strain-accommodating mechanisms were often either not representative of any particular metal (see, *e.g.*, Peczak and Luton [122]) or only symbolic in the sense, that, *e.g.*, they used a single dislocation density to capture the evolution of slip on 12 slip planes (see, *e.g.*, Takaki et al. [164]). The set of methods relying on a crystal plasticity framework belongs to a recent trend, in which the a quantitative description of, *e.g.*, the stress-strain relation, texture evolution, and microstructural evolution com-

plements the qualitative understanding of recrystallization. While extensive work exists on the analysis of materials with a face-centered cubic (fcc) crystallography such as copper (see, *e.g.*, Mellbin et al. [110], Zhao et al. [197, 198]), the work on metals endowed with a hexagonal closed packed (hcp) crystallography currently has limitations. To understand this circumstance, we note that the anisotropy inherent to the hcp structure generally permits for a relatively simple activation of slip on the basal plane, whereas strain accommodation on other planes is not as easy to accomplish. Although this discrepancy is not as pronounced at higher temperatures, at room temperature, it yields poor formability. This class of metals would, therefore, be predominantly subjected to die-casting and other casting methods [2, 115, 192], which may not lead to the desirable ultra-fine grains, but which allow circumventing the formability issues through elevated temperatures (*c.f.* Chapter 1). The lack of dynamic recrystallization in this type of process therefore at least partially explains the inertia in the numerical analysis of hcp metals. Among the most prominent metals that posses a hcp crystallography stands magnesium (Mg) and its alloys. With a density below that of all other structure metal [195], favorable bio-degradability [187] and damping properties [31] along with a competitive specific strength [189], Mg alloys are a promising candidate to replace aluminum, titanium, and steel [192]. Pure Mg, however, suffers under poor corrosion resistance [38] and flammability properties – shortcomings that could only recently be overcome by appropriate alloying with (expensive) rare-earth metals such as gadolinium, yttrium or zirconium and to some extent using less expensive alternatives including calcium, tin, and zinc [38, 100, 120, 192]. With an ever-growing spectrum of applications, however, requirements on the processed metal alloys increase [195]. For the scales at which medical devices operate, for example, a fine-grained microstructure is indispensable; further, the increase in strength through processing is more desirable compared to the addition of (generally heavy) rare earth metals. Addressing this need for tailored processing routes requires an improved numerical framework for the modeling of dynamic recrystallization in hcp metals.

Asadi et al. [11] conducted pioneering work in this field by capturing dynamic recovery and dynamic recrystallization in Mg alloy AZ91 using a 2D cellular automaton. However, the underlying material follows the approach from Mecking and Kocks [106], which does not yield an accurate representation of the anisotropic inelasticity in hcp metals. Furthermore, they assumed homogeneity within grains. Still based on the assumption that flow stress is dependent on a single scalar variable, Wang et al. [180] used the model of Estrin and Mecking [39] within a 2D cellular

automaton to model dynamic recrystallization in Mg alloy ZM21; however, that model neglected linear momentum conservation on the microscale and hence did not capture the heterogeneous deformation within grains. Gentry and Thornton [52] investigated recrystallization in titanium, a metal which also possesses hcp crystallography at room temperature. Their model, however, does not capture twinning and – similar to Chen et al. [28] – introduces nucleation in a simplified, numerically convenient way (new grains emerge as spherical, dislocation-free regions and their associated order parameters are held constant for a period of time to prevent the interface energy from forcing the recrystallized grain to disappear). We note that none of the above models provided the means to capture deformation twinning [29] whose finite twinning shears are not representable by small-strain models. Popova et al. [127] were the first to include a notion of a twin in the numerical simulation of dynamic recrystallization of Mg. Using a crystal plasticity-based approach, they incorporated the anisotropy between the various slip planes, without accounting for the different hardening mechanisms, however (see, *e.g.*, Chang and Kochmann [26]). Further, they tailored the recrystallization model towards the capturing of severe grain enlargement, with the average grain size rising from an initial value of 14 μm to 120 μm at the final tensile strain of 35 %.

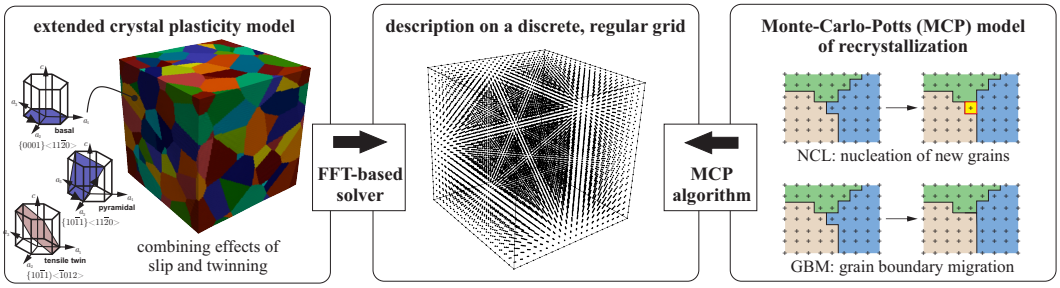

Figure 2.1: Schematic overview of the presented model, which uses an extended crystal plasticity formulation whose FFT-based discrete solution allows for the coupling to a Monte-Carlo-Potts description of recrystallization.

A comprehensive model that simultaneously captures discontinuous dynamic recrystallization at finite deformations, accounts for the statistical nature of grain nucleation as well as migration, and provides a suitable framework for the analysis of extensive inelastic anisotropy is presently missing. The necessity for such a model is, however, high as we seek an improved understanding of the microstructural evolution of hcp metals subjected to severe plastic deformation processes. The goal of this chapter is to fill this gap. Figure 2.1 illustrates the key idea. We perform fully resolved simulations of the plastic deformation in polycrystals using an ex-

tended crystal plasticity model in conjunction with a Fast-Fourier-transform (FFT) based solver. The fully resolved simulation allows us to capture the non-uniformity of plastic deformation at the subgranular level and appropriately mimics the deterministic nature at the time-scale of interest. Simultaneously, we model grain boundary migration and grain nucleation using a statistical MCP model. Since the latter requires a regular grid, we use the FFT-based continuum mechanics solver to blend the continuum and discrete approaches. Each grid point corresponds to a particular grain and carries information about the crystallographic orientation as well as elastic and plastic states. At each Monte-Carlo time step, we either migrate the grain boundary or nucleate a new grain based on probabilities that depend on the elastic and plastic states of the grid point. We subsequently update the elastic and plastic states and iterate. For the time scale of interest, this allows us to couple the deterministic nature of plastic deformation with the stochastic nature of grain nucleation and migration. Representative of the highly anisotropic inelastic deformation mechanisms in hcp metals, we choose an extended crystal plasticity model for pure Mg Chang and Kochmann [26], Chang et al. [27], which includes twinning in an effective, volume-fraction based sense.

The structure of the remainder of this contribution is as follows: Section 2.2 briefly summarizes the constitutive model for Mg as a representative hcp material and the FFT-based homogenization scheme which turns the continuum RVE problem into a discrete grid-based problem. Within this framework, Section 2.3 introduces the model for recrystallization, for which Section 2.4 provides a verification of proper convergence and scaling of the numerical scheme. Once we have laid out the theory and verified the numerics, we present simulations of the microstructural evolution and resulting effective response of Mg during ECAE in Section 2.5. To demonstrate the versatility of the model, Section 2.6 addresses the influence of its various parameters on the material response. Finally, Sections 2.7 and 2.8 discuss the findings and conclude our investigation, respectively.

2.2 RVE-level constitutive model and discretization

2.2.1 Finite-strain crystal plasticity continuum model

Plasticity in hcp metals emerges from the activation of a total of $n_s = 18$ slip systems: ⟨c+a⟩-pyramidal and ⟨a⟩-pyramidal systems each contribute six systems, alongside basal and prismatic slip which each contribute three slip systems. The significantly lower critical resolved shear stresses in the basal plane in comparison to slip on non-basal planes results in the activation of alternative strain-accommodating

processes, which in the case of hcp metals constitutes deformation twinning [29]. Although recent studies relying on density functional theory (DFT) suggest the presence of eleven twin systems [161], we here constrain ourselves to the two most easily activated systems, viz. compression and extension twins (with the respective names referring to the loading along the c-axis). Also, we restrict our model to the inclusion of the basal, prismatic and ⟨c+a⟩-pyramidal systems, while neglecting ⟨a⟩-pyramidal systems following the discussion in Chang and Kochmann [26]. The notion of *slip activities* $\boldsymbol{\gamma} = \{\gamma_1, \dots, \gamma_{n_s}\} \in \mathbb{R}^{n_s}$ quantifies plastic slip. To capture hardening, we define the accumulated plastic slips $\boldsymbol{\varepsilon} = \{\varepsilon_1, \dots, \varepsilon_{n_s}\} \in \mathbb{R}^{n_s}_+$ via the evolution law (with initial condition $\boldsymbol{\varepsilon} = \boldsymbol{0}$)

$$\dot{\epsilon}_\alpha = |\dot{\gamma}_\alpha| \qquad \forall \quad \alpha \in \{1, ..., n_s\}. \tag{2.1}$$

Since twin lamellae may form on length scales far below the granular scale, we follow the strategy of [3, 57, 67, 159, 193] and define the homogenized notion of a *twin volume fraction* $\boldsymbol{\lambda} = \{\lambda_1, \dots, \lambda_{n_{\text{tw}}}\} \in [0,1]^{n_{\text{tw}}}$, capturing the local effective volume fraction[1] of the twinned crystal at any point on the polycrystalline mesoscale, where n_{tw} denotes the number of twin systems. We further impose the constraint $\sum_{\beta=1}^{n_{\text{tw}}} \lambda_\beta \leq 1$.

Following Kalidindi [81], we neglect the effect of kinematic interactions between slip and twinning but instead include relaxation due to both slip and twinning into $\boldsymbol{F}^{\text{in}}$ so as to yield the multiplicative decomposition $\boldsymbol{F} = \boldsymbol{F}^{\text{e}}\boldsymbol{F}^{\text{in}}$ with $\boldsymbol{F} = \text{Grad}\,\boldsymbol{\varphi}$ denoting the deformation gradient. The additive decomposition of the velocity gradient,

$$\boldsymbol{l} = \dot{\boldsymbol{F}}\boldsymbol{F}^{-1} = \boldsymbol{l}^{\text{e}} + \boldsymbol{l}^{\text{in}} = \boldsymbol{l}^{\text{e}} + \boldsymbol{F}^{\text{e}}\tilde{\boldsymbol{l}}^{\text{in}}\,(\boldsymbol{F}^{\text{e}})^{-1} \tag{2.2}$$

with

$$\boldsymbol{l}^{\text{e}} = \dot{\boldsymbol{F}}^{\text{e}}\,(\boldsymbol{F}^{\text{e}})^{-1} \qquad \text{and} \qquad \tilde{\boldsymbol{l}}^{\text{in}} = \dot{\boldsymbol{F}}^{\text{in}}(\boldsymbol{F}^{\text{in}})^{-1}, \tag{2.3}$$

introduces the effects of slip and twinning via the inelastic velocity gradient with an

[1] The *effective* twin volume fractions $\lambda_\beta \in [0,1]$ capture only the effects of crystallographic reorientations at the relevant mesoscopic scale in a homogenized sense (by reorienting the slip and twin systems), without describing individual twin lamellae at lower scales. This model thus captures stress concentrations at twin boundaries only in case of macro-twins on the level of the numerical discretization (and analogous to GBs) while local concentrations near, *e.g.*, nanoscale twin lamellae are not accounted for explicitly.

assumed additive decomposition as $\tilde{\boldsymbol{l}}^{\text{in}} = \tilde{\boldsymbol{l}}^{\text{p}} + \tilde{\boldsymbol{l}}^{\text{tw}}$ [26] where

$$\begin{aligned}\tilde{\boldsymbol{l}}^{\text{p}} &= \sum_{\alpha=1}^{n_{\text{s}}} \dot{\gamma}_\alpha \underbrace{\left[\left(1 - \sum_{\beta=1}^{n_{\text{tw}}} \lambda_\beta\right) \boldsymbol{s}_\alpha \otimes \boldsymbol{m}_\alpha + \sum_{\beta=1}^{n_{\text{tw}}} \lambda_\beta \boldsymbol{s}'_{\alpha\beta} \otimes \boldsymbol{m}'_{\alpha\beta}\right]}_{\equiv \boldsymbol{p}_\alpha}, \\ \tilde{\boldsymbol{l}}^{\text{tw}} &= \sum_{\beta=1}^{n_{\text{tw}}} \dot{\lambda}_\beta \gamma_\beta^{\text{tw}} \boldsymbol{a}_\beta \otimes \boldsymbol{n}_\beta.\end{aligned} \tag{2.4}$$

Here, vectors $(\boldsymbol{s}_\alpha, \boldsymbol{m}_\alpha)$ define slip system α, whereas $(\boldsymbol{a}_\beta, \boldsymbol{n}_\beta)$ define twin system β and γ_β^{tw} denotes the respective twinning strain. The two mirrored slip systems in the twinned crystal result from a Householder mapping applied to the respective parent slip system such that

$$\boldsymbol{s}'_{\alpha\beta} = \boldsymbol{Q}_\beta \boldsymbol{s}_\alpha, \quad \boldsymbol{m}'_{\alpha\beta} = \boldsymbol{Q}_\beta \boldsymbol{m}_\alpha, \quad \boldsymbol{Q}_\beta = \boldsymbol{I} - 2\boldsymbol{n}_\beta \otimes \boldsymbol{n}_\beta. \tag{2.5}$$

We use a variational setting based on the Helmholtz free energy density given by $W = W(\boldsymbol{F}, \boldsymbol{F}^{\text{in}}, \boldsymbol{\varepsilon}, \boldsymbol{\lambda})$ which decomposes into elastic strain energy and plastic stored energy due to slip and twinning according to

$$W(\boldsymbol{F}, \boldsymbol{F}^{\text{in}}, \boldsymbol{\varepsilon}, \boldsymbol{\lambda}) = W_{\text{el}}\left(\boldsymbol{F}\left(\boldsymbol{F}^{\text{in}}\right)^{-1}\right) + W_{\text{sl}}(\boldsymbol{\varepsilon}) + W_{\text{tw}}(\boldsymbol{\lambda}). \tag{2.6}$$

We further define the dual dissipation potential [118] as

$$\Psi^*(\dot{\boldsymbol{\varepsilon}}, \dot{\boldsymbol{\lambda}}) = \Psi^*_{\text{sl}}(\dot{\boldsymbol{\varepsilon}}) + \Psi^*_{\text{tw}}(\dot{\boldsymbol{\lambda}}), \tag{2.7}$$

so that the principle of the minimum dissipation potential yields differential inclusions of the form

$$\begin{cases} 0 \in \dfrac{\partial}{\partial \dot{\gamma}_\alpha}\left(\dot{W} + \Psi^*\right) = -|\tau_\alpha^{\text{p}}| + \dfrac{\partial W_{\text{sl}}}{\partial \epsilon_\alpha} + \dfrac{\partial \Psi^*_{\text{sl}}}{\partial \dot{\epsilon}_\alpha} \quad \forall \quad \alpha \in \{1, \ldots, n_{\text{s}}\}, \\ 0 \in \dfrac{\partial}{\partial \dot{\lambda}_\beta}\left(\dot{W} + \Psi^*\right) = -\tau_\beta^{\text{tw}} + \dfrac{\partial W_{\text{tw}}}{\partial \lambda_\beta} + \dfrac{\partial \Psi^*_{\text{tw}}}{\partial \dot{\lambda}_\beta} \quad \forall \quad \beta \in \{1, \ldots, n_{\text{tw}}\}, \end{cases} \tag{2.8}$$

with the notions of resolved shear stresses τ_α^{p} and τ_β^{tw} for slip and twin, respectively, defined through

$$\tau_\alpha^{\text{p}} = \boldsymbol{\Sigma} \cdot \boldsymbol{p}_\alpha \qquad \text{and} \qquad \tau_\beta^{\text{tw}} = \gamma_\beta^{\text{tw}} \boldsymbol{\Sigma} \cdot \left(\boldsymbol{a}_\beta \otimes \boldsymbol{n}_\beta\right) \tag{2.9}$$

where $\boldsymbol{\Sigma} = (\boldsymbol{F}^{\text{e}})^{\text{T}} \boldsymbol{P} (\boldsymbol{F}^{\text{in}})^{\text{T}}$ denotes the Mandel stress tensor, and the first Piola Kirchhoff stress tensor is described through $\boldsymbol{P} = \partial W / \partial \boldsymbol{F} = \partial W_{\text{el}} / \partial \boldsymbol{F}$.

The elastic strain energy density is modeled using the isotropic compressible Neo-Hookean energy density

$$W_{\mathrm{el}}(\boldsymbol{F}) = \frac{\mu}{2}\left(\frac{I_1}{J^{-2/3}} - 3\right) + \frac{\lambda}{2}(J-1)^2 \quad \text{with} \quad I_1 = \mathrm{tr}\left(\boldsymbol{F}^T\boldsymbol{F}\right), \quad J = \det \boldsymbol{F} \tag{2.10}$$

with μ and λ denoting the shear and bulk modulus, respectively. The choice of an isotropic model draws on the work of Chang and Kochmann [26] who showed that anisotropic elastic models (see, *e.g.*, Schröder et al. [146]) have negligible effects on simulated results – due to the low elastic anisotropy in Mg – while increasing computational costs.

The inelastic strain energy density due to slip comprises self- and latent hardening contributions and adds to the plastic anisotropy inherent in hcp metals:

$$W_{\mathrm{sl}} = W_{\mathrm{sl,lat}} + W_{\mathrm{sl,self}} = \frac{1}{2}\boldsymbol{\varepsilon}\cdot\mathcal{H}\boldsymbol{\varepsilon} + \sum_{\alpha=1}^{n_s}\sigma_\alpha^\infty\left[\epsilon_\alpha + \frac{\sigma_\alpha^\infty}{h_\alpha}\exp\left(-\frac{h_\alpha\epsilon_\alpha}{\sigma_\alpha^\infty}\right)\right], \tag{2.11}$$

where Voce hardening [3, 57] captures the high resistance of prismatic and pyramidal slip [67] with σ_α^∞ and h_α representing the ultimate stress and hardening rate on the α^{th} slip system, respectively. $\mathcal{H}$ is a symmetric matrix endowed with the hardening moduli on its off-diagonals and a zero diagonal (which is positive-definite for all sensible values of ϵ_α). For twinning, we assume quadratic hardening for both self-induced as well as latent twin hardening, with self-hardening moduli h_β and zero-diagonal endowed, symmetric latent hardening matrix $\mathcal{K}$, yielding

$$W_{\mathrm{tw}} = W_{\mathrm{tw,self}} + W_{\mathrm{tw,lat}} \qquad \text{with} \qquad \begin{cases} W_{\mathrm{tw,self}} = \displaystyle\sum_{\beta=1}^{n_{\mathrm{tw}}}\frac{1}{2}h_\beta\lambda_\beta^2 \\ W_{\mathrm{tw,lat}} = \dfrac{1}{2}\boldsymbol{\lambda}\cdot\mathcal{K}\boldsymbol{\lambda} \end{cases}. \tag{2.12}$$

Following Ortiz and Stainier [119], we introduce power-law dissipation potentials of the form

$$\Psi_{\mathrm{sl}}^*(\dot{\boldsymbol{\gamma}}) = \sum_{\alpha=1}^{n_{\mathrm{s}}}\frac{\tau_{0,\alpha}\dot{\gamma}_{0,\alpha}}{m_\alpha+1}\left(\frac{\dot{\gamma}_\alpha}{\dot{\gamma}_{0,\alpha}}\right)^{m_\alpha+1} \quad \text{and} \quad \Psi_{\mathrm{tw}}^* = \sum_{\beta=1}^{n_{\mathrm{tw}}}\frac{\tau_{0,tw,\beta}\dot{\lambda}_{0,\beta}}{m_{\mathrm{tw},\beta}+1}\left(\frac{\dot{\lambda}_\beta}{\dot{\lambda}_{0,\beta}}\right)^{m_{\mathrm{tw},\beta}+1}, \tag{2.13}$$

for plastic slip and twinning, respectively. The slip hardening exponent m_α is close to 0 to approximate rate independence without compromising the ability to explicitly perform internal variable updates. Although recent findings suggest rate independence for twinning [173], in the framework of explicit state updates, we

follow Chang and Kochmann [26] and choose the above dissipation potential where $m_{tw,\beta}$, $\tau_{0,tw,\beta}$ and $\dot{\lambda}_{0,\beta}$ represent the twin hardening exponent, critical resolved shear stress, and reference twin rate for the β^{th} twin system, respectively.

Even though implicit variational constitutive updates [119] allow for significantly larger load/time steps as Chang and Kochmann [26] have shown for the present constitutive model, we here favor explicit updates for the following reasons. Explicit updates improve numerical stability and convergence for high numbers of slip and twin systems as those described here. Also, recrystallization (discussed in Section 2.3) will be treated in an explicit fashion and, at times, requires to be resolved at time steps smaller than those characteristic of implicit updates. Therefore, we solve the evolution laws for both slip and twin ratios explicitly,

$$\dot{\gamma}_\alpha = \dot{\gamma}_{0,\alpha} \left| \frac{\left(|\tau_\alpha^{\text{p}}| - \frac{\partial W^{\text{p}}}{\partial \epsilon_\alpha} \right)^+}{\tau_{0,\alpha}} \right|^{\frac{1}{m_\alpha}} \text{sgn}\left(\tau_\alpha^{\text{p}}\right), \quad \dot{\lambda}_\beta = \dot{\lambda}_{0,\beta} \left| \frac{\left(\tau_\beta^{\text{p}} - \frac{\partial W^{\text{p}}}{\partial \lambda_\beta} \right)^+}{\tau_{0,\beta}} \right|^{\frac{1}{m_{\beta,\text{tw}}}}, \tag{2.14}$$

by explicit time integration using a forward-Euler scheme, provided $m_\alpha, m_{\beta,\text{tw}} \neq 0$. In this context, $(\cdot)^+ = \max(0, \cdot)$ denote Macaulay brackets. Since the nearly rate independence demands small hardening coefficients $m_{\alpha,\text{p}}$, small increments are required to prevent the forward-Euler scheme from overshooting. All numerical values of the model parameters are summarized in Table 2.1.

2.2.2 Polycrystal response and FFT-based homogenization

We employed the above crystal plasticity model within an RVE Ω that contains a representative grain network at the mesoscale. Periodic boundary conditions on its boundary $\partial\Omega$ enforce mechanical equilibrium in order to link the microstructural fields to the effective material behavior at the macroscale, as observed in metal forming processes. To this end, we follow concepts of classical homogenization [51, 87, 112] where the macroscopic deformation gradient $\boldsymbol{F}^*$ is imposed as the RVE average, *i.e.*, $\langle \boldsymbol{F}(\boldsymbol{X}) \rangle = \boldsymbol{F}^*$ where $\langle \cdot \rangle = |\Omega|^{-1} \int_\Omega (\cdot)\, \text{d}V$. Within the RVE, we obtain the deformation mapping from quasistatic linear momentum balance, $\text{Div}\, \boldsymbol{P} = \boldsymbol{0}$, while the internal variables follow the inelastic evolution laws we discussed above. The macroscopically experienced, effective stress equals the RVE average $\boldsymbol{P}^* = \langle \boldsymbol{P}^*(\boldsymbol{X}) \rangle$. In the chosen applications we neglect body forces and inertial effects.

With the MCP model in mind, we discretize the RVE into a regular grid and apply the concepts of Moulinec and Suquet [116] to solve the governing equations in Fourier

Table 2.1: Material parameters used in the extended crystal plasticity model for Mg after Chang and Kochmann [26]. We note that parameter τ_0, the critical resolved shear stress, has been modified from the original model, since we used the formulation of Chang and Kochmann [26] in an implicit context, whereas here we use an explicit formulation that does not suffer from numerical complications by introducing a hard threshold into the rate-dependent model (c.f. Chang et al. [27]).

elastic Lamé moduli

λ	μ
24.0	19.4
GPa	GPa

extension twins

h_0	k_{ij}	$\dot{\lambda}_0$	γ_{tw}	m_{tw}
1.7	40	1	0.129	1
MPa	GPa	s^{-1}	-	-

basal slip

h_α	σ_∞	h_{ij}	τ_0	m	$\dot{\gamma}_0$
7.1	0.70	0	17.5	0.05	1.0
GPa	MPa	MPa	MPa	-	s^{-1}

prismatic slip

h_α	σ_∞	h_{ij}	τ_0	m	$\dot{\gamma}_0$
9.0	85	20	17.5	0.05	1.0
GPa	MPa	MPa	MPa	-	s^{-1}

pyramidal $\langle c+a \rangle$ slip

h_α	σ_∞	h_{ij}	τ_0	m	$\dot{\gamma}_0$
30	150	25	17.5	0.05	1.0
GPa	MPa	MPa	MPa	-	s^{-1}

space (see also Eisenlohr et al. [36], Lebensohn and Needleman [95], Lebensohn et al. [96]). To this end, the RVE is discretized into $n = N^3$ grid points in 3D space, with N denoting the number of grid points per side and $\boldsymbol{X}^k, k \in \{1, ..., n\}$ referring to the position of each grid point in the undeformed configuration. We denote the discretized space including all nodes Ω_Δ.

Our numerical predictor-corrector iterative scheme starts with an initial guess $\boldsymbol{F}^0(\boldsymbol{X}^k)$ for the distribution of $\boldsymbol{F}(\boldsymbol{X}^k)$ in the RVE, which allows to evaluate the stress tensor field $\boldsymbol{P}^0(\boldsymbol{X}^k) = \boldsymbol{P}(\boldsymbol{F}^0(\boldsymbol{X}^k))$ and the stiffness tensor field $\mathbb{C}^0 = \mathbb{C}(\boldsymbol{F}^0(\boldsymbol{X}^k))$. We compute the average stiffness tensor $\mathbb{C}^{\text{avg,m}} \equiv \langle \mathbb{C}^{\text{m}}(\boldsymbol{X}) \rangle$ at each iteration step m by averaging over all grid points in the RVE. Based on the average stiffness tensor as a linear reference medium[2], we define a stress perturbation field $\boldsymbol{\tau}(\boldsymbol{X})$ such that at every point $\boldsymbol{X} \in \Omega$

$$\boldsymbol{\tau}^m(\boldsymbol{X}) = \boldsymbol{P}^m(\boldsymbol{X}) - \mathbb{C}^{\text{avg},m}\boldsymbol{F}^m(\boldsymbol{X}), \tag{2.15}$$

[2]Although it was shown that choosing the average stiffness tensor as a reference may lead to divergence, using $\mathbb{C}^{\text{avg}}$ leads to stable results in our framework, thus avoiding the need for a more elaborated scheme as presented, *e.g.*, by Kabel et al. [80].

Substituting (2.15) into the linear momentum conservation equation yields

$$\operatorname{Div} \boldsymbol{\tau}^m(\boldsymbol{X}) + \operatorname{Div} [\mathbb{C}^{\text{avg},m} \boldsymbol{F}^m(\boldsymbol{X})] = \boldsymbol{0}. \tag{2.16}$$

Applying a discrete Fourier transform to (2.16) along with the definition of the deformation gradient via $\boldsymbol{F}(\boldsymbol{X}) = \operatorname{Grad} \boldsymbol{\varphi}(\boldsymbol{X})$ yields an explicit update rule for the deformation gradient in Fourier space (with $\boldsymbol{K}^k \in \mathcal{T}$ denoting the wave vectors and $\mathcal{T}$ the complete set of the n wave vectors in Fourier space), which becomes, using indicial notation,

$$\hat{F}^{m+1}_{jL}(\boldsymbol{K}^k) = \begin{cases} \left[A^m_{ij}(\boldsymbol{K}^k)\right]^{-1} \hat{\tau}^m_{iJ}(\boldsymbol{K}^k) K^k_J K^k_L & \text{for } \boldsymbol{K}^k \neq \boldsymbol{0}, \\ F^*_{jL} & \text{for } \boldsymbol{K}^k = \boldsymbol{0}, \end{cases} \tag{2.17}$$

with the acoustic tensor components

$$A^m_{ik}(\boldsymbol{K}^k) = \mathbb{C}^{\text{avg},m}_{iJkL} K^k_L K^k_J. \tag{2.18}$$

Starting with $\boldsymbol{F}^0(\boldsymbol{X}^k)$, this provides an iterative update procedure which we solve by fixed-point iteration: we compute $\hat{\boldsymbol{F}}^{m+1}(\boldsymbol{K}^k)$ in Fourier space, we transform it into $\boldsymbol{F}^{m+1}(\boldsymbol{X}^k)$ in real space, which we use to evaluate $\boldsymbol{P}^{m+1}(\boldsymbol{X}^k)$, $\boldsymbol{\tau}^{m+1}(\boldsymbol{X}^k)$ and $\mathbb{C}^{\text{ave},m+1}$. After Fourier transform, we use the resulting $\hat{\boldsymbol{P}}^{m+1}(\boldsymbol{K}^k)$ and $\hat{\boldsymbol{\tau}}^{m+1}(\boldsymbol{K}^k)$ in Fourier space for the next update, until we achieve convergence in the sense of the discrete L_2-norm of the stress perturbation $\boldsymbol{\tau}^m$.

Rather than applying the above FFT-based scheme directly, we use a finite-difference approximation for all spatial derivatives before applying the Fourier transform [95, 117]. This approximation, applied to the related problem of small-strain inelasticity in [176], uses a central-difference approximation and leads to the approximate Fourier transform of a derivative

$$\mathcal{F}\left(\frac{\partial f}{\partial x_i}\right) = -ihk_i \mathcal{F}(f) \approx -\frac{i \sin(hk_i \Delta x)}{\Delta x} \mathcal{F}(f), \tag{2.19}$$

which converges to the exact derivative with decreasing grid size ($\Delta x \to 0$). A major improvement, this finite-difference correction considerably mitigates ringing artifacts and Gibbs phenomena associated with sharp gradients in material properties (such as those across grain or twin boundaries). Vidyasagar et al. [176] and Vidyasagar et al. [177] successfully applied this correction to polycrystals of small-strain ferroelectric ceramics and of finite-strain crystal plasticity in Mg, respectively; the reader is referred to those publications for further information.

We solve the above numerical scheme in a time-incremental fashion to find a sequence of mechanical equilibria, using a constant time step Δt such that, here and in the following, $(\cdot)_\alpha$ denotes[3] a quantity evaluated at time $t_\alpha = \alpha \cdot \Delta t$.

2.3 A stochastic model for recrystallization

Modeling recrystallization requires to account for both grain nucleation (NCL) and migration (GBM), which is accomplished here by a stochastic model. In a nutshell, each point inside the RVE is associated with a particular grain through its crystallographic orientation (manifesting in the model through the slip and twin system orientations, and potentially through elastic anisotropy). Here we refer to the grain association of a material point as a its *state*. Consider an RVE containing n_G grains, so that each point has a unique integer state $s \in [1, n_G]$ describing its crystallographic orientation (in the undeformed configuration). At any point in time, a material point is allowed to undergo a *state switch*, *i.e.*, to either nucleate a new grain (with a fresh crystallographic orientation, raising n_G by one) or, if in the vicinity of a grain boundary (GB), to join a neighboring grain and adopt its orientation. Whether or not such a state switch occurs depends on the current state of the local elastic and inelastic fields as well as on temperature and deformation history. Drawing inspiration from the Monte-Carlo-Potts (MCP) model [128] as well as the Monte-Carlo-Metropolis and Metropolis-Hasting algorithms [111, 114], the probability of switching increases with the stored energy release upon a state switch. The probability also increases with temperature through thermal fluctuations. We exploit the crystal plasticity framework introduced in Section 2.2 to define state switches and the related release of elastic and inelastic energy, and we exploit the FFT-based grid discretization to apply the MCP scheme in a spatially and temporally discrete fashion.

To this end, we will introduce an MCP model to define the probability of a state switch (Section 2.3.1), lay out how a state switch affects the local elastic and internal variables (Section 2.3.2), and integrate the time evolution of the thus-obtained recrystallization model with the RVE-level mechanical boundary value problem (Section 2.3.3). The overall incremental realization of the stochastic model is illustrated in Figure 2.2.

[3] We use Greek indices for time steps to avoid confusion with classical index notation.

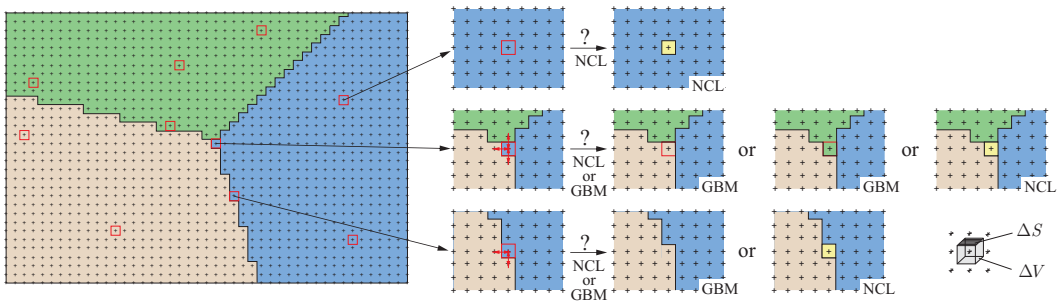

Figure 2.2: Schematic view of the state switch procedure: $n_{\mathrm{MC,GBM}}$ MCP sampling points are chosen from only those grid points adjacent to GBs, and $n_{\mathrm{MC,NCL}}$ sampling points from all n grid points. For each chosen grid point, possible options for state switches include the nucleation of a new grain (shown in yellow) or the adaption of the grain orientation of one of the neighboring points across a GB. In the latter case, the current energy $\mathcal{I}$ of each chosen sampling point is compared to its energy $\tilde{\mathcal{I}}$ after a possible state switch, by adopting the orientation of a neighboring grid point lying within an adjacent grain; the probability of switching depends on the energy difference $E = \tilde{\mathcal{I}} - \mathcal{I}$. Shown is also the definition of volume element ΔV and surface element ΔS.

2.3.1 Monte-Carlo-Potts model: probability of state switching

In order to capture the stochastic nature of state switches, we adopt an MCP-like approach [7, 74, 128, 138, 156, 157]. Unlike the model of Ising [71] which restricts the total number of states to two, our MCP model accounts for as many degenerate states as there are grains present at any given time (and the number of grains, n_G, is allowed to change in case of the nucleation of new grains or the consumption of existing grains). Instead of checking all n points inside the RVE for a potential state switch, we randomly select $n_{\mathrm{MC,GBM}}, n_{\mathrm{MC,NCL}} \ll n$ representative points for GBM/NCL at each time step and check which of those will undergo a state switch based on the criteria to be defined in Section 2.3.2. In a variation of the classical MCP model, we choose the $n_{\mathrm{MC,GBM}}$ points exclusively from those grid points adjacent to the GBs inside the RVE, whereas for the $n_{\mathrm{MC,NCL}}$ points, we generally chose them from the n grid points. For proper scaling, we choose $n_{\mathrm{MC,GBM}} \propto n^{2/3}$ to conserve the number of MCP points chosen from the GBs. The specific choice of the ratios $m_{\mathrm{MC},i} = n/n_{\mathrm{MC},i}$ (with i = GBM or NCL) naturally introduces the characteristic time scales of recrystallization. As shown in Section 2.4, the speed of migrating GBs is preserved if we chose the discrete time step according to $\Delta t \propto n^{-1/3} = N^{-1}$. We further adopt the scaling for $n_{\mathrm{MC,NCL}} \propto \Delta t$ to control the nucleation rate.

The driving force behind a state switch is the reduction of stored energy. The total energy $\mathcal{I}$ of the RVE consists of mechanical (Helmholtz) energy stored within Ω

(including elastic and inelastic contributions) and interface energy concentrated in the GBs with surface energy density γ (and Γ denotes the collection of all GBs), so that[4]

$$\begin{aligned}\mathcal{I} &= \int_\Omega A\left(\boldsymbol{F}(\boldsymbol{X}), \boldsymbol{F}^{\text{in}}(\boldsymbol{X}), \boldsymbol{\varepsilon}(\boldsymbol{X}), \boldsymbol{\lambda}(\boldsymbol{X}); s(\boldsymbol{X})\right) \mathrm{d}V + \int_\Gamma \gamma(s_+, s_-)\,\mathrm{d}S \\ &\approx \Delta V \sum_{k=1}^{n} A\left(\boldsymbol{F}_k, \boldsymbol{F}_k^{\text{in}}, \boldsymbol{\varepsilon}_k, \boldsymbol{\lambda}_k; s_k\right) + \Delta S \sum_{l=1}^{n_\Gamma} \gamma(s_{l^+}, s_{l^-}).\end{aligned} \tag{2.20}$$

Here, we approximate the total energy in Ω by a discrete sum over all n grid points in Ω_Δ (each associated with a pixel volume ΔV), while the surface integral becomes a discrete sum over all n_Γ straight interface segments (each associated with a pixel surface ΔS); see Figure 2.2. Note that the Helmholtz free energy is local and the dependence on state s is implicit through the slip and twin system orientations. The interface energy, in principle, depends on the two states s_{l^+} and s_{l^-} on both sides of a GB. For simplicity, we here assume a constant GB energy density γ_{S} which does not depend on misorientation, *e.g.*, à la Read and Shockley [136] or Wolf [188]. We note that our model can readily include misorientation-dependent GB mobilities [185, 186] or more complex boundary energy formulations [72], although they are neglected in this framework.

Consider a local state switch from s_k to $\tilde{s}_k$, *i.e.*, grid point k change its grain association, which comes with a change in crystal orientation as well as a change of $(\boldsymbol{F}_k, \boldsymbol{F}_k^{\text{in}}, \boldsymbol{\varepsilon}_k, \boldsymbol{\lambda}_k)$ into some $(\tilde{\boldsymbol{F}}_k, \tilde{\boldsymbol{F}}_k^{\text{in}}, \tilde{\boldsymbol{\varepsilon}}_k, \tilde{\boldsymbol{\lambda}}_k)$. Owing to the form of the energy in (2.20), the total change in energy due to this switch is local and given by

$$\begin{aligned}\Delta E =& \tilde{\mathcal{I}} - \mathcal{I} \\ =& \Delta V \left[A\left(\tilde{\boldsymbol{F}}_k, \tilde{\boldsymbol{F}}_k^{\text{in}}, \tilde{\boldsymbol{\varepsilon}}_k, \tilde{\boldsymbol{\lambda}}_k; \tilde{s}_k\right) - A\left(\boldsymbol{F}_k, \boldsymbol{F}_k^{\text{in}}, \boldsymbol{\varepsilon}_k, \boldsymbol{\lambda}_k; s_k\right)\right] \\ &+ \Delta S \sum_{l \in I_k} \gamma(s_k, s_l),\end{aligned} \tag{2.21}$$

where I_k denotes the set of the six nearest-neighboring grid points of point k and

$$\gamma(s_k, s_j) = \gamma_{\text{S}}\, \delta(s_k, s_j) \qquad \text{with} \qquad \delta(s_k, s_j) = \begin{cases} 1 & \text{if } s_k = s_j, \\ 0 & \text{else,} \end{cases} \tag{2.22}$$

so that only interfaces between neighboring grid points that relate to different grains contribute GB energy.

[4] For conciseness, here and in the following we implicitly include the position dependence at position $\boldsymbol{X}^k$ via subscripts $(\cdot)_k$, such that, *e.g.*, $\boldsymbol{F}_k \equiv \boldsymbol{F}(\boldsymbol{X}^k)$, etc.

In light of the above energy difference and in analogy to the well-established Glauber dynamics [53], we define acceptance thresholds as

$$\begin{cases} w_{\mathrm{GBM}}(\Delta E) = \dfrac{1}{2}\left[1 - \tanh\left(\dfrac{\Delta E - \Delta E_{\mathrm{cr,GBM}}}{k_B T_s}\right)\right], \\ w_{\mathrm{NCL}}(\Delta E) = \dfrac{1}{2}\left[1 - \tanh\left(\dfrac{\Delta E - \Delta E_{\mathrm{cr,NCL}}}{k_B T_s}\right)\right] \end{cases} \tag{2.23}$$

with Boltzmann's constant k_B, an effective temperature T_s, and a constant $\Delta E_{\mathrm{cr}} > 0$.

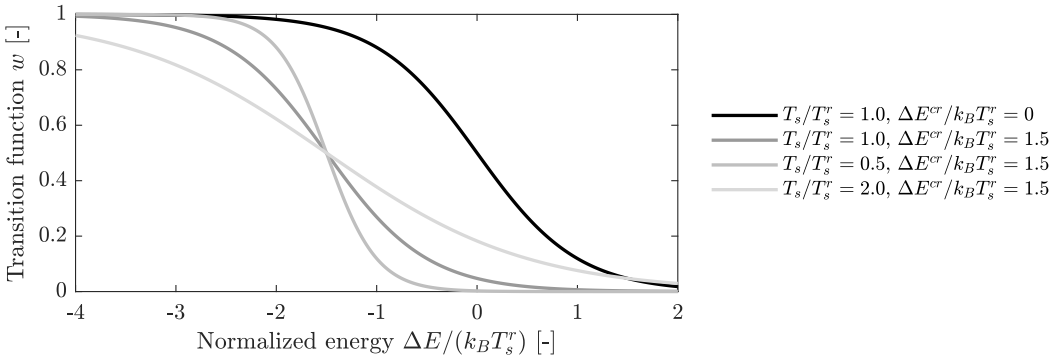

Figure 2.3: Acceptance threshold w as a function of the (normalized) energy difference for various values of T_S and ΔE_{cr} (normalized by some reference temperature T_s^r).

Given a potential energy release ΔE_k, we use the threshold from (2.23) to decide whether or not a material point k switches state by either NCL or GBM. If any of the $n_{\mathrm{MC}} = n_{\mathrm{MC,GBM}} + n_{\mathrm{MC,NCL}}$ sampling points is identified to have $\Delta E_k < 0$ for a possible state switch, we generate a random number $\xi \sim \mathcal{U}[0,1]$ following a uniform distribution $\mathcal{U}[0,1]$. Ultimately, we accept the new state if the condition $\xi \leq w(\Delta E_k)$ is met and reject if $\xi > w(\Delta E_k)$. Since increasing ΔE_{cr} decreases the threshold $w(\Delta E)$ for a given ΔE (see Figure 2.3), $\Delta E_{\mathrm{cr,GBM}}$ aims at capturing the dissipative drag of GBM while $\Delta E_{\mathrm{cr,NCL}}$ sets a nucleation threshold. Table 2.2 summarizes all MCP model parameters from subsequent simulationsf.

Table 2.2: MCP model parameters chosen for the subsequent simulations of dynamic recrystallization, unless otherwise noted.

T_S [K]	γ_S [Jm^{-2}]	$\Delta E_{\mathrm{cr,NCL}}$ [MJm^{-3}]	$\Delta E_{\mathrm{cr,GBM}}$ [MJm^{-3}]
386	0.38	−1.00	−0.60

2.3.2 Monte-Carlo-Potts model: state switches

The calculation of ΔE_k requires comparing the currently stored Helmholtz free energy $A(\boldsymbol{F}_k, \boldsymbol{F}_k^{\mathrm{in}}, \boldsymbol{\varepsilon}_k, \boldsymbol{\lambda}_k; s_k)$ to that of a hypothetical state $A(\tilde{\boldsymbol{F}}_k, \tilde{\boldsymbol{F}}_k^{\mathrm{in}}, \tilde{\boldsymbol{\varepsilon}}_k, \tilde{\boldsymbol{\lambda}}_k; \tilde{s}_k)$ after

a state switch from s_k to $\tilde{s}_k$. Our definition of the latter state draws on recrystallization theory and experimental observations of grain nucleation and migration, and it is based on the following assumptions: (*i*) while nucleation is widely accepted to be predominantly driven by the reduction of elastic strain energy [155, 169], migration is caused by various driving forces associated with the minimization of the total stored energy [169], comprising interfacial as well as (in-)elastic bulk energy. (*ii*) Nucleation is observed to result in pristine, dislocation-starved grains [5, 60, 68], as imposed in the phase field model of Chen et al. [28]. (*iii*) While the literature generally speaks of GBM as an advective process, we still know little about the remains of existing dislocations interacting with migrating GBs [144]. Here, we presume that any material point which joins an adjacent grain will adopt that grain's crystallographic orientation and slip and twin systems in the *current configuration*, implying that not only the state $\tilde{\boldsymbol{s}}$ is adopted but also the elastic and inelastic deformation gradients, since, *e.g.*, the slip system in the current configuration is given by $\left(\boldsymbol{F}^{\mathrm{e}}\boldsymbol{s}, (\boldsymbol{F}^{\mathrm{in}})^{\mathrm{T}}\boldsymbol{m}\right)$. Overall, this motivates defining the state switch such that

$$\tilde{\boldsymbol{F}}_k^{\mathrm{in}} = \begin{cases} \boldsymbol{I} \\ \boldsymbol{I} \end{cases} \quad \tilde{\boldsymbol{F}}_k^{\mathrm{e}} = \begin{cases} \boldsymbol{I} \\ \boldsymbol{F}^{\mathrm{e,neighbor}} \end{cases} \quad \tilde{\boldsymbol{\varepsilon}}_k = \begin{cases} \boldsymbol{0} \\ \boldsymbol{\varepsilon}^{\mathrm{neighbor}} \end{cases} \quad \tilde{\boldsymbol{\lambda}}_k = \begin{cases} \boldsymbol{0} & \text{(NCL)} \\ \boldsymbol{\lambda}^{\mathrm{neighbor}} & \text{(GBM)} \end{cases} \tag{2.24}$$

where the superscript $(\cdot)^{\mathrm{neighbor}}$ refers to a neighboring material point already associated with grain $\tilde{s}_k$. We note that this choice is the authors' conclusion informed by both physical as well as numerical considerations in lack of sufficiently insightful experimental data. Section 2.3.4 discusses alternative approaches that we investigated. Since this method differs from previous MCP models (where at most one internal variable was subject to state switches), we refer to this model as a *Field Monte Carlo Potts* (FMCP) model.

Importantly, we also aim to maintain the same total deformation for compatibility, *i.e.*, $\tilde{\boldsymbol{F}}_k = \boldsymbol{F}_k$, which unfortunately renders the constraints (2.24) mutually exclusive since $\tilde{\boldsymbol{F}}_k = \tilde{\boldsymbol{F}}_k^{\mathrm{e}}\tilde{\boldsymbol{F}}_k^{\mathrm{in}} = \boldsymbol{F}^{\mathrm{e,neighbor}} \neq \boldsymbol{F}_k$ in general. Therefore, we modify the deformation gradient decomposition by introducing a relative configuration $\boldsymbol{F}^{\mathrm{r}}$ such that

$$\boldsymbol{F} = \boldsymbol{F}^{\mathrm{e}}\boldsymbol{F}^{\mathrm{r}}\boldsymbol{F}^{\mathrm{in}}. \tag{2.25}$$

Simo [149] already introduced the idea of a relative or residual deformation gradient as the tangent map of a superposed spatial diffeomorphism to some deformation mapping. Similarly, Asaro [12] used it to measure the reorientation of the lattice with respect to some tensile axis.

When using the decomposition (2.25), we can realize (2.24) by setting $\boldsymbol{F}^{\mathrm{r}} = \boldsymbol{I}$ in the undeformed configuration at all material points and choosing

$$\tilde{\boldsymbol{F}}_k^{\mathrm{r}} = (\tilde{\boldsymbol{F}}_k^{\mathrm{e}})^{-1}\tilde{\boldsymbol{F}}_k(\tilde{\boldsymbol{F}}_k^{\mathrm{in}})^{-1} \tag{2.26}$$

upon each state switch to satisfy compatibility. This also admits a physical interpretation since upon GBM the material point now adopts the slip and twin system orientations of the adjacent grain (in the current configuration).

(2.24) along with (2.25), (2.26) and $\tilde{\boldsymbol{F}}_k = \boldsymbol{F}_k$, completely defines a local state switch at a MCP sampling point k and admits calculating the potential energy differences ΔE_k (for every possible state switch considering the nearest-neighboring grid points of k). Figure 2.4 illustrates the update process upon state switching, which the following explains:

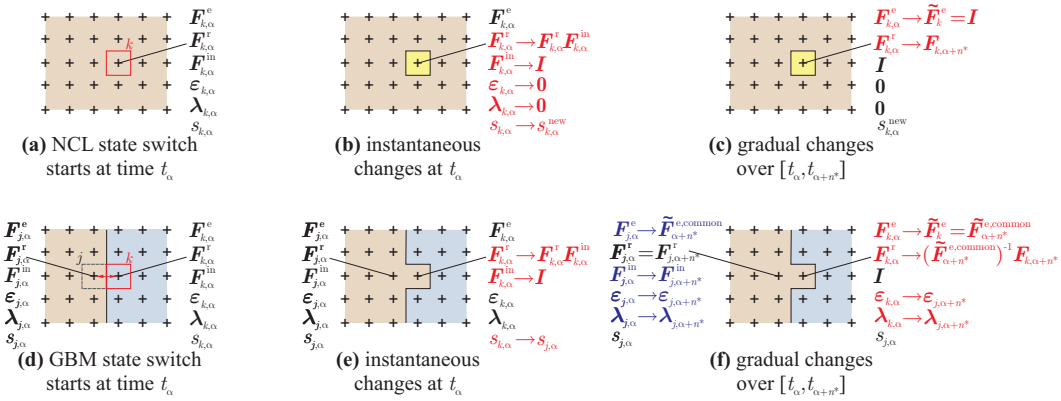

Figure 2.4: Visualization of the update process for NCL (**a**-**c**) and GBM (**d**-**f**): (**a,d**) selection of a sampling point k (*marked in red*) and – in the case of GBM – its neighboring reference point j (*marked in black*) at time t_α, (**b,e**) instantaneous update of the inelastic variables at time t_α, and (**c,f**) gradual update of $\boldsymbol{F}_k^{\mathrm{r}}$ over time $[t_\alpha, t_{\alpha+n^*}]$ along with mechanical equilibration at each time step, resulting in the matching of $\boldsymbol{F}_k^{\mathrm{e}}$ of the chosen sampling point k with identity in the case of NCL and that of the neighboring grid point j in the adjacent grain at the end of the process in the case of GBM. Imposed changes are *red*, while changes resulting from mechanical equilibration appear in *blue*.

2.3.3 Monte-Carlo-Potts model: Incremental realization of a state switch

An instantaneous switch of $\boldsymbol{F}_k^{\mathrm{e}} \rightarrow \tilde{\boldsymbol{F}}_k^{\mathrm{e}}$ would result in considerable convergence problems in the RVE-level boundary value problem (caused by sudden changes in the elastic/inelastic fields and the associated resolved shear stresses), which is why we have chosen the following gradual update protocol. In a nutshell, the

instantaneous state switch is spread over a finite time window Δt^* – which is in line with dynamic recrystallization being a continuous physical process[5].

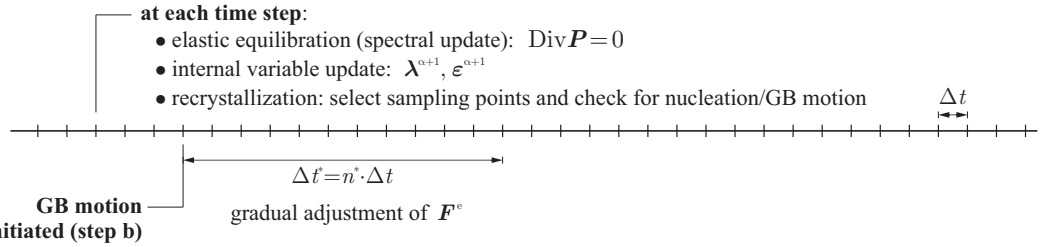

Figure 2.5: Schematic illustration of the time stepping scheme: at each time step the RVE is equilibrated, internal variables are updated, and n_{MC} sampling points are checked for grain nucleation or migration. If either is initiated (step b from Figure 2.4), then the scheme of Figure 2.4 starts, including a gradual adjustment of $\boldsymbol{F}^{\mathrm{e}}$ through adjusting $\boldsymbol{F}^{\mathrm{r}}$ over n^* time steps.

We assume that the inelastic variables $(\boldsymbol{F}_k^{\mathrm{in}}, \boldsymbol{\varepsilon}_k, \boldsymbol{\lambda}_k; s_k)$ – which are tied to the atomic-level crystallographic configuration – change spontaneously and instantaneously into $(\tilde{\boldsymbol{F}}_k^{\mathrm{in}}, \tilde{\boldsymbol{\varepsilon}}_k, \tilde{\boldsymbol{\lambda}}_k; \tilde{s}_k)$. By contrast, the transition from $\boldsymbol{F}_k^{\mathrm{e}}$ to $\tilde{\boldsymbol{F}}_k^{\mathrm{e}}$ is performed gradually, since it is tied to the long-range elastic fields involving both the material point and relaxation mechanisms in its vicinity. It is important to note that we cannot control $\boldsymbol{F}_k^{\mathrm{e}}$ directly (only through $\boldsymbol{F}_k$, $\boldsymbol{F}_k^{\mathrm{in}}$ and $\boldsymbol{F}_k^{\mathrm{r}}$). Since $\boldsymbol{F}_k^{\mathrm{in}} \to \tilde{\boldsymbol{F}}_k^{\mathrm{in}}$ instantaneously as described above, we control $\boldsymbol{F}_k^{\mathrm{r}}$ to adjust $\boldsymbol{F}_k^{\mathrm{e}} \to \tilde{\boldsymbol{F}}_k^{\mathrm{e}}$. Moreover, we gradually change $\boldsymbol{F}_k^{\mathrm{e}}$ into $\tilde{\boldsymbol{F}}_k^{\mathrm{e}}$ over a time period Δt^* through an incremental sequence of $n^* = \lceil \Delta t^*/\Delta t \rceil$ mechanical equilibria (where Δt denotes the time step size of the simulation); see the schematic in Figure 2.5. As the final state of this gradual update (starting at same time t_α and continuing over n^* times steps), we must have $\boldsymbol{F}_{k,\alpha+n^*}^{\mathrm{e}} = \tilde{\boldsymbol{F}}_k^{\mathrm{e}}$ from (2.24) – *i.e.*, either $\boldsymbol{F}_{k,\alpha+n^*}^{\mathrm{e}} = \boldsymbol{I}$ for NCL, or $\boldsymbol{F}_{k,\alpha+n^*}^{\mathrm{e}} = \boldsymbol{F}_{j,\alpha+n^*}^{\mathrm{e}} = \tilde{\boldsymbol{F}}_{\alpha+n^*}^{\mathrm{e,common}}$ (which is a-priori unknown at t_α) for GBM, see Figure 2.4. In summary, this implies that the selected MCP sampling point instantaneously adopts its new crystallography, then experiences an elastic-plastic evolution over Δt^* to continuously adjust grid point k to its target elastic state, thus achieving a relaxation of the stress state by continuous equilibration in the neighborhood of point k.

In order to gradually change $\boldsymbol{F}^{\mathrm{e}}$ in a physically sensible manner, we use the polar decomposition theorem to write $\boldsymbol{F}^{\mathrm{e}} = \boldsymbol{R}^{\mathrm{e}}\boldsymbol{U}^{\mathrm{e}}$ with rotation $\boldsymbol{R}^{\mathrm{e}} = \boldsymbol{F}^{\mathrm{e}}(\boldsymbol{U}^{\mathrm{e}})^{-1} \in \mathrm{SO}(3)$

[5]Recrystallization experiments are usually conducted on time scales significantly larger than the characteristic microscale relaxation times, which makes it difficult to extract information on the exact time-dependent evolution mechanisms. Nonetheless, we here propose a continuous update procedure for the microstructural states as a stable numerical scheme that simultaneously serves as a reasonable hypothesis of the actual kinetic microstructural evolution.

and principal stretch tensor $\boldsymbol{U}^{\mathrm{e}} = \sqrt{(\boldsymbol{F}^{\mathrm{e}})^{\mathrm{T}}\boldsymbol{F}^{\mathrm{e}}} \in \mathrm{GL}(3)$. We accommodate the gradual transformation from some given initial elastic deformation gradient $\boldsymbol{F}^{\mathrm{e}}_{k,\alpha}$ to the target elastic deformation gradient $\tilde{\boldsymbol{F}}^{\mathrm{e,target}}_{\alpha+n^*}$ using an iterative adjustment of, individually, stretch and rotation[6].

If at time t_α, we identify grid point k (with reference neighbor j in the case of GBM) for a state switch, we carry out the gradual update over time steps $\beta \in [\alpha, \alpha + n^*]$ so that $\boldsymbol{F}^{\mathrm{e}}_{k,\alpha} \to \tilde{\boldsymbol{F}}^{\mathrm{e}}_{k}$ from (2.24). We introduce a translational deformation tensor $\hat{\boldsymbol{F}}_\beta$ via

$$\boldsymbol{F}^{\mathrm{e}}_{k,\beta}\,\hat{\boldsymbol{F}}_\beta = \begin{cases} \boldsymbol{I} & \text{(NCL)} \\ \boldsymbol{F}^{\mathrm{e}}_{j,\beta} & \text{(GBM)} \end{cases}, \tag{2.27}$$

which decomposes into $\hat{\boldsymbol{R}}_\beta$ and $\hat{\boldsymbol{U}}_\beta$ as follows to define the stretch and rotational contributions to the elastic deformation mapping required to take point k towards its target at any time step β:

$$\hat{\boldsymbol{F}}_\beta = \hat{\boldsymbol{R}}_\beta\,\hat{\boldsymbol{U}}_\beta, \quad \hat{\boldsymbol{R}}_\beta \in \mathrm{SO}(3),\ \hat{\boldsymbol{U}}_\beta \in \mathrm{GL}(3). \tag{2.28}$$

We break n^* down into $(n^* - n_U)$ and n_U time steps for adjusting the stretches and rotations, respectively. Following the arguments outlined above, we recursively define the update of the elastic deformation at point k at time step $\beta + 1$ as

$$\boldsymbol{F}^{\mathrm{e}}_{k,\beta+1} = \begin{cases} \boldsymbol{F}^{\mathrm{e}}_{k,\beta}\hat{\boldsymbol{U}}_\beta^{-\frac{1}{n_U-(\beta-\alpha)}} & \text{for} \quad \beta \in \{\alpha, \ldots, \alpha + n_U - 1\} \\ \boldsymbol{F}^{\mathrm{e}}_{k,\beta}\hat{\boldsymbol{U}}_\beta^{-1}\hat{\boldsymbol{R}}_\beta^{-\frac{1}{n^*-(\beta-\alpha)}} & \text{for} \quad \beta \in \{\alpha + n_U, \ldots, \alpha + n^* - 1\}, \end{cases} \tag{2.29}$$

This scheme ensures that $\boldsymbol{F}^{\mathrm{e}}_{k,\alpha+n^*}$ equals its target value, viz. $\boldsymbol{F}^{\mathrm{e}}_{k,\alpha+n^*} = \boldsymbol{I}$ for NCL and $\boldsymbol{F}^{\mathrm{e}}_{k,\alpha+n^*} = \boldsymbol{F}^{\mathrm{e}}_{j,\alpha+n^*} = \tilde{\boldsymbol{F}}^{\mathrm{e,common}}_{\alpha+n^*} \in \mathrm{GL}(3)$ for GBM. We note that, while (2.29) is being applied, mechanical equilibration including updates of the internal variables is also enforced, so that all fields are continuously evolving. The choice of the exponents in (2.29) is such that, in the hypothetical case of the absence of any changes to F^{e} by mechanical equilibration, the incremental stretches and rotations applied during each step are constant. (The physics-informed scheme (2.29) is not restricted to recrystallization but can be applied in any constitutive framework where instantaneous state switches are to be avoided.) An algorithmic summary of the statistical model described in this section is provided in Table 1.

Recall that, although the elastic deformation gradient adjusts gradually according to (2.29), the update of the inelastic deformation gradient occurs instantaneously at time

[6]Note that by definition, since $\det \boldsymbol{F}^{\mathrm{in}} = 1$ as well as $\det \boldsymbol{F} > 0$ and $\det \boldsymbol{F}^{\mathrm{r}} > 0$ by construction, $\boldsymbol{F}^{\mathrm{e}}$ is always invertible.

step α. The same applies to the local orientation $s_k \longrightarrow s_j$ (which is unproblematic for elastic isotropy but may require special treatment for anisotropic elastic energy densities).

2.3.4 Alternative definitions of state switches due to GBM

In Section 2.3.2 we presented a particular form of the local kinematic updates of the elastic state ($\boldsymbol{F}^{\mathrm{e}}$) and the inelastic state ($\boldsymbol{F}^{\mathrm{in}}$, $\boldsymbol{\varepsilon}$, $\boldsymbol{\lambda}$) associated with a state switch due to GBM, as defined by (2.24) and complemented by (2.26). We note that this choice is not unique. We considered and discarded various alternatives which are briefly outlined here to justify the particular choices we ultimately adopted:

- **Approach 1:** It is possible to interpret a moving GB as a reconfiguration front which leaves the region over which it has swept in a pristine, defect-free state. In terms of the state variables used in this model, this implies $\tilde{\boldsymbol{\epsilon}}_k = \boldsymbol{0}$, $\tilde{\boldsymbol{\lambda}}_k = \boldsymbol{0}$, $\tilde{\boldsymbol{F}}^{\mathrm{in}} = \boldsymbol{I}$ but $\tilde{\boldsymbol{F}}^{\mathrm{e}} = \boldsymbol{F}^{\mathrm{e}}$ and $\tilde{\boldsymbol{F}}^{\mathrm{r}} = (\boldsymbol{F}^{\mathrm{e}})^{-1}\boldsymbol{F}$, where the tilde denotes the state after the state switch. Unfortunately, a pristine elastic state would lead to excessively high local stresses which, in turn, translate into high flow stresses on certain slip systems. The latter is physically questionable and also leads to convergence failure of the crystal plasticity model employed here. Moreover, although the passage of a GB is expected to dissolve existing defect structures, the recovery of a completely pristine grain is physically unlikely.

- **Approach 2:** Adding a complete relaxation of the stress state can partially overcome the above problem. In terms of the state variables this translates into $\tilde{\boldsymbol{\epsilon}}_k = \boldsymbol{0}$, $\tilde{\boldsymbol{\lambda}}_k = \boldsymbol{0}$, $\tilde{\boldsymbol{F}}^{\mathrm{in}} = \boldsymbol{I}$, $\tilde{\boldsymbol{F}}^{\mathrm{e}} = \boldsymbol{I}$, and $\tilde{\boldsymbol{F}}^{\mathrm{r}} = \boldsymbol{F}$. This, however, equates migration to nucleation, which has little physical justification and implies that severe local deformation gradients $\boldsymbol{F}$ may result in zero local stresses.

- **Approach 3:** In our approach, we assume that the inelastic state of a point that is passed by a migrating GB is independent of its history before GB arrival but affected by the plastic history and defect structure in the expanding grain. This translates into the update laws (2.24). Specifically by assuming that the elastic state of the neighboring grain is also adopted, we avoid the aforementioned excessive stress increase and – in conjunction with the time-continuous adoption process outlined in Section 2.3.3 – achieve numerical stability.

Algorithm 1 Incremental update algorithm applied at each time step α.

1. **Update the macroscopic/average deformation gradient** to $\boldsymbol{F}^*_{\alpha+1}$
2. **Application of the FFT-based method to solve the elastic RVE problem** (at fixed internal variables):

- compute $\boldsymbol{F}_{k,\alpha+1} = \boldsymbol{F}(\boldsymbol{X}_k, t_{\alpha+1}) \forall\, k \in \{1, ..., n\}$

3. **Update the internal variables** (at fixed deformation gradients):
Denoting the sets of nodes that currently undergo a state change in the sense of GBM and NCL by $\mathcal{S}_{\mathrm{GBM}}$ and $\mathcal{S}_{\mathrm{NCL}}$, respectively (*i.e.*, points that are within their n^* time steps to accommodate the state switch), then for all $k \in \{1, \ldots, n\}/(\mathcal{S}_{\mathrm{GBM}} \cup \mathcal{S}_{\mathrm{NCL}})$

- compute $\boldsymbol{\epsilon}_{\alpha+1}(\boldsymbol{X}_k)$, $\boldsymbol{\lambda}_{\alpha+1}(\boldsymbol{X}_k)$, $\boldsymbol{F}^{\mathrm{in}}_{\alpha+1}(\boldsymbol{X}_k)$
- compute $\boldsymbol{F}^{\mathrm{e}}_{\alpha+1}(\boldsymbol{X}_k) = \boldsymbol{F}_{\alpha+1}(\boldsymbol{X}_k) \left(\boldsymbol{F}^{\mathrm{r}}_{\alpha+1}(\boldsymbol{X}_k) \boldsymbol{F}^{\mathrm{in}}_{\alpha+1}(\boldsymbol{X}_k) \right)^{-1}$,

4. **Monte-Carlo-Potts acceptance/rejection**:

- randomly select $n_{\mathrm{MC,GBM}}$ and $n_{\mathrm{MC,NCL}}$ grid points from the set of, respectively, all GB-adjacent and all grid points (not considering those in $\mathcal{S}_{\mathrm{GBM}} \cup \mathcal{S}_{\mathrm{NCL}}$)
- for each of the $n_{\mathrm{MC,GBM}}$ grid points, consider all nearest-neighboring points:
  – compute the minimal $\Delta E_{\mathrm{GBM}} < 0$ and associated $w^{\mathrm{thresh}}_{\mathrm{GBM}} = w_{\mathrm{GBM}}(\Delta E_{\mathrm{GBM}})$
  – generate a random number ξ_{GBM}
  – if $\xi_{\mathrm{GBM}} \leq w^{\mathrm{thresh}}_{\mathrm{GBM}}$: insert grid point into $\mathcal{S}_{\mathrm{GBM}}$
- for each of the $n_{\mathrm{MC,NCL}}$ grid points and a random orientation for the new grain:
  – compute ΔE_{NCL} and $w^{\mathrm{thresh}}_{\mathrm{NCL}} = w_{\mathrm{NCL}}(\Delta E_{\mathrm{NCL}})$
  – generate a random number ξ_{NCL}
  – if $\xi_{\mathrm{NCL}} \leq w^{\mathrm{thresh}}_{\mathrm{NCL}}$: insert grid point into $\mathcal{S}_{\mathrm{NCL}}$

5. **Monte-Carlo-Potts updates**: for each $k \in \mathcal{S}_{\mathrm{GBM}} \cup \mathcal{S}_{\mathrm{NCL}}$:

- if point k has just been inserted during this time step α:
  – if $k \in \mathcal{S}_{\mathrm{GBM}}$: set $\boldsymbol{s}_{0,i} \leftarrow \boldsymbol{s}_{0,j}$ and $\boldsymbol{m}_{0,i} \leftarrow \boldsymbol{m}_{0,j}$, where j denotes the neighboring reference node whose grain association is being advected
  – if $k \in \mathcal{S}_{\mathrm{NCL}}$: set $\boldsymbol{s}_{0,i} \leftarrow \boldsymbol{s}_{0,\mathrm{new}}$ and $\boldsymbol{m}_{0,i} \leftarrow \boldsymbol{m}_{0,\mathrm{new}}$ for a new *random* orientation of the nucleated grain
- update $\boldsymbol{F}^{\mathrm{e}}_{k,\alpha} \rightarrow \boldsymbol{F}^{\mathrm{e}}_{k,\alpha+1}$ according to (2.29) by changing $\boldsymbol{F}^{\mathrm{r}}_{k,\alpha} \rightarrow \boldsymbol{F}^{\mathrm{r}}_{k,\alpha+1}$,
if $k \in \mathcal{S}_{\mathrm{GBM}}$: set $\boldsymbol{\varepsilon}_{k,\alpha+1} \leftarrow \boldsymbol{\varepsilon}_{j,\alpha+1}$ and $\boldsymbol{\lambda}_{k,\alpha+1} \leftarrow \boldsymbol{\lambda}_{j,\alpha+1}$, where j denotes the neighboring reference node whose grain association is being advected
- if α is the n^*-th increment for grid point k (completing the state switch), then:
if $k \in \mathcal{S}_{\mathrm{GBM}}$ remove k from $\mathcal{S}_{\mathrm{GBM}}$, else if $k \in \mathcal{S}_{\mathrm{NCL}}$ remove k from $\mathcal{S}_{\mathrm{NCL}}$

2.4 Verification of the numerical scheme: Scaling and Convergence

We first verify that our model is appropriate to yield results independent of grid size as to demonstrate convergence with grid refinement, before proceeding to polycrystalline benchmark simulations. This is particularly important due to the statistical FMCP model for recrystallization: while the crystal plasticity setup is size-independent and therefore expected to converge with h-refinement, the FMCP model is based on randomly selecting $n_{\mathrm{MC,GBM}}$ and $n_{\mathrm{MC,NCL}}$ grid points for GBM and NCL, respectively. Those parameters – together with the time step Δt – affect results when changing the grid resolution, so that it is necessary to scale their values appropriately. To this end, Section 2.3.1 proposed a scaling aimed at proper convergence of results, which is verified here.

In our simulations the grid spacing is set to $\Delta X = 2.55\ \mu$m. Stochastic models such as the MCP model generally do not possess a physical length scale, so fitting with experiments is required to relate their numerical length scale to a physical one. Leaving the size of the RVE unchanged would result in $\Delta X \propto n^{-1/3}$, which in turn would influence the recrystallization kinetics due to changes in the balance between bulk energy and interface energy (scaling as $\Delta V \propto (\Delta X)^3$ and $\Delta S \propto (\Delta X)^2$, respectively). Therefore, when investigating different RVE resolutions in the following, we automatically imply a respective scaling of the RVE size to circumvent the aforementioned issues. Motivated by the deformation a billet experiences during the extrusion in ECAE, in subsequent benchmark tests we apply the average deformation gradient $\boldsymbol{F}^*(t) = \boldsymbol{I} + \dot{\gamma}_{\mathrm{sh}} t\, \boldsymbol{e}_1 \otimes \boldsymbol{e}_3$ with $\dot{\gamma}_{\mathrm{sh}}$ denoting the applied shear rate.

2.4.1 Scaling of the number of MCP sampling points with changing grid size for GBM

A proper rescaling of $n_{\mathrm{MC,GBM}}$, the number of sampling points for GBM, with the total number of grid points, n, is essential to ensure convergence of the effective GBM kinetics (*e.g.*, GBM speeds) with RVE refinement. To test the chosen scheme, we subject a bicrystal – having c-axis misorientations of $\pm\pi/16$ with respect to the [101] pole and a misorientation of $\pi/8$ to one another – to the controlled nucleation of a new grain at the RVE center, whose c-axis aligns with the [101] pole (see Figure 2.6). Suppressing any other nucleation, we test if the chosen scaling leads to comparable results of the GBM kinetics by comparing $n_{\mathrm{MC,GBM}} = 8$, 18 and 32 on grids with, respectively, $n = 32^3$, 48^3 and 64^3 points (along with properly rescaled Δt) according to the scaling relations of Section 2.3.1. For accelerated

albeit stable results in this example, we here use $T_S = 300\text{K}$, $\gamma_S = 0.31\text{Jm}^{-2}$ and $\Delta E_{\text{cr,GBM}} = -0.05\text{Jm}^{-3}$.

Figure 2.6 illustrates how the qualitative migration behavior is conserved across the three grid resolutions, thanks to properly rescaled $n_{\text{MC,GBM}}$ and Δt. While the growing volume and surface of the new grain compare well between resolutions (c.f. Figure 2.7), differences appear in terms of the non-smooth grain surface (despite identical GB energy γ_S). The shape of the GB becomes smoother and more regular with increasing n, especially at low strain levels. An increasingly similar migration behavior towards higher strains both in terms of propagation velocity as well as surface smoothness leads to the conclusion that the chosen scaling indeed leads to mesh-independent results in the limit of negligible surface penalization effects, which is approximately reached at higher strains, where the difference in Helmholtz free energy dominate the effects of surface penalization.

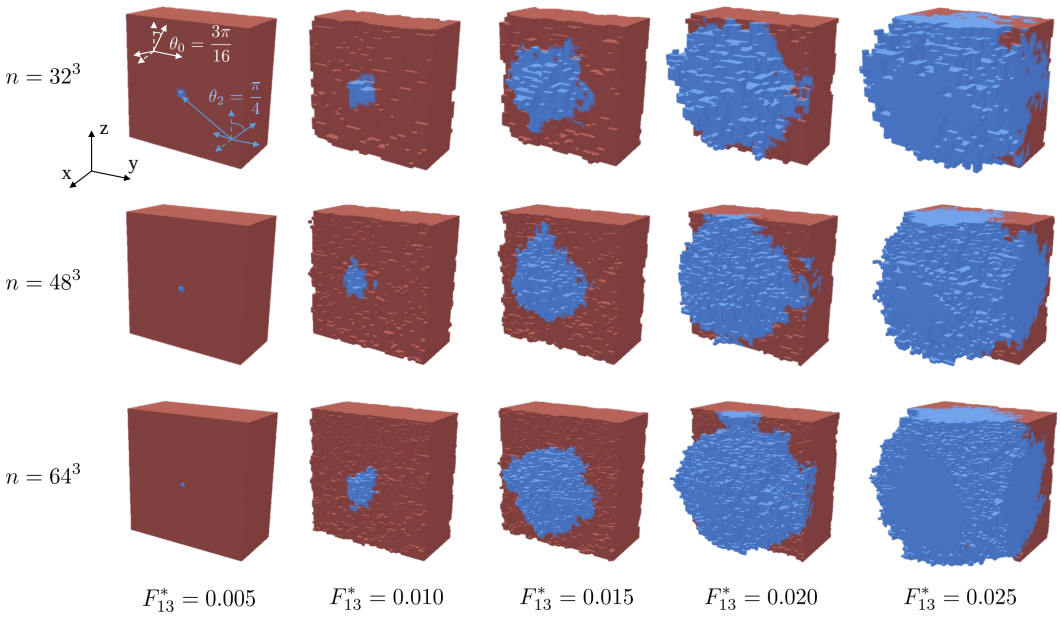

Figure 2.6: Comparison of GBM for a newly nucleated grain (shown in *blue*) embedded within a bicrystal (only one of the two original crystals is shown in *red*) for $n = 32^3$ (*top*), $n = 48^3$ (*center*) and $n = 64^3$ (*bottom*), when using the scaling relations introduced in Section 2.3.1. The five snapshots capture different average strain levels, using the aforementioned simple shear setup.

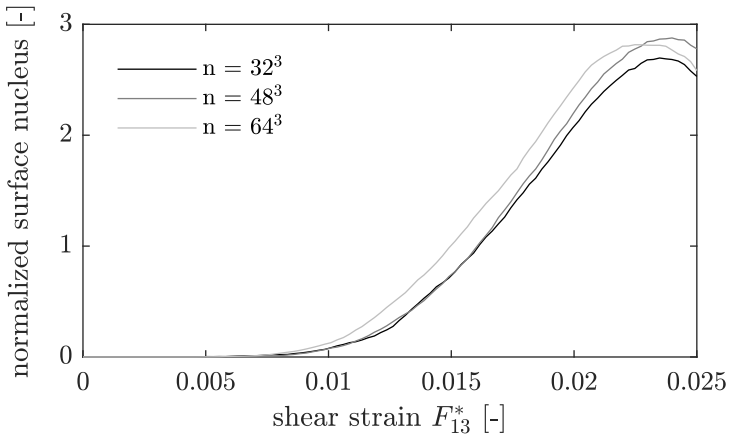

(a) Surface of the nucleus normalized by the RVE's surface area

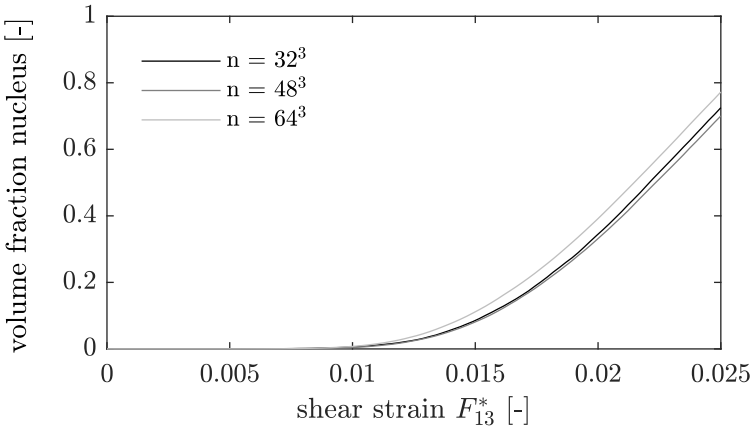

(b) Volume of the nucleus normalized by the RVE's total volume

Figure 2.7: Quantitative comparison of the volume and surface area of the newly nucleated grain in Figure 2.6, demonstrating grid size-independent GBM kinetics across three different RVE discretizations with $n = 32^3, 48^3, 64^3$.

2.4.2 Scaling of the number of MCP sampling points with changing grid size for NCL

Having verified proper scaling of the effective kinetics for GBM, we next study the chosen MC scheme for NCL. As a benchmark, we investigate a polycrystal composed of initially 128 grains with randomly distributed c-axis misorientations within $\leq \pi/16$ from the [101] axis. The choice of a [101]-biased texture is due to relatively poor basal slip under the prescribed simple shear, which promotes prismatic and $\langle c + a \rangle$-slip and thus showcases the full capabilities of the model to treat severe inelastic anisotropy. Due to inconsequential observations about the correlation between initial grain orientations and NCL during recrystallization, we

consider the pseudo-random initial texture around the [101]-pole appropriate[7].

We use the parameters of Table 2.2 and rescale $n_{\mathrm{MC,GBM}}$ and $n_{\mathrm{MC,NCL}}$ for three different grid sizes n, as discussed in Sections 2.3.1 and 2.4.1. Figure 2.8 compares the effective RVE stress–strain response for different choices of n, showing convincing agreement. We observe deviations at larger strains predominantly for the secondary recrystallization cycle. The reduction in peak stress for the relatively coarse choice of $n = 32^3$ owes to the fact that, with increasing n, the $n_{\mathrm{MC,NCL}}$ points selected for potential NCL increasingly lie away from GB triple-junctions, which are energetically preferable sites for nucleation but statistically less often sampled with increasing n.

As a further illustration, the histograms in Figure 2.9 show the changes in the relative grain sizes (measured as fractions of the RVE volume) for the three discretization levels of Figure 2.8. As expected, recrystallization leads to a reduction in the average grain size as well as to a spread in the grain size distribution. A stronger shift towards smaller grain sizes with decreasing grid resolution emphasizes the aforementioned increased nucleation activity at lower resolutions due to the increased probability of selecting MCP points near triple-junctions. However, overall results – both the effective stress–strain response and the microstructural changes – tend to converge with increasing grid resolution.

2.4.3 Dependence of the homogenized behavior on statistical MCP sampling

Although our FMCP approach is stochastic and therefore expected to yield different results when repeated even under identical initial conditions, we expect comparable effective material behavior (*i.e.*, evolution of both macroscopic stresses and microstructural statistics) for sufficiently large RVEs and statistically similar initial orientation distributions (*e.g.*, chosen from a fixed range of orientations around a given pole, as discussed above). As an ensemble study, we conducted four simulations with identical initial microstructures, differing merely by the random seed we used for the MCP point selection. Figure 2.10 illustrates the results of two different examples, each having 128 initial grains but with their initial textures spread around the [101]-pole by less than either $\pi/16$ or $\pi/8$. For both cases, the differences in the homogenized stress–strain response between the four runs is small with the highest

[7]For example, Al-Samman and Gottstein [5] showed that for specific combinations of process temperature and strain rate, texture randomization in Mg alloys could be observed, yet due to the emergence of random textures (as opposed to highly textured microstructures) varied with initial microstructure, we can conclude that there is no clear trend.

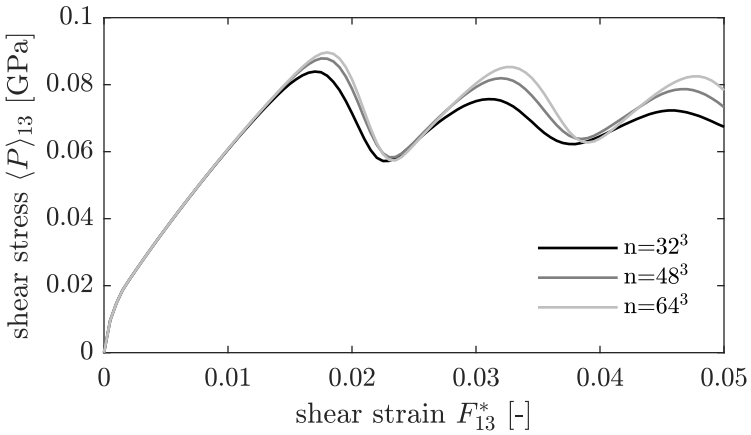

Figure 2.8: Comparison of the average shear stress $P^*_{13} = \langle P_{13} \rangle$ vs. average shear strain F^*_{13} for $n = 32^3, 48^3, 64^3$, using the scaling of the number of MCP sampling points with n as introduced in Section 2.3.1.

relative deviations in the stresses found around 3.5% and 4.2% for the scenarios with, respectively, lower and higher misorientations. Based on the relatively low amount of basal slip for grains with a rotation close to $\pi/4$ under this shear loading, we observe a higher inelastic strain energy density due to increased prismatic and particularly pyramidal slip. This accelerated rise of the inelastic energy density in return causes nucleation at relatively low average strains. The shift in nucleation initiation of the individual recrystallization cycles thus ultimately causes the observable difference in the number of cycles passed until the final strain of $F^*_{13} = 0.05$.

2.5 Results: Microstructural evolution and resulting stress–strain response during ECAE

Motivated by the prevalent simple shear deformation in the process zone of ECAE, the macroscopic load history for all examples in this and subsequent sections has the form $\boldsymbol{F}^*(t) = \boldsymbol{I} + \dot{\gamma}_{\mathrm{sh}} t\, \boldsymbol{e}_1 \otimes \boldsymbol{e}_3$, where $\dot{\gamma}_{\mathrm{sh}}$ denotes the shear rate (we chose $\dot{\gamma}_{\mathrm{sh}} = 10^{-5}$ s^{-1} to mimic quasistatic conditions). The low strain rate allows us to replicate the multi-peak stress–strain behavior characteristic of low-strain-rate/high-temperature discontinuous dynamic recrystallization, in which we can distinguish periods of pure inelastic deformation and of recrystallization, which, in turn, allows us to more cleanly inspect the effects of the various model parameters. In conformity with a classic ECAE setup endowed with a 90° turn, the extrusion direction (ED), transverse direction (TD) and normal direction (ND) are in our setup, respectively, the positive x-axis, positive y-axis and negative z-axis. We set the incremental time step to $\Delta t = 0.5$ s for the case of $n = 64^3$ ($N = 64$) and accordingly scale for all other

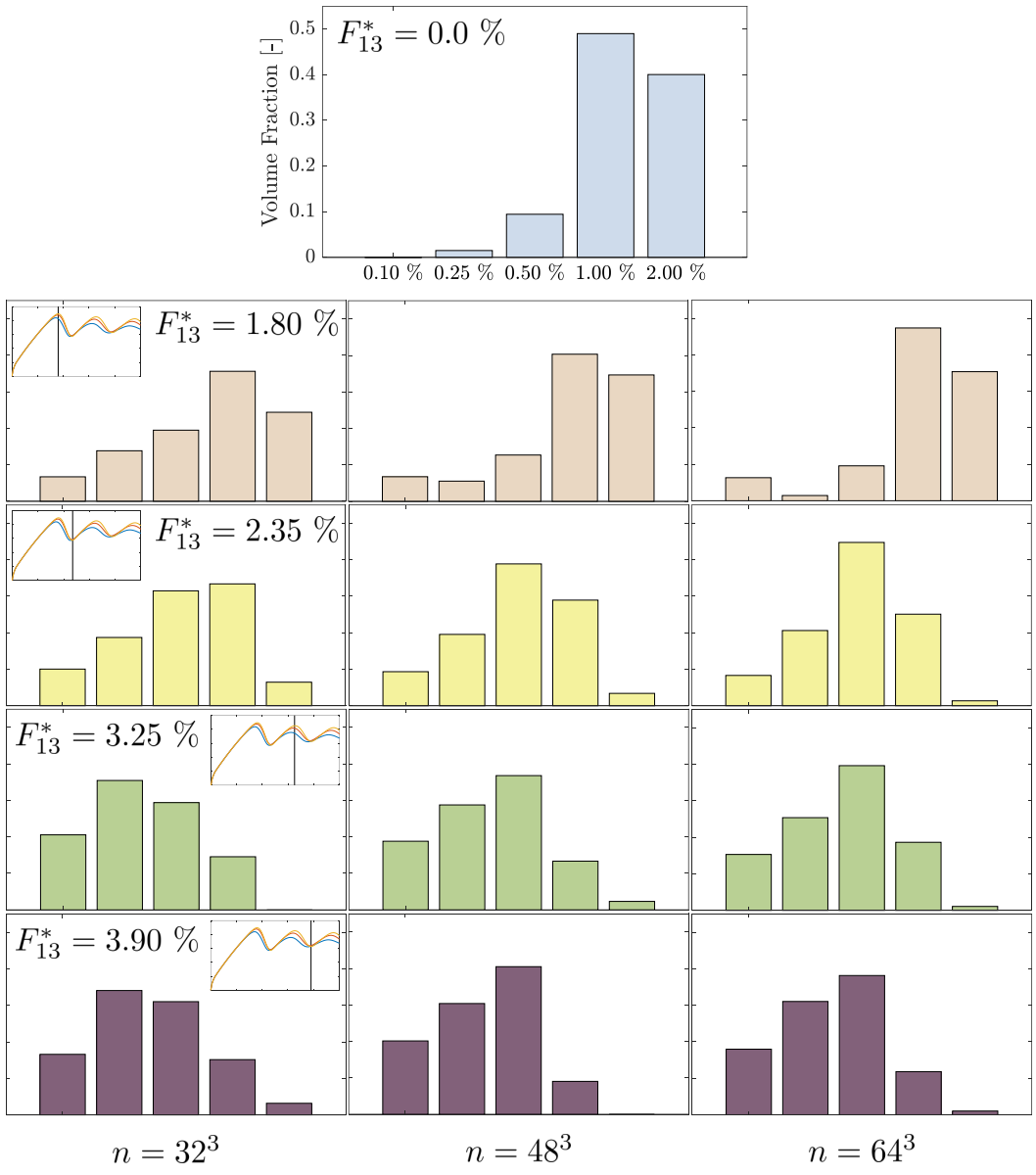

Figure 2.9: Evolution of the grain size distribution shown as histograms of RVE volume fractions of the grain volumes, thresholded by 0.10%, 0.25%, 0.50%, 1.0%, and 2.0% for average shear strain levels of 1.80% (*red*), 2.35% (*yellow*), 3.25% (*green*) and 3.90% (*purple*) as compared to the initial distribution (*blue*, on the top) for $n = 32^3$ (*left*), $n = 48^3$ (*center*) and $n = 64^3$ (*right*).

discretizations. We conduct all investigations up to a maximum strain[8]. This allows

[8]We note that we set the simulation temperature for both GBM and NCL in such a way to observe recrystallization at strains below those observed in experiments (which is beneficial for computational efficiency at such low strain rates). The reason for this choice lies in the nature of the material parameters present in the Mg constitutive model, which were fitted to room-temperature data [26]. This is significantly below the temperatures at which dynamic recrystallization investigations are

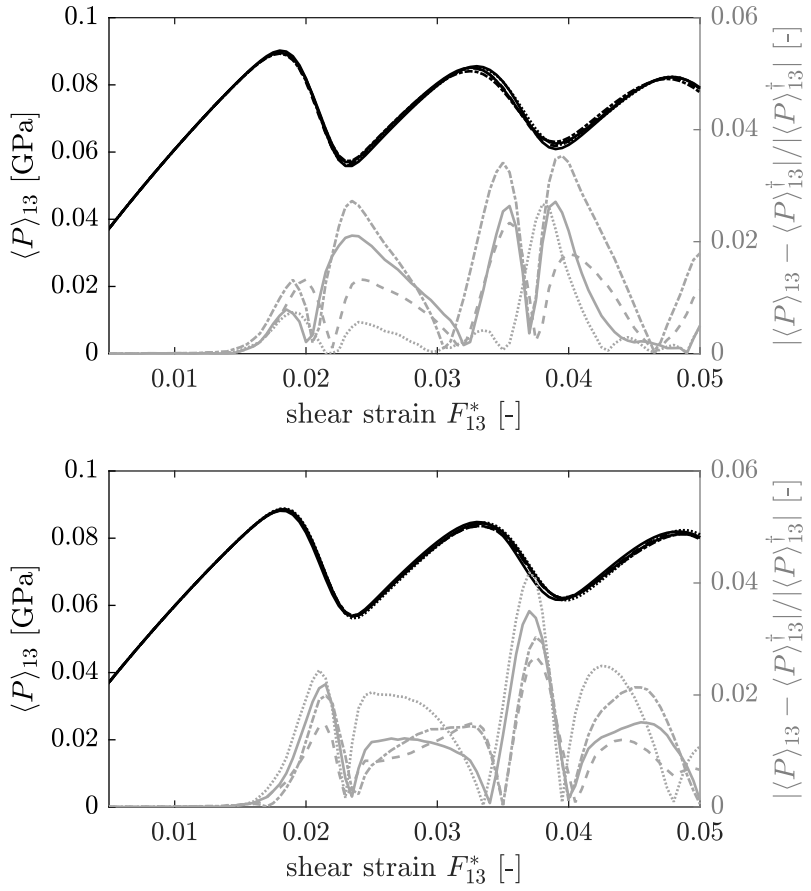

Figure 2.10: Illustration of the (negligible) influence of the random seed used for MCP sampling point selection under otherwise identical conditions including the same initial microstructure comprising 128 grains with two misorientation ranges of the c-axis with respect to the [101]-pole, viz. $\pi/16$ (*top*) and $\pi/8$ (*bottom*). Each set of four curves corresponds to four repeated runs (we have computed relative errors with respect to a fifth run whose homogenized stress levels are referred to as $\langle P^{\dagger}_{13} \rangle$).

us to exploit the simulation temperature for rescaling, which enables large-strain effects at smaller strain levels of $\gamma_{\mathrm{sh,max}} = \dot{\gamma}_{\mathrm{sh}} t_{\mathrm{max}} = 0.05$.

We investigate a polycrystal with initially 128 randomly oriented grains with a maximum misorientation of $\pi/8$ from the [101]-pole. Figure 2.11 illustrates the evolution of the homogenized shear stress $P^{*}_{13} = \langle P_{13} \rangle$ with the applied shear strain F^{*}_{13}. Following an initial phase of recrystallization-free elastic-plastic deformation, we can identify the onset of nucleation by the stress decrease due to the nucleation of new grains (near point B). The subsequent growth of those pristine grains by

conducted and thus only allows the underlying material model to function in a stable manner at low strains. The inclusion of temperature-dependent models is, however, readily possible, in which case recrystallization can be captured at the experimentally observed strain levels

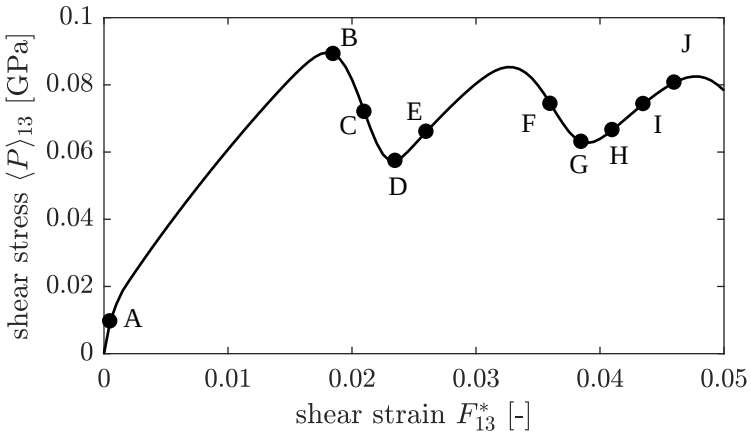

Figure 2.11: Evolution of the $P^*_{13} = \langle P_{13} \rangle$ shear stress vs. the applied shear strain F^*_{13}. Markers denote the strains corresponding to the grain, shear stress and inelastic strain energy density distributions across the RVE appear in Figs. 2.13, 2.12 and 2.14, respectively.

GBM alongside further NCL causes a continuing decrease of the homogenized stress up to point D, where the nucleated grains consumed the entire RVE. The fully recrystallized RVE then undergoes, again, elastic-plastic deformation resulting in a rising average stress. When the inelastic strain energy is again sufficiently high to increase the probability of nucleation, recrystallization results in another stress reduction – overall thus resulting in the classical *multi-peak* stress–strain behavior observed at low strain rates [60]. For higher strain rates, the distinction between time periods in which recrystallization-free deformation is dominant vs. periods in which NCL and GBM are prevalent vanishes gradually. This ultimately results in the classic *single-peak* stress–strain behavior [18, 60, 139], which we can also capture by the present model depending on model parameters and, which we will discuss in Section 2.6.

To elucidate the underlying mesoscale mechanisms, Figs. 2.13, 2.12 and 2.14 illustrate the distributions of, respectively, the grains, the $\langle P_{13} \rangle$ stress, and the inelastic strain energy density (as a driving force for discontinuous dynamic recrystallization) across the RVE. All three illustrations clearly support the identification of the individual stages in which NCL vs. GBM vs. elastic/inelastic deformation is dominant (labels in Figs. 2.13–2.14 correspond to the strain levels in Figure 2.11). The two recrystallization waves become apparent in Figure 2.13 which illustrates the newly nucleated grains. The onset of each wave corresponds to states of high stresses and of high stored energy as seen in Figs. 2.12 and 2.14. In addition, a decrease of

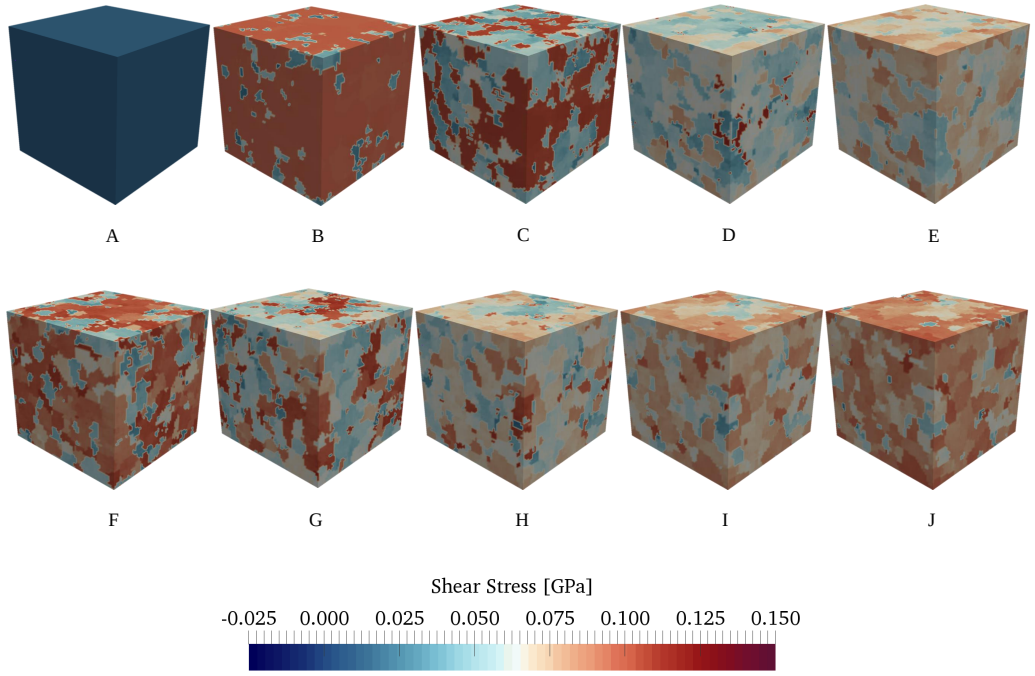

Figure 2.12: Evolution of the P_{13} shear stress distribution at the ten strain levels marked in Figure 2.11. The initiation and completion of each recrystallization wave agrees well with the, respectively, highest and lowest stresses found across the RVE.

the average grain size is observable throughout the two recrystallization cycles as mentioned in Section 2.4.2 (c.f. the decrease in average grain size in Figure 2.9).

It is interesting to compare the above results with a classical model for dynamic recrystallization frequently used in the literature. The JMAK relation [13, 79, 86] approximates the evolution of the volume fraction of recrystallized material, which we denote via $\eta_{\mathrm{RX}} \in [0,1]$, in the form

$$\eta_{\mathrm{RX}}(t) = 1 - \exp\left(-\int_{t_{\mathrm{RX}}}^{t} v(\tau)\,\dot{n}_{\mathrm{NCL}}(\tau)\,\mathrm{d}\tau\right) \approx 1 - \exp(-A(t-t_{\mathrm{RX}})^{p}), \qquad (2.30)$$

where $v(\tau)$ and $\dot{n}_{\mathrm{NCL}}(\tau)$ define, respectively, the reference volume and nucleation rate within previously unrecrystallized material at time τ. $A, p \in \mathbb{R}^{+}$ describe constants dependent on both the material as well as the processing route; p is commonly referred to as the Avrami coefficient. We define t_{RX} as the time at which recrystallization starts, which we set to the time at which 1.0% of the RVE is recrystallized for a fair comparison with the JMAK model. In contrast to our high-fidelity model, JMAK assumes simple GB kinetics (*e.g.*, a constant nucleation rate and a constant growth velocity, thus neglecting any local effects [133]). Since JMAK has been frequently used to infer recrystallization specifics [15, 72, 132, 133], it is interesting to compare (2.30) to the results found here.

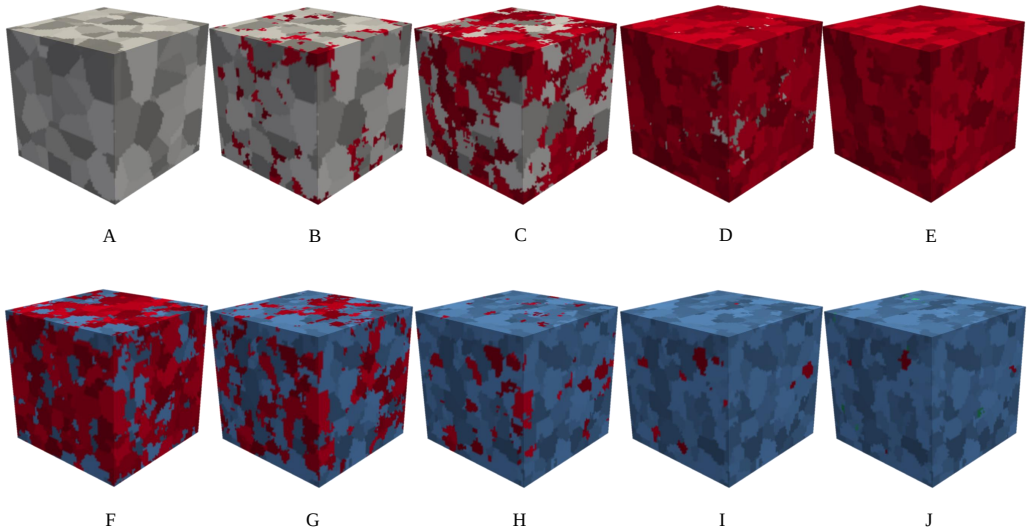

Figure 2.13: Evolution of the grain distribution, shown at the strain levels marked by points A through J in Figure 2.11: the color code emphasizes the microstructural evolution from the initial grain structure (*gray*) through a first recrystallization wave (new grains shown in *red*) and a second recrystallization wave (new grains in *blue*). The observed recrystallization waves correlate well with the stress–strain behavior of Figure 2.11.

Figure 2.15 plots the evolution of η_{RX} as obtained from the simulations in Section 2.5. According to (2.30), we expect $\log[-\log(1-\eta_{RX})]$ to scale linearly with $t-t_{RX}$, and the slope is identified as the Avrami coefficient p. The shown scaling in Figure 2.15 is more complex than linear, as we expect from our high-fidelity model that circumvents the various assumptions underlying JMAK theory. When computing the slope of the obtained curve at $t-t_{RX} = 100$s, 300s and 750s, we obtain coefficients $p = 0.64$, 3.0 and 5.3, respectively. Especially the obtained p-values at 300s and 750s (*i.e.*, when recrystallization is well underway) agree well with the range of previously reported Avrami exponents of $p = 4.0$ [34] and $p = 3.91$ [15], both for 3D simulations.

2.6 Influence of the FMCP model parameters

The recrystallization kinetics in our model are governed by the probability of switching defined in (2.23). The latter depends on several model parameters whose influence is investigated in the following and shown to allow us to fine-tune the model for other applications involving variations in temperature and strain rate.

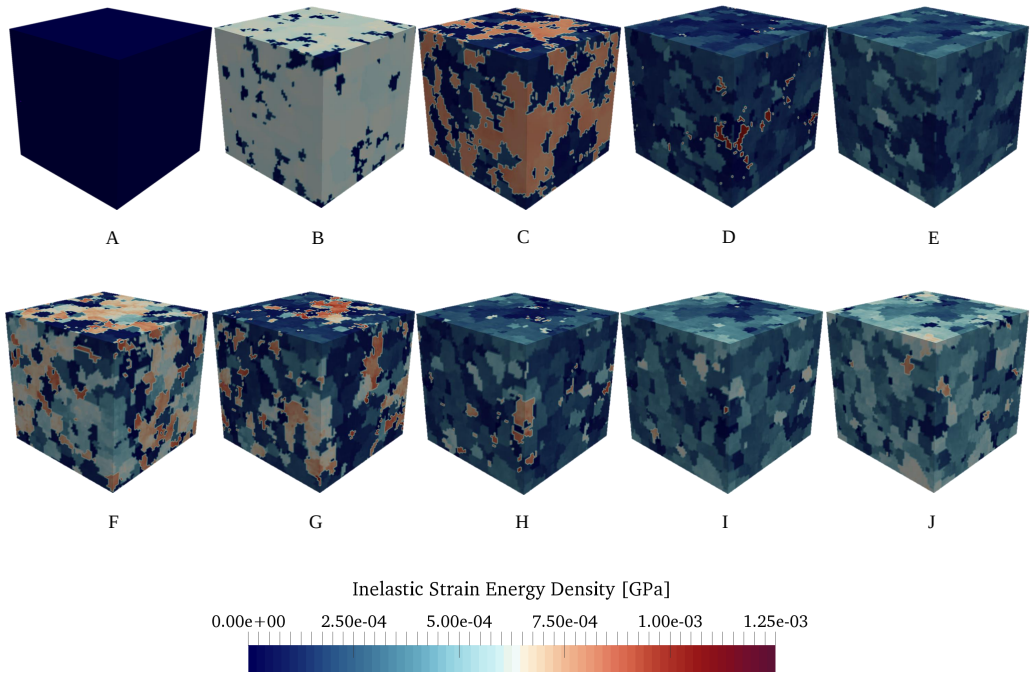

Figure 2.14: Evolution of the inelastic strain energy density $W^{\mathrm{sl}} + W^{\mathrm{tw}}$ at the ten strain levels marked in Figure 2.11. Each recrystallization wave relates to a decrease in the accumulated stored energy density through the nucleation and growth of grains.

2.6.1 Numerical temperature

Due to the lack of a suitable temperature-dependent material model for Mg, temperature T_S introduced in the probabilistic recrystallization kinetics does not imply a true process temperature. However, it is expected to qualitatively show the correct influence of temperature on the recrystallization kinetics through the thermally-activated migration and nucleation kinetics governed by (2.23). Figure 2.16 illustrates the influence of changing T_S on the multi-peak stress–strain behavior and indeed reveals a reduction in peak stress and recrystallization wave period with increasing T_S. Since the underlying crystal plasticity model was calibrated for room temperature and invariant to changes in temperature, the shown results underestimate the reduction in peak stress with increasing temperature.

2.6.2 Critical nucleation and migration thresholds

Changes in the critical energy thresholds in (2.23) affect the recrystallization kinetics and enable the transition from a multi-peak to a single-peak stress–strain behavior, as shown in Figure 2.17. In general, we observe the transition from a serrated to a single-peak flow stress behavior for increasing strain rates or decreasing temper-

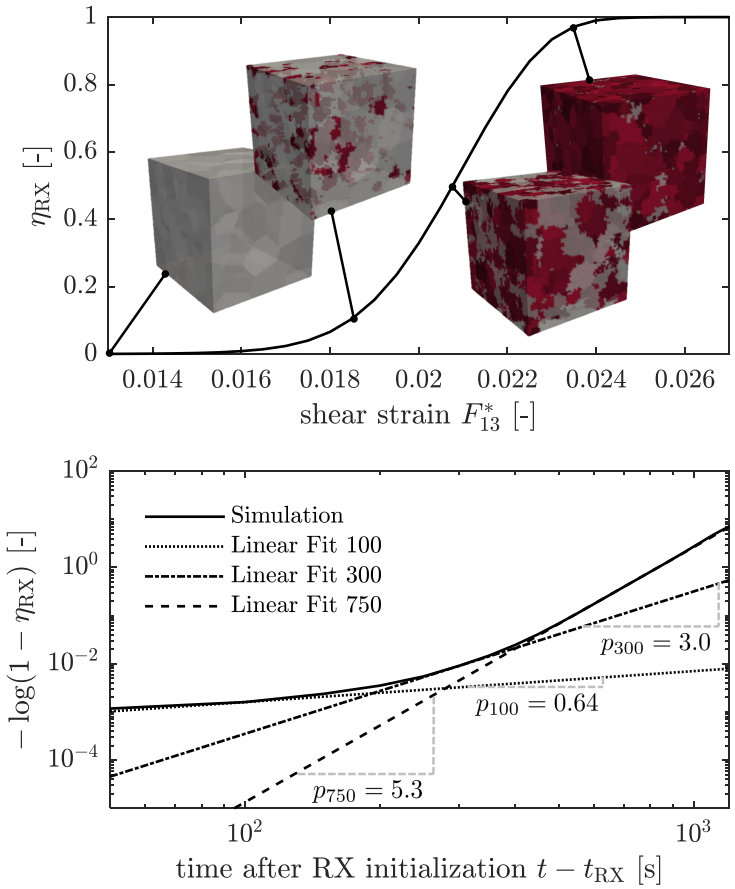

Figure 2.15: Evolution of volume fraction of recrystallized material as obtained from the simulations in Section 2.5, shown both on a linear (*left*) as well as on a double-logarithmic scale (*right*) with three representative slopes p computed at $t - t_{RX}$ = 100s, 300s, 750s.

atures [18, 60, 139], which the gradual overlapping of individual recrystallization waves causes due to accelerated inelastic deformation in the nucleated grains relative to a decreased migration behavior.

For fixed $n_{MC,GBM}$, $n_{MC,NCL}$ and T_S we may interpret changes in ΔE_{NCL} and ΔE_{GBM} by recourse to an empirical rule for the critical dislocation density for NCL [60, 137],

$$\rho_{cr} \sim \left(\frac{\gamma_S \dot{\epsilon}^p_{eff}}{blm\tau^2} \right)^{1/3}, \tag{2.31}$$

where b is the magnitude of the Burgers vector, l the dislocation mean-free path, m the GB mobility, $\tau = \mu b^2/2$ the dislocation line energy, and $\dot{\epsilon}^p_{eff}$ the phenomenological notion of a macroscopic plastic strain rate. In addition, empirical laws predict a variation of the nucleation rate $\dot{n}_{NCL}$ with process parameters such as temperature

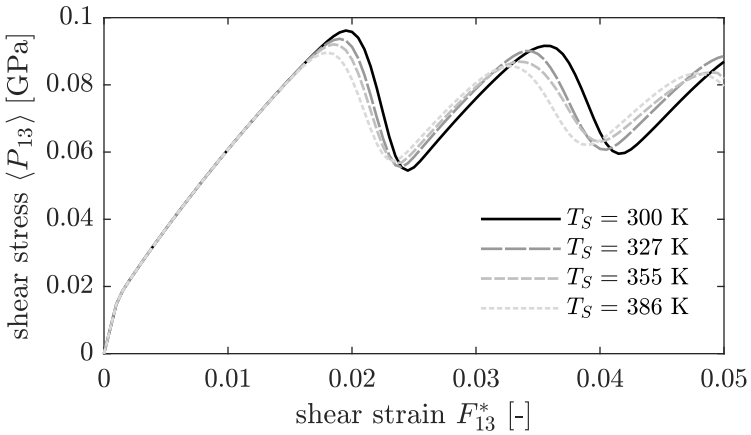

Figure 2.16: Influence of variations in the simulation temperature T_S on the multi-peak stress–strain behavior.

and strain rate according to the classical form [60, 123]

$$\dot{n}_{\mathrm{NCL}} \sim \dot{\epsilon}^{\mathrm{p}}_{\mathrm{eff}} \exp\left(\frac{Q}{RT}\right), \tag{2.32}$$

where Q represents an activation energy, and R is the gas constant. Comparing (2.31) and (2.32) yields $\dot{n}_{\mathrm{NCL}}/\rho_{\mathrm{cr}} \sim \left(\dot{\epsilon}^{\mathrm{p}}_{\mathrm{eff}}\right)^{2/3}$. We can therefore associate a relative decrease in ρ_{cr} with respect to the nucleation rate $\dot{n}_{\mathrm{NCL}} \sim n_{\mathrm{MC,NCL}}/\Delta t$ with an increase in $\dot{\epsilon}^{\mathrm{p}}_{\mathrm{eff}}$. Given $\Delta E_{\mathrm{cr,NCL}} \sim \rho_{\mathrm{cr}}$ [110], the tendency towards a single-peak flow stress evolution with decreasing $\Delta E_{\mathrm{cr,NCL}}$, as we observe in Figure 2.17, therefore agrees well with increasing strain rates.

2.6.3 Number of MCP sampling points

The phenomenological relation for $\dot{n}_{NCL}$ in (2.32) captures the transition from multi- to single-peak stress–strain behavior with increasing strain rate and decreasing temperature. It was previously employed in phase field models [164], cellular automata [32] as well as MCP models [72], where the dependence on strain rate was, in principle, included in a term measuring the Hamiltonian change through nucleation. Practically, however, that Hamiltonian change was set to a constant, thus eliminating the dependence on strain rate.

In our approach, we capture the Arrhenius-type dependence on temperature through the modified Glauber dynamics, while the dependence on strain rate emerges naturally from the rate-dependent constitutive model, and $\dot{n}_{NCL}$ relates directly to the choice of the number of MCP sampling points, $n_{\mathrm{MC,NCL}}$. We examine the latter relationship by increasing $n_{\mathrm{MC,NCL}}$, which, as Figure 2.18 shows, decreases the peak

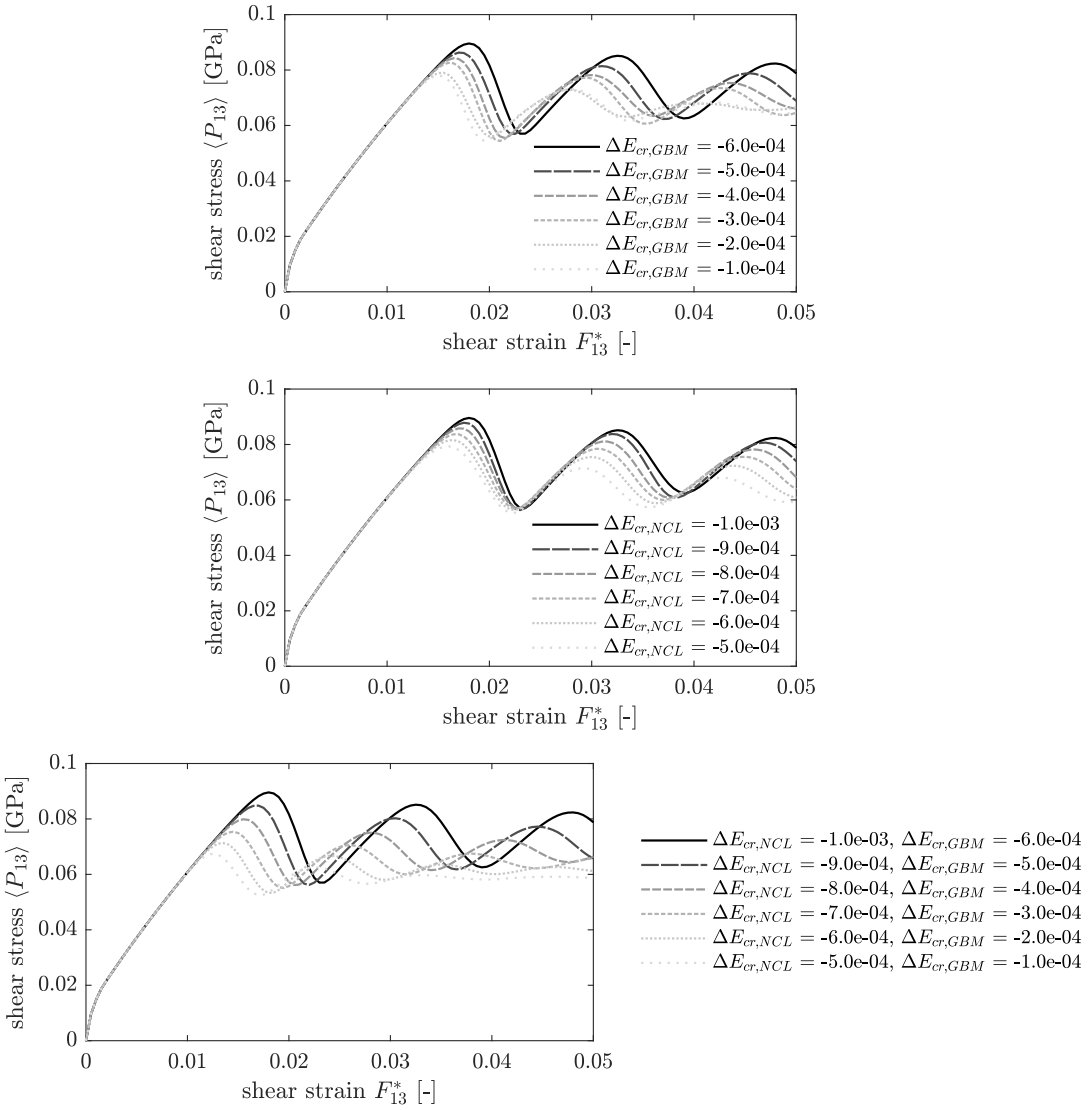

Figure 2.17: Effects of variations in $\Delta E_{\text{cr,NCL}}$ and $\Delta E_{\text{cr,GBM}}$ on the homogenized stress–strain behavior (all energy densities given in units of GPa). Unless otherwise indicated, we used the critical energy thresholds listed in Table 2.2.

stresses. This is explained through an increase in nucleation activity, not only by shifting the NCL probability to lower strain levels but also by increasing the total number of nuclei. At the same time, it does not significantly affect the multi-peak character of the stress–strain curve. By contrast, increasing $n_{\text{MC,GBM}}$ yields the expected more pronounced multi-peak stress–strain behavior, since an increased migration speed promotes the completion of individual recrystallization waves, thus making an overlap of recrystallization waves – as required for single-peak behavior – less likely.

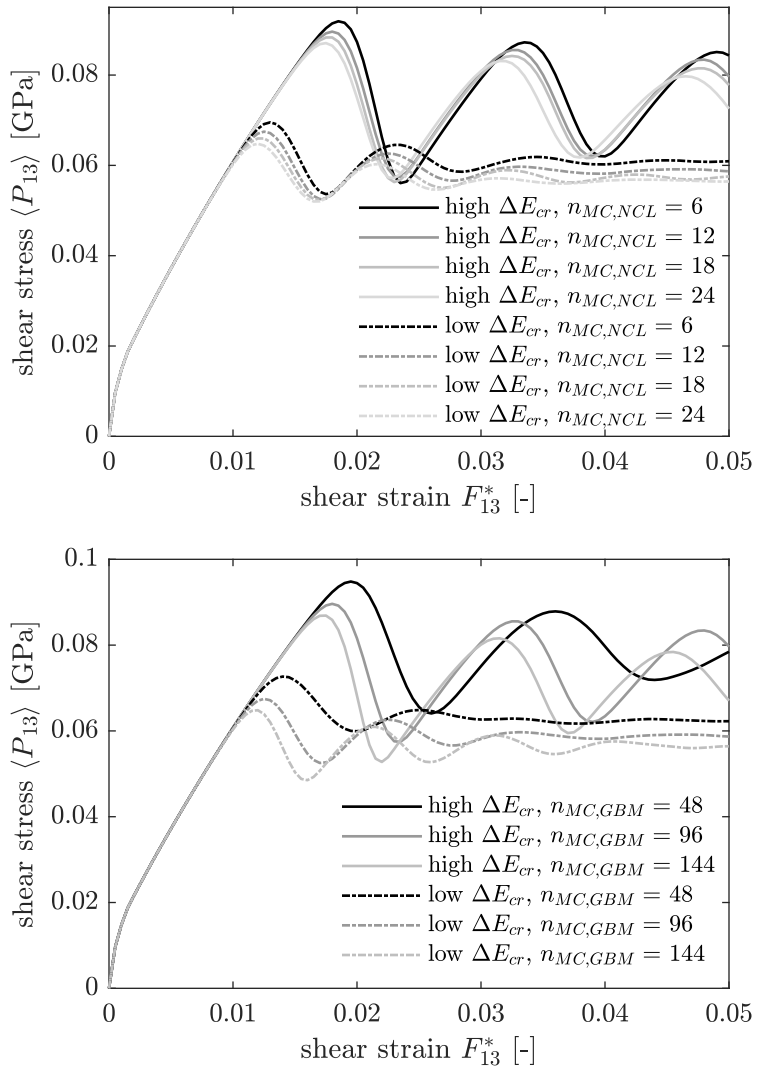

Figure 2.18: Effects of variations in $n_{\mathrm{MC,NCL}}$ and $n_{\mathrm{MC,GBM}}$ on the homogenized stress–strain behavior for *high* critical energy thresholds $\Delta E_{\mathrm{cr,NCL}} = -10^{-3}$ Jm^{-3} and $\Delta E_{\mathrm{cr,GBM}} = -6 \cdot 10^{-4}$ Jm^{-3}, and in like manner *low* critical energy thresholds $\Delta E_{\mathrm{cr,NCL}} = -5 \cdot 10^{-4}$ Jm^{-3} and $\Delta E_{\mathrm{cr,GBM}} = -10^{-4}$ Jm^{-3}.

2.7 Discussion

The previous sections demonstrated that the FMCP model introduced here provides a high-fidelity, mesh-independent technique for modeling discontinuous dynamic recrystallization at finite strains by NCL and GBM in a statistical fashion, whose kinetics are controlled by the FMCP model parameters – capturing both single- and multi-peak stress–strain behavior as well as qualitatively describing the influence of process temperature. While previous approaches – some of which were mentioned in Section 2.1 – showed advances in replicating the characteristic single- and/or multi-

peak flow stress response for this type of recrystallization seen in experiments (see, *e.g.*, Figure 2.19), to the best of our knowledge, no previous model has presented a comparably general framework for arbitrary load paths and general, finite-strain constitutive models including deformation twinning.

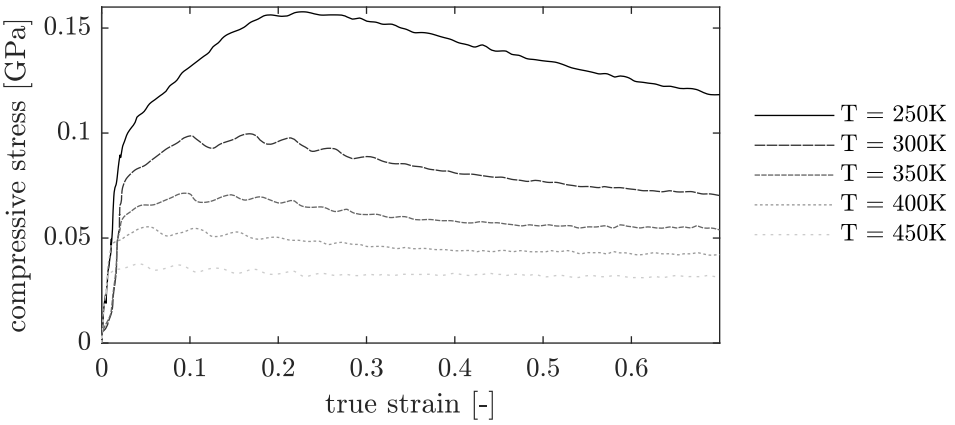

Figure 2.19: Evolution of the temperature-dependent single-to-multi-peak transition for Mg alloy AZ61 (Mg-6.1Al-1.1Zn-0.18Mn (wt%)) subjected to hot isothermal compression tests at a constant strain rate of 0.1 s^{-1} performed by a thermal simulation machine posterior to annealing conducted at 400°C for 60 min; data taken from Liao et al. [101].

In Section 2.6, we showed how the single- vs. multi-peak stress–strain behavior depends on the FMCP model parameters. A refined model (particularly including a temperature-aware crystal plasticity model) may hence be used to study the influence of process parameters such as temperature, loading rate and path.

Early recrystallization models were based on single scalar fields capturing the microstructure (such as the dislocation density; see, *e.g.*, Takaki et al. [164]), where the temporal evolution was frequently governed by the phenomenological model of Mecking and Kocks [106] or an ad-hoc generated, oftentimes time-invariant stored energy field (see, *e.g.*, Ivasishin et al. [72]). Recent work combined cellular automata with crystal plasticity models to show how it is possible to integrate anisotropic inelasticity into the framework of recrystallization [127]. However, the way in which nucleation was implemented in those models could not describe the emergence of a second recrystallization wave and therefore restricted the simulations to a single recrystallization cycle.

The model presented here went from a pure description of GBM to an FMCP formulation that couples GBM and NCL, further using physically motivated state

change definitions that take into account the full elastic and inelastic state of a material point. This not only allows us to capture multiple recrystallization waves but also leads to the convergence towards a steady state for rising strains as well as a transition between single- and multi-peak stress–strain behavior dependent on model parameters. Liao et al. [101] observed exactly this transition, dependent on process temperature, for Mg alloy AZ61 (see Fig 2.19). The flexibility to capture this phenomenon in the model is readily given; yet, we perceive the necessity of a careful parameter fitting as well as a temperature-aware constitutive model. Parameter identification is challenging when studying ECAE since stress–strain data are hard to extract from experimental force-displacements curves corrupted by friction in the device; therefore, alternative experimental setups may be preferable.

We point out that the particular combination of the FMCP model with the grid-based FFT solver of the mechanical homogenization problem requires a careful treatment of local state switches, which the gradual update procedure of Section 2.3.3 helped achieve. Abrupt local changes would cause numerical instability due to enormous jumps in the resolved shear stress on the individual slip and twin systems upon state switching. Our time-continuous interpretation of state switches – accommodated by individually adopting the new stretch and rotation – provides a physics-informed stabilization of the underlying mechanical solver. The formulation we have presented is sufficiently general to be applied to, in principle, arbitrary constitutive models that involve sudden changes of the fields of deformation, providing increased numerical stability while mechanical compatibility and invertability of the deformation gradient.

2.8 Conclusions

We presented a computational framework to model discontinuous dynamic recrystallization at finite strains while accounting for strongly anisotropic inelasticity as well as alternative strain-accommodating microstructural mechanisms such as deformation twinning in hcp metals. We combined an extended crystal plasticity model for Mg with a Monte-Carlo-Potts approach to recrystallization. The latter treats both grain nucleation and grain boundary migration in a statistical fashion, so that the kinetics of discontinuous dynamic recrystallization are described in a natural fashion that is based on the local energetics of the polycrystalline microstructure. The mechanical homogenization problem is solved on the RVE-level by recourse to an FFT-based solver whose regular spatial grids provides the natural basis for the described coupling to the discrete, stochastic Monte-Carlo framework. In addition,

the FFT efficiency admits simulations at high spatial resolution. Simulation results showed that (*i*) the chosen Monte-Carlo protocol achieves convergence of the recrystallization kinetics with grid resolution, (*ii*) results are (to a good approximation) insensitive to the random selection of MCP sampling points, (*iii*) we can describe single- and multi-peak stress–strain behavior by a single model, depending on model parameters that link to the microstructural mechanisms of recrystallization, (*iv*) the qualitative influence of process temperature, (*v*) the typical reduction in average grain size and an increasing spread in grain sizes is observed for ECAE simulations, *(vi)* the obtained effective recrystallization kinetics agree well with JMAK theory at sufficiently high strain levels (when recrystallization is well underway). The presented model is sufficiently general to apply to other constitutive models and can be coupled to temperature-aware constitutive models (beyond the scope of this investigation).

Chapter 3

VALIDATION AND COMPARISON WITH COMPUTATIONALLY INEXPENSIVE ALTERNATIVES – APPLICATION TO COPPER

A.D. Tutcuoglu, Y. Hollenweger, A. Stoy, and D.M. Kochmann. High- vs. low-fidelity models for dynamic recrystallization in copper. *Under review*, 2019.

Preamble

The author (A.T.) established the enhanced recrystallization model, implemented the crystal plasticity model as well as the FFT-based solver on the microscale and mesoscale, respectively, and conducted simulations for different scenarios. Y. Hollenweger (Y.H.) concentrated on simulations for the Taylor model, while A. Stoy (A.S.) provided the genetic algorithm used for retrieving the parameters in the recrystallization model.

3.1 Introduction

In Chapter 1, we compared four numerical methods for simulating dynamic recrystallization, which all differed in their computational cost. As the first attempt to quantitatively describe the microstructural evolution during recrystallization stands the JMAK model, which we introduced in Chapter 2. Based on the assumption of a constant nucleation rate, it describes the volume fraction of recrystallized material with time. Although the homogenizing assumptions inherent to this approach neglect a multitude of microstructural phenomena, it is still a popular model both for the assessment of new models – as we have seen in Chapter 2 or in the works of Goetz and Seetharaman [55] and Ivasishin et al. [72] – as well as a material model for large scale simulations (*e.g.*, Irani and Joun [70], Kim et al. [84]). Continuum models introduced the notion of an average grain size and derived computationally inexpensive evolution laws based on both migration and nucleation and taking into account discontinuous as well as continuous dynamic recrystallization [23, 63, 107]. These models grant an estimate on the final average grain size through equations of the form

$$d = d(\epsilon^{\text{in}}) = \begin{cases} d_0 - (d_0 - d_{\text{f}}) \left[1 - \exp\left(-k_{\text{DRX}}(\epsilon^{\text{in}} - \epsilon^{\text{in}}_{\text{cr}})\right)\right] & \text{if} \quad \epsilon^{\text{in}} > \epsilon^{\text{in}}_{\text{cr}} \\ d_0 & \text{if} \quad \epsilon^{\text{in}} \leq \epsilon^{\text{in}}_{\text{cr}} \end{cases}, \tag{3.1}$$

with initial average grain size d_0, final or saturated average grain size d_f, a notion of migration and nucleation speed k_DRX as well as a scalar notion of accumulated plastic slip ϵ^in and a corresponding critical accumulated plastic slip $\epsilon^\mathrm{in}_\mathrm{cr}$, above which the initiation of nucleation is possible. Apart from the immediate constraint of this model to systems, where we can capture the plastic deformation using a single scalar, the presence of a saturated grain size d_f – which, in general, is not *a priori* known – is defiling the purpose of such simulations. Further, they do not include any information on the effect of nucleation and migration on the average stress state, or at most very approximate laws concerning the steady-state stress as in [107]. This makes it difficult to fit these models against experimental data and leaves their application to highly specialized cases. The assumption of a constant strain rate (see, *e.g.*, Busso [23]) is a further constraint, that renders applications in the simulation of thermo-mechanical processing impossible, as local strain rates generally experience large spatial and temporal variations. Lastly, lacking the explicit notion of a grain, these models do not grant any insight into texture evolution.

The models introduced in Section 1.3 include the notion of a grain, either through explicitly resolving them in space – as in the case of the Monte-Carlo Potts method, cellular automata or the phase field method – or through the phenomenological notion of a volume fraction. Given the large spectrum of fidelity between those models, the question arises whether the gain in accuracy through enhanced fidelity justifies the additional computational expense. Large grains, for example, only afford a relatively small grain boundary area for nucleation. Additional nucleation sites through the emergence of shear bands, subgrains or twin bands are, consequently, important in the estimation of the effective nucleation rate. Heterogeneities within grains can, in general, only be captured by finding a displacement field which satisfies linear momentum conservation. This in return requires the application of solvers such as the finite element method (see, *e.g.*, Bernacki et al. [15, 16], Popova et al. [127]) or FFT-based methods, which are also frequently referred to as spectral methods (see, e.g. Chen et al. [28], Zhao et al. [197, 198]). If, however, the initial grains are sufficiently small and the temperature high, nucleation at existing grain boundaries and fast subsequent migration dominates the recrystallization process. In this case, the capturing of heterogeneities becomes dispensable and a Taylor assumption can provide a good estimation of the recrystallization process, assuming that the material of interest exhibits largely isotropic behavior. For metals experiencing severe anisotropy – as it is the case for, *e.g.*, Mg – this assumption would, again, not hold. A similar argumentation holds for recrystallization models based on a

single scalar variable representing the entire inelastic deformation: for metals that behave in a J2 plasticity fashion (see, e.g,. Ortiz and Stainier [119]) or any other isotropic inelasticity model, this assumption is, by definition, appropriate. Due to the presence of a finite number of slip systems, however, all metals have at least some anisotropy inherent to them. Especially under large deformations, the accommodation of strain on different slip systems is integral and, therefore, the reduction of the inelastic deformation state to only one scalar variable is contestable. Another shortcoming consists in the assumption that recrystallized grains are pristine grains that do not undergo further nucleation. Again, this assumption holds in the case of static recrystallization, where the lack of continuous deformation leaves the recrystallized grains in a pristine state so that recrystallized grains do not undergo further nucleation. Also for dynamic recrystallization up to relatively small strain levels, this can hold if the accumulation of inelastic strain energy density is sufficiently slow. For processes undergoing large deformations, however, the negligence of secondary nucleation cycles is inappropriate, as the recrystallized grains distort in a plastic manner that allows them to overcome the inelastic energy threshold needed for nucleation. This would not only lead to an overestimation of the average grain size, but also to an excessively stiff stress response, as the softening effect due to recrystallization weakens gradually in the absence of nucleation.

In this chapter, we aim to quantify the predominantly qualitative expectations from above. For this, we require a constitutive model which we understand sufficiently well to be able to identify recrystallization effects and distinguish them from, *e.g.*, slip-based phenomena. We accomplish this using the finite strain crystal plasticity model for pure Cu provided by Mellbin et al. [110] and experimental data on dynamic recrystallization – again in pure Cu – by Blaz et al. [18]. Since Cu is face-center cubic, we accept the limitation of the extent of our analysis to all topics that do not address the impact of severe anisotropic inelasticity. Again, in the idea of improved comparability, we introduce two derivative models based on the FMCP model presented in the previous section. One of these two models distinguishes itself from the FMCP model in that it replaces the governing equation of linear momentum conservation through a Taylor model ansatz. This is representative of a number of related approaches, *e.g.*, by Takaki et al. [164] or Mellbin et al. [110], who imposed a grainwise constant strain in their phase-field approach. For simplicity, we refer to the new model as FMCP×Taylor, whereas we term our original model from Chapter 2 FMCP×FFT. To achieve yet another simplification of the FMCP×Taylor model, we introduce a Taylor model, in which the notion of a volume fraction

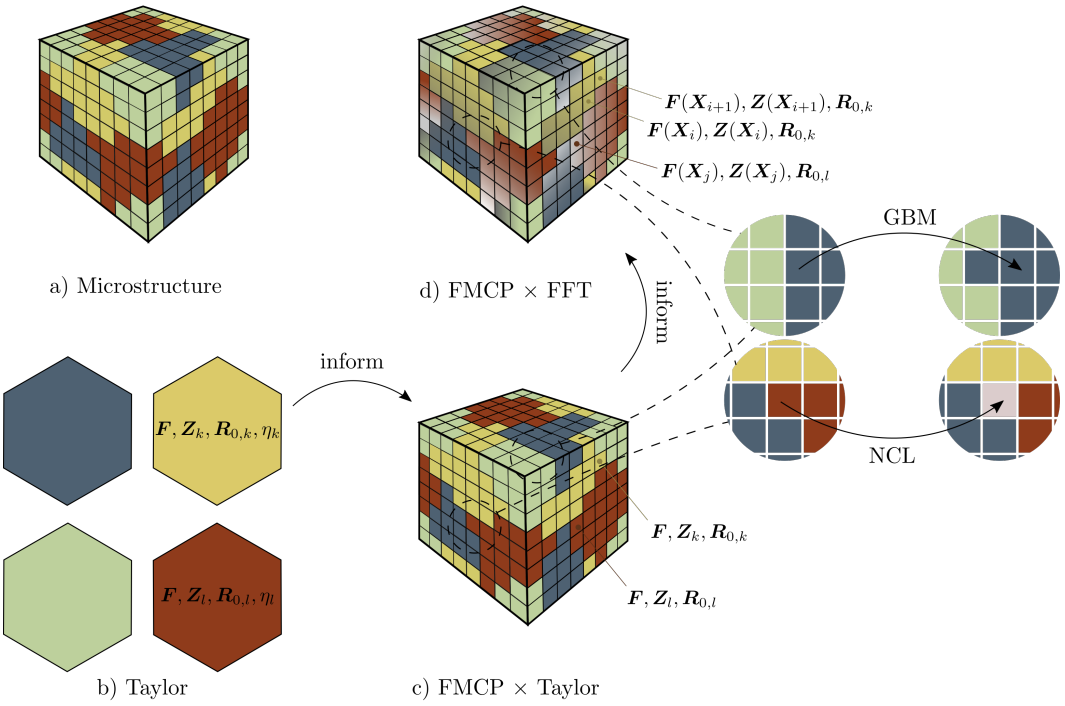

Figure 3.1: Illustration of the optimized fitting process for informing high-fidelity models through computationally inexpensive models.

entirely replaces the notion of the spatial resolution of a grain. This is similar to the approach from Cram et al. [30], which we analyzed in Section 1.3.1.

Along with the quantitative comparison of different levels of fidelity, we also deliver two new features with this study: on the one hand, we aim to verify that it is possible to fit the model from Chapter 2 to experimental data despite the low number of parameters contained in it. Further, by analyzing these three methods in rising order of fidelity, we target to deliver a framework for informed fitting. We initialize the fitting of higher fidelity methods drawing data from an informed guess using the parameters found for the structurally closely related lower fidelity model, which, in theory, reduces the overall computational effort. Lastly, with the advent of machine-learning-based approaches, models that can generate large sets of data for various ranges of parameters become increasingly popular. While the high complexity of models like FMCP×FFT grant us insights into the complex recrystallization effects, their computational expense inhibits them from being used in practical applications. Simpler models like the Taylor model may then be adapted based on the knowledge gained from these complex models to deliver similar results, at least on the homogenized level.

The following contribution is structured as follows: First, we introduce a copper material model in Section 3.2. Section 3.3 follows with the presentation of the Taylor model, for which we fit the recrystallization-related parameters based on experimental data for uniaxial compression. Subsequently, we investigate the microstructural evolution during this process. We introduce the notion of space in Section 3.4, where we present the FMCP×Taylor model in the framework of a mesoscale representative volume element (RVE). Further, for both the FMCP×FFT and the FMCP×Taylor method, we undertake small changes to the nucleation as well as the migration model compared to their counterparts from Chapter 2. These changes are made so that comparison with the Taylor model is facilitated, which in return strengthens the idea of informed learning described before. To complement the comparisons made throughout Section 3.3 and 3.4, Section 3.5 is devoted to an evaluation of the necessity of higher fidelity models. Finally, Section 3.6 concludes this contribution with an assessment of the different methods as well as an outlook on future directions, especially for the Taylor model.

3.2 Crystal plasticity model for single-crystalline Cu

We here provide a brief overview of the material model for Cu used in subsequent sections, whose basis was initially introduced by Mellbin et al. [108]. Cu comprises a total of $n_S = 12$ slip systems derived from its fcc crystal structure [92]. We denote by $\tilde{\boldsymbol{s}}^\alpha$ and $\tilde{\boldsymbol{m}}^\alpha$ ($\alpha \in \{1,...,n_S\}$) the α^{th} slip direction and normal, respectively, in the reference fcc-configuration. Depending on the crystallographic orientation $\boldsymbol{R} \in \mathrm{SO}(3)$ of the crystal, the slip and normal directions, measured in the global reference frame, are $\boldsymbol{s}^\alpha = \boldsymbol{R}\tilde{\boldsymbol{s}}^\alpha$ and $\boldsymbol{m}^\alpha = \boldsymbol{R}\tilde{\boldsymbol{m}}^\alpha$, respectively. The total deformation gradient $\boldsymbol{F} \in \mathrm{GL}_+(3)$ decomposes multiplicatively into its elastic and inelastic contributions, *i.e.*, $\boldsymbol{F} = \boldsymbol{F}^{\mathrm{e}}\boldsymbol{F}^{\mathrm{in}}$. As in classical crystal plasticity, the evolution of $\boldsymbol{F}^{\mathrm{in}}$ follows from

$$\dot{\boldsymbol{F}}^{\mathrm{in}} = \boldsymbol{l}^{\mathrm{in}}\boldsymbol{F}^{\mathrm{in}} \qquad \text{where} \qquad \boldsymbol{l}^{\mathrm{in}} = \sum_{\alpha=1}^{n_S} \dot{\gamma}^\alpha \boldsymbol{s}^\alpha \otimes \boldsymbol{m}^\alpha \tag{3.2}$$

denotes the inelastic velocity gradient, and $\dot{\gamma}^\alpha$ is the plastic slip rate on slip system α. Owing to the pairwise orthogonality $\boldsymbol{s}^\alpha \cdot \boldsymbol{m}^\alpha = 0$ for all $\alpha \in \{1,...,n_S\}$, evolution law (3.2) ensures $\det \boldsymbol{F}^{\mathrm{in}} = 1$. Besides the inelastic deformation gradient $\boldsymbol{F}^{\mathrm{in}}$, the plastic deformation history at any point is captured by a measure $\boldsymbol{g} \in \mathbb{R}^{n_S}$ representative of the total accumulated plastic slip. For convenience, we refer to the set of all internal variables as $\boldsymbol{Z} = \{\boldsymbol{F}^{\mathrm{in}}, \boldsymbol{g}\}$. Thus, the Helmholtz free energy density, comprising Neo-Hookean-type elastic strain energy and inelastic contributions stemming from

plastic work, is written as [108]

$$\Psi(\boldsymbol{F}, \boldsymbol{Z}) = W^{\mathrm{e}}\left(\boldsymbol{F}(\boldsymbol{F}^{\mathrm{in}})^{-1}\right) + \tilde{W}^{\mathrm{in}}(\boldsymbol{g}) \tag{3.3}$$

where

$$W^{\mathrm{e}}(\boldsymbol{F}^{\mathrm{e}}) = \frac{\mu}{2}\left(J^{-2/3}\mathrm{tr}\,\boldsymbol{C}^{\mathrm{e}} - 3\right) + \frac{\kappa}{2}\left(J^2 - 1\right) \text{ and } \tilde{W}^{\mathrm{in}}(\boldsymbol{g}) = \frac{1}{2}\boldsymbol{g}\boldsymbol{H}\boldsymbol{g}. \tag{3.4}$$

Here, $J = \det \boldsymbol{F} = \det \boldsymbol{F}^{\mathrm{e}}$ captures volumetric deformation, and μ and κ represent the shear and bulk moduli, respectively, while $\boldsymbol{C}^e = (\boldsymbol{F}^e)^{\mathrm{T}}\boldsymbol{F}^e$ is the elastic right Cauchy-Green strain tensor. The inelastic energy density depends on the hardening modulus tensor

$$H_{\alpha\beta} = Q\left(\delta_{\alpha\beta} + q(1 - \delta_{\alpha\beta})\right) \tag{3.5}$$

The accumulated slips g^α for all slip systems increase with plastic slip according to

$$\dot{g}^\alpha = (1 - Bg^\alpha)\frac{\tau^\alpha}{G_0 + G^\alpha}\dot{\gamma}^\alpha, \qquad G^\alpha = \frac{\partial \Psi}{\partial g^\alpha} = \sum_{\beta=1}^{n_S} H_{\alpha\beta} g^\beta, \tag{3.6}$$

where B serves as a saturation parameter, and $G_{\mathrm{r}}^\alpha = G_0 + G^\alpha$ is the total slip resistance, including the initial resistance G_0 and the increased resistance G^α due to plastic work. Finally, the plastic slips evolve according to

$$\dot{\gamma}^\alpha = \dot{\gamma}_0 \left(\frac{|\tau^\alpha|}{G_0 + G^\alpha}\right)^m \mathrm{sign}(\tau^\alpha), \quad \alpha \in \{1, ..., n_S\} \tag{3.7}$$

with the reference slip rate $\dot{\gamma}_0$, hardening parameter m, and the resolved shear stress on system α computed as $\tau^\alpha = \boldsymbol{s}^\alpha \cdot \boldsymbol{\Sigma}\boldsymbol{m}^\alpha$. Here, $\boldsymbol{\Sigma} = (\boldsymbol{F}^{\mathrm{e}})^{\mathrm{T}}\boldsymbol{P}(\boldsymbol{F}^{\mathrm{in}})^{\mathrm{T}}$ represents the Mandel stress tensor with $\boldsymbol{P} = \partial\psi/\partial\boldsymbol{F}$ denoting the 1st Piola-Kirchhoff stress tensor.

The above constitutive equations satisfy the Clauius-Duhem inequality for isothermal loading [58, 108], and the total dissipation reads

$$D = \boldsymbol{\Sigma} \cdot \boldsymbol{l}^{\mathrm{in}} - \sum_{\alpha=1}^{n_S} G^\alpha \dot{g}^\alpha \geq 0. \tag{3.8}$$

Consequently, the rate of change in stored energy due to inelastic deformation and excluding dissipation is given by

$$\dot{W}^{\mathrm{in}} = \dot{\tilde{W}}^{\mathrm{in}} - D = \sum_{\alpha=1}^{n_S} \tau^\alpha (1 - Bg^\alpha)\frac{G^\alpha}{G_0 + G^\alpha}\dot{\gamma}^\alpha. \tag{3.9}$$

Thus, even though W^{in} is not known in closed form, we can incrementally integrate (3.9) along a deformation trajectory to obtain W^{in} after each time increment (starting with $W^{\text{in}} = 0$, $\boldsymbol{F}^{\text{int}} = \boldsymbol{I}$, and $g^{\alpha} = g_0$ for all slip systems in the virgin state). This is important since, following Mellbin et al. [109] and the theory outlined in Chapter 2, we assume that the driving force behind both grain nucleation and GB migration during DRX does not include energy dissipated by heat but only depends on W^{in}. For conciseness, in the following we refer to the effective total stored energy density as

$$W = W^{\text{e}} + W^{\text{in}}. \tag{3.10}$$

We calibrate the model by comparison to uniaxial compression experiments performed by Blaz et al. [18], which were performed at a true compressive strain rate of $\dot{\epsilon} = -2.0 \cdot 10^{-3}\text{s}^{-1}$ up to a maximum true compressive strain of $\epsilon_{\text{max}} = -1$. For numerical purposes, each compression test is broken into n equal time steps of size $\Delta t = \frac{\epsilon_{\text{max}}}{n\dot{\epsilon}}$ up to a time $t_{\text{max}} = n\,\Delta t$. Time integration is carried out in an explicit fashion (besides the inelastic evolution equations, the DRX treatment below requires explicit updates). The experimental data by Blaz et al. [18] will also be used to calibrate the below (Taylor and FMCP) models for DRX. This particular set of Cu DRX data was chosen for its meaningful stress-strain data from uniaxial compression tests at multiple dinstics temperature levels. All model parameters used in subsequent sections (unless otherwise specified) are summarized in 3.1. The specific parameters for the above single-crystal Cu model are given in Table 3.1. A detailed comparison of experimental and simulated data will follow below. We stress that all subsequent simulations assume isothermal loading at a fixed processing temperature, which is accounted for in the above crystal plasticity model through the two temperature-dependent parameters Q and G_0, governing the hardening and initial slip resistance, as proposed by Mellbin et al. [110] (see Table 3.1).

3.3 Taylor model for polycrystalline Cu

3.3.1 Theory

We consider a set of $N_g \in \mathbb{N}$ grains, each endowed with a set of inelastic variables $\boldsymbol{Z}_i$ and a volume fraction $\eta_i \equiv V_i/V_0$ based on the ith grain's volume V_i and a total volume V_0. For convenience, we denote the set of all inelastic variables and volume fractions as $\mathcal{Q} = \{\boldsymbol{Z}_i, \ldots, \boldsymbol{Z}_{N_g}; \eta_i, \ldots, \eta_{N_g}\}$ and the set of all crystallographic orientations as $\mathcal{R} = \{\boldsymbol{R}_i, \ldots, \boldsymbol{R}_{N_g}\}$. The Taylor approximation dictates that every grain i experiences the same total deformation gradient, *i.e.*, $\boldsymbol{F}_i = \boldsymbol{F}$ for $i = 1, \ldots, N_g$. Consequently, the deformation is compatible across grains but violates mechanical equilibrium in

Table 3.1: Parameters defining the Cu material model introduced in Section 3.2 as well as the two recrystallization constants from Sections 3.3 and 3.4.

Parameter	**Sym.**	**Unit**	**725 K**	**775 K**	**875 K**	**Source**
Shear modulus	μ	GPa	35	34	32	[46]
Bulk modulus	κ	GPa	129	128	126	[97]
Init. shear res. conjugate	G_0	MPa	8.0	6.5	3.7	[110]
Plastic modulus	Q	MPa	40.2	37.0	32.0	[110]
Latent hard. multiplicator	q	-		1.4		[58]
Hard. exponent	m	-		26		[58]
Saturation factor	B	-		8		[58]
Init. shear res.	g_0	-		0.007		[58]
Reference slip rate	$\dot{\gamma}_0$	s^{-1}		0.001		[58]
Crit. energy density thres.	$W^{\mathrm{in,cr}}$	MPa	0.669	0.424	0.159	[110]
Nucleation exponent	d	-		4.4		[197]

general; the Taylor approximation therefore leads to the well-known upper bound of the average stress and stiffness. The total strain energy density of a polycrystal follows as the weighted average over all grains:

$$E = E(\boldsymbol{F}, \mathcal{Q}, \mathcal{R}) = \sum_{i \in \{1,\dots,N_g\}} \eta_i W_i(\boldsymbol{F}, \boldsymbol{Z}_i) - \nu \left(\sum_{i \in \{1,\dots,N_g\}} \eta_i - 1 \right), \tag{3.11}$$

where the Lagrange multiplier ν constrains the sum of all volume fractions to unity. Here, we write $W_i(\cdot)$ to emphasize the dependence of the grain-wise strain-energy density on the respective grain orientation $\boldsymbol{R}_i$ through the resolved shear stresses. Consequently, the effective stress tensor follows as the weighted average

$$\boldsymbol{P} = \frac{\partial E}{\partial \boldsymbol{F}} = \sum_{i \in \{1,\dots,N_g\}} \eta_i \frac{\partial W_i(\boldsymbol{F}, \boldsymbol{Z}_i)}{\partial \boldsymbol{F}}. \tag{3.12}$$

In an extension of the classical Taylor model, we model the evolution of the volume fraction using a gradient flow assumption:

$$\dot{\eta}_i = -\frac{1}{\kappa_{\mathrm{GBM}}} \frac{\partial E(\boldsymbol{F}, \mathcal{Q}, \mathcal{R})}{\partial \eta_i} = -\frac{W_i(\boldsymbol{F}, \boldsymbol{Z}_i) - \nu}{\kappa_{\mathrm{GBM}}}, \tag{3.13}$$

where κ_{GBM} denotes the GB mobility during migration. This has the immediate consequence, that for the evolution of microstructure posterior to loading – also referred to as post-dynamic recrystallization [144] – in the hypothetical scenario of $t \to \infty$, almost surely (in the mathematical sense) only one grain survives. This is unsurprising as (3.11) does not carry information about the contribution of surface

energy. Keeping in mind that, in general, DRX is usually followed by a decrease in process temperature, we accept this model's constraint to realistic post-loading process environments and note that an extension of the formulation in (3.11) by an additional surface-penalizing term is straightforward.

Using the property $\sum_{i\in\{1,\dots,N_g\}} \eta_i = 1$ and thus $\sum_{i\in\{1,\dots,N_g\}} \dot{\eta}_i = 0$, we infer from (3.11) and (3.13) that

$$0 = \sum_{i\in\{1,\dots,N_g\}} W_i(\boldsymbol{F}, \boldsymbol{Z}_i) - N_g \nu \qquad \Leftrightarrow \qquad \nu = \frac{1}{N_g} \sum_{i\in\{1,\dots,N_g\}} W_i(\boldsymbol{F}, \boldsymbol{Z}_i). \tag{3.14}$$

Substituting the above result for ν into (3.13) yields the kinetic evolution of the grain volume fractions as

$$\dot{\eta}_i = -\frac{1}{\kappa_{\mathrm{GBM}}} \left(W_i(\boldsymbol{F}, \boldsymbol{Z}_i) - \frac{1}{N_g} \sum_{j\in\{1,\dots,N_g\}} W_j(\boldsymbol{F}, \boldsymbol{Z}_j) \right). \tag{3.15}$$

After each load increment, (3.15) is used in a backward-Euler fashion to explicitly update all grain volume fractions based on their energetics. We eliminate each grain i whose $\eta_i \leq 0$ during a given load step and prevent it from reappearing; we ensure that the total volume fraction is reset to 1 in cases of $\eta_i < 0$ (any negative volume is redistributed among the remaining grains).

The above framework is suitable for the growth and shrinkage of the N_g existing grains, but it lacks capabilities for the nucleation of new grains. Nucleation of new grains is more complex. We respect that the time and length scales of the underlying atomic-level processes are well below the polycrystalline mesoscale of interest here [197]. We therefore model nucleation as the spontaneous creation of a small nucleus of (arbitrarily chosen) initial size $\eta_0 = 1/64^3$ within a single load step[1]. With the dependence of nucleation on thermal fluctuations in mind, we propose a stochastic nucleation criterion[2] which assumes the probability of nucleation to depend on the

[1] The choice $\eta_0 = 1/64^3$ is motivated by the attempt to allow for a comparison with the FMCP model. As introduced in Section 3.4 later, the RVE is chosen to have a resolution of 64^3, thus having a voxel size and therefore a smallest volume fraction to be captured of $1/64^3$.

[2] We note that, with similar intentions Zhao et al. [197] considered a sub-grid with significantly smaller grid size compared to their continuum-level polycrystal, and every sub-grid point could independently undergo a phase transformation; nucleation at the larger-scale continuum was assumed to occur only if a minimum number of sub-grid points transformed. This is quite analogous to our nucleation model, assuming that the transformation of a local sub-grid point is represented by an inhomogeneous Poisson process and that the dislocation density as the critical state variable for nucleation can be replaced by the inelastic energy density, as done here.

stored inelastic energy density as

$$w^{\mathrm{th}}(W_i^{\mathrm{in}}) = \eta_i^c \Delta t\, \kappa_{\mathrm{NCL}} \left[1 - \exp\left\{ - \left(\frac{W_i^{\mathrm{in}}}{C W^{\mathrm{in,cr}}} \right)^d \right\} \right], \tag{3.16}$$

where the last term corresponds to a cumulative Weibull distribution. κ_{NCL} serves as a nucleation rate, constant C allows shifting peak nucleation activities away from $W^{\mathrm{in,cr}}$, and d is a nucleation exponent. For simplicity, we set $c = 1$, assuming that the nucleation rate varies linearly with the parent grain's volume available for nucleation. A viable alternative, which we do not further investigate here, is $c = 2/3$, which is results from assuming a linear dependence of the nucleation rate on the available grain boundary area (although $c = 2/3$ leads to better model predictions of the final average grain size, the predicted average compressive stress worsens significantly, which motivated the choice $c = 1$).

For every grain $i \in \{1, \ldots, N_g\}$ with $W_i^{\mathrm{in}} > W^{\mathrm{in,cr}}$ at a given time step, we initiate nucleation if

$$w_i < w^{\mathrm{th}}(W_i^{\mathrm{in}}) \qquad \text{with} \qquad w_i \sim \mathcal{U}([0,1]), \tag{3.17}$$

and reject otherwise (*i.e.*, w_i is obtained from a normal distribution). Concerning the individual state switch rules, we follow the same strategy as in Chapter 2. The only adaption consists in the update of the internal variables specific to this finite strain crystal plasticity model, in that we set g^α equal to g_0 for all $\alpha = 1, \ldots, n_s$ upon nucleation.

In favor of a reduced number of model parameters, we assume a linear relation between the critical dislocation density ρ_{cr} and the critical inelastic energy density [110] according to

$$W^{\mathrm{in,cr}} = \frac{\mu b^2}{2} \rho_{\mathrm{cr}}, \tag{3.18}$$

where b denotes Burgers' vector (for Cu $b = 0.259$ nm). Hallberg et al. [64] tracked the evolution of the dislocation density in Cu for the temperature levels of interest and defined ρ_{cr} as the necessary minimum dislocation density for nucleation, which is adopted here. This leaves us with only three material parameters to be obtained from fitting to experimental data, viz. κ_{GBM}, κ_{NCL} and C.

3.3.2 Model calibration and convergence study without recrystallization

Before calibrating the DRX model, we verify that the crystal plasticity model (in the absence of pronounced effects of DRX) matches experimental findings of compression tests performed on polycrystalline Cu samples. Specifically, we consult the

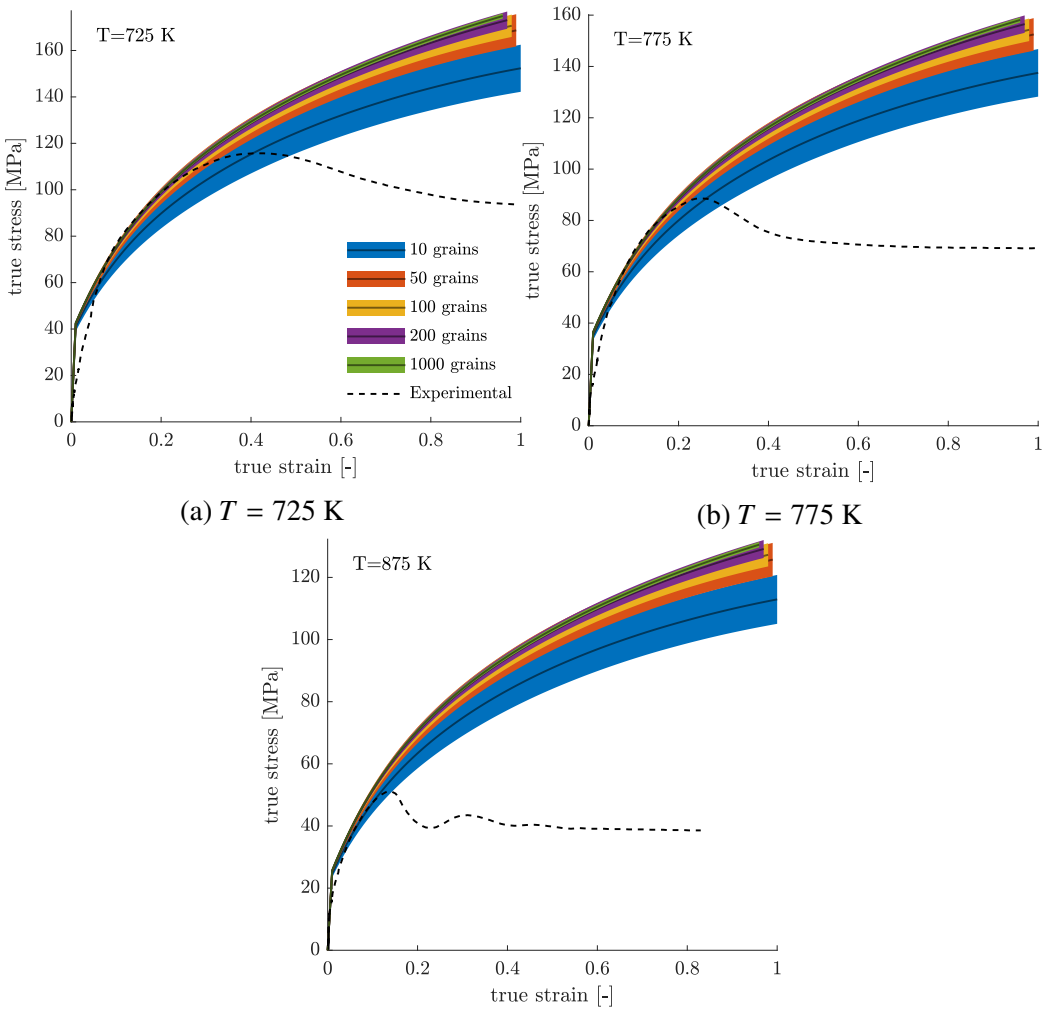

(a) $T = 725$ K

(b) $T = 775$ K

(c) $T = 875$ K

Figure 3.2: Homogenized stress-strain behavior for a uniaxial compression test up to 100% true compressive strain in 100,000 load steps for grain counts of 10 (*blue*), 50 (*orange*), 100 (*yellow*), 200 (*red*), and 1000 (*green*) and temperatures of 725 K (*left*), 775 K (*right*), and 875 K (*bottom*). Each data point is based on 100 repetitions with each run characterized by a different random initial texture. The one-sigma stress band correspond to the interval around the mean (*emphasized using solid lines*) with a total width of two standard deviations. Results are compared to experimental data (*dashed*) from Blaz et al. [18]. (We note that results are plotted up to slightly different maximum strain levels for better differentiability.)

experimental data from Blaz et al. [18] and assume that recrystallization only kicks in at significant stress levels (so that the early elastic-plastic stress-strain response is characteristic of the material behavior without recrystallization). As shown in Figure 3.2 the model reproduces the low-strain regime of the stress-strain data at each temperature level reasonably well. (Although we do not fully capture the elastic and

incipient plastic response, we observe a reasonable fit for the plastic slip-dominated regime and consider the model appropriate for DRX simulations where plasticity and the associated stored inelastic energy are the dominant driving forces.

The stiff Taylor approximation is understood to overpredict the stress evolution (we set $\dot{\eta}_i = 0$ and only perform the Taylor averaging without DRX). In addition, the predicted response is expected to vary with the number of grains in the ensemble, until convergence is achieved as $N_g \to \infty$. We show that for sufficiently large N_g a random texture[3] in the Taylor model does show a converging stress-strain response (see Figure 3.2). To achieve the initial texture, we adopt the approach used in Mellbin et al. [110] and randomly generate the three Bunge-Euler angles as $\phi_1 = 2\pi r_1$, $\Phi = \arccos(1 - 2r_2)$, $\phi_2 = 2\pi r_3$ with $r_i \sim \mathcal{U}([0,1])$, $i \in 1,2,3$. We analyze three different temperature levels (725 K, 775 K and 875 K) and five different grain counts ($N_g \in \{10, 50, 100, 200, 1000\}$). For every simulation, we run 100 iterations to compute ensemble averages, each run endowed with a different randomized orientation distribution across the equi-sized grains.

Figure 3.2 depicts the homogenized stress evolution visualized as a band representing $\mathbb{E}[-\sigma_{33}(t)] \pm \sqrt{\mathbb{V}\mathrm{ar}[\sigma_{33}(t)]}$. The standard deviation decreases monotonically, while the mean increases due to the Taylor-type averaging (unlike in spatially resolved RVE-based calculations as shown by Vidyasagar et al. [177]; increasing the number of grains here does not offer avenues for stress relaxation by cooperative inter-grain mechanisms and therefore leads to a stiffer response). We note that an initial grain count of 48 (as used, *e.g.*, in Mellbin et al. [110]) still experiences a significant deviation from the experimental stress evolution in terms of its mean. Based on Figure 3.2 and as a compromise between a sufficiently general representation and computational efficiency, we set the initial number of grains for all remaining tests to 200, unless otherwise indicated. To assess the grain refinement in subsequent chapters where simulations include the notion of recrystallization, we further set the initial volume fraction of every grain to $\eta_i(t = 0) = 0.05$. Although the Taylor model does come with a characteristic length scale per se, we may define a total initial volume V_0 of the entire grain ensemble in order to match the initial grain size in experiments based on the number of grains in the ensemble. Here, we set $V_0 = 4.8 \times 10^5\ \mu\mathrm{m}^3$, which yields an average initial grain size of 78 μm. Consequently, we may also interpret changes in grain volume fractions as changes

[3] Absent of any information regarding texture, we consider the assumption of an initially fully randomized texture to be valid.

in grain size in the following. (We note that, in general, both the migration mobility κ_{GBM} and nucleation mobility κ_{NCL} may depend on V_0.)

3.3.3 Simulated material response with recrystallization

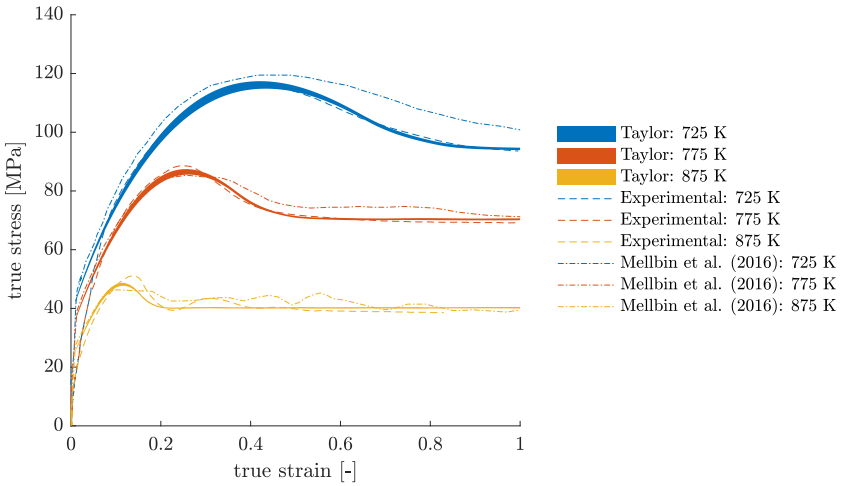

Figure 3.3: One-sigma band of the true compressive stress vs. true compressive strain as obtained from our Taylor model with DRX (averaged over 200 random initial textures), compared to experimental data from Blaz et al. [18] (*dashed*) and numerical results from Mellbin et al. [110] (*dash-dotted*) for $T \in \{725, 775, 875\}$ K.

Figure 3.3 illustrates the stress-strain response as obtained from our Taylor model with DRX, compared to experimental data from Blaz et al. [18] as well as to simulated data from Mellbin et al. [110] (this latter model is based on the same crystal plasticity description for Cu as employed here but uses a vertex-based approach to DRX instead of our Taylor setup). We used a genetic algorithm to fit the three DRX parameters κ_{GBM}, κ_{NCL}, and C (at each temperature level), based on the experimental stress-strain data. For temperatures of 725 K and 775 K, we observe an excellent match between the experimental and simulated stress-strain data, which capture both the single-peak response and the final steady stress state well. Deviations[4] for these two temperatures lie at 4.0% and 3.9%, respectively. The steady-state behavior is also closely reproduced in the case of 875 K – however, as we fail to capture the peak stress as well as the initial multi-peak behavior, the deviation of 5.2% is higher. Apparently, this is one of the limitations of the relatively simple Taylor model. At the two lower temperatures, we will show that not only does the stress-strain curve

[4] All deviations in this contribution correspond to the discrete l^2-norm across the full strain range, unless otherwise indicated.

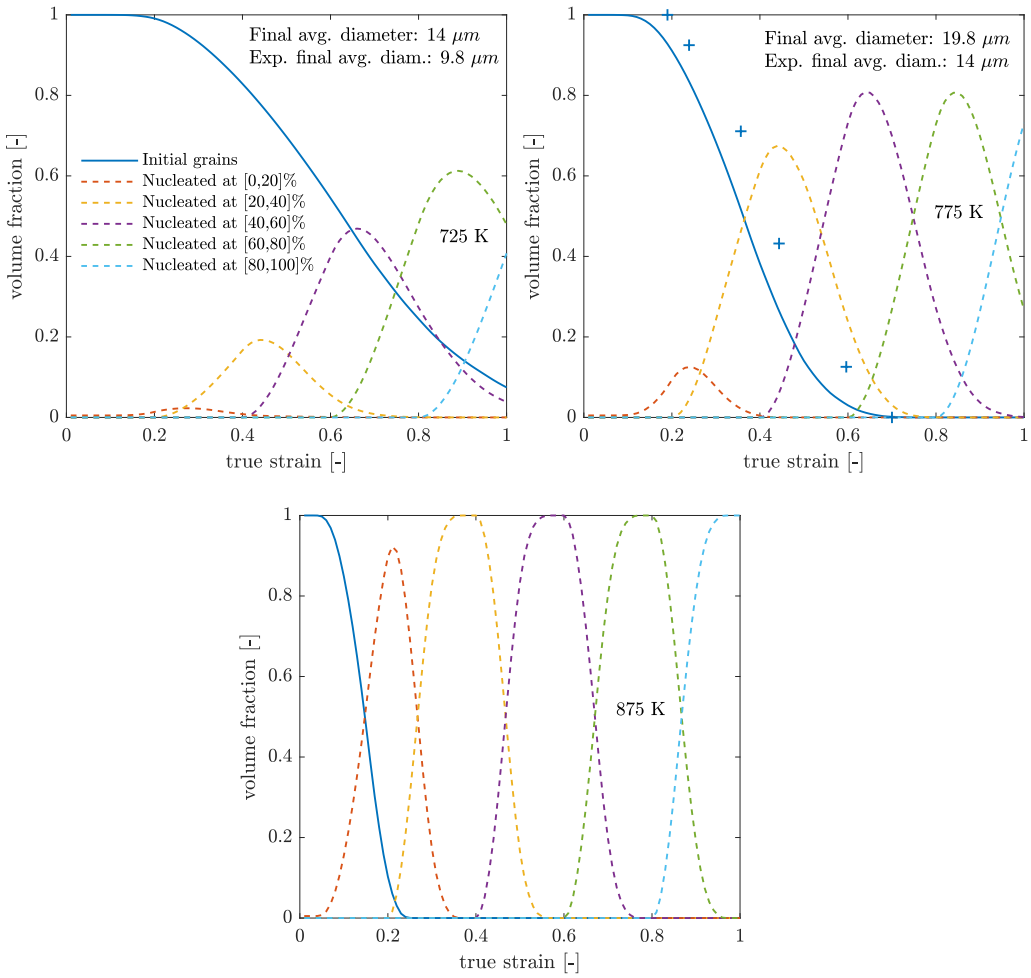

Figure 3.4: Evolution of the non-recrystallized volume fraction for all initial grains (*solid line*) and for all grains nucleated within the outlined ranges of strains (*dashed lines*) for temperatures of 725, 775 and 875 K. The initial average grain diameter is at 78 μm in the experiments. The experimental and numerical final average diameter at 875 K lie at 34 μm and 30 μm, respectively. Blue crosses for 775 K denote the experimentally estimated fraction of material that has not yet undergone recrystallization.

fit well to the experimental data, but the associated evolving microstructures also match experimental observations.

A convenient metric to assess the microstructure evolution is the total volume fraction of non-recrystallized material in the sample (or in the Taylor ensemble). Figure 3.4 visualizes the evolution of the non-recrystallized volume fractions, showing both simulation outcomes and experimental data[5]. Shown from our simulations

[5]We note that the methodology behind the experimental estimation of the non-recrystallized volume

is the predicted total non-recrystallized volume fraction at two temperature levels as well as the recrystallized volume fractions during each recrystallization wave, the latter being defined as the total volume of all grains nucleated within certain strain intervals. Already in the case of 725 K – where the stress-strain evolution showed a single-peak behavior – recrystallized grains are subjected to further recrystallization. This is made possible by the natural implementation of recrystallization in our Taylor model: as we allow recrystallized grains to undergo plastic deformation, they can again attain a state of sufficiently high inelastic energy to promote further grain nucleation or to be consumed by other, lower-energy grains. In the case of 775 K, we observe a stabilizing level of the total volume fraction of each recrystallization wave at around 80% of the total volume. The convergence to this steady-state level is closely related to reaching the steady-state stress, as seen in Figure 3.3.

All experiments started with an average initial grain size of 78 μm, while the final measured grain sizes are included in Figure 3.4, as obtained from both experiments and our Taylor model (of course, the Taylor ansatz has no notion of grain size; however, it captures the relative change in grain volume fractions, so that assuming an initial average grain size of 78 μm lets us predict the final average grain size). Based on the set of active grains $\mathcal{A}$ – which we define as the set of all initial grains with volume fraction greater than 0 and all recrystallized grains with grain ID greater than the oldest recrystallized grain[6] with volume fraction larger than 0 – we thus compute the average grain diameter via $\eta_{\text{avg}}(t) = \sum_{i\in\mathcal{A}} \eta_i/|\mathcal{A}|$. Considering that our genetic parameter fitting only involved the stress-strain data, the predicted final average grain sizes for all three temperature levels are relatively close to the ones reported by experiments.

The Taylor simulations also admit the observation of texture evolution. Figure 3.5 illustrates the evolving [111]-poles of all grains. To incorporate information on the relative volume and age of every grain, we linearly scale the size of every grain

fraction is not sufficiently clear and may include errors due to postprocessing and inexact estimation of the areas belonging to the newly nucleated grains. A perfect fit is therefore not expected, particularly since a further source of errors may lie in the simplified crystal plasticity model for Cu and its shortcomings in replicating the purely elastic part of the stress-strain response. Since nucleated grains are initially pristine and therefore at a zero stress state, the steady-state stress is influenced by the steady-state nucleation rate, which also explains that both are reached around the same strain level.

[6] We note that this includes some grains that have already reached zero volume fraction. The reason we still include them in the set of active grains is that, in general, the speed at which grains shrink should decrease significantly before they are fully consumed by surrounding grains as the final spherical shape promotes stability. Since we do not aim to make *ad-hoc* changes to the growth model, we found this assumption to be a reasonable compromise.

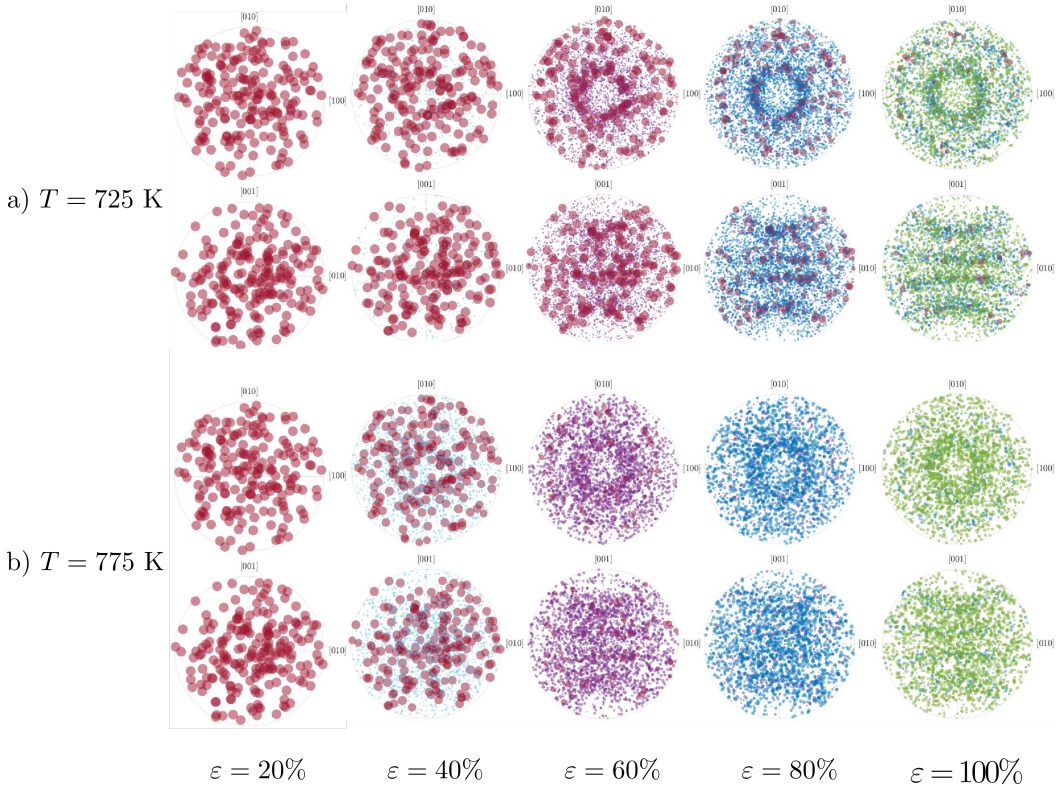

Figure 3.5: Pole figures of the [111]-pole for $T \in \{725, 775, 875\}$ K with point sizes scaled by the respective grain volume fractions at five different true compressive strain levels $\varepsilon_{\text{true}}$. Colors indicate initial grains (red) and grains nucleated up to a true compressive strain of 25% (bright-blue), 50% (purple), 75% (dark-blue), and 100% (bright-green).

in the pole figure with the respective grain's volume fraction. We also marked poles belonging to grains of the same recrystallization wave by the same color (*c.f.* Figure 3.4). We observe the most pronounced texture formation at 725 K, while a more diffuse texture develops at 775 K. This is attributed to the interaction of shorter recrystallization wave cycles and the randomization of grain orientations. We note that the respective texture for both 725 K and 775 K in Mellbin et al. [110] is slightly more evident, which is unsurprising as their simulations defined the initial misorientation of a recrystallized nucleus to 15° compared to its parent grain at the time of nucleation, which causes a correlation between the texture of already existing and recrystallized grains. We further point towards Lallit [92] and Hallberg et al. [64], where 3D uniaxial compression tests were simulated with similar emerging textures when considering the ⟨111⟩ pole family. Bronkhorst et al. [22] demonstrated such textures in experimental compression tests.

3.4 Field Monte-Carlo Potts Models

The Taylor model for DRX introduced above has reproduced the salient features of DRX in Cu and provided a good account of the stress-strain response and the microstructure evolution during severe compression testing, yet the accuracy – especially at high temperature levels – could be improved. This is not surprising as the Taylor assumption of uniform strains across grains and the lack of any spatial correlation between grains prevents localized phenomena and many of the DRX-related mechanisms originating at GBs or triple junctions. Therefore, we here introduce a spatially-resolved model for DRX based on a polycrystalline mesoscale RVE.

3.4.1 FMCP model for DRX

The FMCP model for DRX introduced here is an extension of the model presented in Chapter 2 for DRX in Mg, which is why we briefly review that model to the extent necessary for our purposes here. We define a cubic RVE $\Omega = [0, L)^3$ whose homogenized mechanical response is obtained from imposing appropriate boundary conditions. We discretize Ω into a regular grid with N grid points along each side length and spatial increments $\Delta x = L/N$, resulting in a total of N^3 grid points. In favor of a sufficiently high resolution we choose $n = 64$ in subsequent simulations, which – for an initial grain count of 200 – yields an average of ca. 1,311 nodes per grain.

In order to model DRX, we randomly select from within Ω at every time step a total of $n_{\mathrm{MC,GBM}} \ll n$ and $n_{\mathrm{MC,NCL}} \ll n$ grid points as possible sites for GB migration or grain nucleation, respectively. Since the number of MC points per total GB area is to be conserved, we impose a scaling of the type

$$n_{\mathrm{MC},i}(t) = \rho_{\mathrm{MC},i} \times \text{number of nodes on boundary at } t, \quad i \in \{\mathrm{GBM}, \mathrm{NCL}\}, \tag{3.19}$$

where $\rho_{\mathrm{MC,GBM}}$ and $\rho_{\mathrm{MC,NCL}}$ denote the number of MC points for migration and nucleation per total GB area, respectively.[7] Following the selection of MC nodes, we apply the state switch rules defined in Chapter 2: we compute the hypothetical

[7] The conservation of MC points per GB area constitutes a new feature compared to the model we presented in Chapter 2. It becomes essential in capturing the migration behavior during strong grain refinement, which is more pronounced in this contribution compared to the Mg simulations reported there. For nucleation, the differences are marginal, as nodes within the grain were significantly less likely to nucleate compared to those at the GBs. By reducing the number of sampling points on the GBs only, we thus reduce the total number of MC points while conserving the number of sampling points per GB area. This change allows us to decrease the computational time without altering the physics of the simulation.

change in total elastic and inelastic energy for each grid point, assuming that it either nucleated a new, pristine grain with a random orientation or – for MC points on existing GBs – if it underwent GB migration (thus adopting the same orientation and internal state as the grid points on the respective other side of the GB). Responsible for a state switch (*i.e.*, either nucleation or GB migration) is a reduction in energy $\Delta E = \mathit{I}_{\text{after}} - \mathit{I}_{\text{before}}$ where I denotes the total RVE energy before or after the state switch (and its discrete numerical approximation computed over the set of all grid points, Ω_Δ):

$$\mathit{I} = \int_\Omega W \, \mathrm{d}V + \int_\Gamma \gamma_S \, \mathrm{d}S \approx \Delta V \sum_{\boldsymbol{X}_k \in \Omega_\Delta} W(\boldsymbol{X}_k) + \Delta S \sum_{l=1}^{n_\Gamma} \gamma_S. \tag{3.20}$$

For simplicity, we consider a constant, isotropic GB energy γ_S (n_Γ denotes the number of boundary segments), and we assume that the GB migration speed does not depend on misorientation. Since the accumulation of defects causes the instability inherent to grain nucleation and we do not want pure elastic deformation to cause nucleation, we replace W by W^{in} in the above total energy for nucleation only (we note that the elastic strain energy density was found to be at most around 2% of the inelastic strain energy density in our simulations, so that its effect is marginal).

Having identified potential grid points for state switches (grain nucleation or GB migration) and having computed the hypothetical reduction in energy ΔE_k for each such site $\boldsymbol{X}_k \in \Omega_\Delta$ for both cases, we proceed with a statistical approach: we generate a random number $w_k \sim \mathcal{U}([0,1])$ from a uniform distribution, based on which we accept the state switch if $w_k \leq w(\Delta E_k)$ and reject otherwise, where the threshold $w(\Delta E_k)$ decreases monotonously with energy; *i.e.*, a state switch becomes more likely, the higher the resulting reduction in energy. For grain nucleation, we employ the same criterion used for the Taylor model in Section 3.3, thus defining the threshold as

$$w_{\mathrm{NCL}}(\Delta E) = \begin{cases} \Delta t \kappa_{\mathrm{NCL}} \left[1 - \exp\left\{ -\left(\dfrac{\Delta E / \Delta X^3}{C W^{\mathrm{in,cr}}} \right)^d \right\} \right], & \text{if } -\dfrac{\Delta E}{\Delta X^3} > W^{\mathrm{in,cr}} \\ 0, & \text{otherwise.} \end{cases} \tag{3.21}$$

For GB migration we take a different approach for suitable for the continuum length scales at play. We assume a linear relation between migration speed and driving force in the form of the stored energy difference [175], thus defining a threshold

$$w_{\mathrm{GBM}}(\Delta E) = -\frac{\Delta t}{\kappa_{\mathrm{GBM}}} \Delta E, \tag{3.22}$$

with a GB mobility κ_{GBM}. We note that this linear dependence is standard, *e.g.*, in phase-field [155] and vertex [110] models. It is also closely related to the gradient-flow approach in Section 3.4.2, which has the advantage of providing good comparability between the two models. The factors Δt ensures convergence under temporal refinement. This linear relation is an alternative to the kinetics of Glauber [53], which are well established in Monte-Carlo Potts models (see, *e.g.*, Hallberg [60] and the threshold function we used in Chapter 2) based on the inherent exponential form of atomic jump probabilities.

The thresholds defined by (3.21) and (3.22) are used to accept or reject a state switch at every chosen MC grid point. There are now two strategies to employ this FMCP model for DRX, which differ in the way the mechanical boundary value problem on the RVE-level is solved – as described in the following: Section 3.4.2 applies the statistical model for DRX outlined above while violating local mechanical equilibrium and deforming the RVE in an affine manner, following the Taylor assumption of equal strains (FMCP×Taylor). By contrast, Section 3.4.3 applies the above DRX model to a spatially resolved RVE whose mechanical equilibrium is enforced through FFT-based periodic homogenization scheme (FMCP×FFT). The temperature-dependent parameters used for both models are listed in Table 3.2.

3.4.2 FMCP model under the Taylor assumption (FMCP×Taylor)

Motivated by the reduced computational expenses, we first employ the FMCP model for DRX in conjunction with the Taylor assumption of affine RVE deformation (expected to yield Voigt's upper bound on the mechanical RVE response). Besides demonstrating its (in)accuracy, we use this simplified framework to assess the importance of the surface energy contributions in (3.20) especially towards grain nucleation, which is frequently neglected [55, 72, 110]. In a direct comparison, Figure 3.6 demonstrates that the exclusion of surface contributions leads to an overly fast adoption of the steady state compared to experimental results. Including surface contributions naturally elevates GB junctions to preferential nucleation sites and thus recovers the necklace formation characteristic for discontinuous DRX. This behavior, in turn, leads to a more gradual convergence towards the steady stress state, as the new grains must consume the initial grains in a circular, necklace-forming fashion emanating from the GBs. This leads to the improved accuracy observed in Figure 3.6. Deviations from the experimental data (in the discrete l^2-sense) are around 3.6% and 3.2% for 725 K and 775 K, respectively. Necklace-like structures can also appear in approaches excluding surface contributions for nucleation. Most

often, however, this is the result of ad-hoc approaches including the intentional placement of nuclei at high-energy sites (see, *e.g.*, Popova et al. [127]).

The overestimation of nucleation activity can also be observed in Figure 3.7, which compares the recrystallized volume fractions. At 725 K, both simulations with and without surface contributions experience a decrease in the total volume of a recrystallization wave as soon as the next recrystallization wave initiates. Since a further increase of the total volume would only be achievable through migration, the above observation together with the discontinuity in the slope implies a substantial contribution of nucleation as compared to migration. At small strains, this effect is even more pronounced in the case without surface contribution, which – again – stems from the overestimation of nucleation due to the non-preferential treatment of grain boundaries or triple junctions. At larger strains, this difference is mitigated as both cases experience an almost fully recrystallized microstructure, and effects due to repeated necklace formations weaken. The 775 K case shows good agreement with the estimated volume fraction of non-recrystallized material from Blaz et al. [18]. Further, we note the precise (delayed) prediction of the onset of significant DRX with surface contributions as opposed to the case without.

Figure 3.7 also reveals differences from the predicted recrystallized volume fractions in the Taylor model (*c.f.* Figure 3.4). At 725 K, the total volume fraction of the individual recrystallization waves experiences a smoother progression, thus implying a

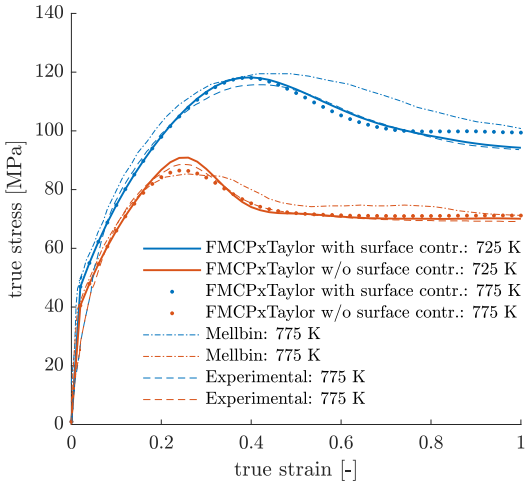

Figure 3.6: Stress evolution captured by the FMCP×Taylor model including (*solid*) and excluding (*dotted*) surface contributions within the energetic grain nucleation criterion. We compare the results to experimental data from Blaz et al. [18] (*dashed*) and numerical results from Mellbin et al. [110] (*dash-dotted*).

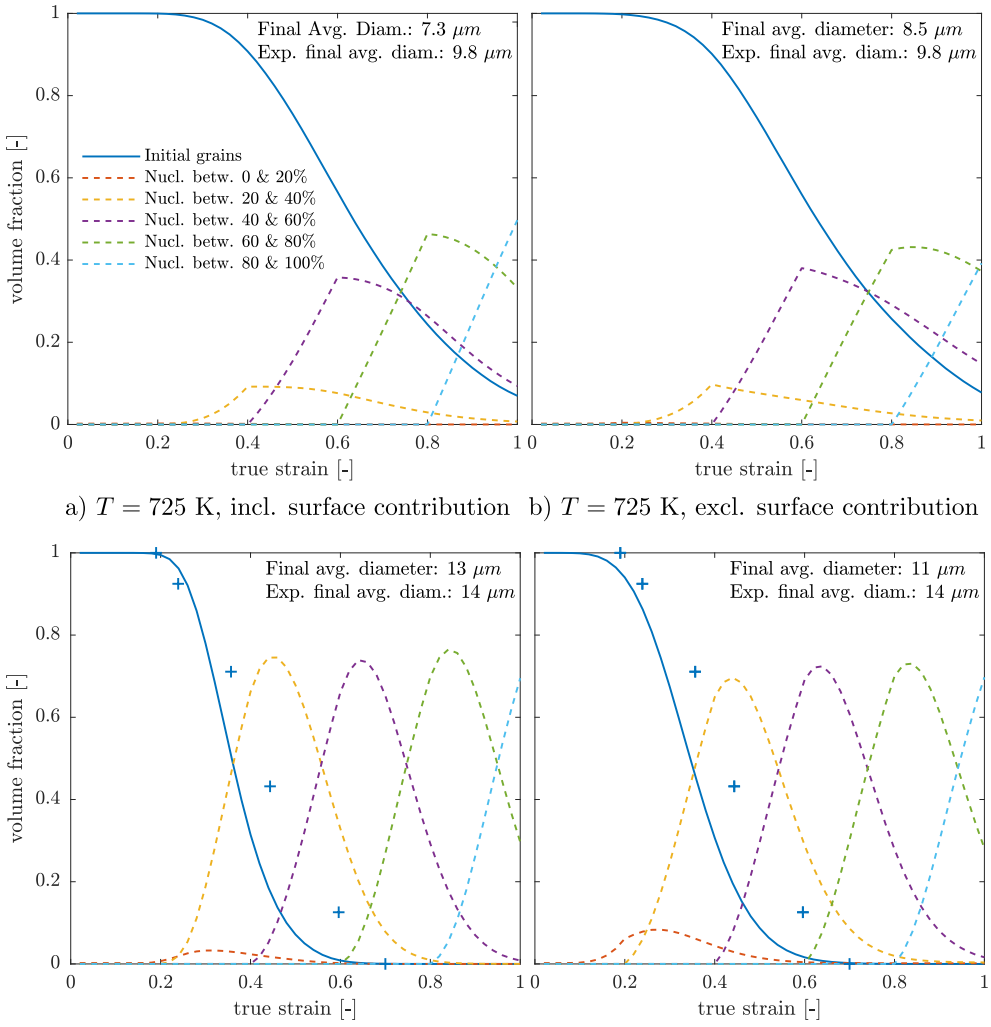

a) $T = 725$ K, incl. surface contribution b) $T = 725$ K, excl. surface contribution

c) $T = 775$ K, incl. surface contribution d) $T = 775$ K, excl. surface contribution

Figure 3.7: Volume fraction evolution of recrystallization waves defined in 20 % true strain intervals for $T \in \{725\,\mathrm{K}, 775\,\mathrm{K}\}$ including and excluding surface contributions to the energetic nucleation criterion in the FMCP×Taylor model. Crosses correspond to the estimated data from the experimental microstructure evolution at 775 K reported by Blaz et al. [18]. Also reported in the diagrams are predicted average grain diameters based on average grain volume fractions and the total volume V_0 we have introduced before.

more significant role of migration. The reason lies in the introduction of the notion of space: while the FMCP model experiences circular necklace layers of new grains, leading to an impediment of migration of earlier recrystallization waves, the Taylor model sees interactions between all of its grains exclusively based on their respective energy states, as schematically shown in Figure 3.8. Although the values for parameter C in the Taylor model served as a good initial guess for the FMCP×Taylor model, the absence of interaction between grains partially explains the difference

in the optimal C found for these two models (*c.f.* Table 3.2). At 775 K, however, differences in the predicted recrystallized volumes are weaker, as the importance of the necklace effect decreases and the role of migration increases. Owing to the similarities in the energetic description of both Taylor and FMCP×Taylor approaches concerning migration (*c.f.* (3.15) and (3.22)) and nucleation (*c.f.* (3.16) and (3.21)), the efficient reduced-order Taylor model predicts a comparable DRX evolution as the FMCP×Taylor model at this temperature level.

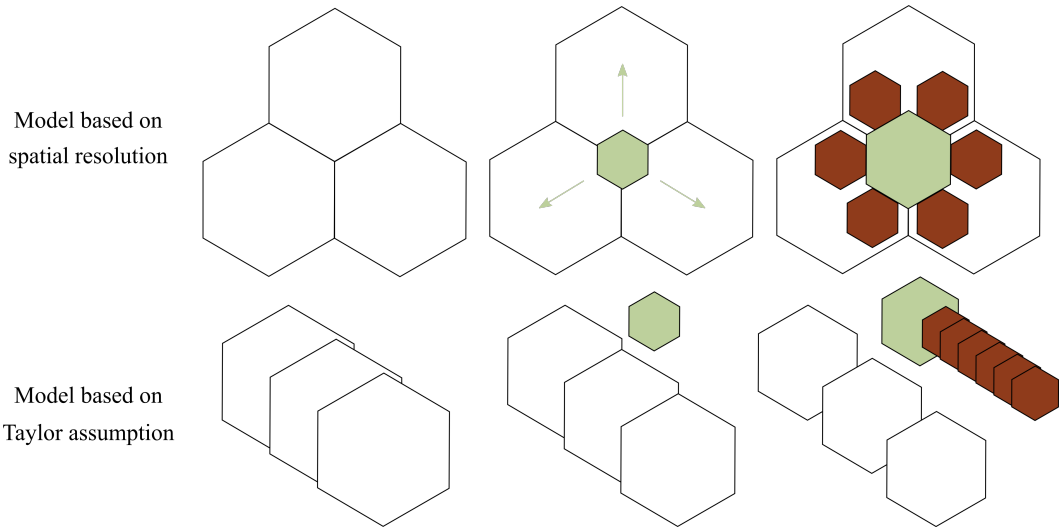

Figure 3.8: Illustration of the difference in migration behavior due to necklace formation as obtained from the FMCP models and the Taylor model. Once a nucleated grain (green) is surrounded by newly nucleated grains (red), that grain experiences an impediment to GB migration despite a possibly lower energy state compared to the original grains (white). On the contrary, in the Taylor model (*c.f.* Section 3.2) a nucleated grain will grow as long as its energy density is lower than the unweighted average energy density (see (3.15)) without any constraint from neighboring grains.

Table 3.2: Further parameters used for the Taylor, the FMCP models (both FMCP×Taylor and FMCP×FFT).

			Taylor			FMCP	
Parameter	**Sym.**	**Unit**	**725 K**	**775 K**	**875 K**	**725 K**	**775 K**
GBM rate	κ_{GBM}	GPa·s	680	204	23.5	5.0	0.42
NCL rate	κ_{NCL}	s^{-1}	61.8	57.4	54.4	110	50
NCL parameter	C	-	13.4	10.9	8.00	12	8.5
MCP density NCL	$\rho_{\mathrm{MC,NCL}}$	10^{-4}		N.A.		1.6	1.6
MCP density GBM	$\rho_{\mathrm{MC,GBM}}$	10^{-3}				1.2	1.2

3.4.3 FMCP under full field simulation (FMCP×FFT)

The above assumption of affine deformations across the polycrystalline RVE does, in general, not satisfy equilibrium (see, *e.g.*, Khadyko et al. [83] or Shanthraj et al. [148]). Therefore, to capture heterogeneity in the deformation, including shear bands and stress localizations at GBs, we relax the assumption of affine deformations and instead solve for mechanical equilibrium inside the RVE while imposing periodic boundary conditions. The latter is done through a finite-strain FFT-based solver, thus resulting in our FMCP×FFT model. The FFT scheme solves the mechanical equations of quasistatic equilibrium in a computationally efficient manner (see, *e.g.*, Moulinec and Suquet [116], Lebensohn and Needleman [95], and Vidyasagar et al. [177]), exploiting the same regular grid required for our FMCP model of DRX. Following the theory outlined in Chapter 2, we employ a discrete finite-difference approximation of the Fourier transform $\mathcal{F}$ of a function $f(\boldsymbol{x})$ with wave vectors $\boldsymbol{k}$ and grid spacing Δx according to

$$\mathcal{F}\left(\frac{\partial f}{\partial x_i}\right) = -2\pi i k_i \mathcal{F}(f) \approx -\frac{i \sin(2\pi k_i \Delta x)}{\Delta x}\mathcal{F}(f), \tag{3.23}$$

with the purpose of mitigating ringing artifacts associated with the Gibbs phenomenon (a problem that is signifcant at the strain levels considered in this study. The use of this improved FFT-based solver allows reaching high strain levels. To illustrate the severe deformation and the various deformation mechanisms at play, Figure 3.9 visualizes the deformed RVE at different strain levels up to 100% true compressive strain; the shown simulations are for ten grains only (showing severely heterogeneous deformation stemming from the grain orientations), for 200 grains (showing a more homogeneous average deformation across the RVE), and for 200 grains with the FMCP-DRX model (showing an even more homogeneous deformation due to the large strain-accommodating effects of DRX). Case c) with DRX also instructively illustrates the nucleation of grains in regions of high stress concentrations near GBs and the typical necklace formation (see, *e.g.*, $\varepsilon_{\text{true}} = -0.4$ in Figure 3.9c). Based on these results, we deem an initial number of 200 grains sufficient for subsequent simulations.

Figures 3.10a and 3.10b reflect the average stress evolution as obtained from 20 independent simulations using the FMCP×FFT model without DRX. As expected, the Taylor model provides an upper bound, while the FFT-based solver converges from below with increasing numbers of grains. The apparent differences between the mean stresses computed from both Taylor and FMCP×Taylor models for 200 grains are sufficiently small to retain the same material parameters for the Cu

constitutive model, while using the three parameters for the FMCP model of DRX from Section 3.4.2. Figure 3.10c demonstrates the evolution of the homogenized stress over time with DRX. We overall observe convincing agreement, although the total deviations increased to 4.4% and 4.0% as compared to 3.6% and 3.2% for FMCP×Taylor [8].

[8]We note that a renewed fitting of the plasticity or DRX model parameters could lead to a better match. However, since the precision of the measurements reported in Blaz et al. [18] is unclear and because the primary focus of this paper is not on parameter fitting but on describing DRX with varying levels of model fidelity, we choose to retain the parameters obtained from calibration in Section 3.4.2

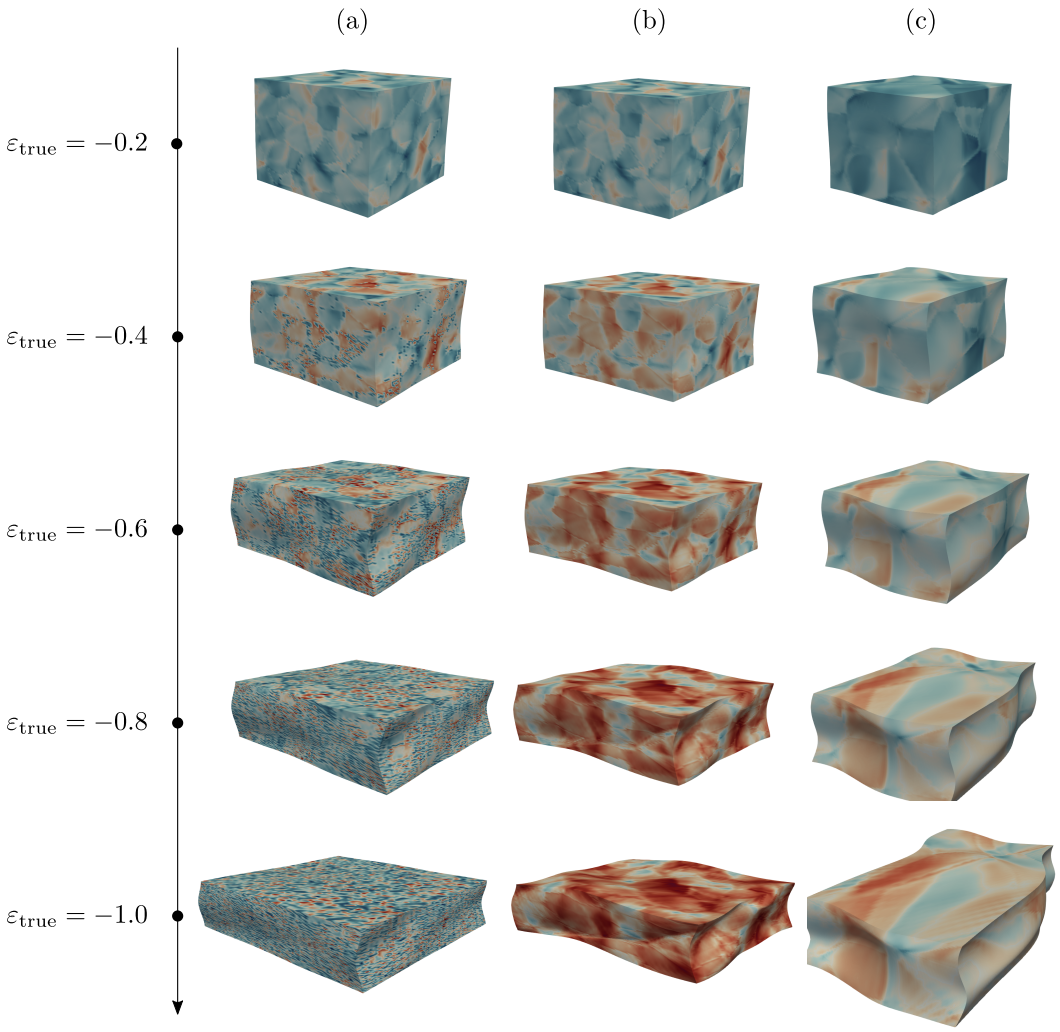

Figure 3.9: Evolution of the σ_{33} distribution over the deformed RVE across five true strain levels for a) 10 grains, b) 200 grains as well as c) 200 grains including recrystallization. We amplifiy local deviations from the affine deformation by a factor of 100 for visualization purposes.

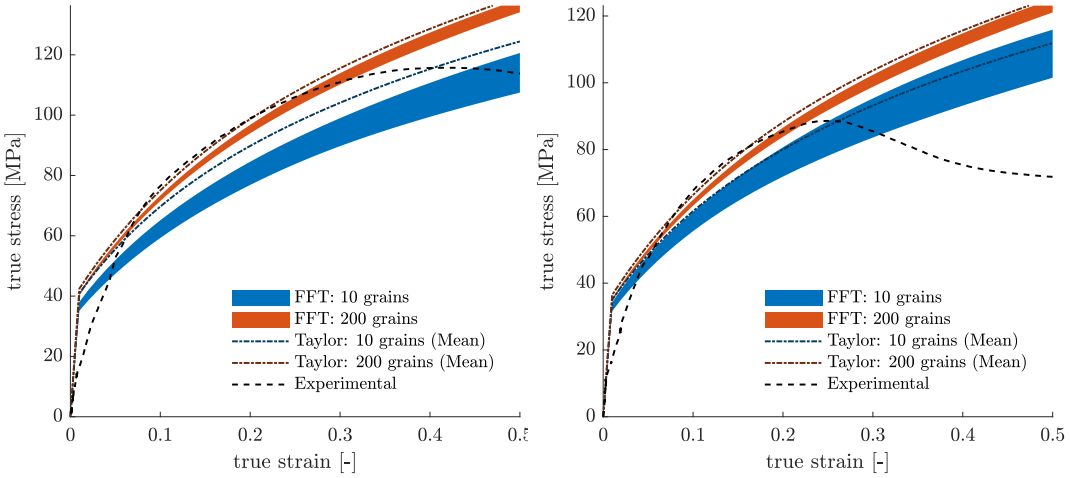

(a) Comparison of FFT and Taylor models (excluding DRX) to experiments at $T = 725$ K.

(b) Comparison of FFT and Taylor models (excluding DRX) to experiments at $T = 775$ K.

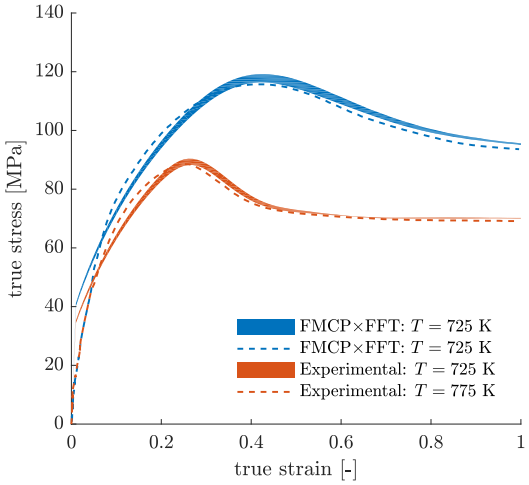

(c) Results from the FMCP×Taylor model including DRX vs. experiments.

Figure 3.10: Mean stress evolution from 20 RVE realizations of the FMCP×FFT model (*solid*) compared to experimental data from Blaz et al. [18] (*dashed*). Conducted with the original values for Q and G_0 from Table 3.1 both without DRX at a) 725 K and b) 775 K (in order to stress the over-approximation of stresses when using the Taylor assumption) and c) with DRX (to elucidate the differences to the results obtained in Figure 3.6).

Figure 3.11 summarizes the evolving $\langle 111 \rangle$ pole family (obtained using MTEX [66]). Since grains display heterogeneous orientation distributions in the FMCP×FFT model, we do not show a discrete pole figure (as for the Taylor model in Figure 3.5) but instead use orientation distribution functions [66]. The graphics still expose a

strong texture at both temperature levels (at lower temperature even more pronounced than in the Taylor model). While all our models endow recrystallized nuclei with random orientations, it is the new grains in the FMCP×FFT model that are influenced by the stress state of their neighbors. This interaction in turn leads to a correlation between the orientation of the already recrystallized grains and the new grains, thus explaining the more pronounced texture in the FMCP×FFT model.

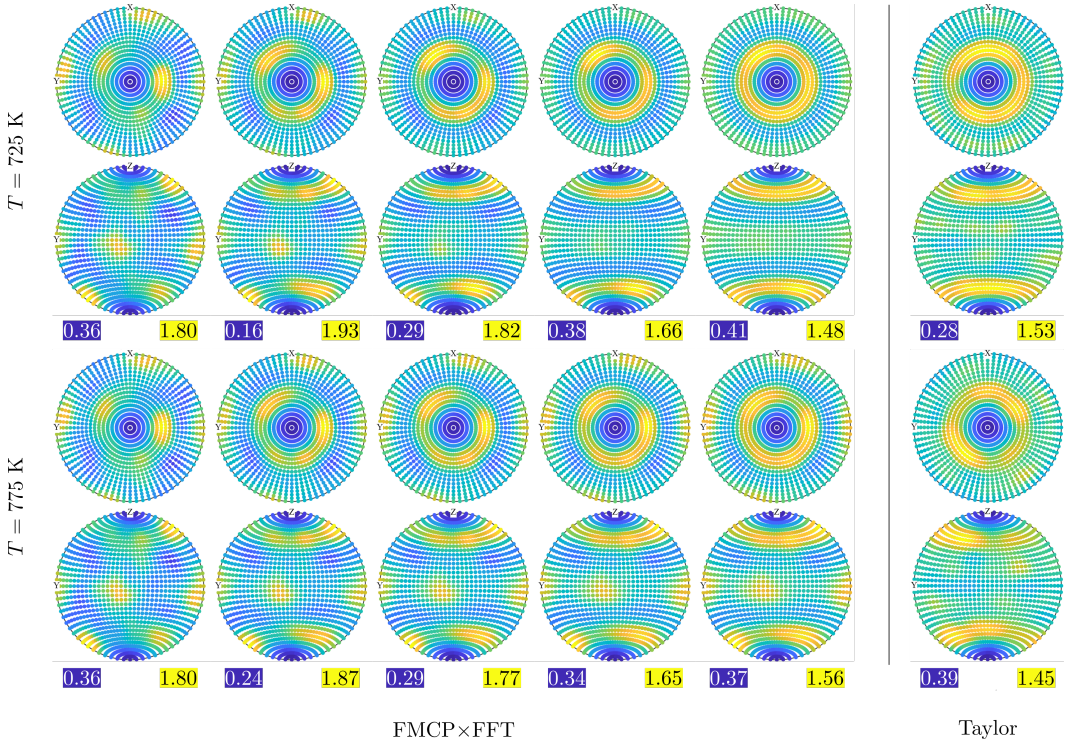

Figure 3.11: Pole figure of the ⟨111⟩-pole family for 725 K (*top*) and 775 K (*bottom*), illustrated using a *de la Vallée Poussin* orientation distribution function). We display the pole data from FMCP×FFT simulations at five different levels of true compressive strain, viz. $\varepsilon_{\text{true}} \in \{-0.2, -0.4, -0.6, -0.8, -1.0\}$, and complement them by the corresponding pole data for the Taylor model at $\epsilon_{\text{true}} = -1.0$ for comparison. The shown intensities (with blue and yellow values corresponding, respectively, to the minimum and maximum intensities) were obtained by weighting the orientation associated with (i) each grid point by $1/n$ in the FMCP model and (ii) each grain by its volume fraction in the Taylor model.

We close by pointing out, although all three models presented here for DRX in Cu focus on modeling discontinuous DRX through the nucleation and growth of grains (which is the prevalent means of DRX for metals with low stacking fault energy), the spatially resolved FMCP×FFT model also has capabilities to capture continuous DRX through the formation of subgrains. Figure 3.12 illustrates such an example, where a large, initially uniform grain through the course of severe

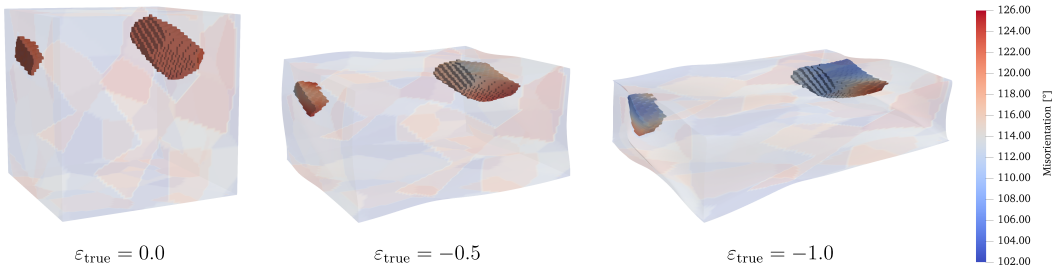

Figure 3.12: Tracking the misorientation of the [111] poles with the compression axis within a large grain inside the RVE (shown as two bodies due to the periodic boundary conditions) reveals the formation of two subgrains within the grain. The colors of the transparent grains do not refer to the misorientation – they solely represent different grains.

compression breaks up into regions of approximately constant albeit distinct local orientations. While the undeformed grain exhibits a uniform misorientation of the [111] pole with the compression axis, the orientation takes two different paths in the two subgrains whose final misorientation, at 100% true compressive strain, differs by approximately 23°. The latter may be interpreted as a high-angle GB. Such subgrain formation is indeed feasible within the FMCP×FFP model given sufficient spatial resolution to capture the underlying processes within grains.

3.5 Discussion

Both the Taylor and FMCP models in this contribution were calibrated based on stress-strain curves, as these commonly constitute the sole available and reliable source of continuous data for recrystallization processes (rather than pre- and post-treatment data only). With deviations of 2 to 5% relative to the experimental stress data recorded at 725 K and 775 K, all three models were able to find a good agreement despite the low number of model parameters to fit, especially considering the approximation of an inherently atomistic phenomenon on the continuum scale. Being not a part of the parameter identification process, the available experimental data on the average grain size after compression was used to validate the microstructure predicted by the FMCP model. The models further accurately capture the convergence towards a steady stress state and the stress level at steady state, as well as the final average grain size (except for the Taylor model at 725 K). Specific observations like the formation of necklace structures prior to full recrystallization – as captured by the FMCP schemes – are further observations made both experimentally (see, *e.g.*, Ponge and Gottstein [126], Sakai et al. [144]) and numerically (see, *e.g.*, Hallberg [60], Mellbin et al. [110]). Experimental data on the estimated volume fraction

of non-recrystallized material at 775 K are also well captured by the models, apart from an offset of the initiation of visible recrystallization. At 775 K, the volume fraction evolutions obtained from both the Taylor and FMCP×Taylor models show compelling agreement. This increased similarity of the predicted volume fractions is understood since the role of GB migration at 775 K is more pronounced than at 725 K. The more dominant role of GB migration is related to lower hardening moduli as well as lower initial slip resistance than at 725 K, which, in turn, accelerates the accumulation of inelastic strain energy density at 775 K. Rising differences in the inelastic energy between two grains relative to the effect of surface tension further alleviate the disparities of the Taylor model and the spatially resolved FMCP models.

As is apparent from Table 3.3, the Taylor model is significantly less expensive computationally. A reduction of the wall time by a factor of 160 and 280 compared to the two FMCP models (with and without Taylor assumption for the RVE deformation, respectively) adds to the conclusion that the reduced-order Taylor model can be a viable alternative for expensive high-fidelity models when interested in the evolving microstructure and the homogenized stress-strain behavior. However, Sections 3.3 and 3.4 also showed that the Taylor model does deviate from experimental findings, especially if the spatial distribution on the RVE-level matters; *e.g.*, at 725 K, where necklace formation of nuclei at GBs dominates DRX, the Taylor model fails to replicate such radially propagating recrystallization fronts. This shortcoming stems from the local grain interactions (see Figure 3.8 and Section 3.4.2) as well as from the stabilizing effect of surface tension, both of which are not captured by the Taylor model.

Although the resulting texture is generally well replicated by both Taylor and FMCP models, the fully resolved model predicts a slightly more pronounced texture at lower temperature while, again, at higher temperature these differences tend to vanish. The observation that both models qualitatively capture the texture formation is remarkable as newly nucleated grains are endowed with a random orientation and a shorter life cycle compared to the initial grains but still manage to reorient to yield a strong texture.

We also emphasize our strategy of identifying model parameters in a computationally efficient manner. More than a feasible alternative to higher fidelity models, the Taylor model provided an excellent, informed initial guess for fitting the material parameters of the FMCP×Taylor model (as compared to, *e.g.*, Mellbin et al. [110]

	Taylor	FMCP×Taylor	FMCP×FFT
simulation time	6 min	16 h	28 h

Table 3.3: Difference in computational expenses for one simulation at 725 K, using 24 physical cores and description of the flow for the reduced-order based parameter fitting.

who used a considerably more expensive vertex-model for fitting their temperature-dependent parameters G_0 and Q). Owing to the same functional form of the nucleation criterion, the grain nucleation constant C found for the Taylor model further helped us find the analogous parameter for the FMCP model. This left κ_{GBM} and κ_{NCL} as the only fitting parameters of the FMCP model for DRX (used with both the FMCP×Taylor and FMCP×FFT models).

Despite marginal differences in the homogenized stress-strain response between the FMCP×Taylor and FMCP×FFT models, the former fails at capturing various mesoscale deformation mechanisms such as the aforementioned necklace formation. Importantly, we demonstrated that the FMCP×FFT model under severe plastic deformation displays the formation of subgrains and high-angle GBs, which is impossible for both Taylor and FMCP×Taylor models. Although we assumed discontinuous DRX to be the dominant mechanism, our model also proved itself as a promising candidate for future studies on metals with moderate to high stacking fault energies, where the simultaneous occurrence of continuous and discontinuous DRX is observed. Blaz et al. [18] analyzed the importance of heterogeneous effects such as subgrain growth and deformation bands, resulting in mechanical instabilities and their associated flow softening effects, further acting as additional nucleation sites – a phenomenon that can also occur during the necklace-like consumption of a grain as described by Ponge and Gottstein [126]. This behavior, however, is more pronounced for large initial grain sizes above 100 μm [18], which is almost 30% above the average grain size analyzed here. In principle, continuous DRX can also be included in the inexpensive Taylor model, however, this is challenging due to the required assumptions describing the breaking up of grains into subgrains. Here, insight gained from the higher-fidelty FMCP models can be essential. Similar in spirit, Cram et al. [30] introduced the phenomenological notion of a subgrain size fraction.

3.6 Conclusions

We have shown how the effects of DRX during quasistatic hot compression of Cu can be described by three models of varying levels of computational efficiency and accuracy. Starting with a temperature-dependent, finite-strain crystal plasticity model for Cu, we introduced three distinct avenues to model DRX: a most efficient Taylor model, the FMCP×Taylor model (with an expensive description of DRX but still inexpensive affine grain deformations), and the FMCP×FFT model (with expensive but accurate full-field resolution of both DRX and intra-grain deformation mechanisms). Once calibrated, predictions from all three models showed convincing agreement with experimental data, both considering the effective stress-strain response and the microstructure evolution. We specifically evaluated the homogenized stress-strain behavior up to 100% true compressive strain along with the resulting grain size reduction, the resulting texture (starting from initially random grain orientations), and the volume fraction of recrystallized material. To calibrate the models, we first identified the parameters of the single-crystal Cu model by fitting stress-strain data at low strains (below the onset of significant recrystallization). Next, we found the three DRX parameters in the models (viz., κ_{GBM}, κ_{NCL}, and C) by fitting the full available stress-strain data. Not a surprise, the fully resolved FMCP×FFT model provided highest accuracy (*i.e.*, best agreement of stress-strain data, of grain size reduction and recrystallized volume fraction), the lower-fidelty Taylor model and the rather expensive FMCP×Taylor model as a compromise between the former two revealed their merits. First, the Taylor model captured all salient features and, especially at 775 K, provided good quantitative agreement at a small fraction of the computation time (*c.f.* Table 3.3). Second, the Taylor model provided a convenient means to identify model parameters: rather than carrying out expensive fitting simulation feedback loops with the high-fidelity model, the inexpensive Taylor model served to identify good initial guesses through a least-square fit; those initial guesses helped narrow down the high-fidelty model parameters quickly and inexpensively. Surely, high-fidelity multiscale models are promising candidates for predictive, bottom-up approaches to simulating DRX during severe plastic deformation in metals. Yet, their computational expenses severely limit their applicability and, as our study demonstrates, many salient features – from the microstructural evolution to the macroscale mechanical response – may be obtained sufficiently accurately from inexpensive Taylor-type models (and we further point out the beneficial feedback loops between the three models presented here which may serve to calibrate and validate each model).

Chapter 4

MODELING THERMO-MECHANICAL PROCESSES INVOLVING DYNAMIC RECRYSTALLIZATION – APPLICATION TO ECAE

A.D. Tutcuoglu, S. Kumar, Y. Hollenweger, and D.M. Kochmann. A multiscale meshfree approach to modeling ECAE. *In Preparation*, 2019.

Preamble

The work presented in this chapter is the result of a collaboration between the author (A.T.) and S. Kumar (S.K.). While S.K. provided the numerical implementation on the macroscale, A.T. established the numerical framework on the micro- and mesoscale. S.K and A.T. conducted simulations for different scenarios.

4.1 Introduction

In previous chapters, we concerned ourselves with the numerical modeling of dynamic recrystallization on the micro- and mesoscale. We introduced a novel high-fidelity model in the form of the Field-Monte-Carlo Potts method which allows capturing dynamic recrystallization in hcp metals such as Mg in a qualitative manner. Experimental data on Cu was used to validate the model. We further introduced the computationally inexpensive Taylor model to investigate the influence of the notion of space and linear momentum conservation in the modeling of dynamic recrystallization. We used the experimental data on Cu to conduct meaningful comparative analyses with the higher fidelity model and found, that – under specific processing conditions – the Taylor model readily replicates the microstructural evolution as well as the progression of homogenized measures such as the average true compressive stress. The availability of a scheme that provides sufficient accuracy on the micro- and mesoscale and at the same time ensures computational feasibility allows extending the analysis to the macroscale.

In Chapter 1, we introduced severe plastic deformation techniques as a means to achieve the inelastic deformation needed for nucleation, which can ultimately lead to grain refinement and the associated increase in yield strength [59, 124]. One of the central constraints of these methods lies in the size of workable samples. High-pressure torsion belongs to the most studied severe plastic deformation tech-

niques since it yields meaningful data on the internal stress state and readily provides efficient grain refinement [40]. The maximum size of the samples it can treat, however, is heavily constrained, which compromises its use for large scale industrial purposes. Equal channel angular extrusion (ECAE) mitigates this issue and further affords a wide range of advantages compared to other thermo-mechanical processes. The principles of ECAE lie in the shear deformation induced at the corner of the channel. Shear deformation promotes inelastic deformation and, therefore, allows to achieve ultra-fine grain refinement, *i.e.*, a final grain size on the submicron scale [73]. The primary advantages in this treatment of metals lie in the conservation of the cross-sectional area, while simultaneously avoiding degradation through porosity [73]. Although the apparatus is comparatively simple, repeated extrusions allow for the treatment of different crystal structures [174]. A single extrusion can preferentially activate specific slip systems based on the orientation of the processed sample and the extrusion direction. Subsequent rotation of the sample between two extrusions can shift this preferential treatment onto other slip planes. We distinguish between four different types of rotations – commonly referred to as routes – including route A (no turning), B_A (alternatively turning by 90° in clockwise/anti-clockwise orientation), B_C (steadily turning by 90° in either clockwise or anti-clockwise orientation), and C (turn by 180°) [200]. Depending on the metal's crystal structure and the route, the activation of a high number of slip systems is possible. Along with an efficient increase in inelastic deformation and the associated efficient grain refinement, the rotations between passes provide a high level of isotropy and homogeneity in the sample, both desirable properties in the procfessing of metals.

Despite the relatively simple apparatus, the combination of processing parameters alongside possibly expensive samples raises the need for a numerical framework that allows for the tailoring of ECAE processes. Factors of central interest in this optimization process include microstructural properties such as the texture or the average grain size. On the macroscale, we concern ourselves with the strain homogeneity across the sample, as well as the evolution of the plunger force. Previous attempts to model ECAE, therefore, cover a broad spectrum of fidelity. In the work of Iwahashi et al. [73], the authors constrained their analysis to the macroscale and derived an analytical form for the strain induced through various passes. They assumed negligible effects due to friction and generalized their analysis to cases with variable die channel and outer corner angles. Sivakumar and Ortiz [150] used a material point approach to address microstructural evolution in the sense of sequential lamination for the treatment of aluminum and copper under

ECAE, which allowed them to obtain qualitative agreement with experimental data in terms of texture and lamellar size. Their approach is useful for low temperatures, at which the formation of (shear-)laminates dominates the grain refinement process; however, it does not account for conditions under which grains nucleate through discontinuous dynamic recrystallization. Higher fidelity approaches that extended the analysis from a material point level to a full spatial resolution of the macroscale primarily relied on the finite element method (FEM). Among the first attempts stands the work of Luis et al. [103], who analyzed the impact of friction and inner die channel angle. Their approach was, however, based on a purely elastic material model as well as plane strain conditions. Apart from ECAE, they also analyzed equal channel angular drawing (ECAD), which differs from ECAE in terms of the boundary conditions: while ECAE generally refers to the pushing of a sample (i.e. free surface conditions at the billet's end), ECAD describes the drawing of the sample through the channel (*i.e.*, displacement conditions at the billet's end). Fu et al. [47] alleviated the constraint to a exclusively elastic model. They modeled three different combinations of outer and inner channel angles and qualitatively compared their results to experimental observations. Although they provided a thorough description of the friction model, they were unclear as to which plastic model they use. [4] attempted to reproduce experimental results, where – again – a power law defines the material point level, with the objective of approximating the plastic behavior of pure aluminum. They reported a good agreement based on the values for the force exerted. However, since they do not specify how they obtained parameters including the plastic exponent for the power law, it remains unclear whether this agreement follows from the model accurately representing the underlying physics or if parameters were merely fitted.

Multiscale simulation of ECAE also presents its challenges at the macroscale due to the large distortion inherent to ECAE. Mesh-based modeling such as FEM [4, 33] requires remeshing due to ill-deformed or entangled elements as the mesh deforms around the corner. The application of remeshing, however, assumes interpolation laws regarding the data at the quadrature points to map material point descriptions – including information of all grains at each material point – from the old to the new mesh. While simple plasticity laws based on the additive decomposition of elastic and inelastic strains in a small strain framework can provide acceptable conditions, crystal plasticity frameworks in finite deformations with a multiplicative decomposition of the deformation gradient represent a more challenging environment.

Meshfree methods have recently gained attention as an alternative to FEM with the aim of circumventing the issue associated with large distortions. The primary idea behind meshfree methods consists of the abandoning of a mesh from classic FEM and to represent geometries via discrete mass points. Thanks to the local interpolation based on mass points, it is possible to replicate the continuous field without experiencing the deteriorating effects of distorting elements. In the context of ECAE, Fagan et al. [41] provided an analysis of ECAE using SPH. Using a small-strain framework, they applied a simple linear hardening law without accounting for microstructural evolution effects through recrystallization. They compared their results based on plane-strain conditions with those from classic FEM and found good agreement with deviations possibly stemming from the distortion-based inaccuracies in the FEM model we mentioned earlier. Ma and Hartmaier [104] afforded a more in-depth discussion. Aiming to capture anisotropic effects inherent to the face center cubic (fcc) crystallographic structure, they were among the first to track the (in)elastic deformation of copper using a crystal plasticity model instead of a linear hardening model or an even simpler power law stress-strain relationship. Using smooth particle hydrodynamics, they were able to identify the rotation of crystals in specific regions of the working sample. These grains were on the same length scale as the working sample, which constitutes an interesting scenario from an academic perspective. From an industrial standpoint, however, there is little interest as the texture evolution of a group of grains at individual points of the working sample cannot be identified, consequently resulting in a lack of information on the local texture evolution. They further conducted simulations in a dynamic framework, which is a debatable assumption given the pronounced quasistatic nature of ECAE.

Although the main purpose of ECAE is the efficient refinement of grains, only a few models capture the evolution of the microstructure due to dynamic recrystallization. Saitoh and Ohnishi [142] as well as Hallberg et al. [63] incorporate grain refinement in their constitutive model. Their approaches, however, do not include the notion of individual grains, which is necessary to capture texture evolution and the impact of nucleation and migration on the homogenized stress state. The challenge in providing the means of modeling this multiscale problem lies in the computational expense of currently established mesoscale recrystallization models, including cellular automata, Monte-Carlo Potts and vertex methods. Using the Taylor model from Chapter 3, we can accurately model the microstructural evolution, the texture evolution as well as the homogenized stress response at significantly reduced computational costs for sufficiently high temperatures. In this chapter, we adopt a vertical

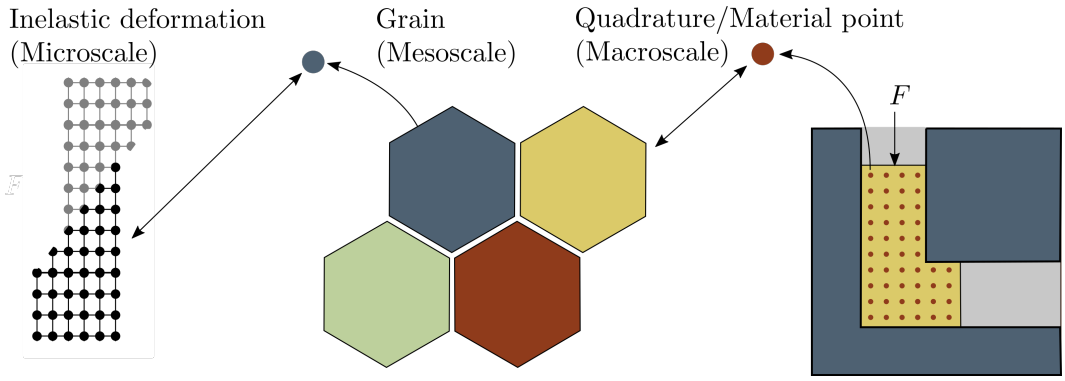

Figure 4.1: Illustration of the vertical homogenization framework coupling max-ent at the macroscale with the Taylor model at the mesoscale and a crystal plasticity model on the subgranular microscale.

homogenization approach, in which we use the maximum-entropy (max-ent) based meshfree method introduced by Kumar et al. [91] that affords enhanced stability and a quasistatic updated-Lagrangian framework at the macroscale, coupled to the Taylor model from Chapter 3 at the mesoscale as Figure 4.1 illustrates. To our best knowledge, this constitutes the first multiscale simulation of ECAE in which every grain at the mesoscale is endowed with an individual set of elastic and inelastic states. In line with the large deformations inherent to ECAE, we adopt a finite deformation framework and use quasistatic conditions to accurately replicate the processing conditions.

The structure of the rest of the contribution is follows: In Section 4.2, we briefly introduce the theory behind the maximum-entropy meshfree method. This method constitutes the macroscale model in our simulation and we emphasize the communication with the meso- and microscale represented by, respectively, the Taylor model and the Cu model, presented in Chapter 3. In Section 4.3, we address numerical challenges including the numerical time-integration, the treatment of boundary conditions as well as the mesh-generation. Section 4.4 addresses the results using this multiscale approach to model the processing of pure Cu through ECAE. A convergence analysis in Section 4.4.1 justifies the temporal resolution used throughout all subsequent simulations. In Section 4.4.2, we investigate the strain heterogeneity in the sample as this constitutes one of the major shortcomings of ECAE compared to, *e.g.*, high-pressure torsion. We benefit from the notion of individual grains at the mesoscale and analyze the texture evolution due to reorientation of grains in Section 4.4.3. As one of the central elements of thermo-mechanical processing, we investigate grain refinement in Section 4.4.4 and further address the impact of

recrystallization on the texture evolution in Section 4.4.6. Next, we influence the impact of recrystallization on the plunger force and homogenized energy evolution in Section 4.4.5. Section 4.4.7 introduces the notion of a multipass as an idealization of a repeated extrusion of the billet with particular attention to the texture evolution after the second pass. Finally, Section 4.5 concludes with a comment on our contribution as well as on previous and future works.

4.2 Max-ent and updated-Lagrangian

In Section 4.1, we addressed the shortcomings of the finite element method in the framework of large deformations and proposed to employ a meshfree method to mitigate issues associated with severely distorted elements. To this end, the enhanced max-ent meshfree approximation scheme and the stable updated-Lagrangian formulation introduced by Kumar et al. [91] promise the best fit for simulating the quasistatic boundary value problem associated with ECAE. In this section, we give a brief overview over the structure of this scheme, how it overcomes the issues related to finite elements, and how it circumvents limitations commonly faced in meshfree simulations [1].

We introduce a macroscale domain $\Omega \subset \mathbb{R}^3$. In close analogy to the discretization of a finite element mesh into elements, we perform a discretization into a set $\mathcal{X} = \{\boldsymbol{x}^a \in \mathbb{R}^3,\ a = 1,\dots,n_n\}$ of n_n distinct nodes. We introduce a set of linearly independent shape functions $\mathcal{N} = \{N^a : \Omega \to \mathbb{R},\ a = 1,\dots,n_n\}$ subject to the following constraints

$$N^a(\boldsymbol{x}) \geq 0, \quad \sum_{a=1}^{n_n} N^a(\boldsymbol{x}) = 1, \quad \sum_{a=1}^{n_n} N^a(\boldsymbol{x})\boldsymbol{x}^a = \boldsymbol{x}, \quad \forall \boldsymbol{x} \in \Omega. \tag{4.1}$$

These constraints allow the interpretation of shape functions in a probabilistic/information-theoretic fashion, ensure consistency under h-refinement, and provide exact interpolation of affine functions. We approximate the continuous displacement field $\boldsymbol{u} : \Omega \to \mathbb{R}$ using a set of nodal displacements $\{\boldsymbol{u}^a \in \mathbb{R}^3,\ a = 1,\dots,n_n\}$:

$$\boldsymbol{u}^h(\boldsymbol{x}) = \sum_{a=1}^{n_n} \boldsymbol{u}^a N^a(\boldsymbol{x}), \quad \boldsymbol{x} \in \Omega. \tag{4.2}$$

We introduce a measure of non-locality or width as $\mathcal{U} = \mathcal{U}[\mathcal{N}, \boldsymbol{\beta}]$ deriving from

[1] Since meshfree methods are not the focus of this thesis, we direct the interested reader to Kumar et al. [91] for detailed derivations, algorithms, and references.

the choice of shape functions $\mathcal{N}$ via

$$\begin{aligned} U[\mathcal{N}, \boldsymbol{\beta}] &= \int_\Omega \sum_{a=1}^{n_n} N^a(\boldsymbol{x}) \, \|\boldsymbol{x} - \boldsymbol{x}^a\|_{\boldsymbol{\beta}}^2 \, \mathrm{d}V \\ &= \int_\Omega \sum_{a=1}^{n_n} N^a(\boldsymbol{x}) (\boldsymbol{x} - \boldsymbol{x}^a)^T \boldsymbol{\beta} (\boldsymbol{x} - \boldsymbol{x}^a) \, \mathrm{d}V, \end{aligned} \tag{4.3}$$

where the locality parameter tensor $\boldsymbol{\beta} \in \mathbb{R}^{d \times d}$ is positive-definite. As a measure of the interference bias, we further introduce the information entropy via

$$H[\mathcal{N}] = -\int_\Omega \sum_{a=1}^{n_n} N^a(\boldsymbol{x}) \ln N^a(\boldsymbol{x}) \, \mathrm{d}V. \tag{4.4}$$

Optimally, we aim for a compromise between the two, which we formalize through a Pareto optimality condition of the form

$$\mathcal{N}_\beta = \arg\min_{\mathcal{N}} \left(U[\mathcal{N}, \boldsymbol{\beta}] - H[\mathcal{N}] \right) \quad \text{s.t., (4.1)}, \tag{4.5}$$

which admits a pointwise unique solution

$$N^a(\boldsymbol{x}) = \frac{1}{Z(\boldsymbol{x}, \boldsymbol{\lambda}^*(\boldsymbol{x}))} \exp\left[-\|\boldsymbol{x} - \boldsymbol{x}^a\|_{\boldsymbol{\beta}}^2 + \boldsymbol{\lambda}^*(\boldsymbol{x}), \bullet \, (\boldsymbol{x} - \boldsymbol{x}^a) \right], \; a = 1, \ldots, n_n, \tag{4.6}$$

where

$$Z(\boldsymbol{x}, \boldsymbol{\lambda}) = \sum_{a=1}^{n_n} \exp\left[-\|\boldsymbol{x} - \boldsymbol{x}^a\|_{\boldsymbol{\beta}}^2 + \boldsymbol{\lambda}^* \bullet (\boldsymbol{x} - \boldsymbol{x}^a) \right], \tag{4.7}$$

and $\boldsymbol{\lambda}^*$ denotes the minimizer of the information entropy $\ln Z(\boldsymbol{x}, \boldsymbol{\lambda})$. Using (4.6), we can compute the strain via

$$(\nabla \boldsymbol{u})^h(\boldsymbol{x}) = \sum_{a=1}^{n_n} \boldsymbol{u}^a \nabla N^a(\boldsymbol{x}), \quad \boldsymbol{x} \in \Omega, \tag{4.8}$$

and hence all strain-dependent states, such as stress or stiffness. Figure 4.2 illustrates how different representations of $\boldsymbol{\beta}$ impact the support and the anisotropy of the shape functions. This property is particularly important for the treatment of boundary conditions as the above setup along with an appropriate choice of $\boldsymbol{\beta}$ allows to render the interpolation at the boundary independent of internal nodes [91].

Again, in close analogy to the quadrature points in the finite element method, we introduce a set of n_p material points located at $\{\boldsymbol{x}^p, p = 1, \ldots, n_p\}$ for numerical

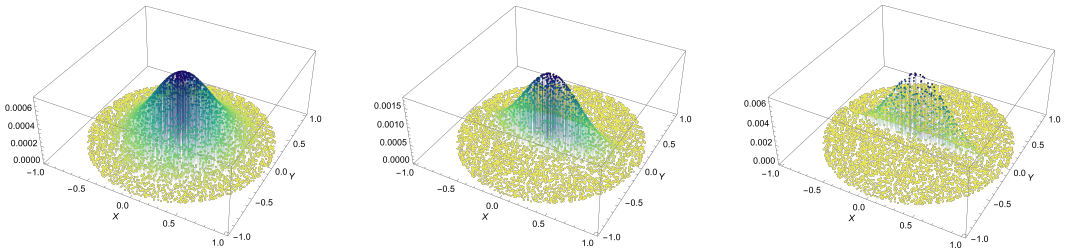

(a) $\boldsymbol{\beta} = \begin{pmatrix} 5 & 0 \\ 0 & 5 \end{pmatrix}$ (b) $\boldsymbol{\beta} = \begin{pmatrix} 5 & 0 \\ 0 & 30 \end{pmatrix}$ (c) $\boldsymbol{\beta} = \begin{pmatrix} 5 & 0 \\ 0 & 500 \end{pmatrix}$

Figure 4.2: Illustration of the influence of $\boldsymbol{\beta}$ on the support of the shape functions. We randomly generated 7000 nodes in a two-dimensional space and endowed each one with a shape function N^a as per (4.6). The column at each node corresponds to the value of the associated shape function at $\boldsymbol{x} = (0,0)^T$. The different choices in $\boldsymbol{\beta}$ reflect growing levels of anisotropy starting from an isotropic approximation in (b) to a severely anisotropic representation in (c).

integration. The distribution of the mass m^p of every material point – and consequently also its density ρ^p – follows from the discretization of the density field via

$$\rho(\boldsymbol{x}) = \sum_{p=1}^{n_p} \rho^p V^p \delta(\boldsymbol{x} - \boldsymbol{x}^p) = \sum_{p=1}^{n_p} m^p \delta(\boldsymbol{x} - \boldsymbol{x}^p), \tag{4.9}$$

where V^p denotes the volume of the material point at $\boldsymbol{x}^p$. Material points carry a locality parameter $\boldsymbol{\beta}^p$, so that any integral involving shape functions or shape function derivatives can be evaluated numerically. They are further endowed with a constitutive model, which means they possess the notion of a strain energy density, which – in our case – the energy formulation for the Taylor model in (3.11) provides. Using this strain energy density along with a set of elastic and inelastic variables – both of which we store at the individual material points – we can evaluate the local stress and stiffness, which in return yields the forces acting on the nodes as well as the global stiffness matrix. While the evolution of the elastic state follows from the macroscale problem, the update of the inelastic state is generally dependent on the communication with the mesoscale as outlined in Figure 4.1. Details on the numerical time integration are provided in Section 4.3.

Among the primary reason for employing the meshfree method by Kumar et al. [91] lies the updated-Lagrangian setting. The updated-Lagrangian setting affords a solution through updating the reference configuration to the deformed configuration from the last step, which outperformed the total-Lagrangian formulations in Kumar et al. [91]. We introduce an incremental deformation gradient $\boldsymbol{F}_{n\to n+1}$ as the gradient

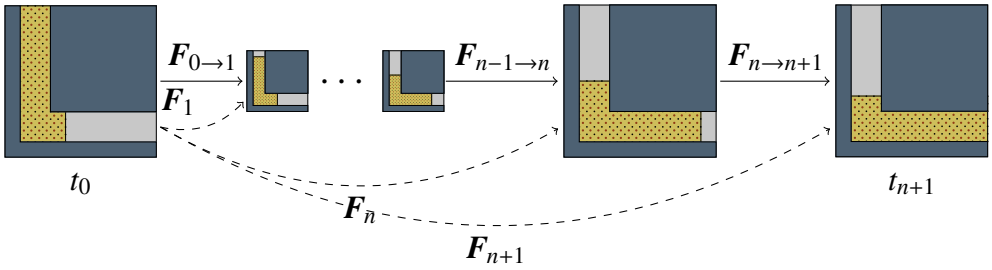

Figure 4.3: Illustration of the differences between the total- and the updated-Lagrangian formulation using the example of ECAE. Nodes and material points are visualized by black and red points, respectively. In the total-Lagrangian setting (*dashed*), the total deformation gradient $\boldsymbol{F}_{n+1}$ is a mapping from the initial configuration to the deformed configuration, while the updated-Lagrangian setting interprets $\boldsymbol{F}_{n+1}$ a mapping from the previous configuration (at time t^n) to the current configuration.

of the deformation mapping at step $n+1$, $\boldsymbol{\varphi}_{n+1}$, with respect to the geometry in step n via

$$\boldsymbol{F}_{n\to n+1} = \frac{\partial \boldsymbol{\varphi}_{n+1}}{\partial \boldsymbol{x}_n} = \boldsymbol{I} + \boldsymbol{\nabla}_n(\boldsymbol{u}_{n+1} - \boldsymbol{u}_n), \tag{4.10}$$

with $\boldsymbol{u}_n$ and $\boldsymbol{u}_{n+1}$ denoting the deformation mapping at time t_n and t_{n+1}, respectively. Assuming that the change in deformation gradient within one step is small, the total deformation gradient at step $n+1$, $\boldsymbol{F}_{n+1}$, which we can approximate through

$$\boldsymbol{F}_{n+1} \approx \frac{\partial \boldsymbol{\varphi}_{n+1}}{\partial \boldsymbol{x}_0} = \boldsymbol{F}_{n\to n+1}\boldsymbol{F}_n. \tag{4.11}$$

At every step, using the configuration at t_n and the change in deformation gradient $\boldsymbol{F}_{n\to n+1}$, we update the connectivity and shape functions. Further, we also evaluate the volumetric weights at t_{n+1} via $V^p_{n+1} = \det(\boldsymbol{F}_{n\to n+1})V^p_n$. By incrementally updating the locality parameter as

$$\boldsymbol{\beta}^p_{n+1} = (\boldsymbol{F}_{n\to n+1})^{-T}\boldsymbol{\beta}^p_n(\boldsymbol{F}_{n\to n+1})^{-1}, \quad p = 1,\dots,n_p, \tag{4.12}$$

we adaptively adjust the form of the shape functions, which again helps to deal with large deformations. A summary of the idea of the updated-Lagrangian formulation is illustrated in Figure 4.3.

Having established the max-ent framework, we can solve the governing equation of quasistatic force equilibrium on the macroscale, which requires all nodal forces to

vanish via

$$\begin{aligned} \boldsymbol{f}^a_{n+1} &= 0, \quad \forall a = 1, \dots, n_n, \quad \text{where} \\ \boldsymbol{f}^a_{n+1} &= \sum_{p=1}^{n_p} \frac{V^p_n}{J^p_n} \boldsymbol{P}(\boldsymbol{F}^p_{n+1}, \mathcal{Q}^p_n, \mathcal{R}^p_n) \boldsymbol{F}^{p\mathrm{T}}_n \boldsymbol{\nabla}_n N^a(\boldsymbol{x}^p_n) - \boldsymbol{f}^a_{\mathrm{ext},n+1} = \boldsymbol{0}. \end{aligned} \tag{4.13}$$

Here, $\boldsymbol{f}^a_{\mathrm{ext}}$ describes the external force acting node a, whereas $\mathcal{R} = \{\boldsymbol{R}_{i\in\{1,\dots,N_g\}}\}$ and $\mathcal{Q} = \{\boldsymbol{Z}_{i\in\{1,\dots,N_g\}}, \eta_{i\in\{1,\dots,N_g\}}\}$ denote grain orientations and the set of internal variables inherited from the mesoscale, respectively. The first Piola-Kirchhoff stress tensor at material point p is given by $\boldsymbol{P}(\boldsymbol{F}, \mathcal{Q}) = \partial E(\boldsymbol{F}, \mathcal{Q}, \mathcal{R})/\partial \boldsymbol{F}$.

4.3 Computational challenges in ECAE modeling

4.3.1 Time integration

Section 4.2 introduced the numerical modeling on the macroscale level and described its communication with the meso- and microscale using vertical homogenization. Based on the quasistatic nature of severe plastic deformation processes such as ECAE, we ignore inertial effects on the macroscale. Although we address changes on the macroscale with time, the majority of this section concerns to the description of the time-integration of internal variables on the meso- and microscale. Concerning the time integration of the internal variables, implicit update schemes are in general preferable as they allow to use larger time-steps. They do, however, assume a variational structure and their computational benefit largely depends on the optimization method employed to find the infimizer of the minimum dissipation potential rule associated with the variational energy and dissipation formulation. Since a variational formulation generally permits an analytical derivative, we formulate this contribution based on explicit updates and mention, that the multiscale structure allows for implicit time integration, too. We note that the opposite – *i.e.*, the transformation of an explicit scheme into an implicit scheme – is, in general, theoretically possible. As the case of the Cu-model presented in Section 3 shows, finding a closed form concerning the dissipation potential is challenging, as the denominator in the update law, itself, depends on internal variables.

We consider a continuous time field $\mathcal{T} = [0, t_{\max}]$ with $t_{\max}$ denoting the final time. Based on $\mathcal{T}$, we introduce a discretization of $\mathcal{T}$ as $\mathcal{T}_\Delta = [0, \Delta t, 2\Delta t \dots, N\Delta t]$ with $\Delta t = t_{\max}/N$ and N describing the incremental time step and the number of timesteps, respectively. On the macroscale, stepping from $t_n \in \mathcal{T}_\Delta$ to $t_{n+1} = t_n + \Delta t$ relates to changes in the boundary conditions. Section 4.3.2 lays out the specific changes in boundary conditions in the ECAE setting. Using these new boundary

conditions and the meshfree approach we described in Section 4.2, we find $\boldsymbol{F}_{n+1}$, *i.e.*, the deformation gradient at every material point at time t_{n+1}. Based on the Taylor assumption, every grain at a material point is associated with that same new deformation gradient. As the remaining part of this section is devoted to the material point level, we omit the superscript p as an association of the deformation gradient to a specific material point. We use the total deformation gradient $\boldsymbol{F}_{n+1}$ to evaluate an intermediate version of the elastic deformation gradient $(\boldsymbol{F}^{\mathrm{e}}_{i,n+1})^* = \boldsymbol{F}_{n+1}(\boldsymbol{F}^{\mathrm{in}}_{i,n})^{-1}$ for every grain $i \in \{1,\dots,N_g\}$. Using $(\boldsymbol{F}^{\mathrm{e}}_{i,n+1})^*$ and $\boldsymbol{F}^{\mathrm{in}}_{i,n}$, we find the resolved shear stress on every slip system (cf. Section 3.2) and compute $\boldsymbol{\gamma}_{i,n+1}$, $\boldsymbol{g}_{i,n+1}$, and $\boldsymbol{F}^{\mathrm{in}}_{i,n+1}$ for every grain using forward Euler schemes.

The explicit integration scheme requires small time-steps for convergence, mainly because of the power law in (3.7) and the relatively high magnitude of the hardening exponent m (see, *e.g.*, Knezevic et al. [85]). At each time step, the meshfree solver performs computationally expensive operations that include assembling the consistent stiffness matrix and solving the nonlinear equations (4.13). To permit for such a small time-step on the microscale, while avoiding the increase in computational time on the macroscale, we employ a multi-stepping approach based on the spectral decomposition, which we borrow from the spectral decomposition-based ansatz in Chapter 2. At every material point, we obtain the incremental deformation gradient $\boldsymbol{F}_{n\to n+1}$ via $\boldsymbol{F}_{n+1} = \boldsymbol{F}_{n\to n+1}\boldsymbol{F}_n$. Spectral decomposition of this transformation tensor via $\boldsymbol{F}_{n\to n+1} = \hat{\boldsymbol{R}}\hat{\boldsymbol{U}}$, with principal stretch tensor $\hat{\boldsymbol{U}} = \sqrt{(\boldsymbol{F}_{n\to n+1})^T\boldsymbol{F}_{n\to n+1}}$ and rotation $\hat{\boldsymbol{R}} = \boldsymbol{F}_{n\to n+1}\hat{\boldsymbol{U}}^{-1}$, allows decomposing the update into several steps through

$$\boldsymbol{F}_{n+m/(2n_m)} \equiv \begin{cases} \hat{\boldsymbol{U}}^{1/n_m}\boldsymbol{F}_{n+(m-1)/(2n_m)} & \text{if} \quad m \le n_m, \\ \hat{\boldsymbol{R}}^{1/n_m}\boldsymbol{F}_{n+(m-1)/(2n_m)} & \text{if} \quad m > n_m, \end{cases} \quad \text{for} \quad 1 < m \le 2n_m, \tag{4.14}$$

with $n_m > 0$ denoting the multi-step number. This results in a relatively large timestep on the macroscale, while effectively reducing the timestep on the microscale to $\Delta t^* = \Delta t/(2n_m)$. The updates from $\boldsymbol{\gamma}_{i,n+(m-1)/(2n_m)}$, $\boldsymbol{g}_{i,n+(m-1)/(2n_m)}$, and $\boldsymbol{F}^{\mathrm{in}}_{i,n+(m-1)/(2n_m)}$ to $\boldsymbol{\gamma}_{i,n+m/(2n_m)}$, $\boldsymbol{g}_{i,n+m/(2n_m)}$, and $\boldsymbol{F}^{\mathrm{in}}_{i,n+m/(2n_m)}$ are conducted using the resolved shear stress evaluated using $\boldsymbol{F}^{\mathrm{in}}_{i,n+(m-1)/(2n_m)}$ and $(\boldsymbol{F}^{\mathrm{e}}_{i,n+m/(2n_m)})^* = \boldsymbol{F}_{n+m/(2n_m)}(\boldsymbol{F}^{\mathrm{in}}_{i,n+(m-1)/(2n_m)})^{-1}$ for $m \in \{1,\dots,2n_m\}$. We note that $\boldsymbol{F}_{n+1}$ does not depend on internal variables specific to any of the grains, which is why the decomposition in (4.14) only has to be computed once per macroscale material point. Figure 4.4 provides a visualization of the above description.

The optimal choice of the multi-step n_m to ensure a stable time-integration is integral in reducing the computational cost of the update of internal variables from t_n

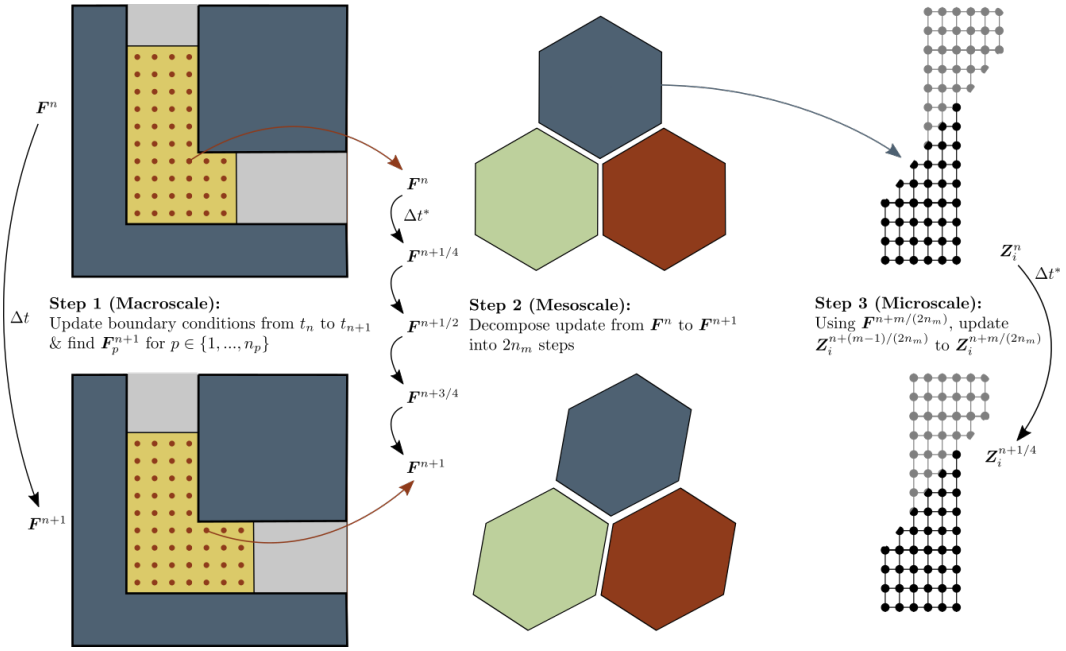

Figure 4.4: Illustration of the time-integration on the macro-, meso- and microscale. We note, that subscripts denoting the association of a grain with a macroscale point were omitted everywhere but in the description of the first step in favor of improved readability.

to n_{n+1}. While the material undergoing severe shear deformation through the bend in the channel requires higher multi-step numbers, imposing the same multi-step number for material further away from the bend incurs unnecessary computational overhead. Since this observation is closely related to the problem of exponentiation we mentioned above, we leverage this information and tailor the number of multi-steps depending on the evolution of the normalized flow stress, namely, $\tau^{\alpha}_{n+m/(2n_m)}/G^{\alpha}_{r,n+m/(2n_m)}$. At the beginning of the simulation, *i.e.*, at t_0, we set n_m to some predefined lower bound $n_{m,l}$. Using this first trial of $n_{m,l}$, we compute the evolution of the internal variables. At each of the $2n_m$ steps, we evaluate the change in normalized flow stress as

$$\xi_{n+m/(2n_m)} = \max_{\alpha \in \{1,\ldots,n_s\}} \left| \frac{\tau^{\alpha}_{n+m/(2n_m)}/G^{\alpha}_{r,n+m/(2n_m)}}{\tau^{\alpha}_{n+(m-1)/(2n_m)}/G^{\alpha}_{r,n+(m-1)/(2n_m)}} \right|. \tag{4.15}$$

High values of $\xi_{n+m/(2n_m)}$ indicate a higher susceptibility to instabilities due to the high exponentiation. We define a critical threshold ξ_{cr} and consider the evolution from $t_{n+(m-1)/(2n_m)}$ to $t_{n+m/(2n_m)}$ as stable if $\xi_{n+m/(2n_m)} < \xi_{\mathrm{cr}}$. If this condition is not met, we restart the simulation from time t_n and increase the number of multi-steps by a factor of 2. If $\xi_{n+m/(2n_m)} < \xi_{\mathrm{cr}}$ is satisfied throughout all multi-steps from t_n to t_{n+1},

we store n_m. Since the incremental loading at every time step is relatively small, we assume that the number of multi-steps needed for a stable evolution of the internal variables does not change significantly from one time-step to another. Motivated by this, we redefine n_m at the new timestep as either half of the n_m from the last time step or $n_{m,l}$, whichever is higher. We provide a summary of the adaptive choice of the multi-stepping number n_m with the help of a pseudo-code using Algorithm 2.

Algorithm 2 : Adaptive multi-step evolution of internal variables at a given material point

Input at time t_n :
- Number of multi-steps: n_m (equal to $n_{m,l}$ if $t_n = t_0$)
- Total deformation gradient at material point: $\boldsymbol{F}_n$
- Internal variables of each grain: $\{\boldsymbol{\gamma}_{i,n},\ \boldsymbol{g}_{i,n},\ \boldsymbol{F}^{\text{in}}_{i,n}\}_{i\in\{1,\dots,N_g\}}$

ErrorFlag := true
while (ErrorFlag) **do**
  ErrorFlag := false
  for $m = 1,\dots,2n_m$ **do**
    Compute $\boldsymbol{F}_{n+m/(2n_m)}$ using (4.14)
    for $i = 1,\dots,N_g$ **do**
      Compute $(\boldsymbol{F}^{\text{e}}_{i,n+m/(2n_m)})^{*} := \boldsymbol{F}_{n+m/(2n_m)}(\boldsymbol{F}^{\text{in}}_{i,n+(m-1)/(2n_m)})^{-1}$
      Compute $\boldsymbol{\gamma}_{i,n+m/(2n_m)}$ using (3.7)
      Compute $\boldsymbol{g}_{i,n+m/(2n_m)}$ using (3.6)
      Compute $\boldsymbol{F}^{\text{in}}_{i,n+m/(2n_m)}$ using (3.2)
      Compute $\xi_{n+m/(2n_m)}$ using (4.15)
      if $(\xi_{n+m/(2n_m)} > \xi_{\text{cr}})$ **then**
        ErrorFlag := true
        break
      end if
    end for
    if (ErrorFlag) **then**
      break
    end if
  end for
  if (ErrorFlag) **then**
    $n_m := 2n_m$
  end if
end while
$n_m := \max\{n_m/2,\ n_{m,l}\}$

4.3.2 ECAE process & boundary conditions

The updated-Lagrangian setting we described in Section 4.2 helps us to naturally include boundary conditions where we consider them to be necessary. Since we

operate in the context of the current configuration, we benefit from the ability to update boundary conditions depending on their position. In that way, we can initially subject nodes to Dirichlet boundary conditions in the sense of zero wall-penetration without incurring issues as they pass through the channel bend. In a total Lagrangian setting, this is not possible, as boundary conditions are formulated with respect to the initial configuration.

Figure 4.5 illustrates the numerical setup of the ECAE process. We consider a 3D billet to alleviate the plane strain assumption imposed in previous studies (see, *e.g.*, Hallberg et al. [63], Luis et al. [103], Ma and Hartmaier [104]) and to allow for future investigations of different processing routes. The lateral walls past the channel's bend are modeled using cubic wall potentials that penalize the orthogonal penetration. Furthermore, we included approximations of an inner and outer channel arc by including chamfers of length w_1 and w_2 at the outer and inner corner, respectively (see Figure 4.5). These chamfers are again incorporated using the cubic wall potentials. In Section 4.3.1, we mentioned that the transient nature of the ECAE process translates into our macroscale simulation by updating the boundary conditions. With this, we refer to the plunger displacement at the top of the billet in the form of Dirichlet boundary conditions, which we update following a constant strain rate ϵ via $u_{\text{top}} = u_{\text{top}}(t) = \dot{\epsilon} t$. Here, u_{top} denotes the negative y-displacement of the upper face of the billet, as illustrated in Figure 4.5.

Previous studies attempted to include the effect of friction via a shear friction model which took into account the shear strength of the billet and the friction coefficient between wall and billet (see, *e.g.*, Fu et al. [47]); these simulations, however, were predominantly conducted under dynamic loading conditions, thus ignoring the quasistatic nature of small strain rates. Although quasistatic friction can impact the through-thickness heterogeneity of the deformed billet, we follow Luis et al. [103], Saitoh and Ohnishi [142], and Fagan et al. [41] and assume that sufficient lubrication of the channel (through, *e.g.*, MoS_2) allows constraining quasistatic friction effects to a negligible level.

4.3.3 Simulation protocol

The parameters defining the micro- and macroscale follow directly from the parameters used for the Taylor model in Chapter 3 at 775 K, the temperature at which we found a compelling agreement between the results from the Taylor model and the experiment by Blaz et al. [18]. On the macroscale – unless otherwise indicated –

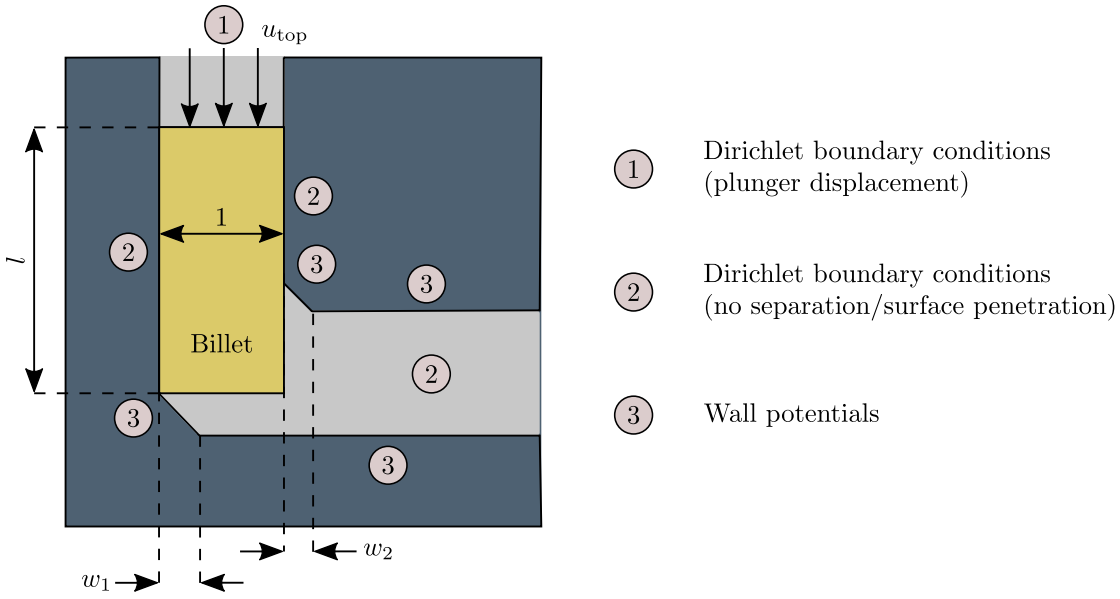

Figure 4.5: Schematic depiction of the initial configuration of the billet along with boundary conditions and dimensions. We used Dirichlet boundary conditions for imposing the plunger displacement (1) and to constrain the nodes on all surfaces with normal parallel to the in-plane z-component as well as the walls above the chamfers (2). Further, we modelled the outer and inner chamfer with dimensions w_1 and w_2, respectively, using wall potentials. Wall potentials also describe the lower and upper wall past the bend (3).

we employ the parameters from Table 4.1. Concerning the generation of the mesh, we pursue the same procedure outlined in detail in Kumar et al. [91].

4.4 Results

4.4.1 Convergence

Although previous studies addressed the impact of resolution on the ability to capture sufficiently the microstructural changes in the metal billet, there are no thorough studies on the convergence behavior in the spatial or the temporal sense. In a multiscale framework, where the interaction of different scales makes it difficult to relate observations to specific sources, we aim to minimize these uncertainties. Since the quasistatic nature of the meshfree approach on the macroscale requires the choice of both a a temporal resolution dt as well as a spatial resolution – which we define via the number of nodes we employ per unit length – we conduct spatial and temporal convergence analyses.

Based on four different resolutions $dt \in \{0.4, 0.2, 0.1, 0.05\}$ s and first excluding recrystallization effects, we test temporal convergence. Again, for the lowest temporal

Parameter	Symbol	Unit	Value
Temperature	T	[K]	775
Initial length of billet†	l	-	4
Lower-left chamfer dimension†	w_1	-	0.25
Upper-right chamfer dimension†	w_2	-	0.1
Initial max-ent locality parameter	$\boldsymbol{\beta}_0^p$	-	$(3/h^{p2})\boldsymbol{I}$
Shape function cut-off tolerance	ϵ_{cut}	-	10^{-7}
Initial connectivity cut-off region	$\boldsymbol{M}_0^p$	-	$-1/\log(\epsilon_{\text{cut}}) \times \boldsymbol{\beta}_0^p$
Time step	Δt	s	0.2 s
Nodes per non-dimensionalized length	-	-	6
Plunger displacement per step†	-	-	2.0×10^{-4}
Lower bound on multi-step number	$n_{m,l}$	-	8
Multi-stepping criterion	ξ_{cr}	-	1.1

Table 4.1: Macroscale parameters defining the geometry, boundary conditions, and the meshfree solver. Variables marked with a † refer to variables normalized with respect to length. For a description of the shape function cut-off tolerance ϵ_{cut} and the initial connectivity cut-off region $\boldsymbol{M}_0^p$, we refer to Kumar et al. [91].

resolution of $dt = 0.4$ s, we observe oscillations in the total energy, which are still visible for $dt = 0.2$ s, but which disappear for lower resolutions. The origin for these oscillations originates in the way we model the inner and outer channel walls that causes these oscillations. In a quasistatic framework, we update the inelastic state based on the change in deformation gradient from one step to the other. If the timesteps are sufficiently small, the nodes achieve to follow the form of the chamfer and the predominant loading type is shear, which is beneficial for inelastic deformation. If, however, the timesteps are large, the nodes fail to follow the exact form of the chamfer leading to an increasingly compression-like behavior. The compressive loading aggravates the ability for dislocations to slip and therefore initially leads to an energetically less favorable elastic deformation. An overly elastically deformed area can, however, incite an improved shear behavior of the material in the region above. As the billet passes through, we initially observe a poor capturing of the wall, which improves with time. The periodic occurrence of elastically deformed zones together with the gradual improvement of the flow of nodes around the wall explains, on the one hand, the oscillatory behavior and, on the other hand, the relaxation of the oscillations with time. Although the convergence in Figure 4.6a is readily visible, we provide a logarithmic depiction of the total energy for the four different resolutions at four discrete times to emphasize the convergent behavior.

Concerning the spatial convergence, we analyzed four different resolutions, namely

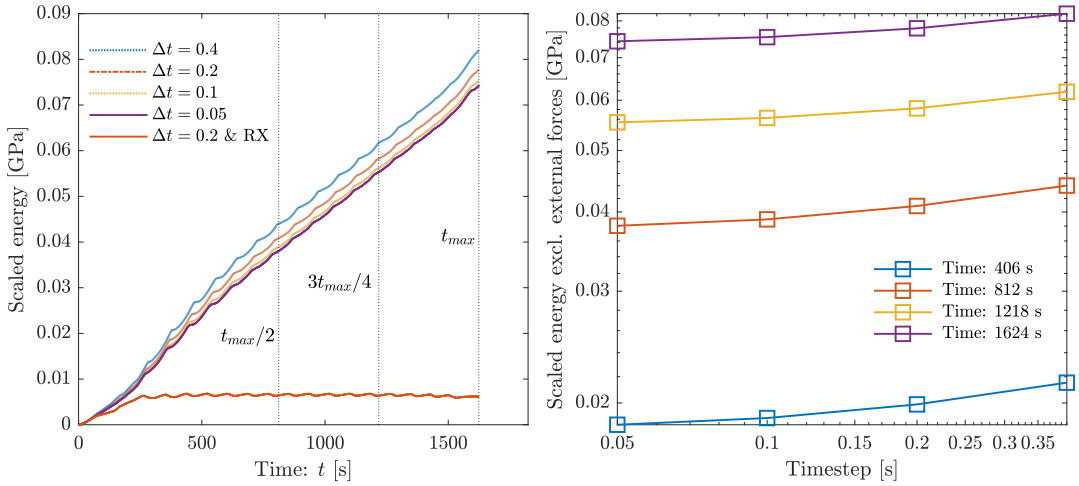

(a) Transient energy development

(b) Discrete energy values

Figure 4.6: Temporal convergence as depicted via four different timesteps *dt* excluding recrystallization. For comparison, we also provide the energy evolution for the case that includes both migration and nucleation capabilities.

4, 5, 6 and 8 nodes per unit length. While the temporal convergence is heavily dependent on the time-integration of the inelastic variables, the spatial convergence is predominantly dependent on macroscale effects. As the focus of this thesis comprises micro- and mesoscale concerns, we refer to Kumar [90] for an elaborate spatial convergence analysis, which exposes six nodes per unit length as a sufficiently accurate spatial resolution.

4.4.2 Strain homogeneity

Figure 4.7 presents the position of nodes and material points throughout the extrusion process. For an easier isolation of sources for observations, we first conduct a simulation without recrystallization. Without explicitly illustrating strains, the distortion grants a first insight into the homogeneity across the sample. Starting with an initially uniform distribution of nodes and associated material points, the intersection of the two channels causes a shearing behavior. Comparing an initially horizontal line between two nodes in the initial configuration and the configuration past the bend, we notice that the new connecting line adopts a value of 45°. Turning the frame of reference by 45° in the anticlockwise direction leaves us with a shearing strain of close to 200%, which corresponds to theoretical considerations by Segal et al. [147]. Apart from the shear zone, two more regions bear significance in this analysis. The end of the billet does not undergo the same shearing motion as the

center part of the billet. Instead, we note that the initial bottom nodes of the billet stay at a close distance to the bottom wall. Furthermore, the region above the intersection experiences the highest density in nodes. We associate this behavior with a compressive action, which constitutes a valuable insight, as theoretical considerations are generally constrained to a purely shear-based deformation. Concerning the shear distribution across the cross-section at the center of the final processed billet, we observe a relatively homogeneous distribution. In this configuration, the maximum observed shear strain magnitude is attained towards the center of the sample with a value of $F_{12,\max} = -1.05$, while we find the lowest magnitude of the shear strain close to the lower wall with a value of $F_{12,\min} = -0.95$. The qualitative heterogeneity in the shear strain agrees well with both the numerical as well as experimental findings from Bowen et al. [20].

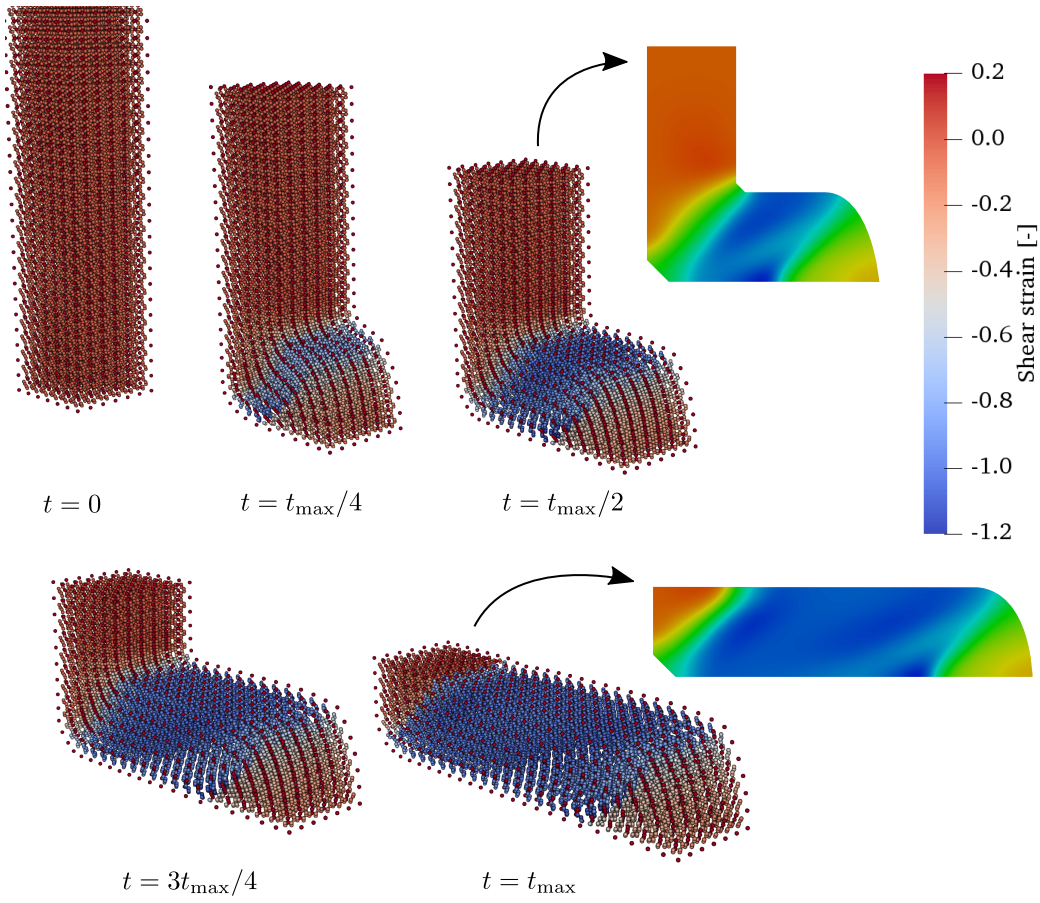

Figure 4.7: Illustration of the deformation of the billet via the displacement of nodes (*red*) and material points. The coloring of material points scales with the local in-plane shear strain F_{12}. The F_{12} distribution is further illustrated using a 2D view on the xy-plane at $z = 0.5$ based on an interpolation using radial-basis function kernels (rbf) at $t_{\max}/2$ and $t_{\max}$.

In Segal et al. [147], the authors hypothesize that a decrease in the inner and outer channel curvatures is directly related to a mitigation of the sample's heterogeneity away from the two ends of the billet. Although strain heterogeneity forms a central concern in the optimization of ECAE processes, the focus of this thesis lies on meso- and microscale developments. For a numerical study using our approach to test the hypothesis from In Segal et al. [147], we refer to the Kumar [90].

4.4.3 Reorientation excluding recrystallization effects

We use orientation plots to interpret the nature of the local loading and the impact of the position along the (initial) cross-sectional area. Figure 4.8 shows the evolution of the $\langle 111 \rangle$ family of crystallographically equivalent poles with regards to the underlying fcc structure at three material points which initially differ solely through their x-coordinate in space and their randomized texture. The initial pressing of the billet through the channel causes small changes in the texture. We associate this reorientation with the compressive action in the region right above the shear zone, which we previously addressed in Section 4.4.2. However, the short duration of this compressive loading does not allow deducing distinct compression textures as we obtained in Chapter 3. The subsequent shear the billet experiences, when it passes through the bend, is more pronounced and leads to the characteristic six preferred poles in the stereographic projection applied in this visualization. This texture is in good agreement with the results from the numerical work of Sivakumar and Ortiz [150] and the experimental investigation by Vogel et al. [179]. Although this behavior repeats at all three material points, we observe a stronger texture evolution with proximity to the outer channel wall. One possible origin for the weaker texture of the material closer to the upper wall consists in tensile loading of this region through the downwards bend of the end of the billet, which compromises the effects due to shear. We note, that numerical reasons, too, can cause this discrepancy. As the shearing process spreads to a finite space for non-zero chamfer wall lengths, the time over which the shearing takes place determines the effective timestep experienced by the lower scale inelastic update scheme. Since the chamfer wall length is longer on the outer channel, the effective timestep felt by the inelastic update near the inner corner is smaller compared to its equivalent on the outer edge. This difference in the effective temporal resolution can explain a better capturing of the evolution of inelastic variables and their influence on reorientation. Since we based our choice of the temporal resolution for our simulation on the convergence study from Section 4.4.1, the possibility of a predominantly numerical origin of this

behavior is, however, unlikely.

4.4.4 Grain refinement

Although frequently ignored in previous literature, the central purpose of ECAE lies in grain refinement. Figure 4.9 depicts the distribution of the average volume fraction across the $z = 0.5$ plane after inclusion of recrystallization effects. Among the most valuable observations lies the start of the recrystallization phase. Deviations of the average volume fraction to the initial value first occur in a zone right before the bend. We expect the compressive action on the material directly above the curve – which we previously addressed in Sections 4.4.2 and 4.4.3 – to be responsible for the onset of grain refinement above the region of severe plastic deformation, *i.e.*, the bend. The location of the material point with the smallest average volume fraction at the intersection of the two channels is representative of the extensive local nucleation activity.

After the billet shears into the horizontal part of the channel, the material continues translating without significant deformation. In a process termed post-dynamic recrystallization (*c.f.* Section 4.1), we experience a decrease in the average grain volume. As we can see from the histogram, however, despite the final growth of grains, the average grain size at the majority of material points ends up at a much smaller size compared to the average volume fraction. We note that the absence of curvature driven growth in a Taylor model leads to an exaggeration of the average volume fraction in this case, as new grains grow so long as there is a non-zero difference in stored energy to the already existing grains.

4.4.5 Plunger force and homogenized energy evolution

Using data from ECAE experiments for fitting purposes is an ill-posed problem. Data on the microstructure is generally solely available in *a priori* and *a posteriori* form, as the channel itself does not allow for continuous tracking of the microstructure, which by itself is challenging. The sparsity of data concerning the microstructural evolution is, however, an issue which is not confined to ECAE, as we have demonstrated in Chapter 3. Processes including uniform compression or hot-pressure torsion mitigate this issue by providing meaningful stress data in the sense that it is possible to directly associate the stress we recorded with the internal stresses in the body. In ECAE, this is not the case. A force versus displacement curve is generally readily obtained by measuring the force recorded by the plunger; the contribution due to friction effects, however, is unclear.

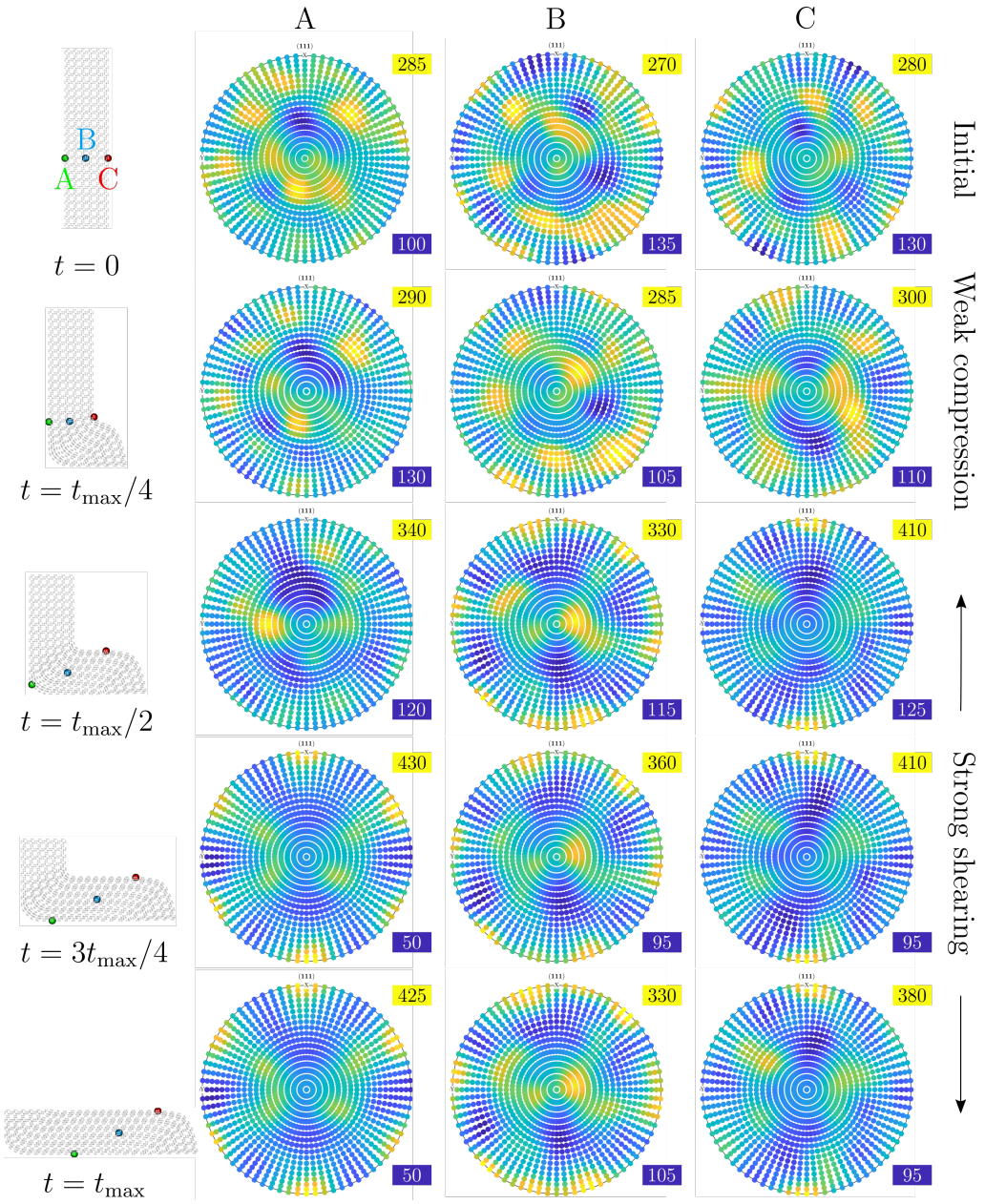

Figure 4.8: Reorientation evolution of the ⟨111⟩ pole family illustrated via a stereographic projection onto the (001)-plane at 0, $t_{\max}/4$, $t_{\max}/2$, $3t_{\max}/4$, and $t_{\max}$. The blue and yellow labels next to each pole figure represent, respectively, the minimum and maximum intensity. The reorientation evolution in each of the three columns labelled A, B and C correspond to the associated material points marked in the leftmost column. This analysis excludes recrystallization.

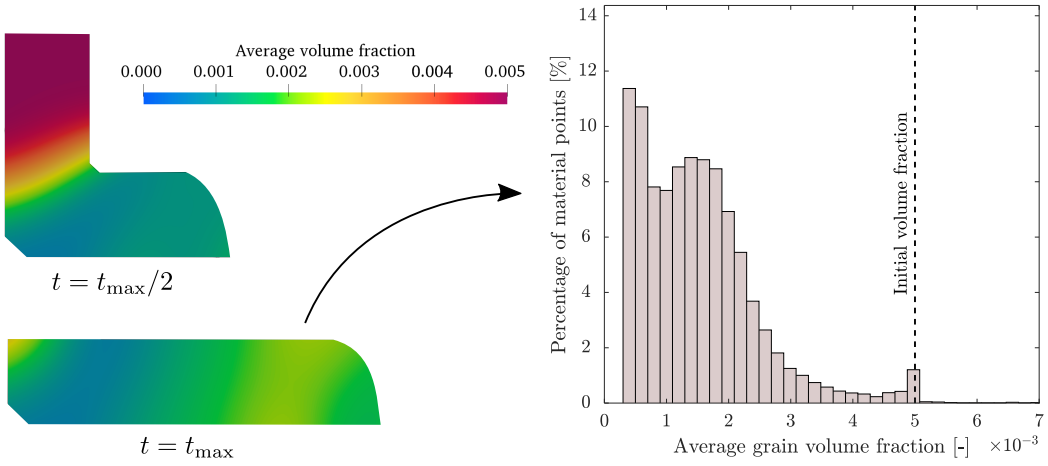

Figure 4.9: Interpolation of the distribution of the average grain volume across the $z = 0.5$ plane using radial-basis function kernels (rbf) at $t_{\max}/2$ and $t_{\max}$.

Despite this shortcoming, we conduct a qualitative analysis of the force that the plunger exerts. Figure 4.10 illustrates the evolution of the area-normalized plunger force. We included simulations with and without recrystallization capabilities to elucidate the effect of dynamic strain softening through the nucleation and migration of pristine grains. In both cases, we see a comparable rise in the force stemming from the progressive compression of the billet against the bottom wall of the channel. As the billet bends into the horizontal part of the channel, both force curves transform into an oscillatory behavior. This type of periodic evolution of the force is frequently observed in ECAE processes, where the local texture allows for shear bands to evolve. These shear bands, however, generally also impact the roughness of the top surfaces of the processed billet. Given the smooth final billet in this framework along with numerical oscillations observed in the energy plot, it is more likely that this behavior – despite having justified the choice of time-step and spatial resolution via Section 4.4.1 – are remnants of the insufficient temporal or spatial resolution. This insufficient resolution, however, must be localized, as the size of oscillations is more pronounced in comparison to those illustrated in Figure 4.6a.

We report good qualitative agreement between the force evolution curve without recrystallization effects and the experimentally measured force evolution during ECAE of 5083 aluminum alloy at room temperature by Pérez [130]. Following an initial fast increase, both approaches experience a shallower slope, which again rises until to the onset of the last section, where a moderate rise in plunger force is registered. As the differences in underlying materials and process temperatures render a quantitative comparison insignificant, we constrain our attention to this

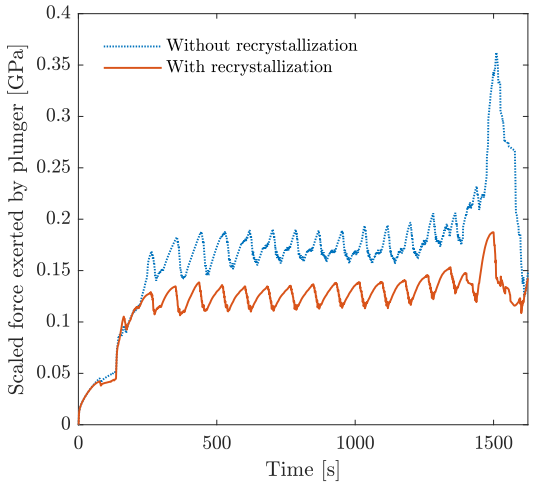

Figure 4.10: Evolution of the scaled plunger force via integration of the Cauchy stress over the top surface for simulations including and excluding recrystallization.

compelling qualitative comparison.

In Figure 4.6, we previously conducted a convergence analysis concerning the temporal resolution. We use the results for the case without recrystallization and compare it to the case including recrystallization effects. Similar to (4.10), the total energy corresponding to the case including recrystallization capabilities is lower compared to the simulation based entirely on elastic and slip-based deformation. Although oscillations are observable in this case, too, their amplitude is significantly reduced. This observation in return backs up our previous hypothesis regarding the distinct influence of the two corner regions onto the plunger force and the resulting pronounced oscillations.

4.4.6 Reorientation including recrystallization

In Section 4.4.3 we investigated the texture evolution of the grains associated with three material points without recrystallization. Since the orientation of a nucleus is assumed to be random in our model, we are interested in the extent to which nucleation and migration influence this development. *A priori*, we expect either a more diffuse texture due to the randomness of orientation or an even more pronounced texture in case the stress state of the already existing grains influences the newly recrystallized grains. Figure 4.11 presents the evolution of the $\langle 111 \rangle$ pole family of the grains at one material point in the billet with stereographic projection onto the (001)-plane. For improved comparability, we included the texture at the same material point without the influence of recrystallization.

The simulation including nucleation and migration experiences a similar primary deformation pattern representative of the shear loading at the intersection of the two channels. At $t_{\max}/2$, small differences between the two cases arise without significant deviations in the intensity. We can relate these marginal differences in local reorientation to the impact of an overall softer response in the case of recrystallization due to material points that are already experiencing the decrease in stress state following the emergence and migration of pristine nuclei. At $3t_{\max}/4$, the texture in the case of recrystallization is mostly diffuse with the difference between the highest and lowest intensity staying similar compared to the case without recrystallization. This diffuse texture is testimony of the random orientation of newly nucleated grains. As soon as the material points pass past the shear region, nucleation and particularly migration continue during the post-dynamic recrystallization phase. Although the local deformation after the shear region closely resembles rigid body motion and no further slip-based distortion occurs, the available inelastic strain energy still partially allows for nucleation of new grains. The effects of post-dynamic recrystallization are visible through the continued rise in intensity to a final level of 1950 and 3000 for the lowest and highest intensity, respectively. Other than at $3t_{\max}/4$, we notice a clear texture at $t_{\max}$. We associate this more pronounced texture with grain migration favoring grains that are aligned energetically convenient with respect to the small remnant loading due to the distortion of the billet as well as the change of the material point's stress state following recrystallization. The former source of residual loading also explains why this texture possesses some of the characteristics of a shear texture for fcc polycrystals despite the predominantly diffuse texture at $3t_{\max}/4$.

We note that the final texture in neither case shows all six pronounced poles expected for the texture of an fcc metal undergoing severe shear deformation (see, *e.g.*, Vogel et al. [179]). Given the distance of the material point of interest to the lower wall, this observation is in line with the findings from Section 4.4.3, where the texture of the processed billet was the least pronounced towards the upper wall, which we related to the increasing role of alternative loading modes such as tension in these regions.

4.4.7 Multipass

We aim to investigate multiple passes of the same billet. In general, this is performed by first extracting the billet in its original form through the die, which corresponds to the scenario we analyzed in previous sections. Next, the billet is turned around

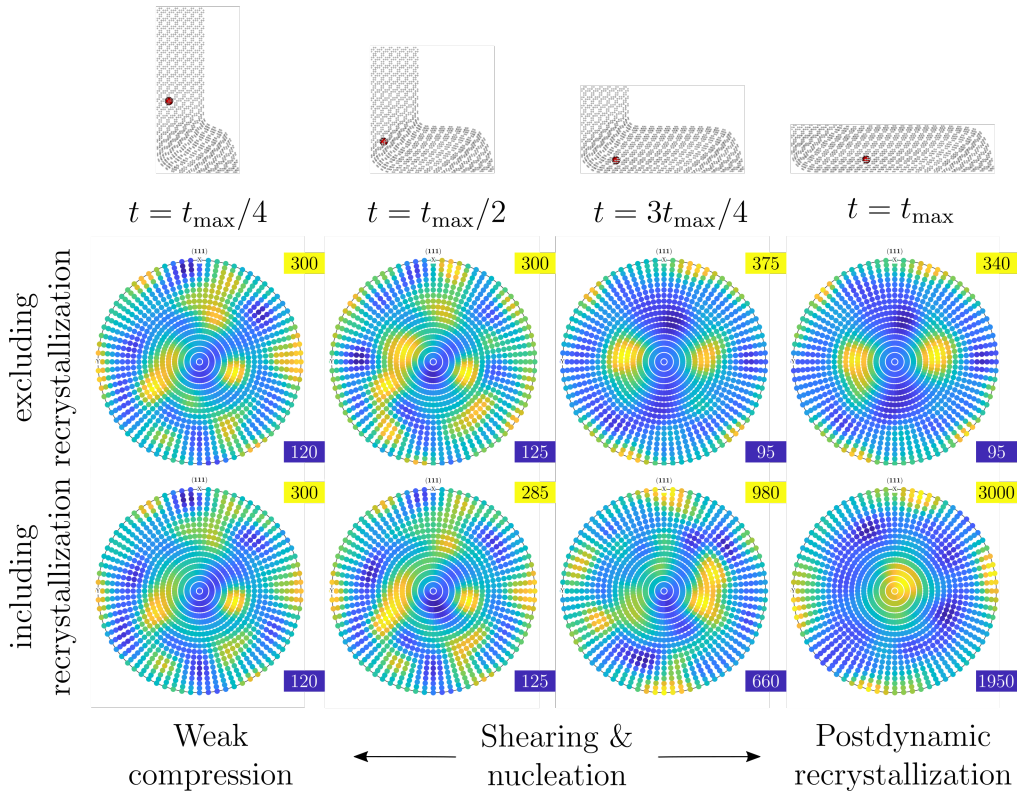

Figure 4.11: Reorientation evolution of the ⟨111⟩ pole family illustrated via a stereographic projection onto the (001)-plane at $t_{\max}/4$, $t_{\max}/2$, $3t_{\max}/4$, and $t_{\max}$ for scenarios excluding (top) and including (bottom) recrystallization effects. The blue and yellow labels next to each pole figure represent, respectively, the minimum and maximum intensity. The pole figures correspond to the current orientation of all grains at the material point marked in red.

its axis, < the extrusion direction, in line with one of the routes we introduced in Section 4.1. Following the turn, we extrude the already processed billet again through the same die. Mainly for reasons of simplicity, we reinterpret this process: Instead of pulling the sample analyzed earlier out of the die, we investigate a longer sample and push it through a channel with two bends, the latter one of which we embed in a fashion to approximate the route we try to simulate. In this case, we test a sample of normalized length $L = 7$ subjected to route C. We idealize the notion of a 180° turn, by providing a second bend, which again redirects the billet into the negative y-direction.

Figure 4.12 illustrates the evolution of the material points as we extrude the sample through the channel. For reasons of computational expense, we conduct this simulation without recrystallization effects. Despite the inherent inelastic deformation, the

sample managed to revert the strong shearing effect, as the distribution of material points with time in the texture plots shows. At the point where the billet first comes into contact with the wall of the channel corner, both shear and compression effects are dominant. The orientation plots are testimony to these loading cases as we discussed in Section 4.4.3. Similar to the results from Section 4.4.3, we observe a texture after the first bend that is characteristic of fcc crystal structures undergoing shear. At $t = 5t_{\max}/8$ – just before the second pass – we can still observe some diffuse texture towards the [001] pole. The reversal of the shear leads to a more diffuse texture, which the decrease in the intensity range from $t_{\max}/2$ to $t_{\max}$ indicates. This reversal is one of the reasons why route C is unsuitable for the processing of metals where the dominant catalyst of grain refinement is the formation of shear bands. Zhu and Lowe [200] provides a discussion on the impact of different routes on the efficiency of grain refinement for different classes of metals; a subject which to this day is heavily debated.

4.5 Conclusion

Using a multiscale framework, we were able to provide a numerical framework to investigate the principal factors inherent to the thermo-mechanical processing of metals, namely the evolution of texture, homogenized stress as well as the average grain diameter. Using the enhanced maximum-entropy based meshfree approach on the macroscale coupled to the Taylor model at the mesoscale and the finite deformation crystal plasticity model for pure Cu at the microscale, we managed to incorporate the nature of thermo-mechanical processes on all scales. Numerical tools comprising the multistep method and the updated Lagrangian framework provided the necessary means to deal with the challenges associated with the large deformations on the macroscale and the update of the inelastic state on the microscale. Using this model – which to our best knowledge is the first to provide the above capabilities in a natural way – we were able to investigate the plunger force evolution, the strain and stress distribution across the billet, the texture evolution, as well as the influence of recrystallization capabilities on these measures and the progression of the average volume fraction.

The softening effect of nucleation and grain migration resulted in the expected impact on macroscale measures. We found both the homogenized energy as well as the plunger force to be lower in magnitude compared to the case where the two recrystallization phenomena are excluded. The severe plastic deformation induced through the shear of the billet at the intersection of the two channels caused a grain

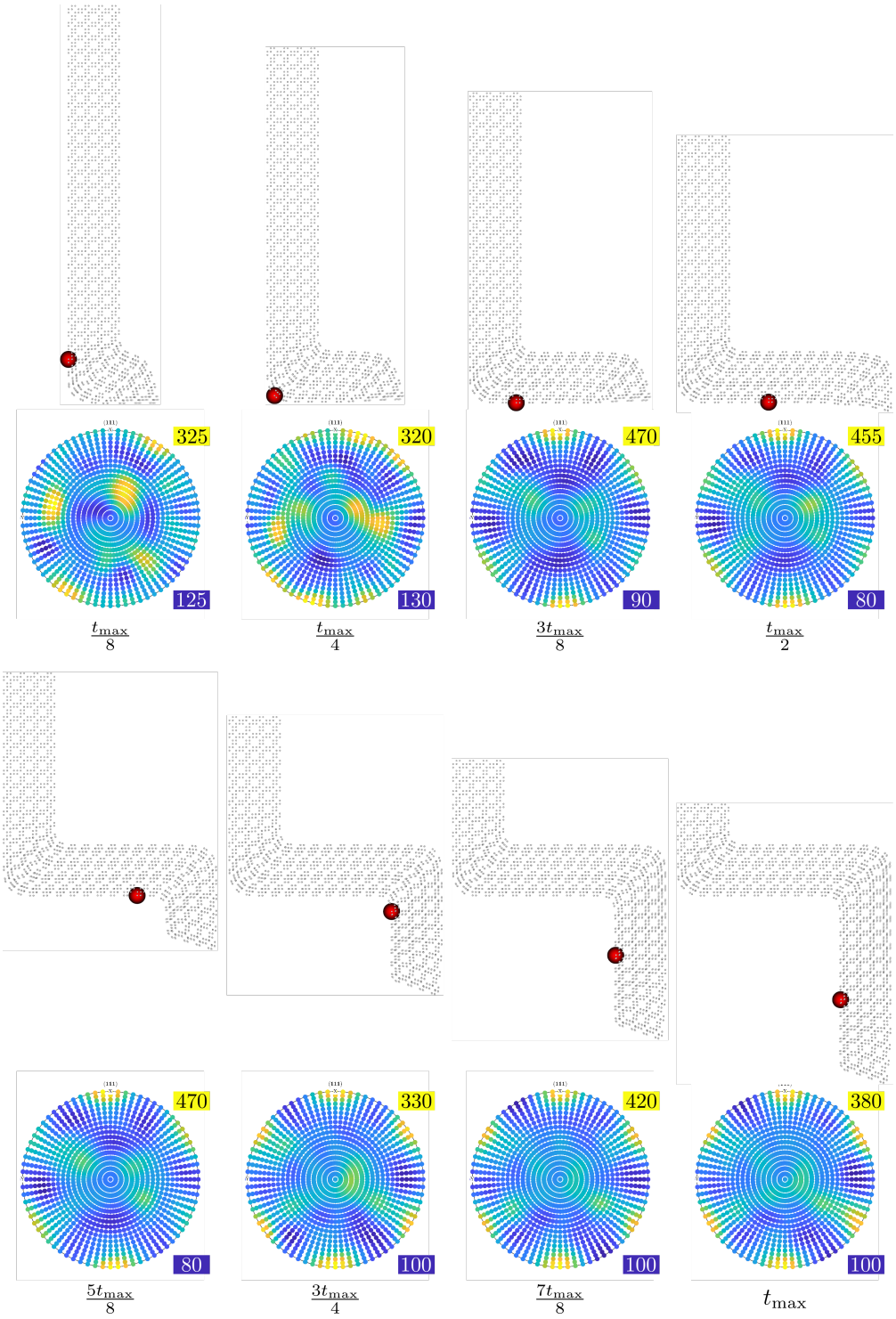

Figure 4.12: Evolution of the material points during a multipass idealizing a 180° turn including the impact on the texture and of the ⟨111⟩ pole family in stereographic projection onto the (001)-plane at $t_{\max}/8$, $t_{\max}/4$, $3t_{\max}/8$, $t_{\max}/2$, $5t_{\max}/8$, $3t_{\max}/4$, $7t_{\max}/8$, and $t_{\max}$. The blue and yellow label next to each pole figure represent, respectively, the minimum and maximum intensity, while the red marking highlights the material point to which the pole figure corresponds.

refinement at the mesoscale. The onset of nucleation extended to the region above the shear bend which we associated with a compressive action on this part of the billet. During post-dynamic recrystallization, the average grain size experienced a relative grain enlargement; the final average grain volume, however, was still smaller than the initial one. In both cases, the deformation of the individual grains led to a pronounced texture development, which is in good agreement with experimental observations for fcc metals undergoing shear deformation.

Concerning the strain heterogeneities, we obtained good qualitative agreement with both numerical and experimental results from Bowen et al. [20]. Quantitatively, the magnitude of the heterogeneities close to the walls did not attain the levels reported by Bowen et al. [20] or Pérez [130] who used a finite element approach. Although the origin of the more pronounced heterogeneities in their case can lie in the inaccuracies associated with severe mesh distortion, an insufficient spatial resolution in our case can also hide these artifacts.

We approximated routes involving multiple passes through a modified channel design. Although this approach does not capture the effects associated with cooling between two extrusions, it granted insights into the impact of multiple bends on the texture evolution. For metals endowed with severe inelastic anisotropy, such as magnesium (see, *e.g.*, Suwas et al. [163]), consecutive passes and the associated turning of the sample is vital to activate various slip systems. For the case of fcc copper, however, the effect on texture was not as pronounced. While the reversal of the shear strain after turning the sample by 180° resulted in a more diffuse texture, the final texture still exhibited six pronounced poles characteristic of extensive shear loading, which is related to the irreversible plastic deformation.

Applying the multiscale approach to ECAE allowed us to replicate findings from previous work on both the numerical as well as the experimental domain. In some instances, however, we challenged hypothesis from related numerical work based on the finite element method. In future studies, we aim for a higher number of nodes with the objective of identifying whether these discrepancies stem from a mitigated susceptibility to large deformation or from insufficient spatial resolution.

Chapter 5

CONCLUSIONS & OUTLOOK

5.1 Summary

In Chapter 1, we summarized previous numerical works on dynamic recrystallization, with particular emphasis on the mesoscale. These works granted valuable insights into numerous aspects of recrystallization. The results were, in general, of qualitative nature, although a number of contributions conducted comparative analyses with experiments. Due to the limited computational resources as well as the challenges associated with numerical stability, the assumptions inherent to these approaches constrained their respective applicability to specific scenarios.

In Chapter 2 we proposed a novel scheme for the modeling of dynamic recrystallization. The general structure of the Field-Monte-Carlo Potts model – which hinges on the idea of interpreting both migration and nucleation in terms of energy-based state switches – allowed to avoid previous constraints. Using a finite deformation framework, we accounted for the challenges involved with metals experiencing severe anisotropic inelasticity. We alleviated the Taylor assumption – which previous works on the modeling of dynamic recrystallization have readily employed – to account for cases with significant intra-granular heterogeneity or stress concentrations near grain or twin boundaries and incorporated an FFT-based solver to satisfy linear momentum conservation. Previous works already included linear momentum conservation; however, they circumvented computational challenges associated with the simultaneous change of the stress field due to recrystallization using simplifying assumptions such as permanently pristine nuclei. To account for the possibility of large strains, in which the capturing of inelastic deformation in nuclei is indispensable, we abandoned this ad-hoc measure. Using a transient interpretation of both migration and nucleation, we accomplished to capture slip- and twin-based deformation in recrystallized material and at the same time retain stability of both the elastic and inelastic solver. We used a variational slip-twinning interaction model for pure magnesium to prove the functionality of this new material model and analyzed the influence of processing parameters on, *e.g.*, the transition of single- to multi-peak stress-strain curves. Since the parameters associated with Monte-Carlo Potts methods are frequently grid-dependent, analyses on the convergence of the scheme

under h-refinement are rare. We elucidated the stability of the Field-Monte-Carlo Potts method by showcasing convergence under h-refinement, first only for grain boundary migration and afterward including nucleation.

Owing to the lack of transient experimental data for dynamic recrystallization in pure magnesium, in Chapter 3, we used data on the uniform compression of pure copper at elevated temperatures to test whether our model can fit experiments. Particularly in view of only three parameters to fit, the agreement in the sense of homogenized stress as well as the microstructural evolution was compelling. Given the computational expense associated with these fully-resolved simulations, however, we introduced and investigated the low-fidelity Taylor model, which deprives grains of their notion of space. Although these computationally inexpensive models fail to accurately replicate the microstructural evolution for low temperatures due to the inability of capturing phenomena such as necklace formations, they show good agreement at higher temperatures. The Taylor model in its current form is not able to track intra-granular heterogeneities such as continuous dynamic recrystallization. At elevated temperatures – when migration effects are dominating nucleation effects – it can, however, capture three central measures of dynamic recrystallization including texture evolution, grain refinement as well as the homogenized stress evolution.

In Chapter 4 we benefited from the computational efficiency of the Taylor model and extended our analysis to the investigation of large scale thermo-mechanical processes. Using the enhanced maximum-entropy based meshfree method developed by Kumar et al. [91], we coupled the macroscale to the Taylor model at the mesoscale and the finite-deformation crystal plasticity model for pure copper at the microscale. Owing to the severe distortion and the simultaneous change of the stress state due to recrystallization at the lower scales, we used equal channel angular extrusion as a challenging test case for this multiscale framework. The results were compelling from both a qualitative as well as a quantitative point of view. On the one hand, the texture evolution showed good agreement with experimental results. On the other hand, the natural implementation of recrystallization in the Taylor model allowed to incorporate both the initial grain refinement at the intersection of the two channels as well as the subsequent post-dynamic recrystallization.

5.2 Future directions

The work presented in this thesis yielded two main accomplishments. On the one hand, we provided the first generalized continuum level framework for the

capturing of dynamic recrystallizations under finite deformations for metals that possess a severe level of anisotropic inelasticity. On the other hand, we established a computationally inexpensive model capable of providing information on the three primary measures of dynamic recrystallization mentioned earlier. Despite these advances, the modeling of dynamic recrystallization is by no means exhausted. In this section, we aim to provide a collection of topics that require further treatment to accomplish the final objective of *materials by design*. We note that this collection solely reflects the author's subjective assessment of the field and is not an exhaustive list of future topics of research in dynamic recrystallization.

5.2.1 Retrieving parameters from the lower scale

Experimental data on the precise migration and nucleation behavior of metals is sparse. Methods such as three-dimensional X-ray diffraction (3DXRD) granted insights into the growth kinetics of individual grains (see, *e.g.*, Lauridsen et al. [94], Schmidt et al. [145]; however, these methods are still too complex for the systematic investigation of specific grain boundaries. Inexpensive insights into grain nucleation and grain boundary migration, therefore, necessitate lower scale numerical models. Possible applications cover the assessment of the assumptions we made in Section 2 concerning the state mappings associated with these two recrystallization phenomena. More than a means of validation, it can also be useful in fitting parameters for the Field-Monte-Carlo Potts model. Simple numerical experiments on the lower scale – such as the migration of a flat grain boundary – can yield information on continuum-level parameters including, *e.g.*, the migration rate κ_{GBM}. This in return circumvents the need for involved experiments to obtain transient data necessary for fitting these parameters.

The work of Somekawa and Mukai [154] provides insights into the range of capabilities afforded by lower scale simulations. Using molecular dynamics, they captured grain boundary migration for different types of grain boundaries (*i.e.*, for different misorientations) in magnesium. Moreover, they analyzed the influence of twinning on grain boundary migration and showed that the addition of solute atoms impeded grain boundary migration as well as the formation of twins. Since experimental data is – in general – of homogenized nature, it is difficult to infer migration rates for specific grain boundary types, which becomes increasingly important with rising levels of anisotropic inelasticity. Godiksen et al. [54] presents a similar approach to model the boundary migration during recrystallization again using molecular dynamics. They investigate flat boundaries, which corresponds to the test case we proposed

earlier for a systematic fitting of larger scale parameters such as the migration and nucleation rate in the Field-Monte-Carlo Potts method.

5.2.2 Coupling the Field Monte Carlo Potts scheme to a vertex method

In Chapter 3, we borrowed the Cu material model from Mellbin et al. [110], which itself concerned the study of dynamic recrystallization in Cu. In their two-dimensional analysis, they used a vertex model to control the emergence and movement of nodes in the sense of both grain nucleation and grain boundary migration. This approach allows eliminating the dependence of migration and nucleation on the mesh, which constitutes a shortcoming in the Field-Monte-Carlo-Potts model. As the grid in a vertex model is irregular and application of, *e.g.*, a finite element method to satisfy linear momentum conservation requires cumbersome remeshing and interpolation rules which are frequently unavailable, they adopted the simplifying Taylor assumption. We propose a hybrid model that combines the benefits of the Field-Monte-Carlo-Potts scheme and the vertex model in a hybrid method.

First, however, we provide a short introduction to vertex models. For simplicity, we describe the 2D-case as employed by Mellbin et al. [110]. Given a space $\Omega \in \mathbb{R}^2$, we define a discrete set of nodes (or vertices) as $\Omega_\Delta \subset \Omega$. At every timestep, we aim to capture the interaction of some node $\boldsymbol{r}_i$ with all nodes $\boldsymbol{r}_j$ from its neighborhood $\mathcal{S}_i$. Based on $\boldsymbol{r}_{ij} = \boldsymbol{r}_i - \boldsymbol{r}_j = \left(x_i - x_j, y_i - y_j\right)^T$ we compute the force acting on node r_i via

$$\boldsymbol{f}_i = -\sum_{j \in \mathcal{S}_i} \gamma_{ij} \frac{\boldsymbol{r}_{ij}}{\left\|\boldsymbol{r}_{ij}\right\|} - \frac{1}{2} \sum_{j \in \mathcal{S}_i} \boldsymbol{n}_{ij} \left\|\boldsymbol{r}_{ij}\right\| \Delta W_{ij}, \tag{5.1}$$

with $\boldsymbol{n}_{ij}$ denoting the normal to $\boldsymbol{r}_{ij}$ and γ_{ij} measuring the surface energy, which can vary with the misorientation between the two grains separated by $\boldsymbol{r}_i$ and $\boldsymbol{r}_j$. ΔW_{ij} denotes the difference in strain energy density as $\Delta W_{ij} = W_i - W_j$ between the two grains adjacent to the boundary outlined by $\boldsymbol{r}_i$ and $\boldsymbol{r}_j$. We define a mobility tensor as

$$\boldsymbol{D}_{ij} = \frac{1}{3 m_{ij} \left\|r_{ij}\right\|} \begin{bmatrix} y_{ij}^2 & -x_{ij} y_{ij} \\ -x_{ij} y_{ij} & x_{ij}^2 \end{bmatrix}, \tag{5.2}$$

where m_{ij} denotes the mobility between the two adjacent grains depending on their misorientation. Using the mobility tensor, we can relate the velocity of the nodes to the nodal forces via

$$\sum_{j \in \mathcal{S}_i} \boldsymbol{D}_{ij} \left(\boldsymbol{v}_i + \frac{1}{2} \boldsymbol{v}_j \right) = \boldsymbol{f}_i . \tag{5.3}$$

Since interpolation rules for a finite deformations crystal plasticity framework are cumbersome, we refrain from using remeshing in our approach. Instead, we suggest decoupling the discretization of space due to the vertex model and due to the elastic solver. More precisely, we propose the inclusion of a regular grid following the approach we adopted in Chapter 2, with grid points holding information on both the elastic deformation as well as the inelastic state variables. Using those grid points, we apply an FFT-based solver to find the deformation field which solves linear momentum conservation. The coupling to the vertex model along with its irregular grid is twofold. First, we define W_i from (5.1), namely the energy inherent in a grain, as the volume average over the entire grain. This addendum to the vertex method is integral, as the alleviation of the Taylor assumption eliminates the notion of a homogeneous energy across the grain. Secondly, as soon as a grain boundary sweeps over a node, we interpret this as migration and subject this node to a state switch similar to the ones defined in Chapter 2.

Since the description of nucleation in the context of vertex models is more involved than the above discussion on migration, we refer the interested reader to Mellbin et al. [110]. We note, however, that a hybridized interpretation for nucleation is straightforward and follows the same principle we pursued in the hybridization of grain migration.

A comparison of the computational expense between this method and the FMCP model from Chapter 2 is not trivial. The hybrid model incurs additional cost through the computation of the average energy per grain, which is not required in the FMCP model. However, the FMCP model involves the evaluation of energy-based state switches at a possibly large number of points, which is why the hybrid model from this chapter is not necessarily computationally more expensive.

5.2.3 Improved Taylor model

In Chapter 3, we analyzed the advantages and shortcomings of the Taylor model. Although the absence of a notion of space is not *per se* an issue, the lack of surface-penalization is. For future purposes – where, *e.g.*, curvature driven growth dominates growth due to gradients in free energy – we propose to amend the model in the following way. Using the notation from Chapter 3, we extend the energetic

formulation from (3.11) by a nonlinear term via

$$\begin{aligned} E &= E(\boldsymbol{F}, Q, \mathcal{R}) \\ &= \sum_{i \in \{1,\dots,N_g\}} \eta_i W(\boldsymbol{F}, \boldsymbol{Q}_i, \boldsymbol{R}_i) + \sum_{i \in \{1,\dots,N_g\}} \gamma \eta_i^{c_s} - \nu \left(\sum_{i \in \{1,\dots,N_g\}} \eta_i - 1.0 \right), \end{aligned} \tag{5.4}$$

where γ denotes a surface penalization constant, and c_s denotes the surface penalization exponent. Using a gradient flow Ansatz yields

$$\dot{\eta}_i = -\frac{1}{\kappa_{\mathrm{GBM}}} \left(W(\boldsymbol{F}, \boldsymbol{Q}_i, \boldsymbol{R}_i) + c_{\mathrm{s}} \eta_i^{c_{\mathrm{s}}-1} - \nu \right) \tag{5.5}$$

and hence

$$\sum_{i=1}^{N_g} \eta_i = 1 \Rightarrow \sum_{i=1}^{N_g} \dot{\eta}_i = 0 \Leftrightarrow \nu = \frac{1}{N_g} \sum_{i=1}^{N_g} \left[W(\boldsymbol{F}, \boldsymbol{Q}_i, \boldsymbol{R}_i) + c_{\mathrm{s}} \eta_i^{c_{\mathrm{s}}-1} \right]. \tag{5.6}$$

The natural choice for penalizing surfaces is given by $c_{\mathrm{s}} = 2/3$. We note, however, that this is not necessarily equivalent to the introduction of a stable grain size. As we can see from the effective update law for the volume fraction

$$\dot{\eta}_i = -\frac{1}{\kappa_{\mathrm{GBM}}} \left(W(\boldsymbol{F}, \boldsymbol{Q}_i, \boldsymbol{R}_i) + \frac{2\gamma}{3} \eta_i^{-1/3} - \frac{\sum_{i=1}^{N_g} \left[W(\boldsymbol{F}, \boldsymbol{Q}_i, \boldsymbol{R}_i) + \frac{2\gamma}{3} \eta_i^{-1/3} \right]}{N_g} \right), \tag{5.7}$$

for grains that possess the same strain energy density but different initial volumes, this scheme would force the initially largest grain to consume all other grains, as the total surface is minimal in the case of one grain. The model can, however, avoid the overapproximation of the average grain diameter in the process of post-dynamic recrystallization. To this end, the sole driver of migration in the Taylor model, which we presented in Chapter 3 is the reduction of stored energy, regardless of the volume fraction of the individual grains. Including a surface term of the above form could achieve an equilibrium between new grains and their low energy state on the one side as well as large grains with their more favorable surface contribution on the other side.

BIBLIOGRAPHY

[1] K. Adam, D. Zöllner, and D.P. Field. 3D microstructural evolution of primary recrystallization and grain growth in cold rolled single-phase aluminum alloys. *Modelling and Simulation in Materials Science and Engineering*, 26(3):035011, 2018. URL http://stacks.iop.org/0965-0393/26/i=3/a=035011.

[2] E. Aghion, B. Bronfin, and D. Eliezer. The role of the magnesium industry in protecting the environment. *Journal of Materials Processing Technology*, 117 (3):381 – 385, 2001. ISSN 0924-0136. doi: https://doi.org/10.1016/S0924-0136(01)00779-8. URL http://www.sciencedirect.com/science/article/pii/S0924013601007798. Containing keynote papers presented at the proceedings of THERMEC'2000, the International conference on Processing and manufacturing of Advanced Materials.

[3] S.R. Agnew, M.H. Yoo, and C.N. Tomé. Application of texture simulation to understanding mechanical behavior of Mg and solid solution alloys containing li or y. *Acta Materialia*, 49(20):4277 – 4289, 2001. ISSN 1359-6454. doi: https://doi.org/10.1016/S1359-6454(01)00297-X. URL http://www.sciencedirect.com/science/article/pii/S135964540100297X.

[4] F. Al-Mufadi and F. Djavanroodi. Finite element modeling and mechanical properties of aluminum proceed by equal channel angular pressing process. *Int. J. of Mech., Aero., Ind. and Mechatr. Engg*, 8:1411–1416, 2014.

[5] T. Al-Samman and G. Gottstein. Dynamic recrystallization during high temperature deformation of magnesium. *Materials Science and Engineering: A*, 490(1):411 – 420, 2008. ISSN 0921-5093. doi: https://doi.org/10.1016/j.msea.2008.02.004. URL http://www.sciencedirect.com/science/article/pii/S0921509308002098.

[6] S.M. Allen and J.W. Cahn. Ground state structures in ordered binary alloys with second neighbor interactions. *Acta Metallurgica*, 20(3):423 – 433, 1972. ISSN 0001-6160. doi: https://doi.org/10.1016/0001-6160(72)90037-5. URL http://www.sciencedirect.com/science/article/pii/0001616072900375.

[7] M.P. Anderson, D.J. Srolovitz, G.S. Grest, and P.S. Sahni. Computer simulation of grain growth - I. Kinetics. *Acta Metallurgica*, 32(5):783 – 791, 1984. ISSN 0001-6160. doi: https://doi.org/10.1016/0001-6160(84)90151-2. URL http://www.sciencedirect.com/science/article/pii/0001616084901512.

[8] M.P. Anderson, G.S. Grest, and D.J. Srolovitz. Computer simulation of normal grain growth in three dimensions. *Philosophical Magazine B*, 59(3):

293–329, 1989. doi: 10.1080/13642818908220181. URL https://doi.org/10.1080/13642818908220181.

[9] S. Andiarwanto, H. Miura, and T. Sakai. Strain rate effect on dynamic nucleation at triple junctions in a copper tricrystal. *Materials Transactions*, 44(10):2213–2219, 2003. doi: 10.2320/matertrans.44.2213. URL https://doi.org/10.2320/matertrans.44.2213.

[10] M. Arroyo and M. Ortiz. Local maximum-entropy approximation schemes: a seamless bridge between finite elements and meshfree methods. *International Journal for Numerical Methods in Engineering*, 65(13):2167–2202, 2006. ISSN 1097-0207. doi: 10.1002/nme.1534. URL http://dx.doi.org/10.1002/nme.1534.

[11] P. Asadi, M.K.B. Givi, and M. Akbari. Microstructural simulation of friction stir welding using a cellular automaton method: a microstructure prediction of AZ91 magnesium alloy. *International Journal of Mechanical and Materials Engineering*, 10(1):20, 2015. doi: 10.1186/s40712-015-0048-5. URL https://doi.org/10.1186/s40712-015-0048-5.

[12] R.J. Asaro. Micromechanics of crystals and polycrystals. In *Advances in Applied Mechanics*, volume 23, pages 1–115. Elsevier, 1983. doi: https://doi.org/10.1016/S0065-2156(08)70242-4. URL http://www.sciencedirect.com/science/article/pii/S0065215608702424.

[13] M. Avrami. Kinetics of phase change – I. general theory. *The Journal of Chemical Physics*, 7(12):1103–1112, 1939. doi: 10.1063/1.1750380. URL https://doi.org/10.1063/1.1750380.

[14] M. Bacca, D.R. Hayhurst, and R.M. McMeeking. Continuous dynamic recrystallization during severe plastic deformation. *Mechanics of Materials*, 90:148 – 156, 2015. ISSN 0167-6636. doi: https://doi.org/10.1016/j.mechmat.2015.05.008. URL http://www.sciencedirect.com/science/article/pii/S0167663615001222. Proceedings of the IUTAM Symposium on Micromechanics of Defects in Solids.

[15] M. Bernacki, H. Resk, T. Coupez, and R.E. Logé. Finite element model of primary recrystallization in polycrystalline aggregates using a level set framework. *Modelling and Simulation in Materials Science and Engineering*, 17(6):064006, 2009. URL http://stacks.iop.org/0965-0393/17/i=6/a=064006.

[16] M. Bernacki, R.E. Logé, and T. Coupez. Level set framework for the finite-element modelling of recrystallization and grain growth in polycrystalline materials. *Scripta Materialia*, 64(6):525 – 528, 2011. ISSN 1359-6462. doi: https://doi.org/10.1016/j.scriptamat.2010.11.032. URL http://www.sciencedirect.com/science/article/pii/S1359646210007906.

[17] Y. Beygelzimer, V.N. Varyukhin, S.G. Synkov, A.N. Sapronov, and V.G. Synkov. New schemes of large plastic deformations accumulating with using of hydroextrusion. *Phys. Technol. High Press*, 9(3):109–111, 1999.

[18] L. Blaz, T. Sakai, and J.J. Jonas. Effect of initial grain size on dynamic recrystallization of copper. *Metal Science*, 17(12):609–616, 1983. doi: 10.1179/030634583790420448. URL https://doi.org/10.1179/030634583790420448.

[19] O. Bouaziz and P. Buessler. Iso-work increment assumption for heterogeneous material behaviour modelling. *Advanced Engineering Materials*, 6(1-2):79–83, 2004. doi: 10.1002/adem.200300524. URL https://onlinelibrary.wiley.com/doi/abs/10.1002/adem.200300524.

[20] J.R. Bowen, A. Gholinia, S.M. Roberts, and P.B. Prangnell. Analysis of the billet deformation behaviour in equal channel angular extrusion. *Materials Science and Engineering: A*, 287(1):87 – 99, 2000. ISSN 0921-5093. doi: https://doi.org/10.1016/S0921-5093(00)00834-0. URL http://www.sciencedirect.com/science/article/pii/S0921509300008340.

[21] P.W. Bridgman. On torsion combined with compression. *Journal of Applied Physics*, 14(6):273–283, 1943.

[22] C.A. Bronkhorst, S.R. Kalidindi, and L. Anand. Polycrystalline plasticity and the evolution of crystallographic texture in fcc metals. *Phil. Trans. R. Soc. Lond. A*, 341(1662):443–477, 1992. doi: 10.1098/rsta.1992.0111. URL https://doi.org/10.1098/rsta.1992.0111.

[23] E.P. Busso. A continuum theory for dynamic recrystallization with microstructure-related length scales. *International Journal of Plasticity*, 14 (4):319 – 353, 1998. ISSN 0749-6419. doi: https://doi.org/10.1016/S0749-6419(98)00008-4. URL http://www.sciencedirect.com/science/article/pii/S0749641998000084.

[24] S.A.E. Buxton and S.C. Browning. Turn-up and turn-down in hot rolling: A study on a model mill using plasticine. *Journal of Mechanical Engineering Science*, 14(4):245–254, 1972. doi: 10.1243/JMES_JOUR_1972_014_032_02. URL https://doi.org/10.1243/JMES_JOUR_1972_014_032_02.

[25] H. Cetinel, O. Kayacan, and D. Ozaydin. Investigation of nucleation and grain growth in 2-dimensional systems by using generalized monte carlo simulations. *Physica A: Statistical Mechanics and its Applications*, 392 (18):4121 – 4126, 2013. ISSN 0378-4371. doi: https://doi.org/10.1016/j.physa.2013.04.040. URL http://www.sciencedirect.com/science/article/pii/S0378437113003531.

[26] Y. Chang and D.M. Kochmann. A variational constitutive model for slip-twinning interactions in hcp metals: application to single-and poly-crystalline magnesium. *International Journal of Plasticity*, 73:39 – 61, 2015. ISSN 0749-6419. doi: https://doi.org/10.1016/j.ijplas.2015.03.008. URL http://www.sciencedirect.com/science/article/pii/S0749641915000637. Special Issue on Constitutive Modeling from Micro-Scale to Continuum in Honor of Prof. Frédéric Barlat.

[27] Y. Chang, J.T. Lloyd, R. Becker, and D.M. Kochmann. Modeling microstructure evolution in magnesium: Comparison of detailed and reduced-order kinematic models. *Mechanics of Materials*, 108:40 – 57, 2017. ISSN 0167-6636. doi: https://doi.org/10.1016/j.mechmat.2017.02.007. URL http://www.sciencedirect.com/science/article/pii/S0167663616303805.

[28] L. Chen, J. Chen, R.A. Lebensohn, Y.Z. Ji, T.W. Heo, S. Bhattacharyya, K. Chang, S. Mathaudhu, Z.K. Liu, and L.-Q. Chen. An integrated fast Fourier transform-based phase-field and crystal plasticity approach to model recrystallization of three dimensional polycrystals. *Computer Methods in Applied Mechanics and Engineering*, 285:829–848, 2015. doi: https://doi.org/10.1016/j.cma.2014.12.007. URL http://www.sciencedirect.com/science/article/pii/S0045782514004861.

[29] J.W. Christian and S. Mahajan. Deformation twinning. *Progress in Materials Science*, 39(1):1 – 157, 1995. ISSN 0079-6425. doi: https://doi.org/10.1016/0079-6425(94)00007-7. URL http://www.sciencedirect.com/science/article/pii/0079642594000077.

[30] D.G. Cram, H.S. Zurob, Y.J.M. Brechet, and C.R. Hutchinson. Modelling discontinuous dynamic recrystallization using a physically based model for nucleation. *Acta Materialia*, 57(17):5218 – 5228, 2009. ISSN 1359-6454. doi: https://doi.org/10.1016/j.actamat.2009.07.024. URL http://www.sciencedirect.com/science/article/pii/S1359645409004480.

[31] Y. Cui, Y. Li, S. Sun, H. Bian, H. Huang, Z. Wang, Y. Koizumi, and A. Chiba. Enhanced damping capacity of magnesium alloys by tensile twin boundaries. *Scripta Materialia*, 101:8 – 11, 2015. ISSN 1359-6462. doi: https://doi.org/10.1016/j.scriptamat.2015.01.002. URL http://www.sciencedirect.com/science/article/pii/S1359646215000160.

[32] R. Ding and Z.X. Guo. Coupled quantitative simulation of microstructural evolution and plastic flow during dynamic recrystallization. *Acta Materialia*, 49(16):3163 – 3175, 2001. ISSN 1359-6454. doi: https://doi.org/10.1016/S1359-6454(01)00233-6. URL http://www.sciencedirect.com/science/article/pii/S1359645401002336.

[33] F. Djavanroodi, B. Omranpour, M. Ebrahimi, and M. Sedighi. Designing of ecap parameters based on strain distribution uniformity. *Progress in Natu-*

ral Science: Materials International, 22(5):452 – 460, 2012. ISSN 1002-0071. doi: https://doi.org/10.1016/j.pnsc.2012.08.001. URL http://www.sciencedirect.com/science/article/pii/S1002007112000883.

[34] R.D. Doherty, K. Kashyap, and S. Panchanadeeswaran. Direct observation of the development of recrystallization texture in commercial purity aluminum. *Acta Metallurgica et Materialia*, 41(10):3029 – 3053, 1993. ISSN 0956-7151. doi: https://doi.org/10.1016/0956-7151(93)90117-B. URL http://www.sciencedirect.com/science/article/pii/095671519390117B.

[35] R.D. Doherty, D.A. Hughes, F.J. Humphreys, J.J. Jonas, D.Juul Jensen, M.E. Kassner, W.E. King, T.R. McNelley, H.J. McQueen, and A.D. Rollett. Current issues in recrystallization: a review. *Materials Science and Engineering: A*, 238(2):219 – 274, 1997. ISSN 0921-5093. doi: https://doi.org/10.1016/S0921-5093(97)00424-3. URL http://www.sciencedirect.com/science/article/pii/S0921509397004243.

[36] P. Eisenlohr, M. Diehl, R.A. Lebensohn, and F. Roters. A spectral method solution to crystal elasto-viscoplasticity at finite strains. *International Journal of Plasticity*, 46:37 – 53, 2013. ISSN 0749-6419. doi: https://doi.org/10.1016/j.ijplas.2012.09.012. URL http://www.sciencedirect.com/science/article/pii/S0749641912001428. Microstructure-based Models of Plastic Deformation.

[37] M. Elsey, S. Esedoglu, and P. Smereka. Large-scale simulations and parameter study for a simple recrystallization model. *Philosophical Magazine*, 91(11): 1607–1642, 2011. doi: 10.1080/14786435.2010.546377. URL https://doi.org/10.1080/14786435.2010.546377.

[38] M. Esmaily, J.E. Svensson, S. Fajardo, N. Birbilis, G.S. Frankel, S. Virtanen, R. Arrabal, S. Thomas, and L.G. Johansson. Fundamentals and advances in magnesium alloy corrosion. *Progress in Materials Science*, 89:92 – 193, 2017. ISSN 0079-6425. doi: https://doi.org/10.1016/j.pmatsci.2017.04.011. URL http://www.sciencedirect.com/science/article/pii/S0079642517300506.

[39] Y. Estrin and H. Mecking. A unified phenomenological description of work hardening and creep based on one-parameter models. *Acta Metallurgica*, 32(1):57–70, 1984. doi: https://doi.org/10.1016/0001-6160(84)90202-5. URL http://www.sciencedirect.com/science/article/pii/0001616084902025.

[40] Y. Estrin and A. Vinogradov. Extreme grain refinement by severe plastic deformation: A wealth of challenging science. *Acta Materialia*, 61(3):782 – 817, 2013. ISSN 1359-6454. doi: https://doi.org/10.1016/j.actamat.2012.10.038. URL http://www.sciencedirect.com/science/article/pii/S1359645412007859. The Diamond Jubilee Issue.

[41] T. Fagan, R. Das, V. Lemiale, and Y. Estrin. Modelling of equal channel angular pressing using a mesh-free method. *Journal of Materials Science*, 47(11):4514–4519, Jun 2012. ISSN 1573-4803. doi: 10.1007/s10853-012-6296-3. URL https://doi.org/10.1007/s10853-012-6296-3.

[42] S.M. Fatemi-Varzaneh, A. Zarei-Hanzaki, and H. Beladi. Dynamic recrystallization in AZ31 magnesium alloy. *Materials Science and Engineering: A*, 456(1):52 – 57, 2007. ISSN 0921-5093. doi: https://doi.org/10.1016/j.msea.2006.11.095. URL http://www.sciencedirect.com/science/article/pii/S092150930602507X.

[43] S.M. Fatemi-Varzaneh, A. Zarei-Hanzaki, and R. Vaghar. Discontinuous dynamic recrystallization during accumulative back extrusion of a magnesium alloy. *Journal of Ultrafine Grained and Nanostructured Materials*, 46(1): 25–29, 2013. ISSN 2423-6845. doi: 10.7508/jufgnsm.2013.01.004. URL https://jufgnsm.ut.ac.ir/article_35908.html.

[44] R.B. Figueiredo, P.R. Cetlin, and T.G. Langdon. Using finite element modeling to examine the flow processes in quasi-constrained high-pressure torsion. *Materials Science and Engineering: A*, 528(28):8198 – 8204, 2011. ISSN 0921-5093. doi: https://doi.org/10.1016/j.msea.2011.07.040. URL http://www.sciencedirect.com/science/article/pii/S0921509311008197.

[45] P. Frint, T. Hockauf, M.and Halle, G. Strehl, T. Lampke, and M.F.X. Wagner. Microstructural features and mechanical properties after industrial scale ecap of an al 6060 alloy. In *Nanomaterials by Severe Plastic Deformation: NanoSPD5*, volume 667 of *Materials Science Forum*, pages 1153–1158. Trans Tech Publications, 2 2010. doi: 10.4028/www.scientific.net/MSF.667-669.1153.

[46] H.J. Frost and M.F. Ashby. *Deformation mechanism maps: the plasticity and creep of metals and ceramics*. Pergamon press, 1982.

[47] M. W. Fu, M.S. Yong, Q.X. Pei, and H.H. Hng. Deformation behavior study of multi-pass ecae process for fabrication of ultrafine or nanostructured bulk materials. *Materials and Manufacturing Processes*, 21(5):507–512, 2006. doi: 10.1080/10426910500471557. URL https://doi.org/10.1080/10426910500471557.

[48] M. Furui, C. Xu, T. Aida, M. Inoue, H. Anada, and T.G. Langdon. Improving the superplastic properties of a two-phase mg–8through processing by ecap. *Materials Science and Engineering: A*, 410-411:439 – 442, 2005. ISSN 0921-5093. doi: https://doi.org/10.1016/j.msea.2005.08.143. URL http://www.sciencedirect.com/science/article/pii/S0921509305008907. The Langdon Symposium: Flow and forming of Crystalline Materials.

[49] R. Galeyev, O. Valiakhmetov, and G. Salishchev. Dynamic crystallization of coarse grained titanium base vt8 alloy in (a+ b) field. *Russ. Metall*, 4:97–103, 1990.

[50] W. Gao, A. Belyakov, H. Miura, and T. Sakai. Dynamic recrystallization of copper polycrystals with different purities. *Materials Science and Engineering: A*, 265(1):233 – 239, 1999. ISSN 0921-5093. doi: https://doi.org/10.1016/S0921-5093(99)00004-0. URL http://www.sciencedirect.com/science/article/pii/S0921509399000040.

[51] M.G.D. Geers, V.G. Kouznetsova, and W.A.M. Brekelmans. Multi-scale computational homogenization: Trends and challenges. *Journal of Computational and Applied Mathematics*, 234(7):2175 – 2182, 2010. ISSN 0377-0427. doi: https://doi.org/10.1016/j.cam.2009.08.077. URL http://www.sciencedirect.com/science/article/pii/S0377042709005536.

[52] S.P. Gentry and K. Thornton. Simulating recrystallization in titanium using the phase field method. In *IOP Conference Series: Materials Science and Engineering*, volume 89, page 012024. IOP Publishing, 2015. URL http://stacks.iop.org/1757-899X/89/i=1/a=012024.

[53] R.J. Glauber. Time-dependent statistics of the Ising model. *Journal of Mathematical Physics*, 4(2):294–307, 1963. doi: 10.1063/1.1703954. URL https://doi.org/10.1063/1.1703954.

[54] R.B. Godiksen, Z.T. Trautt, M. Upmanyu, J.Schiotz, D.J. Jensen, and S. Schmidt. Simulations of boundary migration during recrystallization using molecular dynamics. *Acta Materialia*, 55(18):6383 – 6391, 2007. ISSN 1359-6454. doi: https://doi.org/10.1016/j.actamat.2007.07.055. URL http://www.sciencedirect.com/science/article/pii/S1359645407005277.

[55] R.L. Goetz and V. Seetharaman. Modeling dynamic recrystallization using cellular automata. *Scripta Materialia*, 38(3), 1998. doi: https://doi.org/10.1016/j.msea.2017.11.024. URL http://www.sciencedirect.com/science/article/pii/S0921509317314740.

[56] S. Gourdet and F. Montheillet. A model of continuous dynamic recrystallization. *Acta Materialia*, 51(9):2685 – 2699, 2003. ISSN 1359-6454. doi: https://doi.org/10.1016/S1359-6454(03)00078-8. URL http://www.sciencedirect.com/science/article/pii/S1359645403000788.

[57] S. Graff, W. Brocks, and D. Steglich. Yielding of magnesium: From single crystal to polycrystalline aggregates. *International Journal of Plasticity*, 23 (12):1957 – 1978, 2007. ISSN 0749-6419. doi: https://doi.org/10.1016/j.ijplas.2007.07.009. URL http://www.sciencedirect.com/science/article/pii/S0749641907001076.

[58] P. Hakansson, M. Wallin, and M. Ristinmaa. Prediction of stored energy in polycrystalline materials during cyclic loading. *International Journal of Solids and Structures*, 45(6):1570 – 1586, 2008. ISSN 0020-7683. doi: https://doi.org/10.1016/j.ijsolstr.2007.10.009. URL http://www.sciencedirect.com/science/article/pii/S0020768307004192.

[59] E.O. Hall. The deformation and ageing of mild steel: III discussion of results. *Proceedings of the Physical Society. Section B*, 64(9):742, 1951. URL http://stacks.iop.org/0370-1301/64/i=9/a=302.

[60] H. Hallberg. Approaches to modeling of recrystallization. *Metals*, 1(1):16–48, 2011. doi: 10.3390/met1010016. URL http://www.mdpi.com/2075-4701/1/1/16.

[61] H. Hallberg. Influence of process parameters on grain refinement in aa1050 aluminum during cold rolling. *International Journal of Mechanical Sciences*, 66:260 – 272, 2013. ISSN 0020-7403. doi: https://doi.org/10.1016/j.ijmecsci.2012.11.016. URL http://www.sciencedirect.com/science/article/pii/S0020740312002585.

[62] H. Hallberg, M. Wallin, and M. Ristinmaa. Simulation of discontinuous dynamic recrystallization in pure Cu using a probabilistic cellular automaton. *Computational Materials Science*, 49(1):25 – 34, 2010. ISSN 0927-0256. doi: https://doi.org/10.1016/j.commatsci.2010.04.012. URL http://www.sciencedirect.com/science/article/pii/S0927025610002259.

[63] H. Hallberg, M. Wallin, and M. Ristinmaa. Modeling of continuous dynamic recrystallization in commercial-purity aluminum. *Materials Science and Engineering: A*, 527(4):1126 – 1134, 2010. ISSN 0921-5093. doi: https://doi.org/10.1016/j.msea.2009.09.043. URL http://www.sciencedirect.com/science/article/pii/S0921509309010922.

[64] H. Hallberg, B. Svendsen, T. Kayser, and M. Ristinmaa. Microstructure evolution during dynamic discontinuous recrystallization in particle-containing cu. *Computational Materials Science*, 84:327 – 338, 2014. ISSN 0927-0256. doi: https://doi.org/10.1016/j.commatsci.2013.12.021. URL http://www.sciencedirect.com/science/article/pii/S0927025613007714.

[65] T. Hausöl, V. Maier, C.W. Schmidt, M. Winkler, H.W. Höppel, and M. Göken. Tailoring materials properties by accumulative roll bonding. *Advanced Engineering Materials*, 12(8):740–746, 2010. doi: 10.1002/adem.201000044. URL https://onlinelibrary.wiley.com/doi/abs/10.1002/adem.201000044.

[66] R. Hielscher and H. Schaeben. A novel pole figure inversion method: specification of the MTEX algorithm. *Journal of Applied Crystallography*, 41(6):1024–1037, Dec 2008. doi: 10.1107/S0021889808030112. URL https://doi.org/10.1107/S0021889808030112.

[67] M. Homayonifar and J. Mosler. On the coupling of plastic slip and deformation-induced twinning in magnesium: A variationally consistent approach based on energy minimization. *International Journal of Plasticity*, 27(7):983 – 1003, 2011. ISSN 0749-6419. doi: https://doi.org/10.1016/j.ijplas.2010.10.009. URL http://www.sciencedirect.com/science/article/pii/S0749641910001786.

[68] K. Huang and R.E. Logé. A review of dynamic recrystallization phenomena in metallic materials. *Materials & Design*, 111:548 – 574, 2016. ISSN 0264-1275. doi: https://doi.org/10.1016/j.matdes.2016.09.012. URL http://www.sciencedirect.com/science/article/pii/S0264127516311753.

[69] J.W. Hutchinson. Bounds and self-consistent estimates for creep of polycrystalline materials. *Proc. R. Soc. Lond. A*, 348(1652):101–127, 1976. doi: 10.1098/rspa.1976.0027. URL http://doi.org/10.1098/rspa.1976.0027.

[70] M. Irani and M. Joun. Determination of JMAK dynamic recrystallization parameters through FEM optimization techniques. *Computational Materials Science*, 142:178–184, 2018. doi: https://doi.org/10.1016/j.commatsci.2017.10.007. URL http://www.sciencedirect.com/science/article/pii/S0927025617305487.

[71] E. Ising. Beitrag zur Theorie des Ferromagnetismus. *Zeitschrift für Physik A Hadrons and Nuclei*, 31(1):253–258, 1925.

[72] O.M. Ivasishin, S.V. Shevchenko, N.L. Vasiliev, and S.L. Semiatin. A 3-D Monte-Carlo (Potts) model for recrystallization and grain growth in polycrystalline materials. *Materials Science and Engineering: A*, 433(1):216–232, 2006. doi: https://doi.org/10.1016/j.msea.2006.06.115. URL http://www.sciencedirect.com/science/article/pii/S0921509306012597.

[73] Y. Iwahashi, J. Wang, Z. Horita, M. Nemoto, and T.G. Langdon. Principle of equal-channel angular pressing for the processing of ultra-fine grained materials. *Scripta Materialia*, 35(2):143 – 146, 1996. ISSN 1359-6462. doi: https://doi.org/10.1016/1359-6462(96)00107-8. URL http://www.sciencedirect.com/science/article/pii/1359646296001078.

[74] K.G.F. Janssens, D. Raabe, E. Kozeschnik, M.A. Miodownik, and B. Nestler. *Computational materials engineering: An introduction to microstructure evolution*. Academic Press, 2010.

[75] E. T. Jaynes. Information theory and statistical mechanics. *Phys. Rev.*, 106:620–630, 1957. doi: 10.1103/PhysRev.106.620. URL https://link.aps.org/doi/10.1103/PhysRev.106.620.

[76] M. Jedrychowski, B. Bacroix, O.U. Salman, J. Tarasiuk, and S. Wronski. Investigation of SIBM driven recrystallization in alpha zirconium based on EBSD data and monte carlo modeling. *IOP Conference Series: Materials Science and Engineering*, 89:012029, aug 2015. doi: 10.1088/1757-899x/89/1/012029. URL https://doi.org/10.1088/1757-899x/89/1/012029.

[77] Y.H. Ji and J.J. Park. Development of severe plastic deformation by various asymmetric rolling processes. *Materials Science and Engineering: A*, 499(1): 14 – 17, 2009. ISSN 0921-5093. doi: https://doi.org/10.1016/j.msea.2007.11.099. URL http://www.sciencedirect.com/science/article/pii/S0921509308006059. Fifth International Conference on Physical and Numerical Simulations of Material Processing (ICPNS 2007) held at Zhengzhou, China, October 23-27, 2007.

[78] Y.H. Ji, J.J. Park, and W.J. Kim. Finite element analysis of severe deformation in mg–3al–1zn sheets through differential-speed rolling with a high speed ratio. *Materials Science and Engineering: A*, 454-455:570 – 574, 2007. ISSN 0921-5093. doi: https://doi.org/10.1016/j.msea.2006.11.076. URL http://www.sciencedirect.com/science/article/pii/S0921509306024816.

[79] W.A. Johnson and R.F. Mehl. Reaction kinetics in process of nucleation and growth. *Transaction of AIME*, 135:416–458, 1939.

[80] M. Kabel, T. Böhlke, and M. Schneider. Efficient fixed point and Newton–Krylov solvers for FFT-based homogenization of elasticity at large deformations. *Computational Mechanics*, 54(6):1497–1514, 2014. doi: 10.1007/s00466-014-1071-8. URL https://doi.org/10.1007/s00466-014-1071-8.

[81] S.R. Kalidindi. Modeling anisotropic strain hardening and deformation textures in low stacking fault energy fcc metals. *International Journal of Plasticity*, 17(6):837 – 860, 2001. ISSN 0749-6419. doi: https://doi.org/10.1016/S0749-6419(00)00071-1. URL http://www.sciencedirect.com/science/article/pii/S0749641900000711.

[82] K.T. Kashyap and T. Chandrashekar. Effects and mechanisms of grain refinement in aluminium alloys. *Bulletin of Materials Science*, 24(4):345–353, Aug 2001. ISSN 0973-7669. doi: 10.1007/BF02708630. URL https://doi.org/10.1007/BF02708630.

[83] M. Khadyko, C.D. Marioara, I.G. Ringdalen, S. Dumoulin, and O.S. Hopperstad. Deformation and strain localization in polycrystals with plastically heterogeneous grains. *International Journal of Plasticity*, 86:128 – 150, 2016. ISSN 0749-6419. doi: https://doi.org/10.1016/j.ijplas.2016.08.005. URL http://www.sciencedirect.com/science/article/pii/S0749641916301401.

[84] H.S. Kim, P. Quang, M.H. Seo, S.I. Hong, K.H. Baik, H.R. Lee, and M.N. Do. Process modelling of equal channel angular pressing for ultrafine grained materials. *Materials transactions*, 45(7):2172–2176, 2004. doi: 10.2320/matertrans.45.2172. URL https://www.jstage.jst.go.jp/article/matertrans/45/7/45_7_2172/_article.

[85] M. Knezevic, M. Zecevic, I.J. Beyerlein, and R.A. Lebensohn. A numerical procedure enabling accurate descriptions of strain rate-sensitive flow of polycrystals within crystal visco-plasticity theory. *Computer Methods in Applied Mechanics and Engineering*, 308:468 – 482, 2016. ISSN 0045-7825. doi: https://doi.org/10.1016/j.cma.2016.05.025. URL http://www.sciencedirect.com/science/article/pii/S0045782516304364.

[86] A.N. Kolmogorov. On the statistical theory of the crystallization of metals. *Bull. Acad. Sci. USSR, Math. Ser*, 1:355–359, 1937.

[87] V. Kouznetsova, W. A. M. Brekelmans, and F. P. T. Baaijens. An approach to micro-macro modeling of heterogeneous materials. *Computational Mechanics*, 27(1):37–48, Jan 2001. ISSN 1432-0924. doi: 10.1007/s004660000212. URL https://doi.org/10.1007/s004660000212.

[88] T. Krajňák, P. Minárik, J. Stráská, J. Gubicza, K. Máthis, and M. Janeček. Influence of the initial state on the microstructure and mechanical properties of ax41 alloy processed by ecap. *Journal of Materials Science*, 54(4):3469–3484, Feb 2019. ISSN 1573-4803. doi: 10.1007/s10853-018-3033-6. URL https://doi.org/10.1007/s10853-018-3033-6.

[89] V.A. Krasnoveikin, V. Skripnyak, A.A. Kozulin, and O. Senatova. Numerical simulation of severe plastic deformation of titanium specimens under dynamic channel pressing. In *High Technology: Research and Applications*, volume 1040 of *Advanced Materials Research*, pages 107–112. Trans Tech Publications, 11 2014. doi: 10.4028/www.scientific.net/AMR.1040.107.

[90] S. Kumar. *An enhanced maximum-entropy based meshfree method: theory and application*. PhD thesis, California Institute of Technology, 2019.

[91] S. Kumar, K. Danas, and D.M. Kochmann. Enhanced local maximum-entropy approximation for stable meshfree simulations. *Computer Methods in Applied Mechanics and Engineering*, 344:858 – 886, 2019. ISSN 0045-7825. doi: https://doi.org/10.1016/j.cma.2018.10.030. URL http://www.sciencedirect.com/science/article/pii/S0045782518305346.

[92] A. Lallit. Single-crystal elasto-viscoplasticity: application to texture evolution in polycrystalline metals at large strains. *Computer Methods in Applied Mechanics and Engineering*, 193(48):5359 – 5383, 2004. ISSN 0045-7825. doi: https://doi.org/10.1016/j.cma.2003.12.068. URL http://www.sciencedirect.com/science/article/pii/S0045782504002786. Advances in Computational Plasticity.

[93] R. Lapovok, L.S. Tóth, M. Winkler, and S.L. Semiatin. A comparison of continuous spd processes for improving the mechanical properties of aluminum alloy 6111. *Journal of Materials Research*, 24(2):459–469, 2009. doi: 10.1557/JMR.2009.0060.

[94] E.M. Lauridsen, H.F. Poulsen, S.F Nielsen, and D.J. Jensen. Recrystallization kinetics of individual bulk grains in 90cold-rolled aluminium. *Acta Materialia*, 51(15):4423 – 4435, 2003. ISSN 1359-6454. doi: https://doi.org/10.1016/S1359-6454(03)00278-7. URL http://www.sciencedirect.com/science/article/pii/S1359645403002787.

[95] R.A. Lebensohn and A. Needleman. Numerical implementation of non-local polycrystal plasticity using fast Fourier transforms. *Journal of the Mechanics and Physics of Solids*, 97:333 – 351, 2016. ISSN 0022-5096. doi: http://dx.doi.org/10.1016/j.jmps.2016.03.023. URL http://www.sciencedirect.com/science/article/pii/S0022509616301958.

[96] R.A. Lebensohn, A.K. Kanjarla, and P. Eisenlohr. An elasto-viscoplastic formulation based on fast Fourier transforms for the prediction of micromechanical fields in polycrystalline materials. *International Journal of Plasticity*, 32-33:59 – 69, 2012. ISSN 0749-6419. doi: https://doi.org/10.1016/j.ijplas.2011.12.005. URL http://www.sciencedirect.com/science/article/pii/S0749641911001951.

[97] H.M. Ledbetter and E.R. Naimon. Elastic properties of metals and alloys. ii. copper. *Journal of Physical and Chemical Reference Data*, 3(4):897–935, 1974. doi: 10.1063/1.3253150. URL https://doi.org/10.1063/1.3253150.

[98] S.H. Lee, Y. Saito, N. Tsuji, H. Utsunomiya, and T. Sakai. Role of shear strain in ultragrain refinement by accumulative roll-bonding (arb) process. *Scripta Materialia*, 46(4):281 – 285, 2002. ISSN 1359-6462. doi: https://doi.org/10.1016/S1359-6462(01)01239-8. URL http://www.sciencedirect.com/science/article/pii/S1359646201012398.

[99] Y. C. Lee, A. K. Dahle, and D. H. StJohn. *Grain Refinement of Magnesium*, pages 247–254. Springer International Publishing, Cham, 2016. doi: 10.1007/978-3-319-48099-2_41. URL https://doi.org/10.1007/978-3-319-48099-2_41.

[100] Y. Li, C. Yang, X. Zeng, P. Jin, D. Qiu, and W. Ding. Microstructure evolution and mechanical properties of magnesium alloys containing long period stacking ordered phase. *Materials Characterization*, 141:286 – 295, 2018. ISSN 1044-5803. doi: https://doi.org/10.1016/j.matchar.2018.04.044. URL http://www.sciencedirect.com/science/article/pii/S1044580318300445.

[101] C. Liao, H. Wu, C. Wu, F. Zhu, and S. Lee. Hot deformation behavior and flow stress modeling of annealed AZ61 mg alloys. *Progress in Natural Science: Materials International*, 24(3):253–265, 2014. doi: https://doi.org/10.1016/j.pnsc.2014.04.006. URL http://www.sciencedirect.com/science/article/pii/S1002007114000446.

[102] Z.-C. Lin and C.-C. Shen. Three-dimensional asymmetrical rolling of an aluminium flat strip using an elastic-plastic finite element method. *International Journal of Computer Applications in Technology*, 9(5-6):281–297, 1996. URL https://www.scopus.com/inward/record.uri?eid=2-s2.0-0030416802&partnerID=40&md5=a4f8f0bc0e2e45bbc7f7f46d03337f9d. cited By 1.

[103] C. J. Luis, Y. Garcés, P. González, and C. Berlanga. Fem analysis of equal channel angular processes. *Materials and Manufacturing Processes*, 17(2):223–250, 2002. doi: 10.1081/AMP-120003532. URL https://doi.org/10.1081/AMP-120003532.

[104] A. Ma and A. Hartmaier. A crystal plasticity smooth-particle hydrodynamics approach and its application to equal-channel angular pressing simulation. *Modelling and Simulation in Materials Science and Engineering*, 24(8):085011, 2016. URL http://stacks.iop.org/0965-0393/24/i=8/a=085011.

[105] Q. Ma, B. Li, W.R. Whittington, A.L. Oppedal, P.T. Wang, and M.F. Horstemeyer. Texture evolution during dynamic recrystallization in a magnesium alloy at 450°c. *Acta Materialia*, 67:102 – 115, 2014. ISSN 1359-6454. doi: https://doi.org/10.1016/j.actamat.2013.12.025. URL http://www.sciencedirect.com/science/article/pii/S1359645413009609.

[106] H. Mecking and U.F. Kocks. Kinetics of flow and strain-hardening. *Acta Metallurgica*, 29(11):1865 – 1875, 1981. ISSN 0001-6160. doi: https://doi.org/10.1016/0001-6160(81)90112-7. URL http://www.sciencedirect.com/science/article/pii/0001616081901127.

[107] S.F. Medina and C.A. Hernandez. Modelling of the dynamic recrystallization of austenite in low alloy and microalloyed steels. *Acta Materialia*, 44(1):165 – 171, 1996. ISSN 1359-6454. doi: https://doi.org/10.1016/1359-6454(95)00154-6. URL http://www.sciencedirect.com/science/article/pii/1359645495001546.

[108] Y. Mellbin, H. Hallberg, and M. Ristinmaa. Accelerating crystal plasticity simulations using gpu multiprocessors. *International Journal for Numerical Methods in Engineering*, 100(2):111–135, 2014. doi: 10.1002/nme.4724. URL https://onlinelibrary.wiley.com/doi/abs/10.1002/nme.4724.

[109] Y. Mellbin, H. Hallberg, and M. Ristinmaa. A combined crystal plasticity and graph-based vertex model of dynamic recrystallization at large deformations. *Modelling and Simulation in Materials Science and Engineering*, 23(4):045011, 2015. URL http://stacks.iop.org/0965-0393/23/i=4/a=045011.

[110] Y. Mellbin, H. Hallberg, and M. Ristinmaa. Recrystallization and texture evolution during hot rolling of copper, studied by a multiscale model combining crystal plasticity and vertex models. *Modelling and Simulation in Materials Science and Engineering*, 24(7):075004, 2016. doi: 10.1088/0965-0393/24/7/075004. URL http://stacks.iop.org/0965-0393/24/i=7/a=075004.

[111] N. Metropolis, A.W. Rosenbluth, M.N Rosenbluth, A.H. Teller, and E. Teller. Equation of state calculations by fast computing machines. *The Journal of Chemical Physics*, 21(6):1087–1092, 1953.

[112] C. Miehe, J. Schröder, and M. Becker. Computational homogenization analysis in finite elasticity: Material and structural instabilities on the micro- and macro-scales of periodic composites and their interaction. *Computer Methods in Applied Mechanics and Engineering*, 191(44):4971–5005, 2002. doi: 10.1016/S0045-7825(02)00391-2. URL http://www.sciencedirect.com/science/article/pii/S0045782502003912.

[113] N. Moelans, A. Godfrey, Y. Zhang, and D.J. Jensen. Phase-field simulation study of the migration of recrystallization boundaries. *Physical Review B*, 88(5):054103, 2013. doi: 10.1103/PhysRevB.88.054103. URL https://link.aps.org/doi/10.1103/PhysRevB.88.054103.

[114] M. Molkaraie and V. Gómez. Monte carlo methods for the ferromagnetic potts model using factor graph duality. *IEEE Transactions on Information Theory*, 64(12):7449–7464, 2018. ISSN 0018-9448. doi: 10.1109/TIT.2018.2857565. URL https://ieeexplore.ieee.org/abstract/document/8413107.

[115] B.L Mordike and T. Ebert. Magnesium: Properties — applications — potential. *Materials Science and Engineering: A*, 302(1):37 – 45, 2001. ISSN 0921-5093. doi: https://doi.org/10.1016/S0921-5093(00)01351-4. URL http://www.sciencedirect.com/science/article/pii/S0921509300013514.

[116] H. Moulinec and P. Suquet. A numerical method for computing the overall response of nonlinear composites with complex microstructure. *Computer Methods in Applied Mechanics and Engineering*, 157(1):69 – 94, 1998. ISSN 0045-7825. doi: https://doi.org/10.1016/S0045-7825(97)00218-1. URL http://www.sciencedirect.com/science/article/pii/S0045782597002181.

[117] W.H. Müller. Fourier Transforms and their application to the formation of textures and changes of morphology in solids. In *IUTAM Symposium on Transformation Problems in Composite and Active Materials*, pages 61–72. Kluwer Academic Publishers, 1998.

[118] M. Ortiz and E. A. Repetto. Nonconvex energy minimization and dislocation structures in ductile single crystals. *Journal of the Mechanics and Physics of Solids*, 47(2):397 – 462, 1999. ISSN 0022-5096. doi: https://doi.org/10.1016/S0022-5096(97)00096-3. URL http://www.sciencedirect.com/science/article/pii/S0022509697000963.

[119] M. Ortiz and L. Stainier. The variational formulation of viscoplastic constitutive updates. *Computer Methods in Applied Mechanics and Engineering*, 171(3-4):419–444, 1999. doi: https://doi.org/10.1016/S0045-7825(98)00219-9. URL http://www.sciencedirect.com/science/article/pii/S0045782598002199.

[120] H. Pan, Y. Ren, H. Fu, H. Zhao, L. Wang, X. Meng, and G. Qin. Recent developments in rare-earth free wrought magnesium alloys having high strength: A review. *Journal of Alloys and Compounds*, 663:321 – 331, 2016. ISSN 0925-8388. doi: https://doi.org/10.1016/j.jallcom.2015.12.057. URL http://www.sciencedirect.com/science/article/pii/S0925838815318478.

[121] P. Peczak. A monte carlo study of influence of deformation temperature on dynamic recrystallization. *Acta Metallurgica et Materialia*, 43(3):1279–1291, 1995.

[122] P. Peczak and M.J. Luton. A monte carlo study of the influence of dynamic recovery on dynamic recrystallization. *Acta Metallurgica et Materialia*, 41(1):59 – 71, 1993. ISSN 0956-7151. doi: https://doi.org/10.1016/0956-7151(93)90339-T. URL http://www.sciencedirect.com/science/article/pii/095671519390339T.

[123] P. Peczak and M.J. Luton. The effect of nucleation models on dynamic recrystallization I. homogeneous stored energy distribution. *Philosophical Magazine B*, 68(1):115–144, 1993. doi: 10.1080/13642819308215285. URL https://doi.org/10.1080/13642819308215285.

[124] N.J. Petch. The cleavage strengh of polycrystals. *J. of the Iron and Steel Inst.*, 174:25–28, 1953. URL https://ci.nii.ac.jp/naid/10019881123/en/.

[125] C. Pinna, Y. Lan, M.F. Kiu, P. Efthymiadis, M. Lopez-Pedrosa, and D. Farrugia. Assessment of crystal plasticity finite element simulations of the hot deformation of metals from local strain and orientation measurements. *International Journal of Plasticity*, 73:24 – 38, 2015. ISSN 0749-6419. doi: https://doi.org/10.1016/j.ijplas.2015.05.015. URL http://www.sciencedirect.

com/science/article/pii/S0749641915000947. Special Issue on Constitutive Modeling from Micro-Scale to Continuum in Honor of Prof. Frédéric Barlat.

[126] D. Ponge and G. Gottstein. Necklace formation during dynamic recrystallization: mechanisms and impact on flow behavior. *Acta Materialia*, 46 (1):69 – 80, 1998. ISSN 1359-6454. doi: https://doi.org/10.1016/S1359-6454(97)00233-4. URL http://www.sciencedirect.com/science/article/pii/S1359645497002334.

[127] E. Popova, Y. Staraselski, A. Brahme, R.K. Mishra, and K. Inal. Coupled crystal plasticity–probabilistic cellular automata approach to model dynamic recrystallization in magnesium alloys. *International Journal of Plasticity*, 66:85–102, 2015. doi: https://doi.org/10.1016/j.ijplas.2014.04.008. URL http://www.sciencedirect.com/science/article/pii/S0749641914000916.

[128] R.B. Potts. Some generalized order-disorder transformations. In *Mathematical Proceedings of the Cambridge Philosophical Society*, volume 48, pages 106–109. Cambridge University Press, 1952. doi: 10.1017/S0305004100027419.

[129] Mahesh Prakash and Paul W. Cleary. Modelling highly deformable metal extrusion using SPH. *Computational Particle Mechanics*, 2(1):19–38, May 2015. ISSN 2196-4386. doi: 10.1007/s40571-015-0032-0. URL https://doi.org/10.1007/s40571-015-0032-0.

[130] C.J. Luis Pérez. On the correct selection of the channel die in ECAP processes. *Scripta Materialia*, 50(3):387 – 393, 2004. ISSN 1359-6462. doi: https://doi.org/10.1016/j.scriptamat.2003.10.007. URL http://www.sciencedirect.com/science/article/pii/S135964620300664X.

[131] G.-Z. Quan, T.-W. Ku, W.-J. Song, and B.-S. Kang. The workability evaluation of wrought az80 magnesium alloy in hot compression. *Materials & Design*, 32(4):2462 – 2468, 2011. ISSN 0261-3069. doi: https://doi.org/10.1016/j.matdes.2010.11.025. URL http://www.sciencedirect.com/science/article/pii/S0261306910006515.

[132] D. Raabe. Introduction of a scalable three-dimensional cellular automaton with a probabilistic switching rule for the discrete mesoscale simulation of recrystallization phenomena. *Philosophical Magazine A*, 79(10):2339–2358, 1999. doi: 10.1080/01418619908214288. URL https://doi.org/10.1080/01418619908214288.

[133] D. Raabe. Cellular automata in materials science with particular reference to recrystallization simulation. *Annual review of materials research*, 32 (1):53–76, 2002. doi: 10.1146/annurev.matsci.32.090601.152855. URL https://doi.org/10.1146/annurev.matsci.32.090601.152855.

[134] D. Raabe and R.C. Becker. Coupling of a crystal plasticity finite-element model with a probabilistic cellular automaton for simulating primary static recrystallization in aluminium. *Modelling and Simulation in Materials Science and Engineering*, 8(4):445–462, jul 2000. doi: 10.1088/0965-0393/8/4/304. URL https://doi.org/10.1088/0965-0393/8/4/304.

[135] B. Radhakrishnan, G.B. Sarma, and T. Zacharia. Modeling the kinetics and microstructural evolution during static recrystallization—monte carlo simulation of recrystallization. *Acta Materialia*, 46(12):4415 – 4433, 1998. ISSN 1359-6454. doi: https://doi.org/10.1016/S1359-6454(98)00077-9. URL http://www.sciencedirect.com/science/article/pii/S1359645498000779.

[136] W.T Read and W. Shockley. Dislocation models of crystal grain boundaries. *Physical review*, 78(3):275, 1950. doi: 10.1103/PhysRev.78.275. URL https://link.aps.org/doi/10.1103/PhysRev.78.275.

[137] W. Roberts and B. Ahlblom. A nucleation criterion for dynamic recrystallization during hot working. *Acta Metallurgica*, 26(5):801–813, 1978. doi: https://doi.org/10.1016/0001-6160(78)90030-5. URL http://www.sciencedirect.com/science/article/pii/0001616078900305.

[138] A.D. Rollett, M.J. Luton, and D.J. Srolovitz. Microstructural simulation of dynamic recrystallization. *Acta Metallurgica et Materialia*, 40(1):43–55, 1992. doi: https://doi.org/10.1016/0956-7151(92)90198-N. URL http://www.sciencedirect.com/science/article/pii/095671519290198N.

[139] C. Rossard and P. Blain. Evolution de la structure de l'acier sous l'effet de la déformation plastique à chaud. *Mem. Sci. Rev. Metall*, 56:285–300, 1959.

[140] G. Sachs. Zur Ableitung einer Fliessbedingung. In *Mitteilungen der deutschen Materialprüfungsanstalten*, pages 94–97. Springer, 1929.

[141] Y. Saito, H. Utsunomiya, N. Tsuji, and T. Sakai. Novel ultra-high straining process for bulk materials—development of the accumulative roll-bonding (arb) process. *Acta Materialia*, 47(2):579 – 583, 1999. ISSN 1359-6454. doi: https://doi.org/10.1016/S1359-6454(98)00365-6. URL http://www.sciencedirect.com/science/article/pii/S1359645498003656.

[142] K. Saitoh and Y. Ohnishi. Sph analysis of ecap process by using grain refinement model. *MATERIALS TRANSACTIONS*, 50(1):19–26, 2009. doi: 10.2320/matertrans.MD200814.

[143] T. Sakai and J.J. Jonas. Overview no. 35: Dynamic recrystallization: Mechanical and microstructural considerations. *Acta Metallurgica*, 32(2):189 – 209, 1984. ISSN 0001-6160. doi: https://doi.org/10.1016/0001-6160(84)90049-X. URL http://www.sciencedirect.com/science/article/pii/000161608490049X.

[144] T. Sakai, A. Belyakov, R. Kaibyshev, H. Miura, and J.J. Jonas. Dynamic and post-dynamic recrystallization under hot, cold and severe plastic deformation conditions. *Progress in Materials Science*, 60:130–207, 2014. doi: https://doi.org/10.1016/j.pmatsci.2013.09.002. URL http://www.sciencedirect.com/science/article/pii/S0079642513000698.

[145] S. Schmidt, S. F. Nielsen, C. Gundlach, L. Margulies, X. Huang, and D. Juul Jensen. Watching the growth of bulk grains during recrystallization of deformed metals. *Science*, 305(5681):229–232, 2004. ISSN 0036-8075. doi: 10.1126/science.1098627. URL http://science.sciencemag.org/content/305/5681/229.

[146] J. Schröder, P. Neff, and V. Ebbing. Anisotropic polyconvex energies on the basis of crystallographic motivated structural tensors. *Journal of the Mechanics and Physics of Solids*, 56(12):3486 – 3506, 2008. ISSN 0022-5096. doi: https://doi.org/10.1016/j.jmps.2008.08.008. URL http://www.sciencedirect.com/science/article/pii/S0022509608001373.

[147] V.M. Segal, V.I. Reznikov, A.E. Drobyshevskii, and V.I. Kopylov. Plastic treatment of metals by simple shear. *Izv. Akad. Nauk SSSR, Met*, (1):115–123, 1981.

[148] P. Shanthraj, P. Eisenlohr, M. Diehl, and F. Roters. Numerically robust spectral methods for crystal plasticity simulations of heterogeneous materials. *International Journal of Plasticity*, 66:31 – 45, 2015. ISSN 0749-6419. doi: https://doi.org/10.1016/j.ijplas.2014.02.006. URL http://www.sciencedirect.com/science/article/pii/S0749641914000709. Plasticity of Textured Polycrystals In Honor of Prof. Paul Van Houtte.

[149] J.C. Simo. A framework for finite strain elastoplasticity based on maximum plastic dissipation and the multiplicative decomposition: Part I. Continuum formulation. *Computer Methods in Applied Mechanics and Engineering*, 66(2):199–219, 1988. doi: https://doi.org/10.1016/0045-7825(88)90076-X. URL http://www.sciencedirect.com/science/article/pii/004578258890076X.

[150] S.M. Sivakumar and M. Ortiz. Microstructure evolution in the equal channel angular extrusion process. *Computer Methods in Applied Mechanics and Engineering*, 193(48):5177 – 5194, 2004. ISSN 0045-7825. doi: https://doi.org/10.1016/j.cma.2004.01.036. URL http://www.sciencedirect.com/science/article/pii/S0045782504002713. Advances in Computational Plasticity.

[151] V. Sklenička, J. Dvořák, P. Král, M. Svoboda, and I. Saxl. Some factors affecting the creep behaviour of metallic materials processed by equal-channel angular pressing. *International Journal of Materials Research*, 100(6):762–766, 2009.

[152] A. Soares, A.C. Ferro, and M.A. Fortes. Computer simulation of grain growth in a bidimensional polycrystal. *Scripta Metallurgica*, 19(12):1491 – 1496, 1985. ISSN 0036-9748. doi: https://doi.org/10.1016/0036-9748(85)90157-7. URL http://www.sciencedirect.com/science/article/pii/0036974885901577.

[153] K. Soho, X. Lemoine, F. Abed-Meraim, and H. Zahrouni. Investigation of the effect of temper rolling on the texture evolution and mechanical behavior of if steels using multiscale simulation. *International Journal of Material Forming*, 10(1):29–42, Mar 2017. ISSN 1960-6214. doi: 10.1007/s12289-015-1257-4. URL https://doi.org/10.1007/s12289-015-1257-4.

[154] H. Somekawa and T. Mukai. Molecular dynamics simulation of grain boundary plasticity in magnesium and solid-solution magnesium alloys. *Computational Materials Science*, 77:424 – 429, 2013. ISSN 0927-0256. doi: https://doi.org/10.1016/j.commatsci.2013.04.043. URL http://www.sciencedirect.com/science/article/pii/S0927025613002152.

[155] S. Sreekala and M. Haataja. Recrystallization kinetics: A coupled coarse-grained dislocation density and phase-field approach. *Physical Review B*, 76(9):094109, 2007. doi: 10.1103/PhysRevB.76.094109. URL https://link.aps.org/doi/10.1103/PhysRevB.76.094109.

[156] D.J. Srolovitz, M.P. Anderson, G.S. Grest, and P.S. Sahni. Computer simulation of grain growth - III. Influence of a particle dispersion. *Acta Metallurgica*, 32(9):1429 – 1438, 1984. ISSN 0001-6160. doi: https://doi.org/10.1016/0001-6160(84)90089-0. URL http://www.sciencedirect.com/science/article/pii/0001616084900890.

[157] D.J. Srolovitz, M.P. Anderson, P.S. Sahni, and G.S. Grest. Computer simulation of grain growth - II. Grain size distribution, topology, and local dynamics. *Acta Metallurgica*, 32(5):793 – 802, 1984. ISSN 0001-6160. doi: https://doi.org/10.1016/0001-6160(84)90152-4. URL http://www.sciencedirect.com/science/article/pii/0001616084901524.

[158] D.J. Srolovitz, G.S. Grest, and M.P. Anderson. Computer simulation of recrystallization - I. homogeneous nucleation and growth. *Acta Metallurgica*, 34(9):1833 – 1845, 1986. ISSN 0001-6160. doi: https://doi.org/10.1016/0001-6160(86)90128-8. URL http://www.sciencedirect.com/science/article/pii/0001616086901288.

[159] A. Staroselsky and L. Anand. A constitutive model for hcp materials deforming by slip and twinning: Application to magnesium alloy AZ31B. *International journal of Plasticity*, 19(10):1843–1864, 2003.

[160] N. Sukumar. Construction of polygonal interpolants: a maximum entropy approach. *International Journal for Numerical Methods in Engi-*

neering, 61(12):2159–2181, 2004. doi: 10.1002/nme.1193. URL https://onlinelibrary.wiley.com/doi/abs/10.1002/nme.1193.

[161] D. Sun, M. Ponga, K. Bhattacharya, and M. Ortiz. Proliferation of twinning in hexagonal close-packed metals: Application to magnesium. *Journal of the Mechanics and Physics of Solids*, 112:368 – 384, 2018. ISSN 0022-5096. doi: https://doi.org/10.1016/j.jmps.2017.12.009. URL http://www.sciencedirect.com/science/article/pii/S0022509617306968.

[162] Y. Suwa, Y. Saito, and H. Onodera. Phase-field simulation of recrystallization based on the unified subgrain growth theory. *Computational Materials Science*, 44(2):286 – 295, 2008. ISSN 0927-0256. doi: https://doi.org/10.1016/j.commatsci.2008.03.025. URL http://www.sciencedirect.com/science/article/pii/S0927025608001699.

[163] S. Suwas, G. Gottstein, and R. Kumar. Evolution of crystallographic texture during equal channel angular extrusion (ecae) and its effects on secondary processing of magnesium. *Materials Science and Engineering: A*, 471(1):1 – 14, 2007. ISSN 0921-5093. doi: https://doi.org/10.1016/j.msea.2007.05.030. URL http://www.sciencedirect.com/science/article/pii/S092150930700812X.

[164] T. Takaki, T. Hirouchi, Y. Hisakuni, A. Yamanaka, and Y. Tomita. Multi-phase-field model to simulate microstructure evolutions during dynamic recrystallization. *Materials Transactions*, 49(11):2559–2565, 2008. doi: 10.2320/matertrans.MB200805. URL https://doi.org/10.2320/matertrans.MB200805.

[165] T. Takaki, C. Yoshimoto, A. Yamanaka, and Y. Tomita. Multiscale modeling of hot-working with dynamic recrystallization by coupling microstructure evolution and macroscopic mechanical behavior. *International Journal of Plasticity*, 52:105 – 116, 2014. ISSN 0749-6419. doi: https://doi.org/10.1016/j.ijplas.2013.09.001. URL http://www.sciencedirect.com/science/article/pii/S0749641913001733. In Honor of Hussein Zbib.

[166] A. Takayama, X. Yang, H. Miura, and T. Sakai. Continuous static recrystallization in ultrafine-grained copper processed by multi-directional forging. *Materials Science and Engineering: A*, 478(1):221 – 228, 2008. ISSN 0921-5093. doi: https://doi.org/10.1016/j.msea.2007.05.115. URL http://www.sciencedirect.com/science/article/pii/S0921509307011197.

[167] J.C. Tan and M.J. Tan. Dynamic continuous recrystallization characteristics in two stage deformation of Mg–3Al–1Zn alloy sheet. *Materials Science and Engineering: A*, 339(1):124–132, 2003. doi: https://doi.org/10.1016/S0921-5093(02)00096-5. URL http://www.sciencedirect.com/science/article/pii/S0921509302000965.

[168] G.I. Taylor. Plastic strain in metals. *J. Inst. Metals*, 62:307–324, 1938.

[169] G.E. Totten, K. Funatani, and L. Xie. *Handbook of metallurgical process design*. CRC press, 2004.

[170] A.D. Tutcuoglu, Y. Hollenweger, A. Stoy, and D.M. Kochmann. High- vs. low-fidelity models for dynamic recrystallization in copper. *Under review*, 2019.

[171] A.D. Tutcuoglu, S. Kumar, Y. Hollenweger, and D.M. Kochmann. A multi-scale meshfree approach to modeling ECAE. *In Preparation*, 2019.

[172] A.D. Tutcuoglu, A. Vidyasagar, K. Bhattacharya, and D.M. Kochmann. Stochastic modeling of discontinuous dynamic recrystallization at finite strains in hcp metals. *Journal of the Mechanics and Physics of Solids*, 122:590 – 612, 2019. ISSN 0022-5096. doi: https://doi.org/10.1016/j.jmps.2018.09.032. URL http://www.sciencedirect.com/science/article/pii/S0022509618303569.

[173] I. Ulacia, N.V. Dudamell, F. Gálvez, S. Yi, M.T. Pérez-Prado, and I. Hurtado. Mechanical behavior and microstructural evolution of a Mg AZ31 sheet at dynamic strain rates. *Acta Materialia*, 58(8):2988–2998, 2010. doi: https://doi.org/10.1016/j.actamat.2010.01.029. URL http://www.sciencedirect.com/science/article/pii/S1359645410000431.

[174] R.Z. Valiev and T.G. Langdon. Principles of equal-channel angular pressing as a processing tool for grain refinement. *Progress in Materials Science*, 51(7):881 – 981, 2006. ISSN 0079-6425. doi: https://doi.org/10.1016/j.pmatsci.2006.02.003. URL http://www.sciencedirect.com/science/article/pii/S0079642506000120.

[175] R.A Vandermeer, D.J. Jensen, and E. Woldt. Grain boundary mobility during recrystallization of copper. *Metallurgical and Materials Transactions A*, 28 (3):749–754, 1997. doi: 10.1007/s11661-997-0061-2. URL https://doi.org/10.1007/s11661-997-0061-2.

[176] A. Vidyasagar, W.L. Tan, and D.M. Kochmann. Predicting the effective response of bulk polycrystalline ferroelectric ceramics via improved spectral phase field methods. *Journal of the Mechanics and Physics of Solids*, 2017. doi: https://doi.org/10.1016/j.jmps.2017.05.017. URL http://www.sciencedirect.com/science/article/pii/S0022509617300595.

[177] A. Vidyasagar, A.D. Tutcuoglu, and D.M. Kochmann. Deformation patterning in finite-strain crystal plasticity by spectral homogenization with application to magnesium. *Computer Methods in Applied Mechanics and Engineering*, 335:584 – 609, 2018. ISSN 0045-7825. doi: https://doi.org/10.1016/j.cma.2018.03.003. URL http://www.sciencedirect.com/science/article/pii/S0045782518301208.

[178] A. Vinogradov, M. Maruyama, Y. Kaneko, and S. Hashimoto. Effect of dislocation hardening on monotonic and cyclic strength of severely deformed copper. *Philosophical Magazine*, 92(6):666–689, 2012. doi: 10.1080/14786435.2011.630693. URL https://doi.org/10.1080/14786435.2011.630693.

[179] S.G. Vogel, D.J. Alexander, I.J. Beyerlein, M.A. Bourke, and D.W. Brown. Investigation of texture in ecap materials using neutron diffraction. Technical report, Los Alamos National Laboratory, 2003.

[180] L. Wang, G. Fang, and L. Qian. Modeling of dynamic recrystallization of magnesium alloy using cellular automata considering initial topology of grains. *Materials Science and Engineering: A*, 711:268–283, 2018. doi: https://doi.org/10.1016/j.msea.2017.11.024. URL http://www.sciencedirect.com/science/article/pii/S0921509317314740.

[181] H.-R. Wenk. Plasticity modeling in minerals and rocks texture and anisotropy: Preferred orientations in polycrystals and their effect on materials properties ed u kocks et al. *Texture and Anisotropy. Cambridge University Press, Cambridge*, pages 560–595, 1998.

[182] H.-R. Wenk. A voyage through the deformed earth with the self-consistent model. *Modelling and Simulation in Materials Science and Engineering*, 7 (5):699, 1999. doi: 10.1088/0965-0393/7/5/304. URL https://doi.org/10.1088/0965-0393/7/5/304.

[183] H.-R. Wenk and C.N. Tomé. Modeling dynamic recrystallization of olivine aggregates deformed in simple shear. *Journal of Geophysical Research: Solid Earth*, 104(B11):25513–25527, 1999. doi: 10.1029/1999JB900261. URL https://agupubs.onlinelibrary.wiley.com/doi/abs/10.1029/1999JB900261.

[184] A. Williamson and J.-P. Delplanque. Investigation of dynamic abnormal grain growth using the Monte Carlo Potts method. *Computational Materials Science*, 124:114 – 129, 2016. ISSN 0927-0256. doi: https://doi.org/10.1016/j.commatsci.2016.07.025. URL http://www.sciencedirect.com/science/article/pii/S0927025616303524.

[185] M. Winning and A.D. Rollett. Transition between low and high angle grain boundaries. *Acta materialia*, 53(10):2901–2907, 2005. doi: https://doi.org/10.1016/j.actamat.2005.03.005. URL http://www.sciencedirect.com/science/article/pii/S1359645405001503.

[186] M. Winning, G. Gottstein, and L.S. Shvindlerman. Stress induced grain boundary motion. *Acta materialia*, 49(2):211–219, 2001. doi: https://doi.org/10.1016/S1359-6454(00)00321-9. URL http://www.sciencedirect.com/science/article/pii/S1359645400003219.

[187] F. Witte, N. Hort, C. Vogt, S. Cohen, K.U. Kainer, R. Willumeit, and F. Feyerabend. Degradable biomaterials based on magnesium corrosion. *Current Opinion in Solid State and Materials Science*, 12(5):63 – 72, 2008. ISSN 1359-0286. doi: https://doi.org/10.1016/j.cossms.2009.04.001. URL http://www.sciencedirect.com/science/article/pii/S1359028609000357.

[188] D. Wolf. A Read-Shockley model for high-angle grain boundaries. *Scripta Metallurgica*, 23(10):1713–1718, 1989. doi: https://doi.org/10.1016/0036-9748(89)90348-7. URL http://www.sciencedirect.com/science/article/pii/0036974889903487.

[189] W. Xu, N. Birbilis, G. Sha, Y. Wang, J.E. Daniels, Y. Xiao, and M. Ferry. A high-specific-strength and corrosion-resistant magnesium alloy. *Nature materials*, 14(12):1229, 2015. doi: 10.1038/nmat4435. URL https://doi.org/10.1038/nmat4435.

[190] T. Yamaguchi, K. Ohyabu, H. Kuramae, H. Morimoto, Y. Morita, and E. Nakamachi. Process metallurgy analyses of sheet rolling by multi-scale finite element method based on thermal elastic crystal plasticity theory. *AIP Conference Proceedings*, 1618(1):319–322, 2014. doi: 10.1063/1.4897738. URL https://aip.scitation.org/doi/abs/10.1063/1.4897738.

[191] N. Yazdipour, C.H.J. Davies, and P.D. Hodgson. Microstructural modeling of dynamic recrystallization using irregular cellular automata. *Computational Materials Science*, 44(2):566 – 576, 2008. ISSN 0927-0256. doi: https://doi.org/10.1016/j.commatsci.2008.04.027. URL http://www.sciencedirect.com/science/article/pii/S0927025608002255.

[192] S. You, Y. Huang, K.U. Kainer, and N. Hort. Recent research and developments on wrought magnesium alloys. *Journal of Magnesium and Alloys*, 5(3):239 – 253, 2017. ISSN 2213-9567. doi: https://doi.org/10.1016/j.jma.2017.09.001. URL http://www.sciencedirect.com/science/article/pii/S2213956717300464.

[193] J. Zhang and S.P. Joshi. Phenomenological crystal plasticity modeling and detailed micromechanical investigations of pure magnesium. *Journal of the Mechanics and Physics of Solids*, 60(5):945 – 972, 2012. ISSN 0022-5096. doi: https://doi.org/10.1016/j.jmps.2012.01.005. URL http://www.sciencedirect.com/science/article/pii/S0022509612000130.

[194] J. Zhang, W. Li, and Z. Guo. Static recrystallization and grain growth during annealing of an extruded Mg—Zn-–Zr-–Er magnesium alloy. *Journal of Magnesium and Alloys*, 1(1):31 – 38, 2013. ISSN 2213-9567. doi: https://doi.org/10.1016/j.jma.2013.02.012. URL http://www.sciencedirect.com/science/article/pii/S2213956713000133.

[195] J. Zhang, S. Liu, R. Wu, L. Hou, and M. Zhang. Recent developments in high-strength Mg-RE-based alloys: Focusing on Mg-Gd and Mg-Y systems. *Journal of Magnesium and Alloys*, 6(3):277 – 291, 2018. ISSN 2213-9567. doi: https://doi.org/10.1016/j.jma.2018.08.001. URL http://www.sciencedirect.com/science/article/pii/S2213956718300501.

[196] S. Zhang and S. Karato. Lattice preferred orientation of olivine aggregates deformed in simple shear. *Nature*, 375(6534):774, 1995. doi: 10.1038/375774a0. URL https://doi.org/10.1038/375774a0.

[197] P. Zhao, T.S.E. Low, Y. Wang, and S.R. Niezgoda. An integrated full-field model of concurrent plastic deformation and microstructure evolution: Application to 3D simulation of dynamic recrystallization in polycrystalline copper. *International Journal of Plasticity*, 80:38–55, 2016. doi: https://doi.org/10.1016/j.ijplas.2015.12.010. URL http://www.sciencedirect.com/science/article/pii/S0749641915002156.

[198] P. Zhao, Y. Wang, and S. R Niezgoda. Microstructural and micromechanical evolution during dynamic recrystallization. *International Journal of Plasticity*, 100:52–68, 2018. doi: https://doi.org/10.1016/j.ijplas.2017.09.009. URL http://www.sciencedirect.com/science/article/pii/S0749641917304345.

[199] A.P. Zhilyaev and T.G. Langdon. Using high-pressure torsion for metal processing: Fundamentals and applications. *Progress in Materials Science*, 53(6):893 – 979, 2008. ISSN 0079-6425. doi: https://doi.org/10.1016/j.pmatsci.2008.03.002. URL http://www.sciencedirect.com/science/article/pii/S007964250800025X.

[200] Y.T. Zhu and T.C. Lowe. Observations and issues on mechanisms of grain refinement during ECAP process. *Materials Science and Engineering: A*, 291(1):46 – 53, 2000. ISSN 0921-5093. doi: https://doi.org/10.1016/S0921-5093(00)00978-3. URL http://www.sciencedirect.com/science/article/pii/S0921509300009783.